DELAYED FORMATION AND INTRAMOLECULAR MOTION OF MUONIUM-SUBSTITUTED FREE RADICALS

by

Szedung Sun-Mack
B.Sc., Peking University, Beijing, China, 1982
M.Sc., University of Maryland, Maryland, USA, 1987

THESIS SUBMITTED IN PARTIAL FULFILLMENT OF
THE REQUIREMENTS FOR THE DEGREE OF
DOCTOR OF PHILOSOPHY
in the Department
of
Physics

SIMON FRASER UNIVERSITY
January 1994

APPROVAL

Name: Szedung Sun-Mack
Degree: Doctor of Philosophy
Title of thesis: Delayed Formation and Intramolecular Motion of Muonium-Substituted Free Radicals

Examining Committee:

Chairperson: Dr. M. W. W. Thewalt, Professor

Senior Supervisor: Dr. P. W. Percival, Professor

Dr. A. S. Arrott, Professor

Dr. J. F. Cochran, Professor

Internal Examiner: Dr. J. D'Auria, Professor

External Examiner: Dr. D. Williams, Professor
University of British Columbia

Date Approved:

PARTIAL COPYRIGHT LICENSE

Title of Thesis/Project/Extended Essay

Delayed Formation and Intramolecular
Motion of Muonium-Substituted
Free Radicals

Author:
(signature)

SZEDUNG SUN-MACK
(name)

March, 21, 94
(date)

ABSTRACT

The rf technique has been implemented at TRIUMF to study radicals which are too slowly formed to give coherent signals with the more traditional technique, transverse-field muon spin rotation (TF-μSR). While the basic technique was developed at the University of Tokyo Meson Science Laboratory using a pulsed beam, further development was neccessary because of TRIUMF's continuous beam. Several versions of a birdcage cavity, with resonance frequencies ranging from 150 MHz to 180 MHz, have been developed. The dispersion relation of the cavity, the rf magnetic field inside the cavity, and the conditions required to produce a circularly polarized field are calculated. Both theory and experiment find that a circularly polarized field is produced when the angle between the rf input and ground is 135^o and elliptically polarized when the angle is 45^o.

The basic formulas of longitudinal muon polarization for both diamagnetic and radical systems under rf irradiation are also reviewed. It is found that the rf frequency should be chosen such that the rf resonance magnetic fields are far away from zero-crossing, far away from all muon level-crossing resonance (μLCR) fields, and as small as possible.

In a series of the rf integral muon spin resonance (rf-IμSR) experiments, muonium signals were successfully detected in water, ice, fused quartz, and powdered C_{60}. Radical signals were successfully detected in powdered C_{60}, neat liquid C_6H_6, neat liquid C_6F_6, a saturated solution of C_6H_5OH in ethanol, and $C_6H_3(OH)_3$ in aqueous solutions of concentrations 2 M and 5 M. Most importantly, also detected were radicals slowly formed from $C_6H_3(OH)_3$ in dilute aqueous solution (0.02 M). This was the first time that a radical not observed in TF-μSR had been detected in a rf-IμSR experiment.

TF-μSR and μLCR techniques were used to study muonium-substituted isopropyl. The measurements of hyperfine coupling constants for these radicals covered a wide temperature range, including both gas and liquid phases. By fitting theoretical models to the experimental data, it was found that: (1) At the minimum energy configuration, Mu eclipses the p_z orbital of C_α, and the rotation barrier between the staggered and eclipsed configuration is 3.5 kJ/mol. (2) Increased C-Mu bond length in muonium-substituted radicals provides the key role for the isotope shifts in hyperfine coupling constants.

To my father

ACKNOWLEDGMENTS

I would like to express my gratitude to Professor Paul W. Percival, my senior supervisor, for his guidance and support over the years. This support never flagged even when I moved 3000 miles away, as he always kept me up to date on SFUMU activities. Tapping his broad knowledge of chemistry and prodigious memory helped to quickly guide me through a vast literature. Rapid feedback on my thesis drafts was also greatly appreciated!

The birdcage rf cavity could never have been built without the assistance of Dr. Syd R. Kreitzman, a veritable wizard of RF cavities. Over smoldering soldering irons and butane torches we fabricated a series of prototype cavities.

Dr. Emil Roduner often had useful suggestions when it looked like there was no light at the end of the tunnel.

Dr. Jean-Claude Brodovitch provided technical assistance for the experiments in this thesis, and was always there when I needed him. Dr. Dake Yu, friend and fellow student, got me started in the right direction when I first joined the SFUMU group. I am grateful to Ms. Brenda Addison-Jones for mailing copies of important logbook pages and for the buckyball structure figure. Dr. Siu-keung Leung and Ms. Julie Bartlett of the SFUMU group were invaluable, as were the TRIUMF M15 and M20 beam line staff members: Mr. Keith Hoyle, Mr. Curtis Ballard, and Mr. John Worden. The TRIUMF machine shop always got things built in time for the next experiment.

The time and attention that Dr. John F. Cochran spent reading and correcting early drafts of this thesis are greatly appreciated.

I would like to thank my husband for not complaining when my exper-

iments started just as his were finishing, for turning my rough drafts into readable English, and for coming home from work everyday to babysit while I worked at the terminal. Some day my now 9 month old daughter, Yvonne, will be able to read this and will know that I appreciated her taking those long naps so Mommy could write her thesis.

Finally, I would like to thank my parents and sister's family for their support over the years. Dad, now there's another physicist in the family.

Contents

List of Tables

List of Figures

Chapter 1

Introduction

1.1 Generalities

The positive muon, μ^+, is an unstable particle first discovered in 1937 as a component of cosmic rays by Anderson and Neddermeyer [1]. The μ^+ has a rest mass equal to about one ninth the mass of a proton, or 207 times heavier than the electron, and has the same spin and charge as a proton. Some of the properties of μ^+ are summarized in table 1.1 [2].

It was not until 1957 that scientists realized that the positive muon could form a bound state with an electron [3]. This one-electron atom was named muonium (Mu = μ^+e^-). In most gases, liquids, and solids, the μ^+ captures an electron from the medium during the final stages of its thermalization process to form muonium [4, 5, 6]. Some of the properties of Mu are given in table 1.2 [7]. Although muonium has only one ninth the rest mass of a hydrogen atom, the reduced mass in Mu is 0.996 that in hydrogen, and consequently the Bohr radius and ionization potentials of H and Mu are essentially the same. Chemically, Mu can be thought of simply as a light isotope of hydrogen. Its radioactive character enables one to observe it under conditions where H would be obscured, and as a

Table 1.1: Some properties of the positive muon [2].

Property	**Values**
Mass	105.6595 MeV/c^2
	= 206.76835 m_e[a]
	= 0.1126096 m_p[b]
	= 0.7570 m_π[c]
Spin	$\hbar/2$
Charge	+e
Magnetic moment (μ_μ)	4.49048×10^{-23} erg/G
	=3.1833452 μ_p[d]
	=0.004834 μ_e[e]
g-factor (g_μ)	2.002331848
	= 1.000006 g_e[f]
Gyromagnetic ratio ($\gamma_\mu/2\pi$)	13.55342 kHz/G
Mean lifetime	2.19714 μs

---

[a] electron mass.

[b] proton mass.

[c] pion mass.

[d] proton magnetic moment.

[e] electron magnetic moment.

[f] electron g-factor.

Table 1.2: Some properties of muonium [7].

Property	**Values**
Mass	207.8 m_e[a]
	= 0.1131 m_H[b]
Reduced mass	0.9956 m_H
Bohr radius	0.5315×10^{-8} cm
	= 1.0044 a_o[c]
Ionization potential	13.54 eV
	= 0.9956 of H
Thermal de Broglie wavelength (300K)	2.979×10^{-8} cm
	= 2.967 of H
Hyperfine coupling constant (hfcc)	4463 MHz
Mean thermal velocity (300K)	0.75×10^{6} cm/s
	= 2.967 of H

---

[a] electron mass.

[b] hydrogen mass.

[c] Bohr radius of hydrogen.

light isotope Mu is a highly sensitive measure of mass-dependent effects.

In 1963 Brodskii [8] suggested that muonated free radicals could be formed by the addition of Mu to unsaturated molecules. Roduner *et al.* first observed muonated radicals in the liquid phase in 1978 [9].

Several experimental techniques have been developed. One of them is transverse-field muon spin rotation (TF-μSR). In a TF-μSR experiment, a beam of polarized positive muons is stopped in a target mounted in a uniform magnetic field perpendicular to the muon spin polarization direction, and the time evolution of muon spin polarization is monitored. The muon-electron hyperfine coupling constants (hfcc) in many muonated free radicals have been measured by TF-μSR spectroscopy [9, 10]. Details of the technique will be described later in this chapter.

In 1984, Abragam pointed out the possibility of doing muon level-crossing resonance (μLCR) spectroscopy in μSR experiments [11]. The μLCR phenomenon occurs when a muon spin transition frequency is matched, by means of varying the applied magnetic field, to that of some other nucleus in the coupled spin system. At such a field, a pair of nearly degenerate levels having different spin orientations for the muon and another nucleus are mixed by the hyperfine interaction, resulting in a resonant-like change in the muon asymmetry as the magnetic field is swept. (Further details of the μLCR technique will be given later in this chapter.) This spectroscopic method allows the measurement of nuclear hfcc other than that of the muon in muonium-substituted free radicals. μLCR studies on muonated free radicals have been carried out since the middle of 1985 [12, 13].

A μLCR experiment can yield the other nuclear (*i.e.* non-muon) hyperfine parameters of a radical when the ***muon*** hfcc of this radical is already known. In the case of fast reactions, the technique of TF-μSR provides the means to determine muon hfcc. But for many samples of practical chemical interest it is not possible to make the usual TF-μSR measurement because the radical is formed too slowly to give a coherent signal. Therefore, further development was deemed necessary. The rf resonance technique was designed to solve this problem and is the primary focus of this thesis.

1.2 The μSR signal

Positive muons are obtained from positive pions which decay according to [2]

$$\pi^+ \longrightarrow \mu^+ + \nu_\mu \tag{1.1}$$

with an average lifetime of $\tau_\pi = 26$ ns. All other channels account for only 0.01% of π^+ decays [14]. Pions can be produced by proton collisions with nuclei. Typical nuclei used for pion production at accelerators are copper and beryllium, *e.g.*,

$$p + {}^9\mathrm{Be} \rightarrow \pi^+ + \mathrm{X} \tag{1.2}$$

This reaction is efficient at producing pions at the TRIUMF maximum proton kinetic energy, 500 MeV. When a muon decays with a lifetime 2.2 μs, it emits a positron, a neutrino, and an antineutrino [15]

$$\mu^+ \longrightarrow e^+ + \nu_e + \bar{\nu}_\mu \tag{1.3}$$

As a consequence of the conservation of energy, linear momentum, and angular momentum in this three-body decay, the positron is preferentially emitted along the direction of the muon spin [16]. The positrons possess sufficient energy (average kinetic energy is about 35 MeV [17, 18]) to be able to leave the sample. Detection of these positrons serves as a probe of the spin state of the muon in the sample at the time of the decay.

The quantitative treatment of μ^+ decay is based on the weak interaction Hamiltonian which has the form of a current-current interaction [2]. The theoretical positron spectrum has been derived and is given by [19]:

$$\frac{dN(\epsilon,\theta)}{d\epsilon d\Omega} = \frac{\epsilon^2}{2\pi}[(3-2\epsilon) - P_o(1-2\epsilon)\cos\theta] \tag{1.4}$$

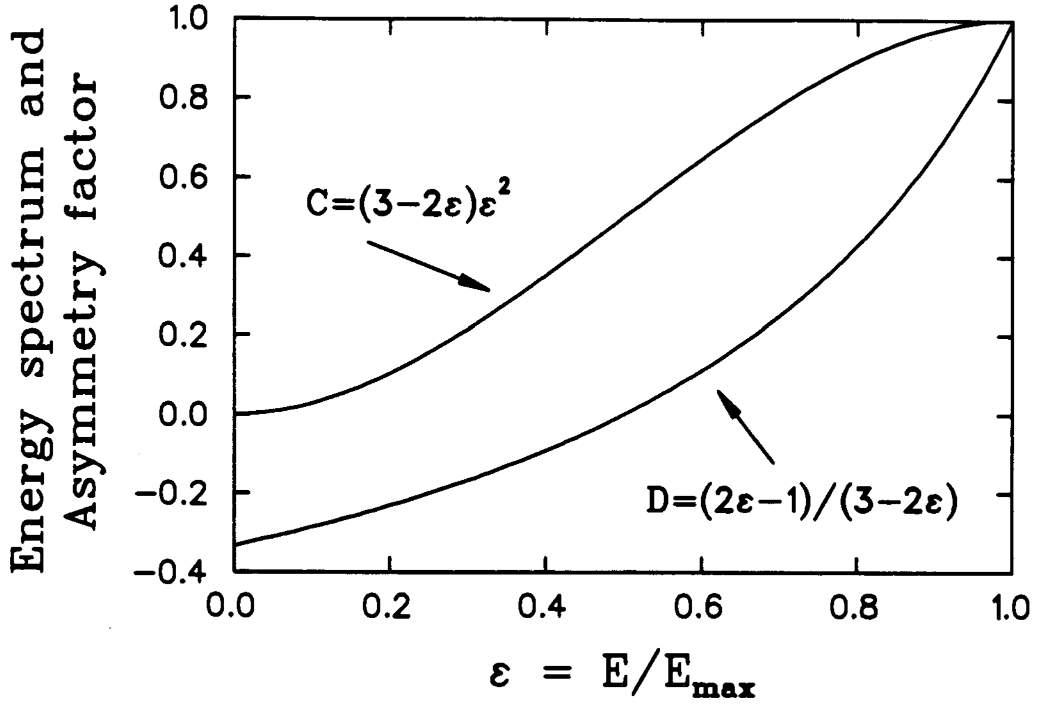

Figure 1.1: The positron energy spectrum C (upper curve) and the energy dependence of the asymmetry parameter D (lower curve) from μ^+ decay with $P_o = 1$ [2].

$$= \frac{C}{2\pi}(1 + D\cos\theta) \tag{1.5}$$

where $N(\epsilon, \theta)$ is the number of positrons with energy ϵ emitted at angle θ with respect to the initial spin polarization of the incoming muons, $\epsilon = E/E_{max}$ is the positron energy in units of the maximum possible energy, $E_{max} = m_\mu/2 = 52.3$ MeV, and P_o stands for the degree of spin polarization of the decaying muons. The positron energy spectrum, $C = \epsilon^2(3\text{-}2\epsilon)$, and the asymmetry parameter, $D = P_o(2\epsilon\text{-}1)/(3\text{-}2\epsilon)$, for $P_o = 1$ are shown in figure 1.1.

In practice, the positrons are detected with an efficiency $\eta(\epsilon)$ which is not constant over their energy range. The observed positron probability distribution then becomes:

$$\frac{dN(\theta)}{d\Omega} = \int_0^1 \frac{dN(\epsilon,\theta)}{d\epsilon d\Omega}\eta(\epsilon)d\epsilon \tag{1.6}$$

$$= \bar{\eta}(1+\bar{A}\cos\theta) \tag{1.7}$$

where $\bar{\eta}$ is the average positron detection efficiency and $\bar{A}$ is the average asymmetry. If positrons of all energies were detected with the same efficiency, the observed average asymmetry $\bar{A}$ would be $P_o/3$. In practice, the detection efficiency of low energy positrons is reduced because the lowest energy positrons are absorbed by matter before reaching the detectors, resulting in $\bar{A}$ larger than $P_o/3$. This effect is counterbalanced by a reduction of the average asymmetry due to the finite detector solid angle. As a result, an empirical muon asymmetry A, which satisfies the expression of counting rate in the positron detector [19],

$$\frac{dN(t)}{dt} = \frac{1}{\tau_\mu}(1+A\cos\theta) \tag{1.8}$$

is introduced.

1.3 The Transverse field μSR (TF-μSR) technique and its spectrum of the diamagnetic signal.

In transverse field μSR (TF-μSR) experiments, an external field B_o is applied perpendicular to the muon spin polarization, causing the muon spins to precess at a muon Larmor angular frequency $\omega_\mu = \gamma_\mu B_o$, where γ_μ is the muon gyromagnetic ratio (table 1.1). This causes θ in equation 1.8 to be replaced by $\omega_\mu t + \phi_\mu$, where ϕ_μ is the initial phase. Thus the probability of detecting the decay positron rises and falls in time as the precessing muon spin swings past the fixed positron detectors.

This positron detection probability also decays exponentially with a lifetime $\tau_\mu = 2.2$ μs due to the disintegration of the muon. Incorporating all the effects mentioned above, the positron detection probability can be expressed by

$$\frac{dN(t)}{dt} = \frac{1}{\tau_\mu} N_o e^{-t/\tau_\mu}[1 + A_D \cos(\omega_\mu t + \phi_\mu)] + BG \tag{1.9}$$

where N_o is a normalization factor, A_D is the amplitude which represents the fraction of diamagnetic species, and BG is a time-independent background due to random accidental events. A diamagnetic state includes free muons, solvated or trapped muons, and any diamagnetic molecule incorporating the muon, such as MuH, MuOH, $C_6H_{13}Mu$, and so on.

Experimentally, one collects data by recording the arrival time t_o of the muon and the decay time t_1, and constructing an elapsed-time histogram for $t = t_1 - t_o$. Thus, the expected number of positron counts in a histogram bin of width Δt at t_i is given approximately by $[dN(t_i)/dt]\Delta t$.

In general, the TF-μSR time histogram has the form [20]

$$\frac{dN(t)}{dt} = N_o e^{-t/\tau_\mu}[1 + A(t)] + BG \tag{1.10}$$

where $A(t)$ is the asymmetry, usually given by the summation of the diamagnetic signal $A_D(t)$ and the muonium signal $A_M(t)$. In the absence of muonium, $A(t)$ is given by

$$\begin{aligned} A(t) &= A_D(t) \\ &= A_D e^{-\lambda_\mu t} \cos(\omega_\mu t + \phi_\mu) \end{aligned} \tag{1.11}$$

where λ_μ is the decay rate of the diamagnetic species (and usually negligible).

By varying the parameters N_o, A_D, ω_μ, ϕ_μ, λ_μ, and BG, the optimal fit of equations 1.10 and 1.11 to the entire histogram may be determined.

A typical TF-μSR time spectrum is shown in figure 1.2, its dominant feature being the exponential muon lifetime upon which is superimposed the oscillating muon asymmetry.

1.4 Muonium and its TF-μSR spectrum.

Muonium is a 'two-spin-1/2' system. In Mu, the muon spin is not only coupled to an external magnetic field B_o but also to the electron spin *via* the isotropic hyperfine (hf) interaction [21]. The spin Hamiltonian for Mu in angular frequency units is thus given by

$$\begin{aligned}\hat{H} &= \gamma_e \vec{S}^e \cdot \vec{B}_o - \gamma_\mu \vec{S}^\mu \cdot \vec{B}_o + A_\mu \vec{S}^\mu \cdot \vec{S}^e \\ &= \omega_e S_z^e - \omega_\mu S_z^\mu + A_\mu \vec{S}^\mu \cdot \vec{S}^e \qquad (1.12)\end{aligned}$$

where γ_i is the gyromagnetic ratio of the particle $i (i = e, \mu)$, ω_i are Zeeman angular frequencies ($\omega_i = \gamma_i B_o$, and $i = e, \mu$), and A_μ is the muon hyperfine constant in angular frequency units. The eigenstates and eigenenergies are given in table 1.3 [7].

The energies as a function of the applied magnetic field are displayed in the form of a Breit-Rabi diagram in figure 1.3. In the absence of a magnetic field, the four states form a triplet and a singlet system. When a magnetic field is applied to muonium, the degeneracy of the triplet is lifted.

Muonium is readily detected by TF-μSR in low fields. There are four spectroscopic transitions which are magnetic dipole allowed [7]. In the low fields, two of them (ω_{14} and ω_{43}, which are shown as broken lines in figure 1.3) are of the order of $A_\mu/2\pi$ (= 4.5 GHz). Since the experimental time resolution of TF-μSR is about 2 ns for conventional apparatus, these two transitions are not observable. For the other two transitions, ω_{12} and

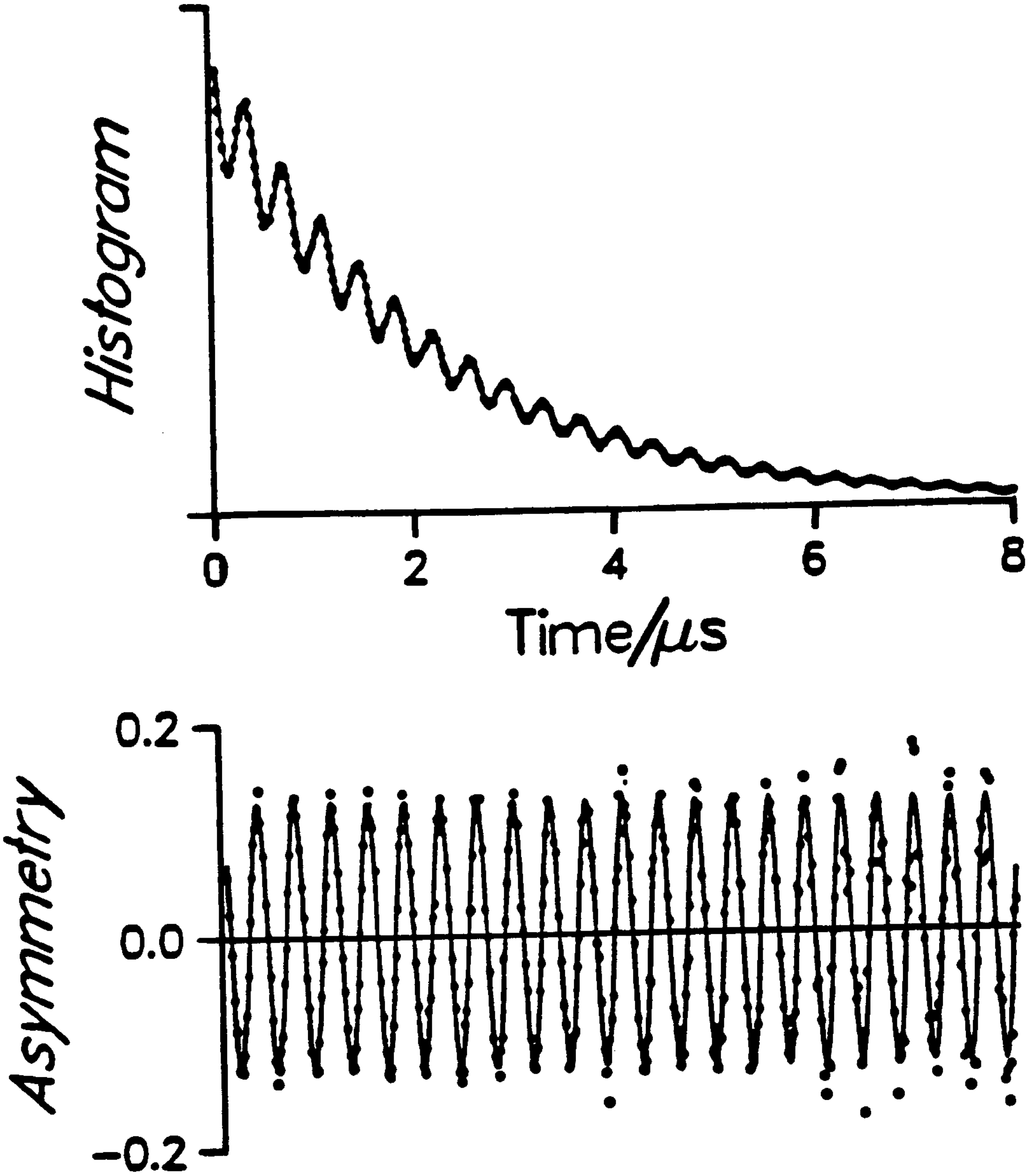

Figure 1.2: TF-μSR time histogram (top) and asymmetry A_D(t) (bottom) of the diamagnetic signal from water in a transverse field of 200 G. The asymmetry A_D(t) is obtained from the time histogram by subtraction of the background and dividing out the exponential decay.

Table 1.3: Eigenstates, eigenvalues, and TF-μSR transition frequencies of $\hat{H}_o$ for an electron-muon system with isotropic hyperfine coupling constant A_μ [7].

State	**Energy**[a]
$\mid 1 >=\mid \alpha^e\alpha^\mu >$	$\omega_1 = 0.25A_\mu + \omega_-$
$\mid 2 >= s \mid \beta^e\alpha^\mu > +c \mid \alpha^e\beta^\mu >$	$\omega_2 = 0.25A_\mu + \Delta$
$\mid 3 >=\mid \beta^e\beta^\mu >$	$\omega_3 = 0.25A_\mu - \omega_-$
$\mid 4 >= c \mid \beta^e\alpha^\mu > -s \mid \alpha^e\beta^\mu >$	$\omega_4 = -0.75A_\mu - \Delta$
Possible TF-μSR transition frequencies [7]:	
$\omega_{12} = \omega_1 - \omega_2 = \omega_- - \Delta$ $\omega_{23} = \omega_2 - \omega_3 = \omega_- + \Delta$ $\omega_{14} = \omega_1 - \omega_4 = \omega_- + \Delta + A_\mu$ $\omega_{43} = \omega_4 - \omega_3 = \omega_- - \Delta - A_\mu$	
The parameters are:	
$c = 1/\sqrt{2}(1 + \omega_+/\sqrt{\omega_+^2 + A_\mu^2})^{\frac{1}{2}}$ $s = 1/\sqrt{2}(1 - \omega_+/\sqrt{\omega_+^2 + A_\mu^2})^{\frac{1}{2}}$ $\omega_- = 1/2(\omega_e - \omega_\mu)$ $\omega_+ = 1/2(\omega_e + \omega_\mu)$ $\Delta = 1/2[\sqrt{\omega_+^2 + A_\mu^2} - A_\mu]$	

---

[a] Energies are in units of angular frequency.

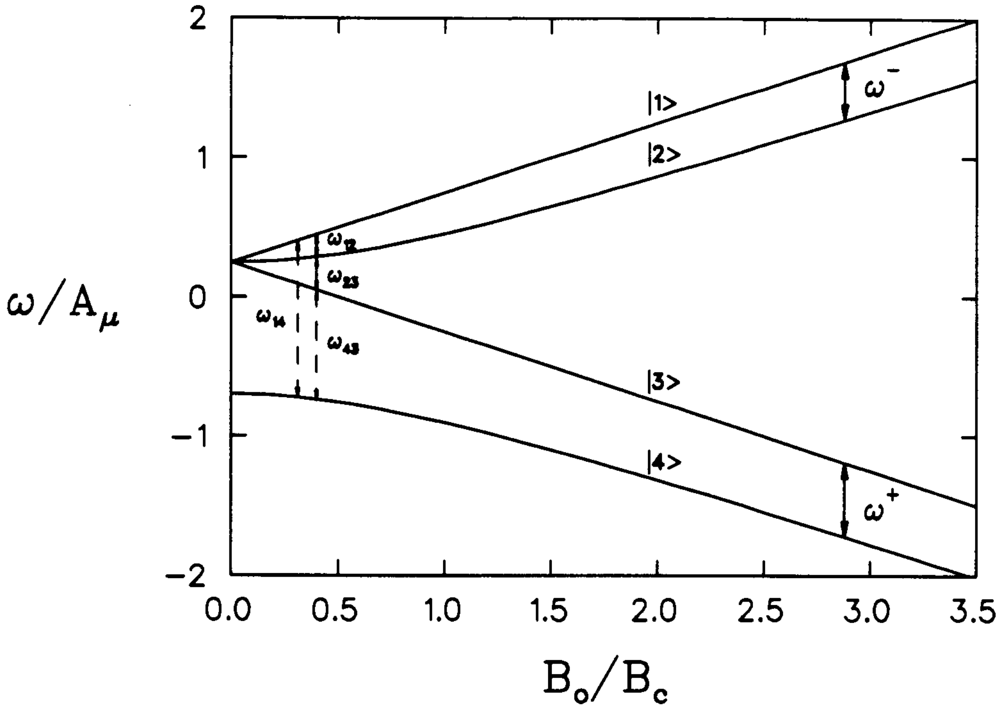

Figure 1.3: Breit-Rabi diagram for a two-spin-1/2 system [22], where B_c = 1590 Gauss is the ratio of the hf frequency of Mu ($A_\mu/2\pi$ = 4463 MHz), to the gyromagnetic ratio of the electron (γ_e = 2.80 MHz/G). Of the four allowed transitions in a low TF-μSR experiment, only the two denoted by full lines are resolvable.

ω_{23}, the spins precess at about the muonium Larmor frequency, $\omega_M = 103$ ω_μ. Therefore, in a TF-μSR experiment, Mu is easily distinguished from muons in a diamagnetic enviroment. Thus including the contribution from muonium, the asymmetry $A(t)$ given in equation 1.10 becomes

$$\begin{aligned} A(t) &= A_D(t) + A_M(t) \\ &= A_D e^{-\lambda_\mu t} \cos(\omega_\mu t + \phi_\mu) \\ &\quad + A_M e^{-\lambda_M t} \cos(\omega_M t + \phi_M) \end{aligned} \tag{1.13}$$

with the same meaning for all the parameters as in equation 1.11 with the subscript D denoting the diamagnetic signal and M denoting the Mu signal.

1.5 Muonium-substituted free radicals.

1.5.1 TF-μSR spectrum of Mu-substituted free radicals.

Radicals are molecular species which are paramagnetic due to an unpaired electron. Most muonated radicals contain, apart from the muon, a considerable number of other magnetic nuclei k which are also coupled to the unpaired electron. The spin Hamiltonian of a gas or non-viscous liquid system for such a multispin system is

$$\hat{H} = \omega_e S_z^e - \omega_\mu S_z^\mu + A_\mu \vec{S}^\mu \cdot \vec{S}^e - \sum_k \omega_k S_z^k + \sum_k A_k \vec{S}^k \cdot \vec{S}^e \tag{1.14}$$

where ω_e, ω_μ, and ω_k are the Zeeman angular frequencies, and A_μ and A_k are the isotropic Fermi contact hfcc [15] in angular frequency units for the muon and the nuclei k, respectively. In gas and non-viscous liquids, anisotropic contributions to the hyperfine coupling arising from direct dipole-dipole interactions average to zero due to rapid tumbling of the radicals. However, in solids the dipolar interaction is no longer negligible.

For N nuclei with spin quantum number S_k the above Hamiltonian leads to $4\Pi_k^N(2S_k+1)$ eigenstates [23]. From quantum mechanics, the selection rule for the transitions between these states is $\Delta M = \pm 1$ [24], where $M = m_\mu + m_e + \Sigma_k m_k$ (m_i is the magnetic quantum number of the particle i). The muon polarization thus oscillates between many of these eigenstates. Consequently, the muon polarization is distributed over many frequencies. For low fields, in particular, this renders the detection of Mu-substituted radicals difficult or even impossible. However in sufficiently high fields ($\omega_e \gg A_\mu$, A_k for all k), where most TF-μSR experiments for radical studies are performed, all the radical frequencies form two degenerate groups, independent of the number of coupled nuclei. The whole polarization distributes equally between them. Therefore in the high-field limit, the selection rule becomes $\Delta m_\mu = \pm 1$, $\Delta m_e = 0$ and $\Delta m_k = 0$. The radical spectrum is thus the same as for Mu with a reduced value of A_μ for the radical and these two TF-μSR transition frequencies in the radical spectrum are [24]:

$$\begin{aligned}\omega^- &= |\,\omega_{12}\,| \\ &= |\,\omega_{mid} - \frac{1}{2}A_\mu\,| \qquad (1.15)\\ \omega^+ &= |\,\omega_{43}\,| \\ &= |\,\omega_{mid} + \frac{1}{2}A_\mu\,| \qquad (1.16)\end{aligned}$$

where

$$\omega_{mid} = \frac{1}{2}[\sqrt{A_\mu^2 + (\omega_e+\omega_\mu)^2} - \omega_e + \omega_\mu] \qquad (1.17)$$

is the muon Larmor angular frequency ω_μ, shifted by a small amount depending on the relative magnitudes of the electron Larmor frequency and the muon hfcc.

The TF-μSR signals of Mu-substituted radicals are usually analysed in

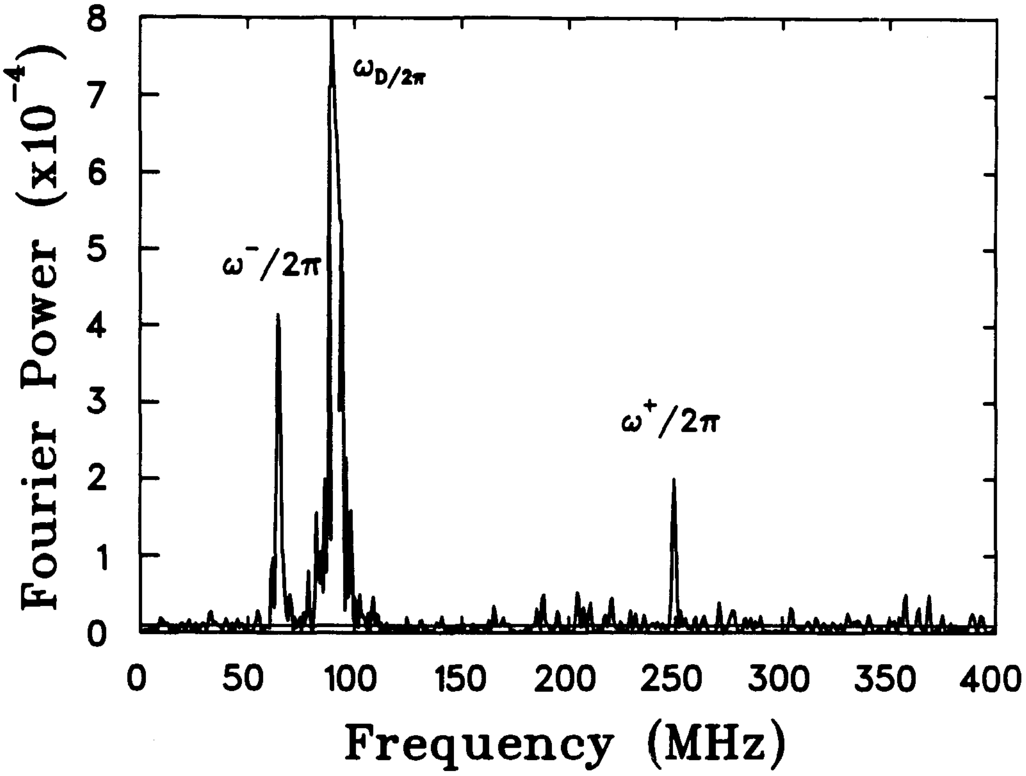

Figure 1.4: TF-μSR Fourier transform spectrum of Mu-substituted isopropyl radical at an external magnetic field 6.7 kG and temperature 263.2 K. $A_\mu/2\pi$ for this radical is 313.65 MHz at 263.2 K (see chapter 6 of this thesis).

frequency space rather than in time space [25]. Figure 1.4 shows a typical TF-μSR Fourier transform spectrum for a Mu-substituted radical.

Muonated radicals can be observed in TF-μSR experiments only if the radical formation rate is large compared with the muon spin precession frequency of the precursor. With muonium as precursor, this imposes a lower limit of about 10^9 – 10^{10} s^{-1} [13]. As a consequence, samples to be studied by TF-μSR must have large radical formation rates or be in high concentration. However, even for concentrations in the molar range the rate constant must be larger than 10^9 M^{-1} s^{-1}. In the case of slower reactions, the radical does not give a coherent TF-μSR signal. The radio frequency (rf) resonance technique was proposed to solve this problem.

1.5.2 Longitudinal field rf integer muon spin resonance (rf-IμSR) spectrum of Mu-substituted free radicals.

Since 1982, the μSR group at KEK has developed a high-power pulsed rf resonance technique suitable for the pulsed muon beam at KEK. A 500 MHz rf cavity has been used routinely there in magnetic resonance experiments. At TRIUMF over the past few years, we have worked toward developing rf capabilities suitable for use in a continuous wave (CW) meson facility. For radical studies on aqueous solutions, where the volume of the sample cell is generally large (about 38 cm^3 in our case) and reducing its size directly counteracts the goal of more efficient beam utilization in rf-IμSR experiment, high rf field strengths, and therefore resonant designs, are necessary. 'Birdcage' resonators (to be discussed in detail in both chapters 3 and 5) have been developed and adapted for use at TRIUMF. The advantages of this design are **i)** the ability to generate circularly polarized rf fields to make full use of the available rf power, and **ii)** its open axial geometry, facilitating beam and sample access.

In rf resonance experiments, in addition to a strong static longitudinal magnetic field B_o, a small rf perturbation field in the transverse direction $2B_1 \cos\omega t$ is applied to the sample. The resonance signal is derived by considering the change in occupation numbers of the Zeeman levels induced by the magnetic rf radiation.

In general, the time-dependent positron distribution for longitudinal studies has the form [2]

$$\frac{dN(t)}{dt} = N_o \lambda e^{-\lambda t}(1 + P_z(t)\cos\theta) \tag{1.18}$$

where λ is the damping rate which describes all processes that take the muons out of resonance, usually muon decay and chemical reactions, N_o is a normalization factor, θ is the angle of positron detection with respect to the initial muon spin polarization of the incoming muons, and $P_z(t)$ is the longitudinal time-dependent muon polarization. Integrating equation 1.18 over time from 0 to ∞, the time-integrated longitudinal field positron distribution is then given by

$$N = N_o(1 + P_z(B_o)\cos\theta) \tag{1.19}$$

where

$$P_z(B_o) = \int_0^\infty e^{-\lambda t}\lambda P_z(t)dt \tag{1.20}$$

is the longitudinal time-integrated muon polarization.

rf longitudinal field μSR (rf-LFμSR) technique and B_1 field measurement.

The most important feature of rf-LFμSR measurements on μ^+ is the capability to measure the rf field (B_1). In a rf-LFμSR experiment with a diamagnetic system, a muon sees both a strong longitudinal field B_o and a weak transverse rf field $2B_1 \cos\omega t$, and begins to precess around an effective field $\vec{B}_{eff}$ within the frame rotating with an angular velocity -ω perpendicular to $\vec{B}_o$. Chapter 4 contains a detailed description.

A rf-LFμSR experiment is performed in time space. Figure 1.5 shows a typical rf-LFμSR time histrogram spectrum obtained at TRIUMF. B_1 can be extracted from the oscillation period of the rf-LFμSR time histogram spectrum (details are found in chapter 4).

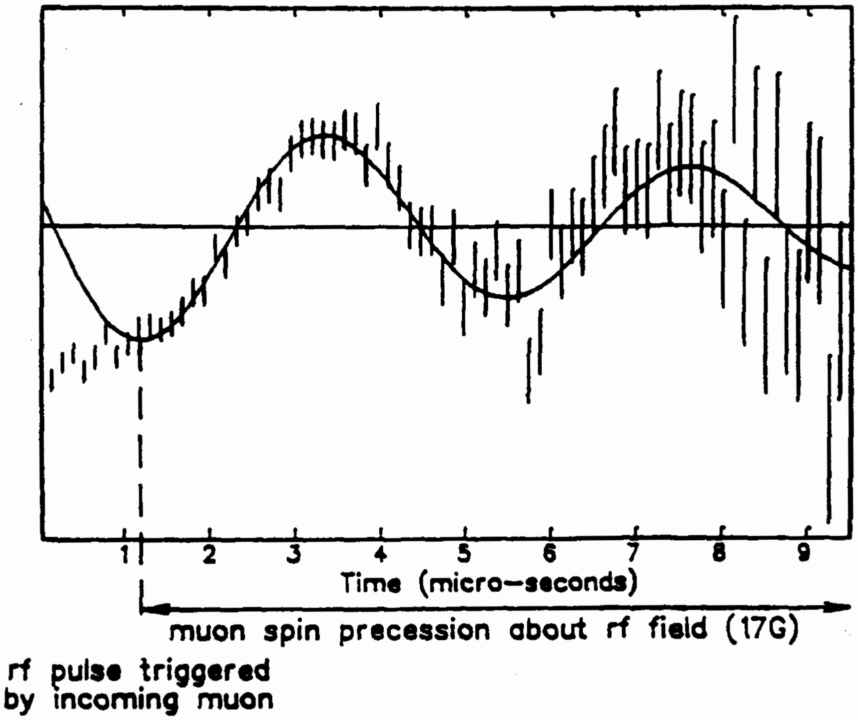

Figure 1.5: rf-LFμSR time histogram spectrum on resonance for water.

rf-IμSR spectrum of Mu-substituted free radicals

The difference between rf-LFμSR and rf-IμSR is that rf-LFμSR yields a time differential spectrum (equation 1.18), while rf-IμSR yields a time-integrated asymmetry (equation 1.19).

At TRIUMF, the rf-IμSR data is collected in the longitudinal field configuration with forward (downstream) and backward positron rates combined to form the normalized active rf asymmetry A_{rf} as follows

$$A_{rf} = A^{rf-on} - A^{rf-off} \tag{1.21}$$

where

$$A^{rf-on} = \frac{N_F^{rf-on} - N_B^{rf-on}}{N_F^{rf-on} + N_B^{rf-on}} \tag{1.22}$$

and similarly for A^{rf-off}. In the above equation, N_F and N_B are positron counts given in equation 1.19 with forward ($\theta = 0^o$) and backward ($\theta = 180^o$) detection, respectively.

Since all the transitions which would be observable in a conventional TF-μSR experiment are permitted in rf-IμSR [26], rf-IμSR experiments usually are performed in a high B_o field, where the transition lines degenerate into two, ω^+ and ω^-, independent of the number of nuclei in the radical system. The experiments are usually performed at a fixed rf frequency ω by sweeping the external longitudinal field B_o around the resonances, $\omega^\mp = \omega$, to have a field-dependent observation. Figure 1.6 shows a typical rf-IμSR muon asymmetry spectrum obtained at TRIUMF.

Using both conventional TF-μSR and rf-IμSR techniques, the vast majority of free radical experiments must be carried out in strong magnetic fields in order to avoid the spread of the initial muon spin polarization over a multitude of frequencies. Both the muon frequency spectra in

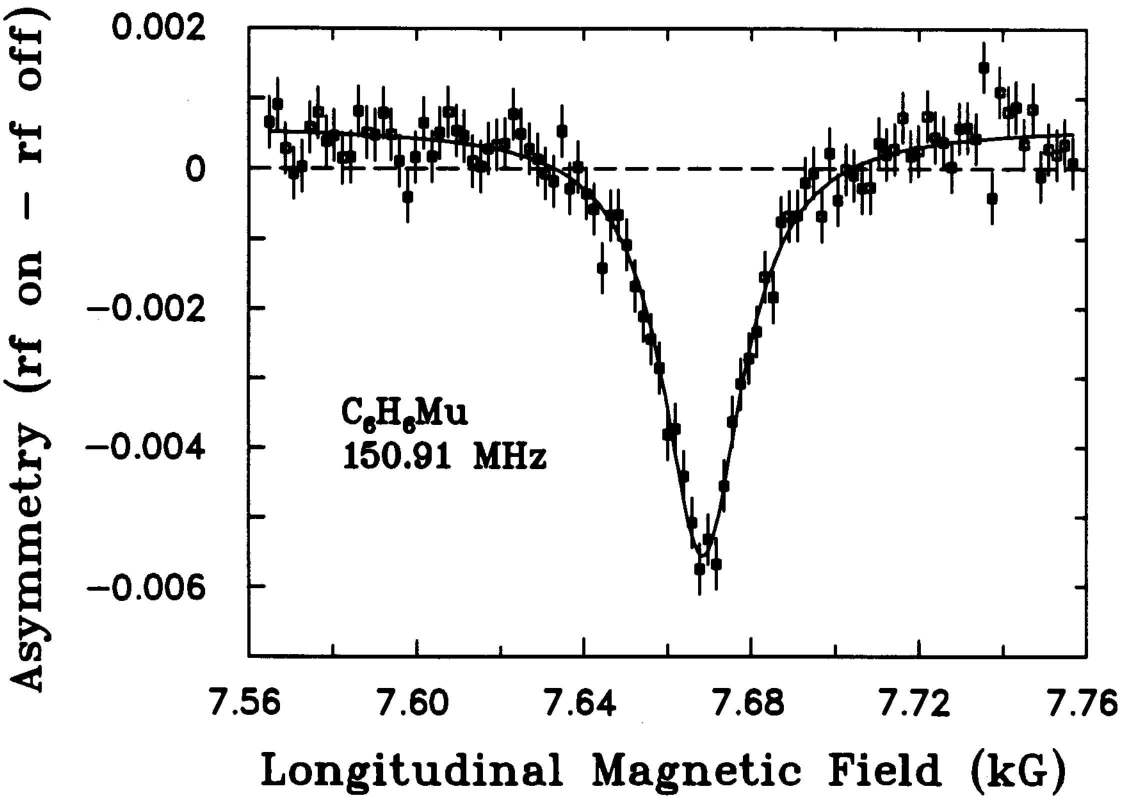

Figure 1.6: rf-IμSR muon asymmetry spectrum of the C_6H_6Mu radical at about 5 °C and rf frequency $= \omega/2\pi = 150.91$ MHz.

TF-μSR experiments and the muon asymmetry spectra in rf-IμSR experiments are insensitive to nuclear hf interactions in high transverse fields and are too complicated to resolve in low fields. As a consequence, the information concerning the nuclear hf coupling is lost. However, μLCR spectroscopy is an ideal tool to probe the other nuclear hyperfine interactions.

1.5.3 μLCR spectroscopy and the μLCR spectrum of Mu-substituted free radicals.

The μLCR effect occurs at specific applied magnetic fields where a muon transition frequency is matched to that of some other nucleus in the coupled spin system. At such a field a pair of nearly degenerate levels having different spin orientations for the muon and another nucleus are mixed by the hyperfine interaction, resulting in a resonant-like change in the μSR spectrum as the magnetic field is swept.

In the gaseous and non-viscous liquid phases, the spin Hamiltonian for a Mu-substituted free radical with N magnetic nuclei as well as the muon is given by equation 1.14, in angular frequency units. In the high field limit where the electronic Zeeman frequency is much larger than the hf frequencies, the eigenstates of a multiple spin system $\mid m>$ can be expressed in terms of the basis of the product of individual eigenkets,

$$\mid m >= \sum_i C_{im} \mid \chi_{ei} >\mid \chi_{\mu i} > \prod_k \mid \chi_{ki} > \qquad (1.23)$$

For a three-$\frac{1}{2}$-spin system with an electron, a muon, and one nucleus, there are eight spin states:

$$\mid \quad \tfrac{1}{2}, \ \tfrac{1}{2}, \ \tfrac{1}{2} \quad >,$$
$$\mid \quad \tfrac{1}{2}, \ \tfrac{1}{2}, -\tfrac{1}{2} \quad >,$$

$$
\begin{array}{l}
|\ \tfrac{1}{2}, -\tfrac{1}{2},\ \tfrac{1}{2}\ >, \\
|\ \tfrac{1}{2}, -\tfrac{1}{2}, -\tfrac{1}{2}\ >, \\
|\ -\tfrac{1}{2},\ \tfrac{1}{2},\ \tfrac{1}{2}\ >, \\
|\ -\tfrac{1}{2},\ \tfrac{1}{2}, -\tfrac{1}{2}\ >, \\
|\ -\tfrac{1}{2}, -\tfrac{1}{2},\ \tfrac{1}{2}\ >, \\
|\ -\tfrac{1}{2}, -\tfrac{1}{2}, -\tfrac{1}{2}\ > .
\end{array}
$$

Due to the dominance of the electron Zeeman term in the Hamiltonian 1.14, the energy levels form two well separated groups according to the sign of m_e (the gap caused by the electron Zeeman term is about 10^4 MHz per Tesla, but for protons the hf energy level gap is typically 2 to 3 orders of magnitude less). For all practical purposes, the transitions to be observed are between states with the same m_e. Therefore the selection rule of μLCR for isotropic spin systems is $\Delta(m_\mu + m_k) = 0$. The 2×2 sub-secular determinant in this basis set in the high field limit after block-diagonalization is [27],

$$
\boldsymbol{D} = \begin{vmatrix} E_{11} + \frac{A_\mu^2}{4\omega_e} + \frac{b^2 A_k^2}{4\omega_e} - E & c\frac{A_\mu A_k}{4\omega_e} \\ c\frac{A_\mu A_k}{4\omega_e} & E_{22} + \frac{c^2 A_k^2}{4\omega_e} - E \end{vmatrix} \tag{1.24}
$$

where

$$
\begin{aligned}
E_{ii} &= m_e\omega_e - m_\mu\omega_\mu - m_k\omega_k \\
&\quad + m_e m_\mu A_\mu + m_e m_k A_k && (1.25) \\
b^2 &= S_k(S_k+1) - M(M+1) && (1.26) \\
c^2 &= S_k(S_k+1) - M(M-1) && (1.27) \\
S^k &\geq M \leq -S^k + 1 && (1.28)
\end{aligned}
$$

By solving the eigenvalue problem 1.24 and then integrating the muon polarization over t from zero to infinity with weight $\lambda e^{-\lambda t}$, the time-integrated signal of μLCR can be obtained. The general expression for the muon polarization in a multi-spin system in the high field limit is given by [27],

$$P_z(B) = 1 - \frac{2}{N}\sum_{i}^{2S_k} \frac{\omega_{oi}^2}{\lambda^2 + \omega_{oi}^2 + [2\pi(B - B_{oi})(\gamma_\mu - \gamma_k)]^2} \tag{1.29}$$

where N is the dimension of the Hamiltonian matrix, γ_i's are the gyromagnetic ratios, $\omega_{oi} = \pi c A_\mu A_k / B_{oi}\gamma_e$ represents the transition frequency on resonance, λ is the damping rate, and B_{oi} is the resonance field given by:

$$B_{oi} = \left| \frac{A_\mu - A_k}{2(\gamma_\mu - \gamma_k)} - \frac{A_\mu^2 - 2MA_k^2}{2\gamma_e(A_\mu - A_k)} \right| \tag{1.30}$$

Near this field the off-diagonal terms of the spin Hamiltonian are no longer negligible, as they serve to mix the two states. The result is actually a non-crossing of the energy levels. Measurement of the field on resonance leads to accurate determination of the magnitude and sign of the nuclear hf frequency relative to that of the muon. Figure 1.7 shows a schematic diagram of energy levels and the calculated muon polarization curve for a μ^+ - e$^-$- p system, while figure 1.8 shows a typical μLCR spectrum obtained at TRIUMF.

There are many advantages of the μLCR technique over conventional TF-μSR and rf-IμSR. One of the most remarkable features of μLCR in high fields is that the position and magnitude of each resonance are insensitive to the number of nuclei off resonance. This characteristic makes the μLCR technique suitable to measure nuclear hf parameters in complicated spin systems. The μLCR technique is also sensitive to the relative signs of the muon hf frequency and that of the coupled nucleus. Another advantage of μLCR is the high resolution obtainable. The errors in the resonance position are primarily due to uncertainty in the field

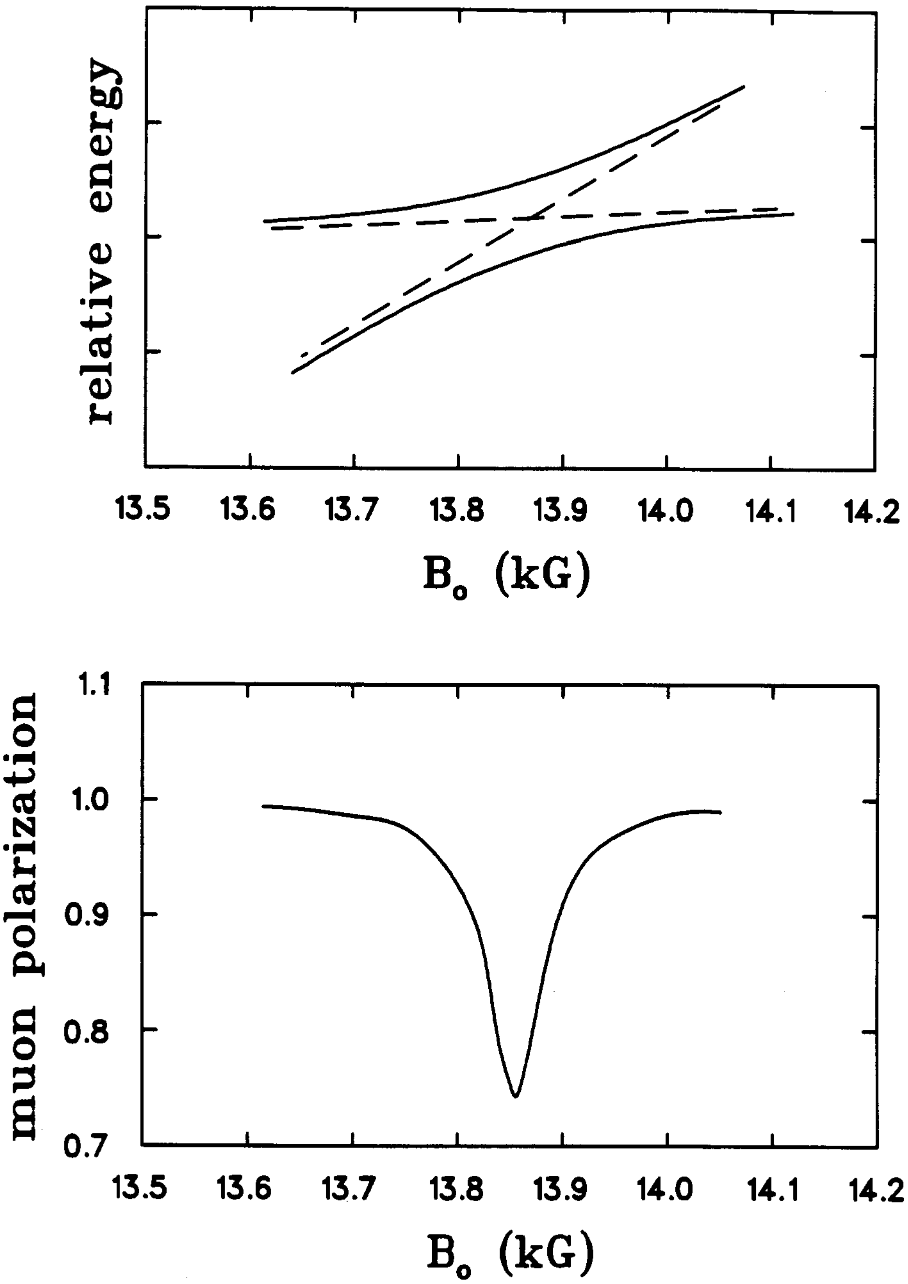

Figure 1.7: Top: A schematic diagram of the energy levels for a μ^+ - e$^-$ - p system. Bottom: A muon polarization curve calculated from equation 1.29 with $A_\mu = 355.9$ MHz and $A_p = 98.4$ MHz for the same system.

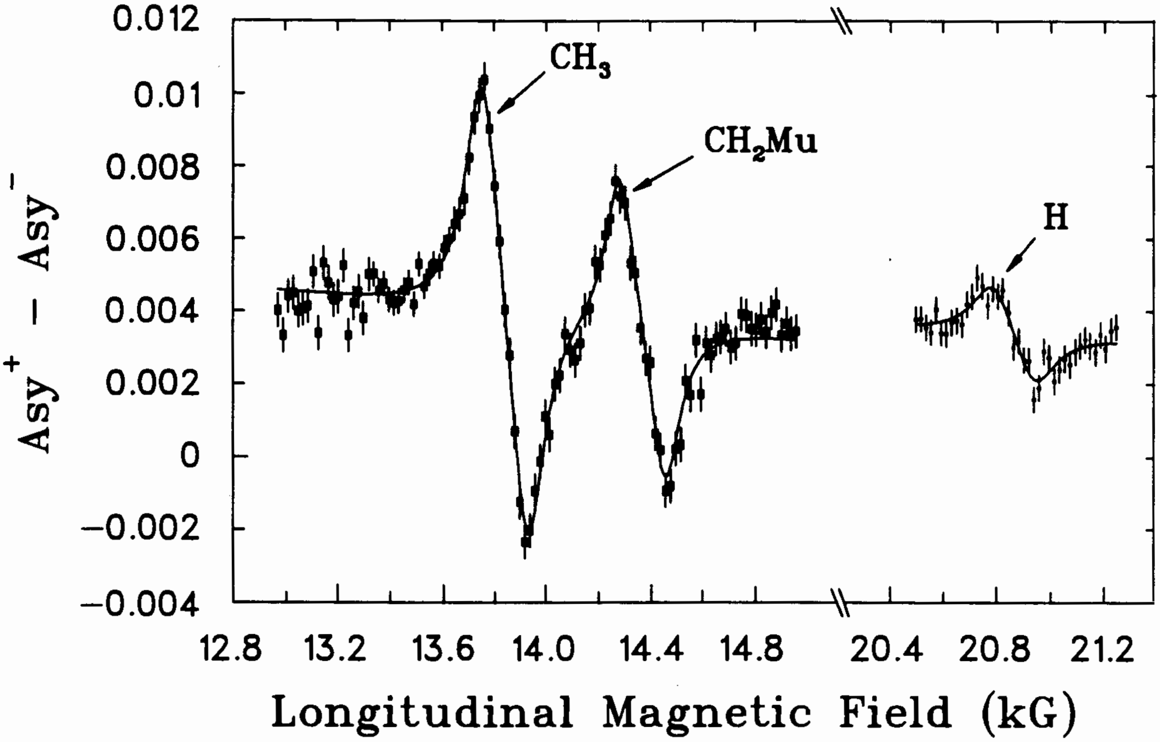

Figure 1.8: Muon level-crossing spectrum of the Mu-substituted isopropyl radical at 122.4 K.

calibration. A few gauss uncertainty in the resonance position leads to hf frequencies precise to about 0.05 MHz. The μLCR technique also provides the possibility of detecting slow forming radicals, including those which are evolving from a radical reaction. Radicals will be observed even when a Mu precursor has a lifetime of a microsecond, as long as the transition frequency ω_{oi} is high enough to produce a significant μLCR signal in the remaining muon lifetime. The loss of polarization during the precursor stage is negligible in high longitudinal magnetic fields.

μLCR studies on muonated radicals show that μLCR is a powerful spectroscopic technique. Its spectra can give extra information about non-muon spin interactions which can be readily used to determine nuclear hf structure in paramagnetic spin systems involving muons. Thus, μLCR complements conventional TF-μSR and rf-IμSR by providing additional information useful in identifying radicals and exploring electron spin distributions and intramolecular motion of muonated radicals.

Chapter 2

Experiment

2.1 The μSR facility at TRIUMF

2.1.1 TRIUMF and the Meson Hall

The TRIUMF cyclotron is a six-sector-magnet cyclotron which accelerates H^- ions to a peak energy of 520 MeV. Three beam lines are currently fed by the cyclotron. The first, beam line 1 (BL1), delivers beam to the meson experimental hall; another, beam line 4 (BL4), provides beam to experiments in the proton experimental hall. The third, beam line 2C (BL2C), delivers low-energy (70–100 MeV) beam for the production of radioisotopes. The energies of BL1 and BL4 may be varied independently between 183 and 520 MeV. The high current capability of the cyclotron — 150 μA at 500 MeV — qualifies TRIUMF as a 'meson factory'. The general layout of the cyclotron and experimental facilities is shown in Figure 2.1.

From the viewpoint of an experimenter, one of the most important features of the TRIUMF cyclotron is the 100% macroscopic duty cycle: seen on a macroscopic time scale (as short as a microsecond), the proton beam appears to be a continuous current without a time structure. The

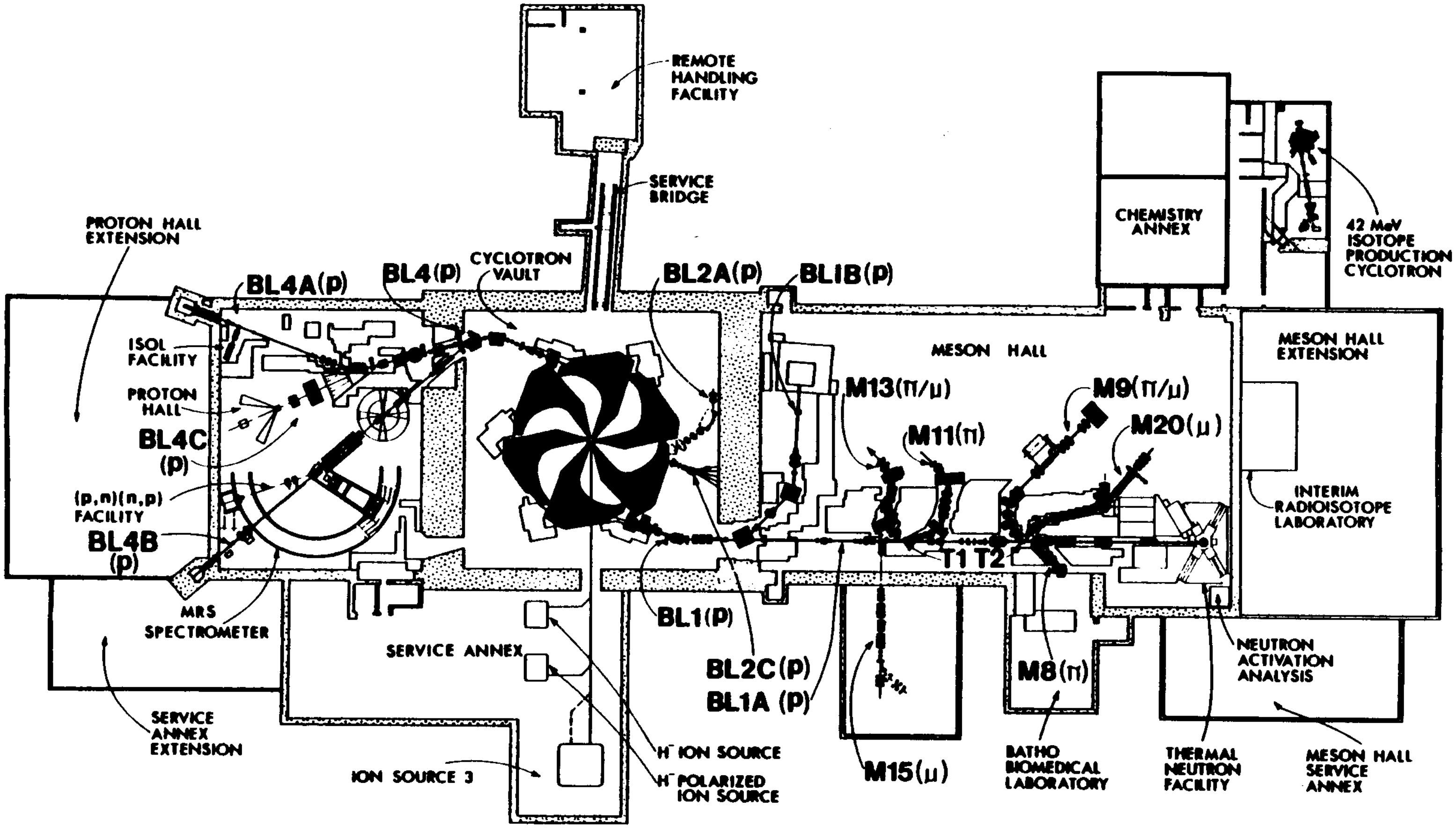

Figure 2.1: TRIUMF cyclotron and experimental end-stations [28].

microscopic proton beam time structure is a 3 ns wide pulse every 43 ns. Both the macroscopic and the microscopic structures of the beam can be changed by a number of devices in the ion source injection line and the cyclotron central region.

In the meson hall, a 100–150 μA beam (BL1A) of 500 MeV protons is passed through two production targets to provide pions and muons to a number of secondary beam channels before being stopped in the thermal neutron facility (TNF). The first production target (T1) provides a small source for three high purity channels: M13, a low energy pion and surface muon channel; M11, a high energy (80–300 MeV), good resolution pion channel; and M15, a dedicated surface muon channel. The second production target (T2) provides the source for three high intensity channels: M9, a low energy pion and cloud muon channel; M20, a general purpose muon channel for both backward decay and surface muons; and M8, a high flux pion channel for cancer therapy research.

2.1.2 Surface muons and decay muons

Surface muons

There are two ways to produce spin polarized muon beams. In the first instance one makes use of very low energy pions which have already stopped near the surface of the primary production target and decay by the reaction

$$\pi^+ \rightarrow \mu^+ + \nu_\mu, \tag{2.1}$$

as shown in figure 2.2. Positive muons emerging from the decay of pions at rest are 100% spin polarized with respect to their momentum vector. This is easily seen as follows. First, the pion decay at rest is a two-

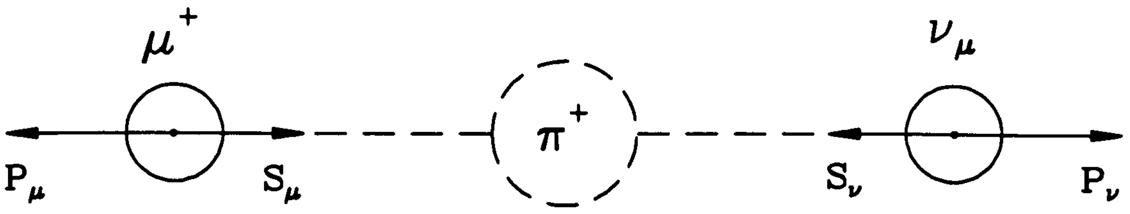

Figure 2.2: A pion decays at rest.

body decay which implies that μ^+ and ν_μ are collinearly emitted (see figure 2.2) and the kinematics of the decay tells us that the muon carries a kinetic energy of 4.1 MeV, or a momentum of 28.6 MeV/c. Secondly, the spin of the pion is zero. The conservation of angular momentum then requires that the total angular momentum of the μ^+ and ν_μ also be zero. Since the helicity of the ν_μ is fixed at H = −1 (*i.e.* the spin of the ν_μ is antiparallel to its momentum), the spin of the emerging μ^+ must also be antiparallel to its momentum, as is evident from figure 2.2. If muons of a certain momentum direction are collected into a beam, this beam will show an almost 100% spin polarization. This type of beam is called a surface μ^+ beam.

Decay muons

The second type of muon beam is formed from pions decaying in flight. Given a certain pion momentum $\mathbf{p}_\pi$, the distribution of muon momenta $\mathbf{p}_\mu$ in the laboratory frame follows from relativistic kinematics [29]. It can be easily shown that the energy of a muon (E_μ) in the laboratory frame as a function of the π^+ momentum is

$$E_\mu = \gamma_\pi E'_\mu (1 + v_\pi v'_\mu / c^2 \cos\theta'). \tag{2.2}$$

Where E'_μ is the total energy of the muon in the rest frame of the pion (*i.e.* E'_μ = kinetic energy + rest energy = 109.8 MeV), v'_μ is the velocity of the muon in the rest frame of pion (*i.e.* $v'_\mu/c = 0.27$), v_π is the velocity of the pion, θ' is the angle between $\mathbf{p}_\pi$ and $\mathbf{p}'_\mu$ in the rest frame of the pion (see figure 2.3) and γ_π is defined as: $\gamma_\pi = \frac{1}{\sqrt{1-(v_\pi/c)^2}}$. In 'conventional' mode, pions decay in flight to give two types of muons, forward and backward muons. In the pion rest frame, a forward μ^+ decays in the pion momentum direction ($\theta' = 0^o$), while a backward μ^+ decays in the opposite direction ($\theta' = 180^o$). Correspondingly, the energies of forward and backward muons in the laboratory frame are the maximum energy E_μ^{max} and the minimum energy E_μ^{min}, respectively, as given by equation 2.2:

$$\begin{pmatrix} E_\mu^{max} \text{ (forward)} \\ E_\mu^{min} \text{ (backward)} \end{pmatrix} = \gamma_\pi E'_\mu (1 \pm v_\pi v'_\mu / c^2). \tag{2.3}$$

The relativistic kinematics dictate that the angular distribution of the muons with respect to $\vec{p}_\pi$ in the laboratory frame follows from

$$\tan\theta = \frac{\sin\theta'}{\gamma_\pi \left[(v_\pi/v'_\mu) + \cos\theta' \right]}, \tag{2.4}$$

where θ is the angle between $\vec{p}_\pi$ and $\vec{p}_\mu$ in the laboratory frame (see figure 2.3). Since the pion decay in the rest frame of the pion is isotropic, θ' varies between 0^o and 360^o with equal probability. By taking the derivative of equation 2.4, it can be shown that, for $v_\pi > v'_\mu$, the muons are emitted into a forward cone along $\vec{p}_\pi$ with a maximum opening angle of

$$\cot\frac{1}{2}\theta_{max} = \gamma_\pi \left[(v_\pi/v'_\mu)^2 - 1 \right]^{1/2}. \tag{2.5}$$

If we take backward muons ($\theta' = 180^o$) as an example, we find that $\vec{p}_\mu\,'$ and $\vec{p}_\mu$ are antiparallel ($\theta = 0^o$, see equation 2.4), and therefore, the

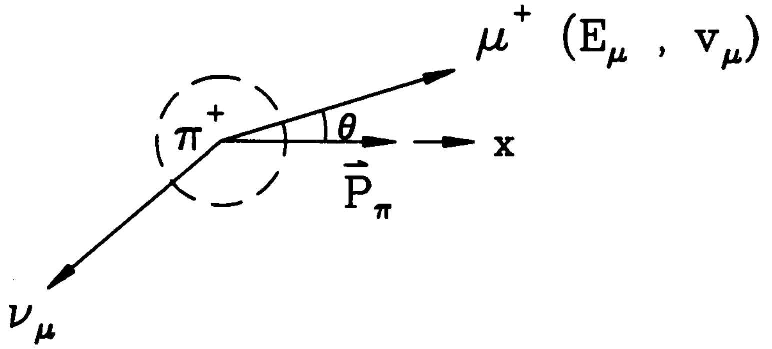

(a) lab frame

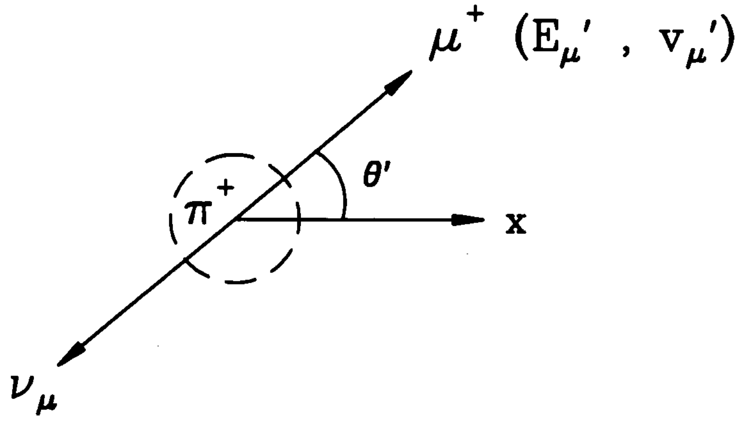

(b) rest frame

Figure 2.3: A pion decays in the laboratory frame (a) and in the rest frame of the pion (b).

muon spin and $\vec{p}_\mu$ are parallel. It is clear that backward muons are 100% spin polarized with respect to their momentum.

For muon channel M20, pions have a central momentum of 165.5 MeV/c [28]. Therefore the forward and backward decay muons will have average momenta of 173 MeV/c and 86.5 MeV/c, respectively. Unfortunately, the 4.3% momentum difference between the forward muons and undecayed pions is insufficient to separate these particles, and there is therefore a large pion contamination in the forward muon beam. The dc separator (described below) is capable of good pion/muon separation only for momenta up to 115 MeV/c. Therefore the backward muon mode is commonly used, as well as the surface muon mode.

2.1.3 M15 and M20 muon channels

The experiments of this work were carried out at TRIUMF's M15 and M20 muon channels. Their main features will be described in this section.

M15 is a dedicated surface μ^+ channel. Figure 2.4 shows a view of M15. Muons come from pions decaying at rest before the first bending magnet (B1), inside of and within a few μm [28] of the surface of the pion production target (T1). Magnets QA, QB, Q1, ..., Q17 are quadrupoles to keep the beam focused and achromatic. Magnets B1, ..., B4 are bending dipoles for momentum selection. The pair of sextupoles, SX1 and SX2, is not energized for most conventional tunes, but is available to reduce second-order effects for specialized tunes.

M20 can be operated as either a backward decay muon channel of 86.5 MeV/c or as a surface muon channel of 28.6 MeV/c. The layout of the M20 channel is shown in figure 2.5. In the backward mode, positive pions

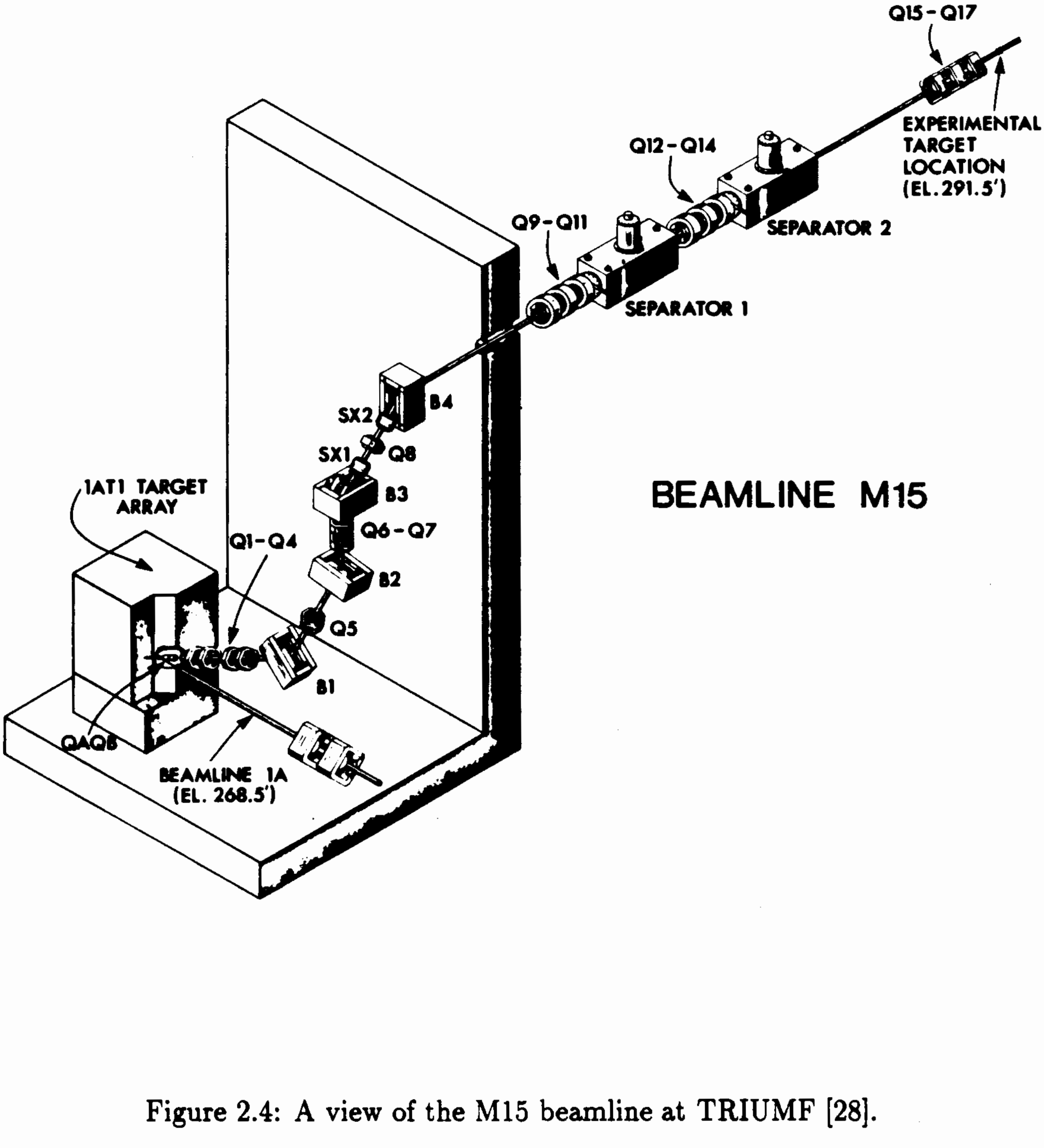

Figure 2.4: A view of the M15 beamline at TRIUMF [28].

produced from T2 are collected by the quadrupole doublet (M20Q1 and M20 Q2) and then momentum selected by the bending magnet (M20B1). The muons are produced from pions decaying in flight after M20B1. The second bending magnet (M20B2) is tuned to momentum select the backward muons (86.5 MeV/c) from the other particles in the beam (e^+, π^+, μ^+, and p). The resultant high momentum polarized backward μ^+ beam is delivered to the μSR apparatus. Both the beam lines, M15 and M20, can be optimized using simple but effective automatic programs which tune more than 20 of their elements.

Surface muons are nearly monoenergetic (4.1 MeV) with a nominal momentum of 28.6 MeV/c. Contamination of the surface muon beam with pions and protons is negligible. However, there are about 100 times more positrons than muons in the surface muon beam. The solution is to use a dc separator to remove the positron contamination in the surface muon beam, and to rotate the muon spin so that it is transverse to its momentum. The spin separator consists of a vertically oriented electric field $\vec{E}$ and a horizontally oriented magnetic field $\vec{B}$. The motion of a charged particle (μ^+ or e^+, in this case) follows the Lorentz force equation:

$$\vec{F} = q\left(\vec{E} + \frac{\vec{v}}{c} \times \vec{B}\right), \tag{2.6}$$

where $\vec{F}$ is the force acting on the charge q and $\vec{v}$ is its speed. Both muons and positrons have the same momentum, selected by the dipoles, but have different speeds due to their mass difference. Thus it is possible to select values of $\vec{E}$ and $\vec{B}$, such that $\vec{F} = 0$, to allow only muons to travel through the separator without deflection. For transverse field experiments (*e.g.* TF-μSR), the spin separator can also be used as a spin rotator. As the spin of a muon 'sees' the magnetic field $\vec{B}$ of the sepa-

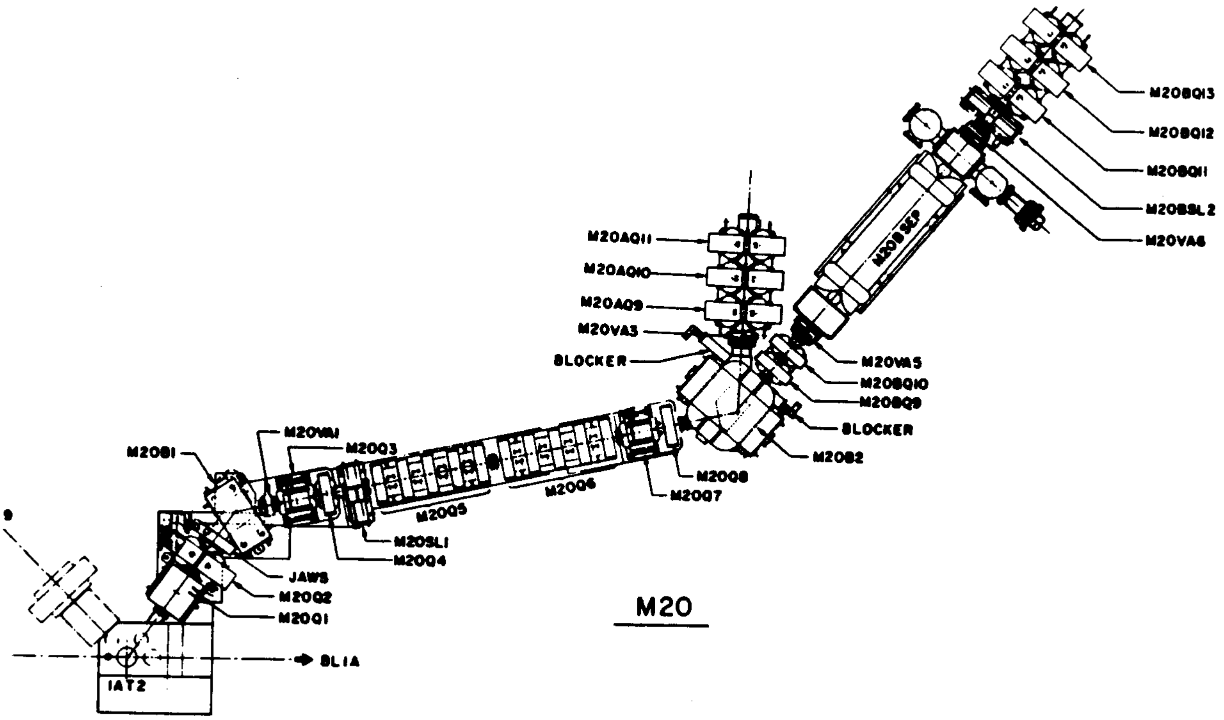

Figure 2.5: A plan view of the M20 beamline at TRIUMF [30].

rator, it will be rotated by 90^o so that it is transverse to its momentum. Therefore the separator can be used at low voltage ($\sim$ 5 kV/cm) to eliminate positron contamination, in which case the muon spins are nearly in the direction of their motion (*i.e.* the beam is longitudinally polarized). Alternatively, the separator can be used at high voltage ($\sim$ 40 kV/cm) to rotate the muon spins up to 90^o, resulting in a transversely polarized beam. Without changing the experimental geometry, both transverse and longitudinal field measurements are possible with the spin rotated and unrotated muons, respectively.

2.2 Detectors

Figure 2.6 shows a schematic layout of a detector used in the experiments, which includes a scintillator, a lightguide, and a photomultiplier. The scintillators used are plastic organic scintillators, which scintillate when exposed to ionizing radiation. The light emitted by the scintillator is collected by the lightguide and conducted to the photomultipler for amplification and conversion to an electrical signal. Because of the sensitivity of the phototube to stray light, both the scintillators and the lightguides are wrapped in black tape. Also, because the high magnetic fields used in the experiments decrease the gain of the photomultipliers, lightguides 1-2 meters long were used so the photomultipliers could be located in a low magnetic field region. Unfortunately, light losses are high in such long lightguides, so this limits the time resolution of μSR experiments to about 1 ns. The high voltage applied to the photomultiplier is normally in the range of 1.5 to 2.5 kV.

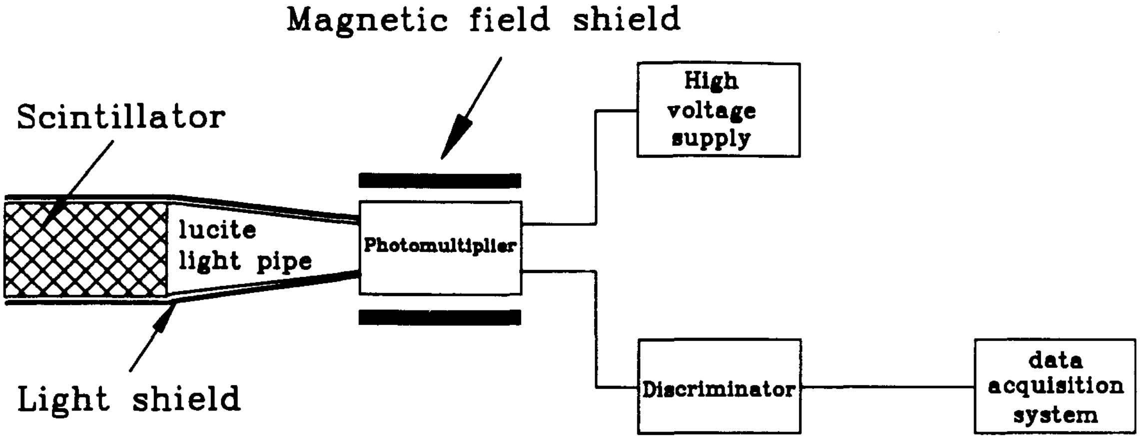

Figure 2.6: Schematic diagram of a scintillation detector.

2.3 TF-μSR experiments

For the free radicals studied in chapter six of this thesis, transverse field experiments were used to measure the muon hfcc and to calibrate the magnetic fields, while longitudinal field μLCR experiments (discussed below in section 2.4) were used to measure the μLCR fields for the nuclei of the radical other than for the muon. HELIOS, a custom-built superconducting solenoid, was used to provide magnetic fields up to 7 tesla. Essentially, the experimental setup for both TF-μSR and μLCR experiments done in this thesis was the same. Figure 2.7 shows a schematic layout of the experimental setup. The only difference is that the field modulation coil (see figure 2.7) is not activated in TF-μSR experiments. For TF-μSR experiments, the muon polarization is perpendicular to the field direction. A thin scintillator counter TM registers the arrival of each incoming muon, and decay positrons are separately detected in the four counters FL, FR, BL, and BR.

The data acquisition system used was the standard TRIUMF TF-

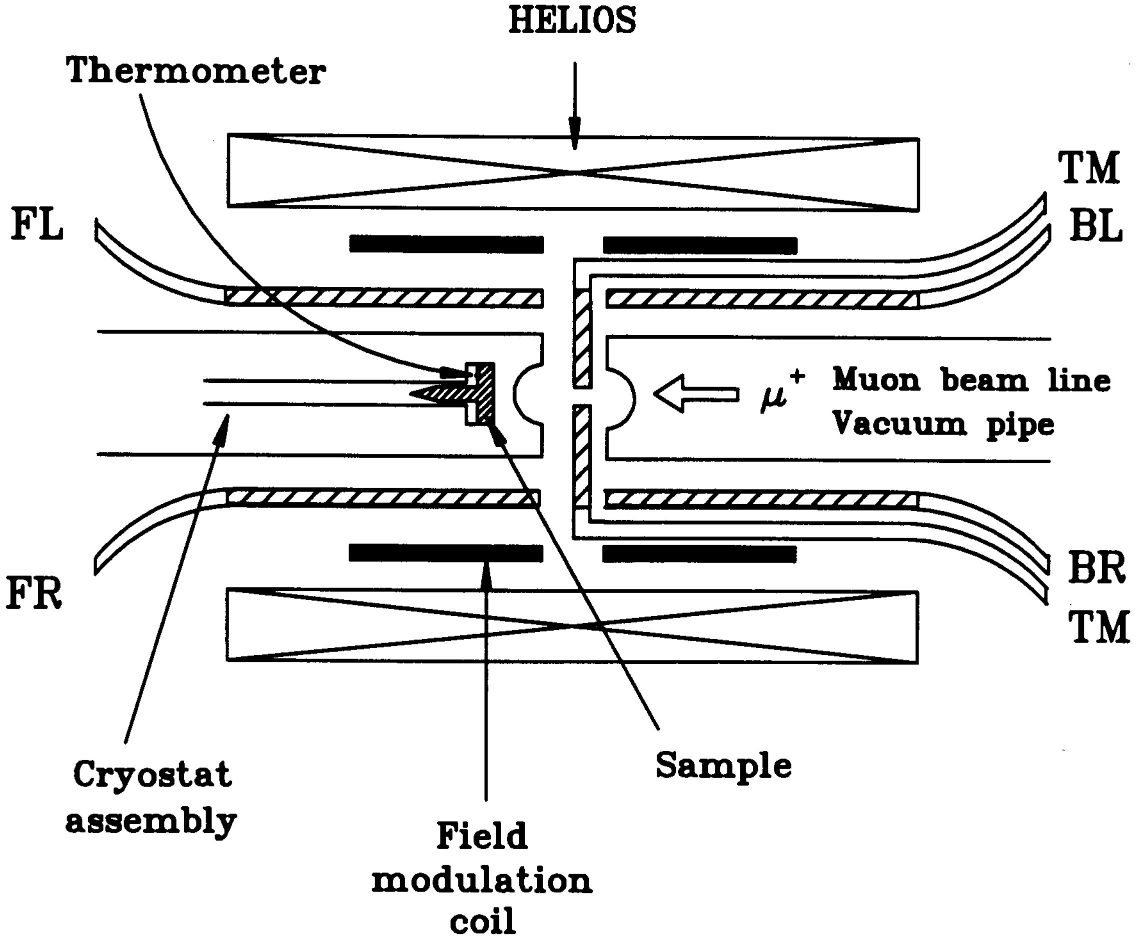

Figure 2.7: Schematic representation of the HELIOS setup.

μSR setup, which is designed to measure the time interval between a muon entering the target and its decay. The diagram of the electronics setup is given in figure 2.8. Signals from the counters are converted to standard Nuclear Instrument and Measurement (NIM) pulses with a width of $\sim$ 20 ns. These pulses are routed through time-delay circuits for time synchronization before they are fed into various electronic units. Incident muons trigger the thin TM (see figure 2.8) counter sending a 'μ-stop' signal to the 'start' input of a time digitizing converter (TDC); then decay positrons detected by either one of the four counters (FL, FR, BL and BR, in figure 2.8) trigger a signal to the 'stop' input of the TDC. The resultant time interval is then routed to the appropriate FL, FR, BL, or BR histograms, and the corresponding channel is incremented by one. When data of sufficient statistics (usually 10^6–10^7 per histogram) have been accumulated, the run is stopped.

At high incident muon rates (*i.e.*, $> \frac{1}{\tau_\mu}$), precautions must be taken to correct for pile-up. A pile-up event is a stopped muon which follows a previously stopped first muon within the time interval defined by the pile-up gate. There are now possibly two muons in the target and a subsequently emerging positron cannot be related unambiguously to the correct parent muon. Thus the timing information in the TDC may be incorrect. Such events must be excluded. Therefore, a 'good' event satisfies the following conditions:

- A muon arrives at t = 0 with pileup not busy ($\overline{B}$, see figure 2.8) and no μ^+ having entered the target in the time interval -p < t < 0, where p is the pileup gate length, usually 6.5 μs for TF-μSR measurements. This muon stop signal, which is in coincidence with the non-busy signal ($\overline{B}$) from the pile up gate, starts the TDC.

- A positron event detected by one of four counters FL, FR, BL or BR occurs at time τ (τ <p) with no second muon having entered the target ($\overline{P}$, see figure 2.8) in the time interval 0 < t < τ. This stops the TDC.

- Multiple stops (such as caused by a second positron) result in a TDC reset. Any further muon detected in the time interval τ < t < p is rejected in software via a 'flag' from stop bit 1 as shown in figure 2.8. Such an event would otherwise result in a spectrum distortion because the observation of long-lived muons has a larger probability of suppression by second muon events than that of the short-lived muons [2]. By rejecting all second muon events regardless of the relative timing of the second muon with respect to the positron, this kind of bias is removed.

Since it is impossible to have positron counters 'see' 100% of the decay events, one must stop waiting, clear the TDC, and prepare for the next stopped muon. This period is called the data gate (see figure 2.8) and usually extends over several muon lifetimes. The data gate is produced by a gate generator triggered by the muon stop signal. After the time interval of the data gate, the TDC is stopped, reset, and made ready for another good muon signature. A good decay positron is identified by a coincidence of the positron signal within the data gate.

2.4 Longitudinal field μLCR experiments

As was mentioned in the last section, longitudinal field μLCR experiments in chapter six of this thesis were used to measure the μLCR fields of the nuclei other than that of the muon. The experiment setup is

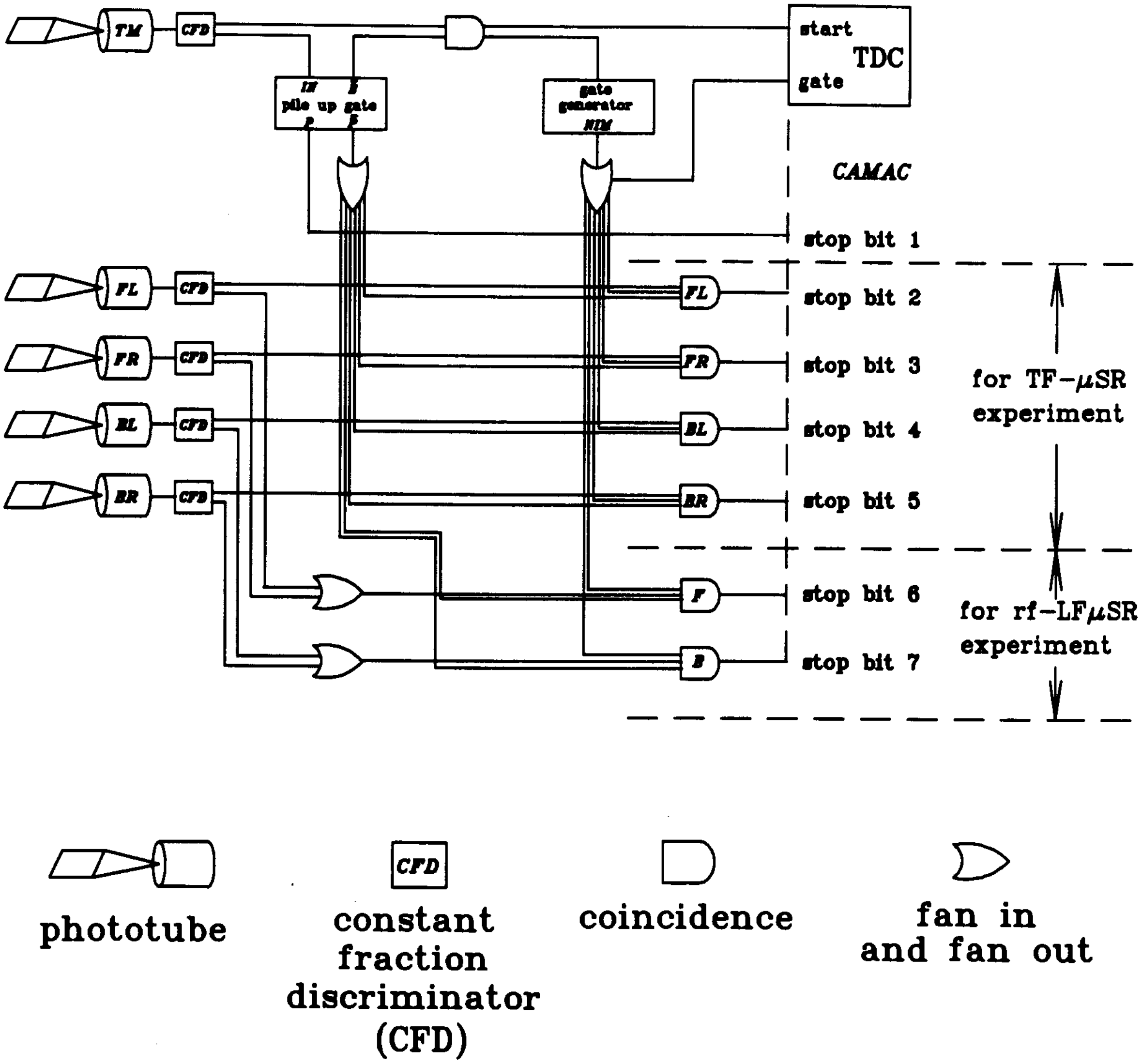

Figure 2.8: The principal electronic components of the time-differential μSR setup.

basically the same as that for TF-μSR, shown in figure 2.7, but the field modulation coil is activated and incoming muon polarization is along the field direction (longitudinal). For μLCR experiments, there is no theoretical limit on the incoming muon rate since it is not required that there be only one muon in the target at a time, as in the time-differential (*e.g.* TF-μSR) technique.

The process of finding the position of μLCR resonance fields involves recording the time-integrated positron rates as a function of magnetic field. However, the raw spectrum is sensitive to systematic effects, such as deviations due to rate-dependent effects. This is minimized by a square-wave field modulation (± 50 G), as shown in figure 2.7. The signal is defined as $A^+ - A^-$, the difference in muon asymmetries measured under opposite modulation phases. The muon decay asymmetries $A^\pm$ are defined as

$$A^\pm = \frac{N_F^\pm - N_B^\pm}{N_F^\pm + N_B^\pm} \tag{2.7}$$

where $N_F^\pm$ and $N_B^\pm$ are the total number of positron events given in equation 1.19 with forward ($\theta = 0^o$) and backward ($\theta = 180^o$) detections, respectively, and the ± refer to the phase of the modulation with respect to the main magnetic field. For a resonance wider than the field modulation width, the lineshape is approximately field-differential [31].

The block diagram of the electronics setup used in a μLCR experiment is given in figure 2.9. The experimental procedure involves accumulating a preset count (typically on the order of 10^6) detected by the sum of forward and backward detectors for each phase of the modulation field. When the preset value is reached, data taking is stopped, scalers are read, and the values stored in the computer. The preset scaler is then cleared and the phase of the modulation field is changed. The number of modulation coil flips is typically 20 per field point (B_o value). When the desired count is reached, the main magnetic field is incremented. (The size of the field increment is usually set at 50 G for rough scans and less, typically, 20 G for detailed scans.) Data taking is inhibited if the beam current strays outside a preset tolerance.

2.5 Longitudinal field rf-IμSR experiments

For free radicals studied in chapter five of this thesis, rf-IμSR experiments were used to measure the muon hfcc, while rf-LFμSR experiments (to be discussed in the next section) were used to measure the rf perturbation fields (B_1). The experimental setup for both rf-IμSR and rf-LFμSR experiments was the same and is given in Figure 2.10.

In the rf-IμSR experiment, the incident muon polarization is longitudinal and the standard μLCR electronics setup is used, but instead of field phase modulation (±) in μLCR, the rf is switched on and off (on/off). The rf part of the block diagram of the electronics of rf-IμSR experiments is given in figure 2.11, where MOD is that in figure 2.9. The rest of the electronics is exactly the same as for the μLCR experiments (figure 2.9). The rf-IμSR signal (A_{rf}) is defined in chapter 1 and given by equations 1.21 and 1.22. At a CW facility like TRIUMF a general difficulty relating to rf duty factors also usually arises. Efficient use of the muons available implies that the rf may be on 50% of the time, typically 1 second rf-on and 1 second rf-off in a rf-IμSR experiment.

In developing rf μSR facilities for use with a CW muon source the selection of an appropriate rf power amplifer is a fundamantal concern. For time integral applications it must be able to operate at high duty

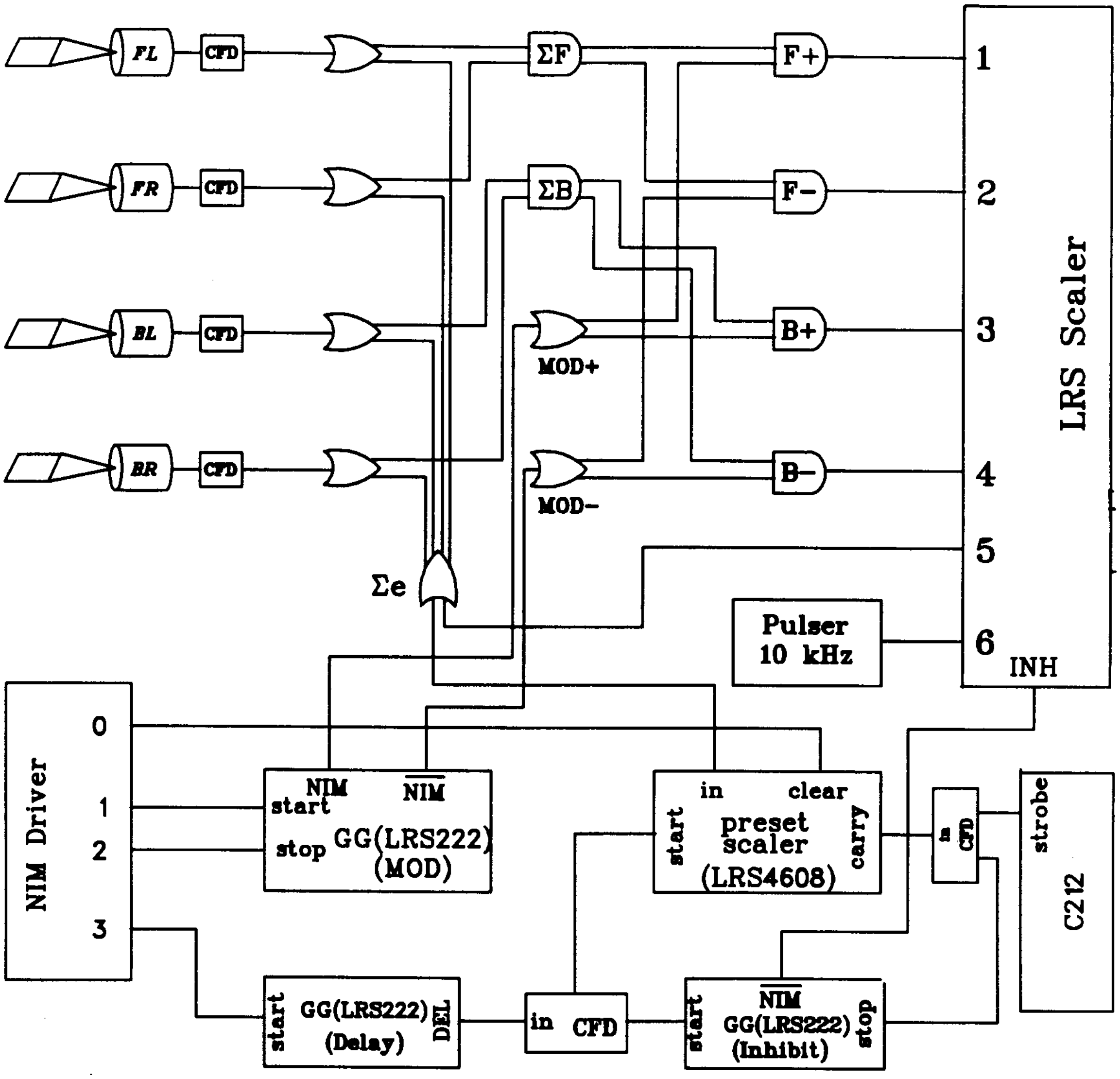

GG: Gate Generator.

Figure 2.9: Block diagram of the electronics setup for μLCR experiments.

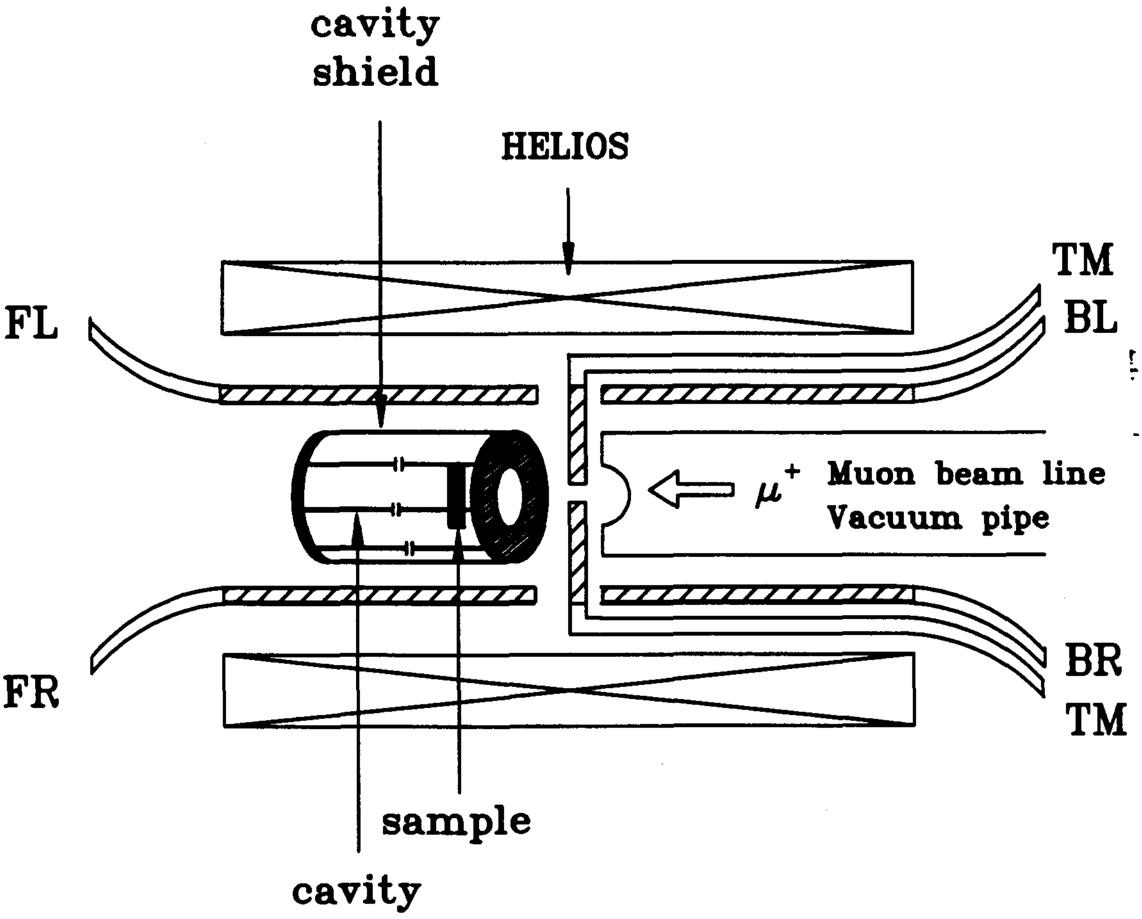

Figure 2.10: Schematic representation of the HELIOS setup with rf cavity.

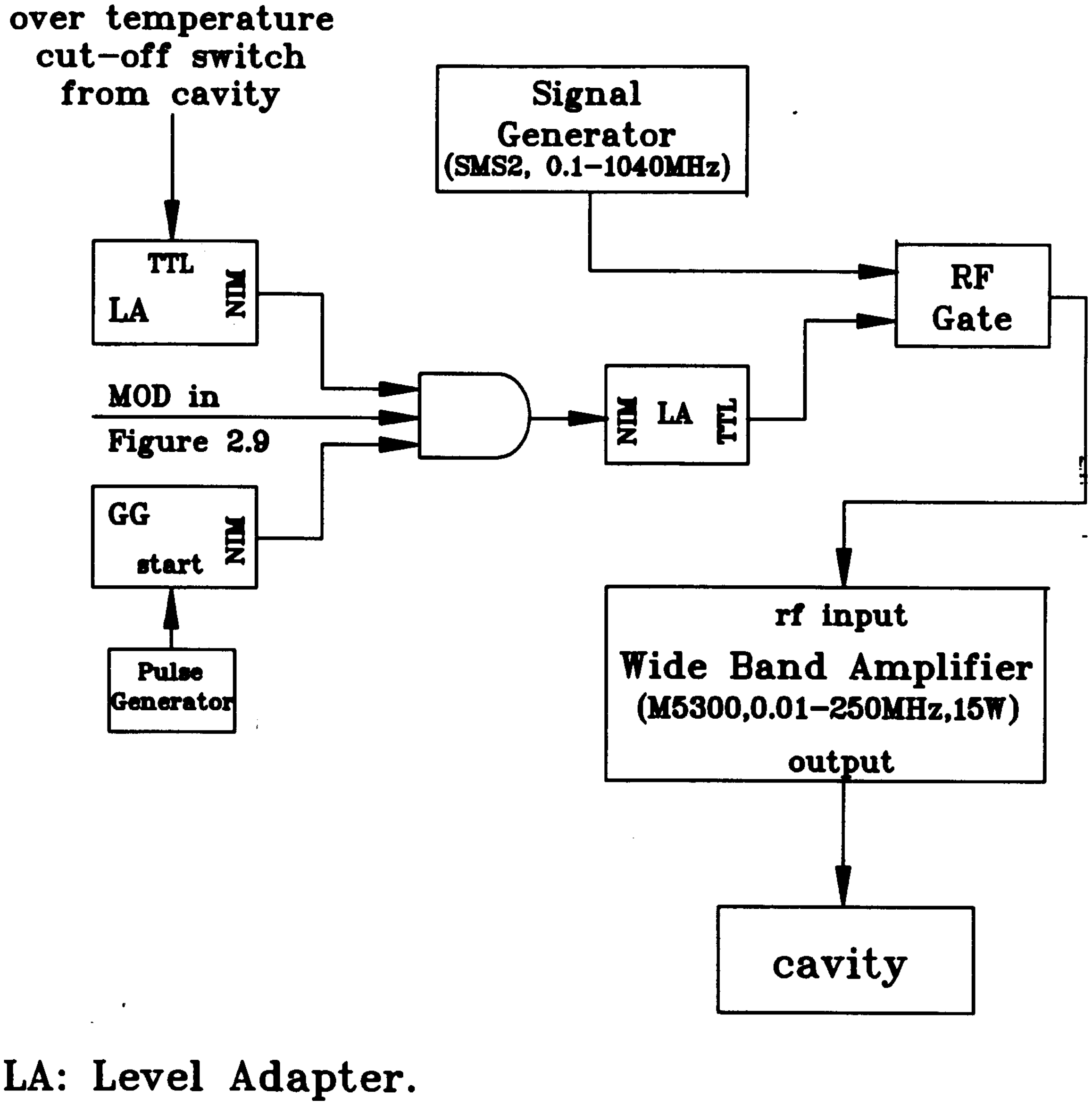

Figure 2.11: Block diagram of the rf source for rf-IμSR experiments.

factors (at least 50%) at full power over extended periods of time. In fact because the frequency spectrum for various types of μSR experiments at TRIUMF varies so widely, it has been found invaluable to use an amplifier that has the largest available rf bandwith (250 MHz is generally available at the power levels requred). The rf fields generated are usually proportional to the volume enclosed by the coil or cavity. Therefore beams of large cross-section will generally require a higher power source to fully utilize the available muons. For sample dimensions of 4 cm or less in diameter (the case at TRIUMF) it has been found that power available from a 2-3 kW broadband amplifier has not been the limiting factor for most experiments.

2.6 rf-LFμSR experiments

As was mentioned in both the last section and chapter 1, rf-LFμSR experiments were used to measure the rf perturbation field (B_1). The experimental setup is the same as that for rf-IμSR and is given in Figure 2.10.

In the rf-LFμSR experiment the incident muon polarization is longitudinal and the standard TF-μSR is used, but with the rf pulse triggered by a μ^+ stop. The rf part of the electronics diagram for rf-LFμSR experiments is given in figure 2.12, where 'CFD' is the CFD after the TM counter in figure 2.8. The rest of the electronics is the same as in figure 2.8. The rf field is usually operated at 50% duty cycle (typically with 3 ms rf-on and 3 ms rf-off).

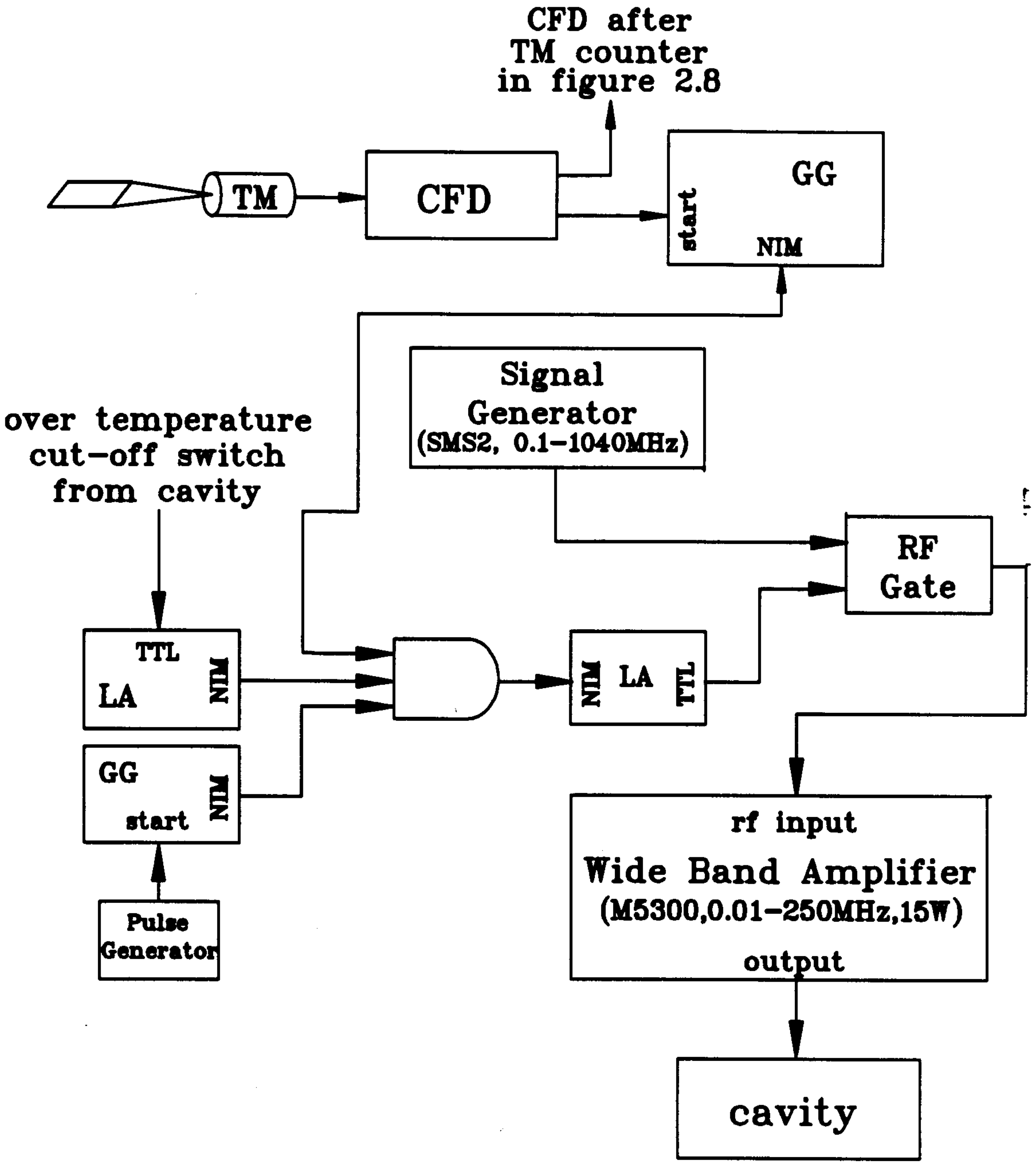

Figure 2.12: Block diagram of the rf source for rf-LFμSR experiments.

2.7 Temperature control systems

Two systems of temperature control were used in the experiments described in this thesis. For temperatures between 0 to 100 °C, the temperatures were controlled by circulating fluid from a constant-temperature bath through copper coils. These copper coils were attached to a thermostating volume surrounding the sample volume for rf-IμSR and rf-LFμSR experiments, and to a copper plate attached to the back of the liquid targets for TF-μSR and μLCR experiments. The tubes which connect the temperature bath to the back of the cell were insulated in order to minimize the temperature gradient between the bath and the sample. In spite of this, there was still a difference of a few degrees. In view of this, a temperature sensor (type K copper-constantan thermocouple) was imbedded in the return line of the thermostating fluid for rf experiments, or between the cell and the copper plate for TF-μSR and μLCR experiments to measure the sample temperature. It was found that this temperature closely represented that of the sample, and the uncertainties of the sample temperature used in μLCR experiments were less than 1 °C.

Low sample temperatures (20 to 270 K) were obtained by using a helium-cooled cold-finger cryostat. The cryostat mainly consists of a cold head and a compressor unit. The control temperature of the cryostat is selected and read directly in Kelvin with a cryogenic digital thermometer with silicon diode sensors. The sample temperature was measured with a silicon diode sensor, a platinm resistance thermometer, or a carbon-glass thermometer. The uncertainty of the sample temperature is estimated to be about 0.5 K.

All rf experiments (*e.g.* rf-IμSR and rf-LFμSR) were done by using a circulator as temperature control system, while μLCR and TF-μSR experiments used both systems.

2.8 Data analysis

The on-line computers in the TRIUMF counting rooms were used for data acquisition and monitoring the experiments. A PDP-11/34 was used initially in M15, but later upgraded to a DECstation 3100. In M20, a PDP-11/60 was first used, and then replaced by a DECstation 3100. Most of the data analysis was performed on the TRIUMF VAX-cluster.

The main software used is a packaged multiparameter chi-squared minimization program called MINUIT, written by James and Roos [32], and distributed in CERNLIB. The program MINUIT can accommodate up to 30 variable parameters, any number of which may be fixed at any time and restored at a later time. Parameters may also be constrained to a physically meaningful numerical range. For the radical studies in chapter six, the eigenstates and eigenfunctions were calculated by using MATH/LIBRARY routines from IMSL [33].

In this thesis, all the TF-μSR time spectra were transformed to frequency space and the peaks fitted with Lorentzian line shapes to determine the frequencies.

The magnetic field calibration is done by measuring the frequencies (ν) of diamagnetic signals as a function of different currents (I) in the superconducting magnet HELIOS. Therefore the magnetic field calibration, $B = B(I)$, can be obtained from

$$B = \nu/\gamma_\mu \tag{2.8}$$

$$= B_o + m \cdot I \tag{2.9}$$

where both B_o and m are constants, and γ_μ is the gyromagnetic ratio of the muon (13.55 kHz/G). The set of the data, $\nu(I)$, is fitted to a straight line for a least-squares fit, and B_o and m are fitting parameters.

Chapter 3

Radio Frequency Resonators

3.1 Radio frequency saddle-Helmholtz coil

Our earliest version of a rf coil was called a 'saddle-Helmholtz' coil, shown in figure 3.1. In order to make the rf field $\vec{B}_1$ perpendicular to $\vec{B}_0$ (the longitudinal static field) and have muons enter the sample without hitting the coil, two half-coils were constructed and connected at both ends as shown in figure 3.1.

The rf resonator is represented by a simple RLC circuit with capacitors C_p in parallel and C_s in series with the rf saddle-Helmholtz coil, L, as shown in figure 3.2. The symbol R in figure 3.2 denotes the equivalent resistance due to the cables, and connectors (about 50 Ω in our case). For simplicity, the small resistance of the rf coil itself is ignored. The term $V_o e^{i\omega t}$ is the rf source. Therefore current passing through the coil, I_L, can be calculated and is given by [34]

$$I_L = I_L^o e^{i(\omega t+\delta)} \tag{3.1}$$

where

$$I_L^o = \frac{1}{1-\omega^2 LC_p}\frac{V_o}{\sqrt{R^2+R_i^2}} \qquad (\omega^2 LC_p \neq 1) \tag{3.2}$$

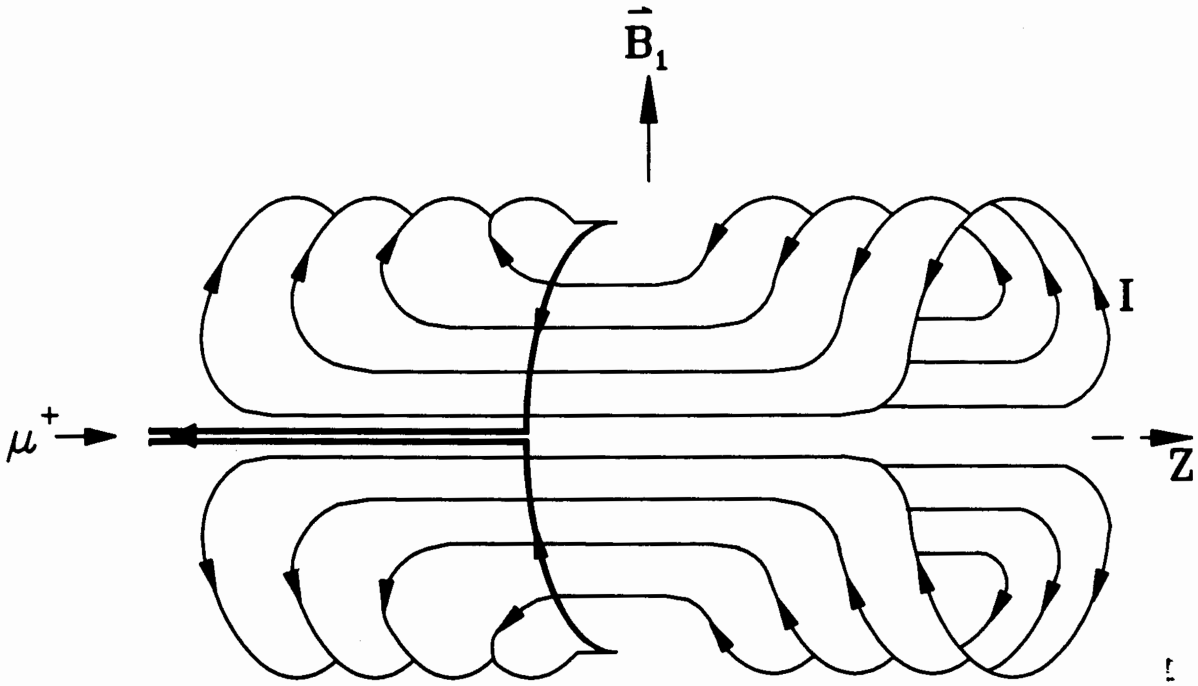

Figure 3.1: A saddle-Helmholtz coil.

$$\delta \;=\; \tan^{-1}(-\frac{R_i}{R}) \tag{3.3}$$

and R_i is the total reactance defined as

$$Z = R + iR_i \tag{3.4}$$

Z is the total impedance of the circuit. R_i can be calculated and is given by

$$R_i = \frac{\omega^2 L(C_s + C_p) - 1}{\omega C_s(1 - \omega^2 LC_p)} \qquad (\omega^2 LC_p \neq 1) \tag{3.5}$$

The circuit is resonant when $R_i = 0$. Therefore the resonant angular frequency and the current passing through the saddle-Helmholtz coil are

$$\omega = \frac{1}{\sqrt{L(C_s + C_p)}} \tag{3.6}$$

and

$$I_L = \frac{V_o}{R}\left(1 + \frac{C_p}{C_s}\right) e^{i\omega t} \tag{3.7}$$

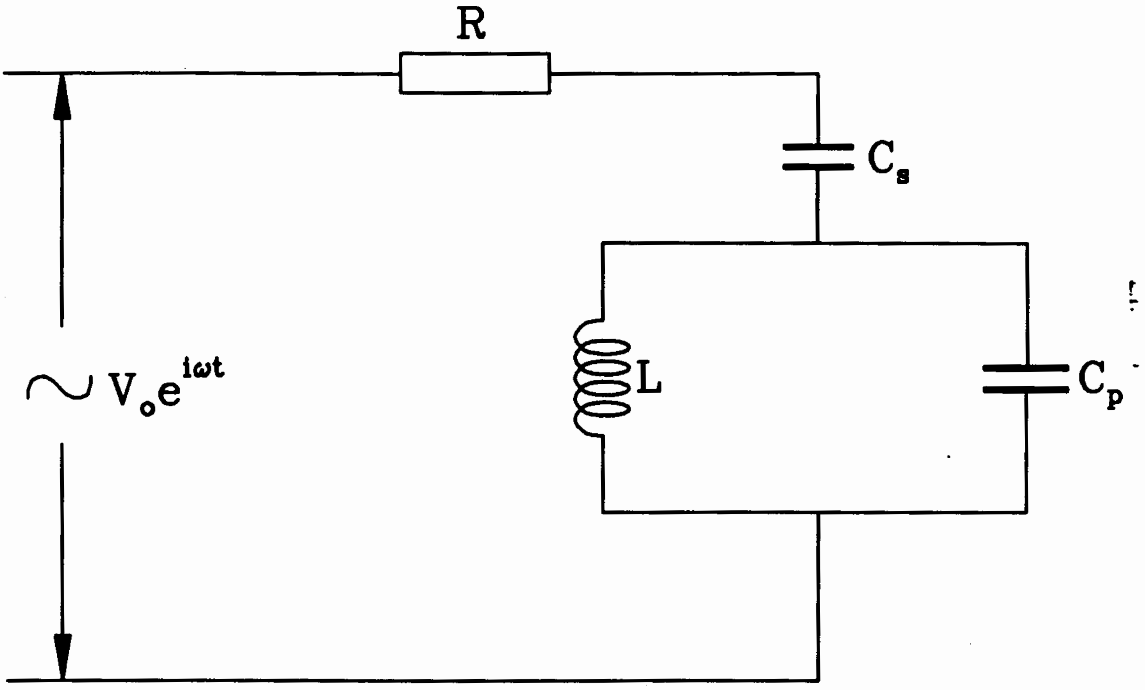

Figure 3.2: RCL circuit, where C_p and C_s are capacitors in parallel and series respectively with the coil, L is the inductance of the saddle-Helmholtz coil and R is the equivalent resistance of the circuit.

respectively.

Both C_p and C_s in our first-generation coil were air-gap capacitors, and were of a nonvariable and variable type, respectively. The desired resonance frequency was tuned by adjusting the series capacitance, C_s. Typical values used in the experiments were $R \sim 50\ \Omega$, $C_s \sim$ 10–100 pF, $C_p \sim 10 - 100$ pF, and $\nu = \omega/2\pi \sim 20 - 30$ MHz.

Although tuning the above circuit is simple in theory, in practice many problems arose due to the high power used. Firstly, the cables which delivered the rf power became very hot. They must not be operated at such a temperature that either they or any equipment they come into contact with (such as the plastic scintillator detectors) are damaged. Secondly, the air-gap capacitors C_s and C_p break down above a critical voltage. From equation 3.7 it is clear that, for a given V_o, an increasing current will flow in the coil for a larger capacitance C_p. Therefore the second-generation saddle-Helmholtz coil was born. Three high voltage (ceramic nonvariable) capacitors in parallel were employed to increase C_p and thus the voltage across them. Thus most of the power was expended on the coil and the three high voltage parallel capacitors rather than on the variable (air-gap) capacitor in series, C_s. In addition, these capacitors (C_p) were put inside the shield parallel with the coil, thus avoiding the need to make external connections which would be heated. The shape of each of these capacitors (C_p) is cylindrical, approximately 1.2 cm in diameter and 1.2 cm in height. High power CW tests showed that the problems of cable heating and capacitor breakdown had been overcome.

For a given current in the saddle-Helmholtz coil, the rf magnetic field strength, B_1, can be calculated and is proportional to the current [34, 35] (or see the section 3.2.3 of this chapter):

$$\vec{B}_1 = cI\,\hat{\mathbf{x}} \tag{3.8}$$

$$= c\frac{V_o}{R}(1+\frac{C_p}{C_s})e^{i\omega t}\,\hat{\mathbf{x}} \tag{3.9}$$

where c is a characteristic of the coil geometry. Because of the symmetry of the saddle-Helmholtz coil, the rf field $\vec{B}_1$ is linearly polarized. A linearly polarized rf field can be resolved into two circularly polarized components. These two components have the same amplitude (half of that of the linearly polarized field strength) and rotate in opposite directions with the same angular frequencies. Only one of these circular polarization components is useful in our experiments, however.

With the saddle-Helmholtz coil described above, the rf-IμSR measurements were successful for μ^+ in water, but unsuccessful for signals from radicals. At the time it was believed that the lack of power could have prevented us from observing signals from radicals. Because the radical decay is much faster than that of the diamagnetic muon state, the radical signal would require an intense rf field in order to be observed. Although full power was being applied, in reality only half this power was useful because the rf field was linearly polarized. The other half of the power was simply wasted and heated the capacitors, the sample, sample cell, and the rf shield.

By applying a circularly polarized rf field to the sample it would be possible to make full use of the available power, and significantly reduce the rf heating. A redesign of the rf resonator enabled us to produce circularly polarized fields, as discussed in the next section.

3.2 Birdcage radio-frequency cavity

3.2.1 Introduction

The final design, called a 'birdcage' resonator (or cavity), is shown in figure 3.3. It consists of two circular end rings connected by N equally spaced straight segments, each of which includes a capacitor C_s (s representing a straight segment). The birdcage resonator can be analyzed using a lumped element balanced delay line, which is shown in figure 3.4, with the ends connected to form a closed loop (points W and X connect to points Y and Z, respectively). All the inductors L_s, representing the straight segments, are coupled to each other by mutual inductance. Likewise, all of the L_r inductors, representing the individual segments of the end rings, are inductively coupled. The resonant nature of the cavity can be understood by considering wave propagation in a periodic structure. Periodic boundary conditions apply to the closed loop.

3.2.2 Low pass filter — analytical circuit of a birdcage cavity

The resonant phenomenon of the periodic structure shown in figure 3.4 is the same as that in figure 3.5, the reason for which will become clear at the end of this section.

The circuit shown in figure 3.5 is a low-pass filter. Equal inductances L_1 and L_2 alternate with equal capacitances C. The capacitances attenuate the high frequencies, while the low frequencies are allowed to pass. To obtain the equations of the circuit shown in figure 3.5, we define Q_n and V_n to be the charge and potential, respectively, on the straight segment n. We also define I_n to be the current flowing in circuit loop n as

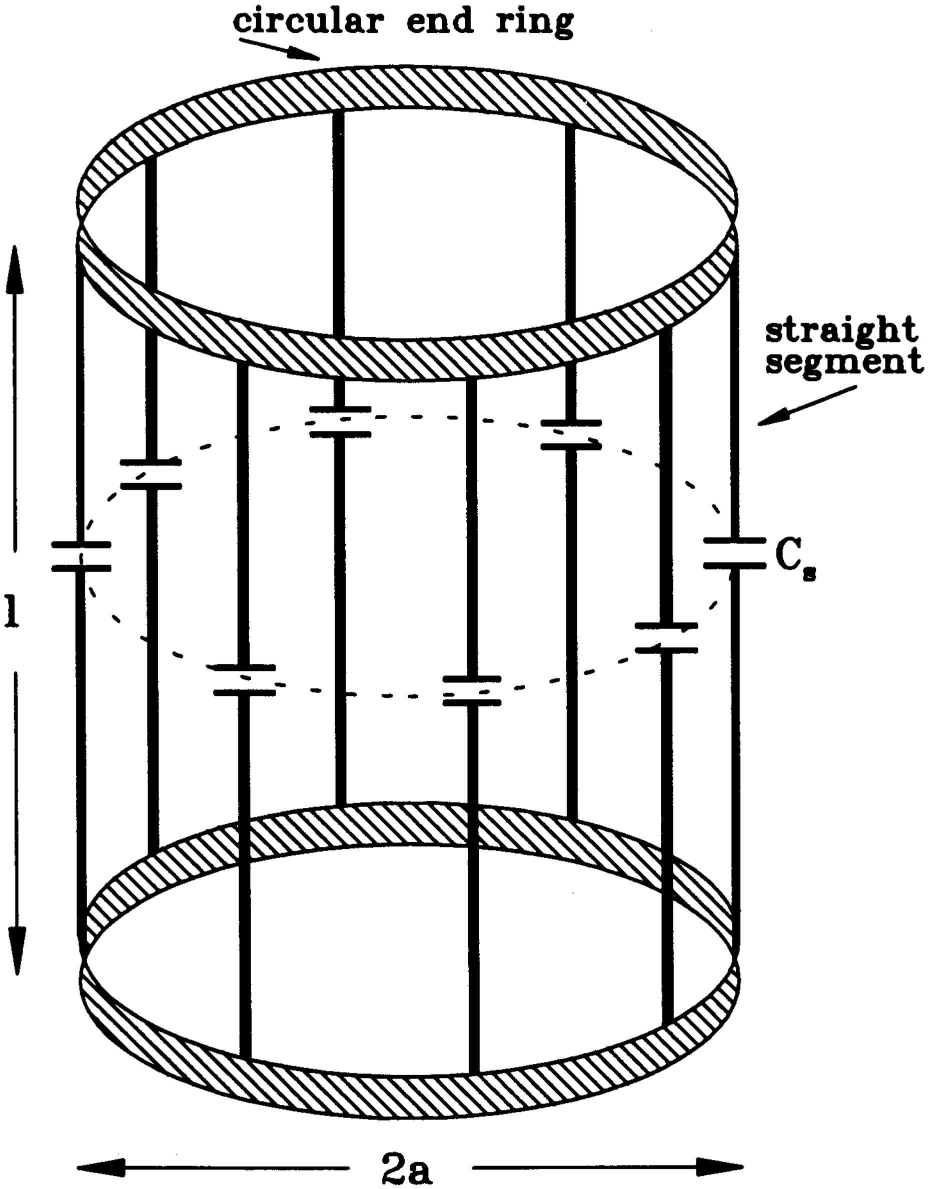

Figure 3.3: A birdcage cavity.

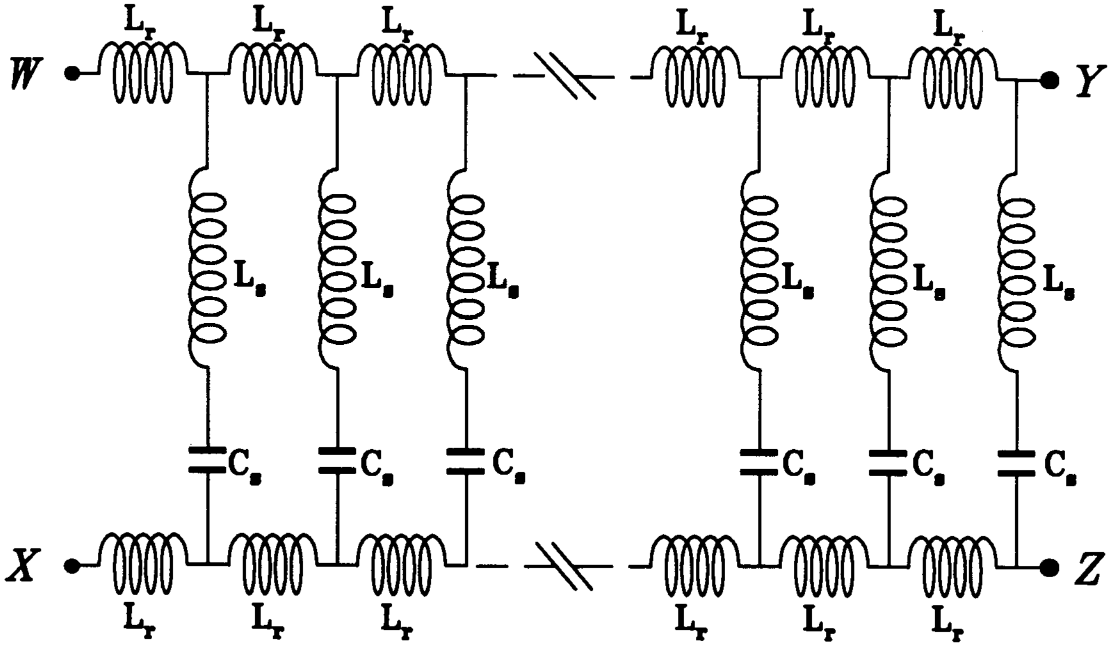

Figure 3.4: Lumped element equivalent circuit of a low-pass birdcage. Points W and X connect to points Y and Z, respectively

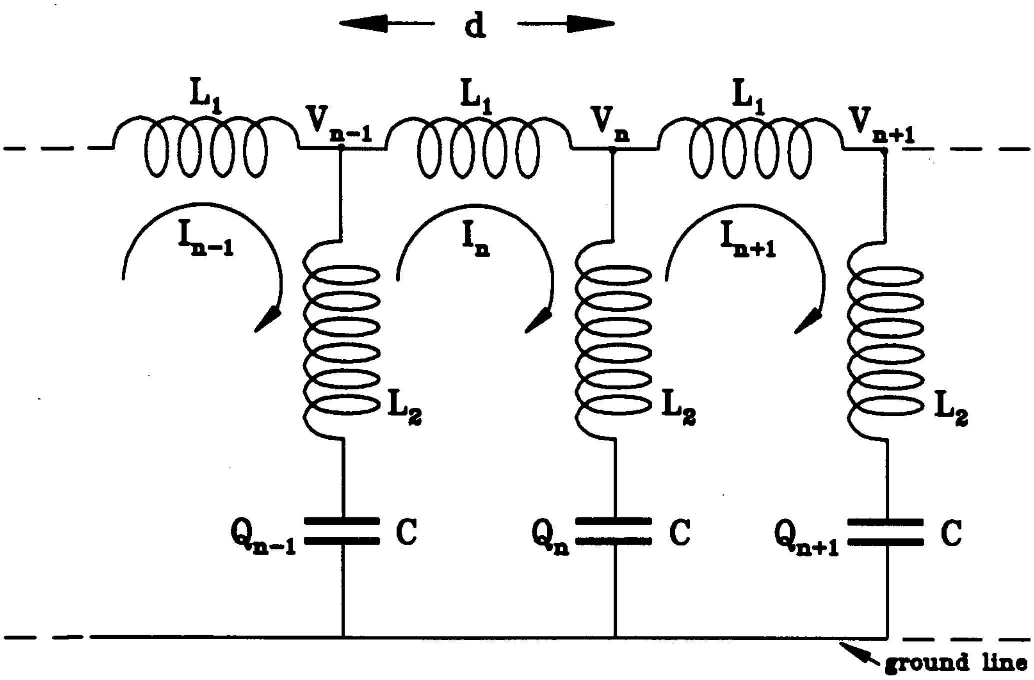

Figure 3.5: Low-pass electric filter.

shown in figure 3.5. Thus the induced EMF is given by

$$\varepsilon = -L_1 \frac{dI_n}{dt} = V_n - V_{n-1} \tag{3.10}$$

where

$$\begin{aligned} V_n &= L_2 \frac{d(I_n - I_{n+1})}{dt} + \frac{Q_n}{C} && (3.11) \\ V_{n-1} &= L_2 \frac{d(I_{n-1} - I_n)}{dt} + \frac{Q_{n-1}}{C}. && (3.12) \end{aligned}$$

and

$$\begin{aligned} I_n - I_{n+1} &= \frac{dQ_n}{dt} && (3.13) \\ I_{n-1} - I_n &= \frac{dQ_{n-1}}{dt}. && (3.14) \end{aligned}$$

Substituting equations 3.11 and 3.12 into equation 3.10 and then differentiating the result, we have

$$L_1 \frac{d^2 I_n}{dt^2} = L_2 \frac{d^2(I_{n-1} + I_{n+1} - 2I_n)}{dt^2} + \frac{1}{C}\frac{dQ_{n-1}}{dt} - \frac{1}{C}\frac{dQ_n}{dt} \tag{3.15}$$

Using equations 3.13 and 3.14, equation 3.15 may be further reduced to

$$L_1 \frac{d^2 I_n}{dt^2} = L_2 \frac{d^2(I_{n-1} + I_{n+1} - 2I_n)}{dt^2} + \frac{1}{C}(I_{n-1} + I_{n+1} - 2I_n) \tag{3.16}$$

The solution of equation 3.16 is the current in the circuit loop n, I_n, as shown in figure 3.5. The voltage and charge can then be obtained from equations 3.11 – 3.14. By considering wave propagation in a periodic structure [29, 36], we may assume a wave solution for equation 3.16:

$$\begin{aligned} I_n &= Ae^{i(\omega t - k'nd)} \\ &\equiv Ae^{i(\omega t - kn)} && (3.17) \end{aligned}$$

with

$$\begin{aligned} k' &= \frac{2\pi}{\lambda} && (3.18) \\ k &\equiv k'd && (3.19) \end{aligned}$$

where d is the period of the circuit loop shown in figure 3.5, λ is the wavelength, ω is the angular frequency, k is the product of the wave number (k') and the period of the circuit loop (d), and A is a constant amplitude.

Equation 3.17 will be a solution of equation 3.16 if the following relation between ω and k is satisfied:

$$\omega^2 = \frac{4\sin^2(k/2)}{C(L_1 + 4L_2\sin^2\frac{k}{2})} \tag{3.20}$$

The above equation is called a dispersion relation.

The same solution of the problem also is obtained for

$$\begin{aligned} k_m &= k + 2\pi m \\ m &= 0,\ \pm1,\ \pm2,\ \cdots \end{aligned}$$

The dispersion relation (equation 3.20) yields the same value of ω for every equivalent k or k_m. Therefore it is sufficient to discuss the properties of the dispersion relation inside one period of k. The most convenient choice is

$$-\pi < k \leq \pi \tag{3.21}$$

because a wave always propagates in the same way to the right and to the left.

From the dispersion relation (equation 3.20), k could be positive or negative for a given value of ω. Therefore the fundamental solution of equation 3.16 would be

$$I_n = Ae^{i(\omega t - kn)} + Be^{i(\omega t + kn)} \tag{3.22}$$

where A is the amplitude for a wave propagating to the right and B to the left. The new range of choice of k for the general solution equation 3.22

is therefore given by

$$0 < k \leq \pi \tag{3.23}$$

The above limitation also means:

$$\lambda \geq 2d \tag{3.24}$$

The shortest wavelength is thus equal to twice the distance between two adjacent straight segments and corresponds to a certain critical frequency or cutoff frequency ν_{max}, where $\nu_{max} = \omega_{max}/2\pi$ is characteristic of the structure and ω_{max} is given by equation 3.20 with $k = \pi$ (*i.e.* $\lambda = 2\text{d}$). That is,

$$\omega_{max} = \frac{2}{\sqrt{C(L_1 + 4L_2)}} \tag{3.25}$$

Angular frequencies above ω_{max} are strongly attenuated and, thus, the system works as a low-pass filter for all angular frequencies

$$\omega \leq \omega_{max} \tag{3.26}$$

The double-line structure in figure 3.6 can be constructed from the single-line structure in figure 3.5. Both circuits shown in figures 3.5 and 3.6 have the same wave solution and dispersion relation. Figure 3.6 can be simplified further in the scheme of figure 3.7. Comparing the analytical circuit of the birdcage resonator (figure 3.4) with figure 3.7, it is obvious that these two circuits are identical provided

$$L_r = L_1, \qquad L_s = 2L_2, \qquad C_s = \frac{C}{2} \tag{3.27}$$

Hence, the birdcage resonator circuit has exactly the same properties as that for the single-line circuit shown in figure 3.5, namely

$$I_n \;=\; Ae^{i(\omega t - kn)} + Be^{i(\omega t + kn)} \tag{3.28}$$

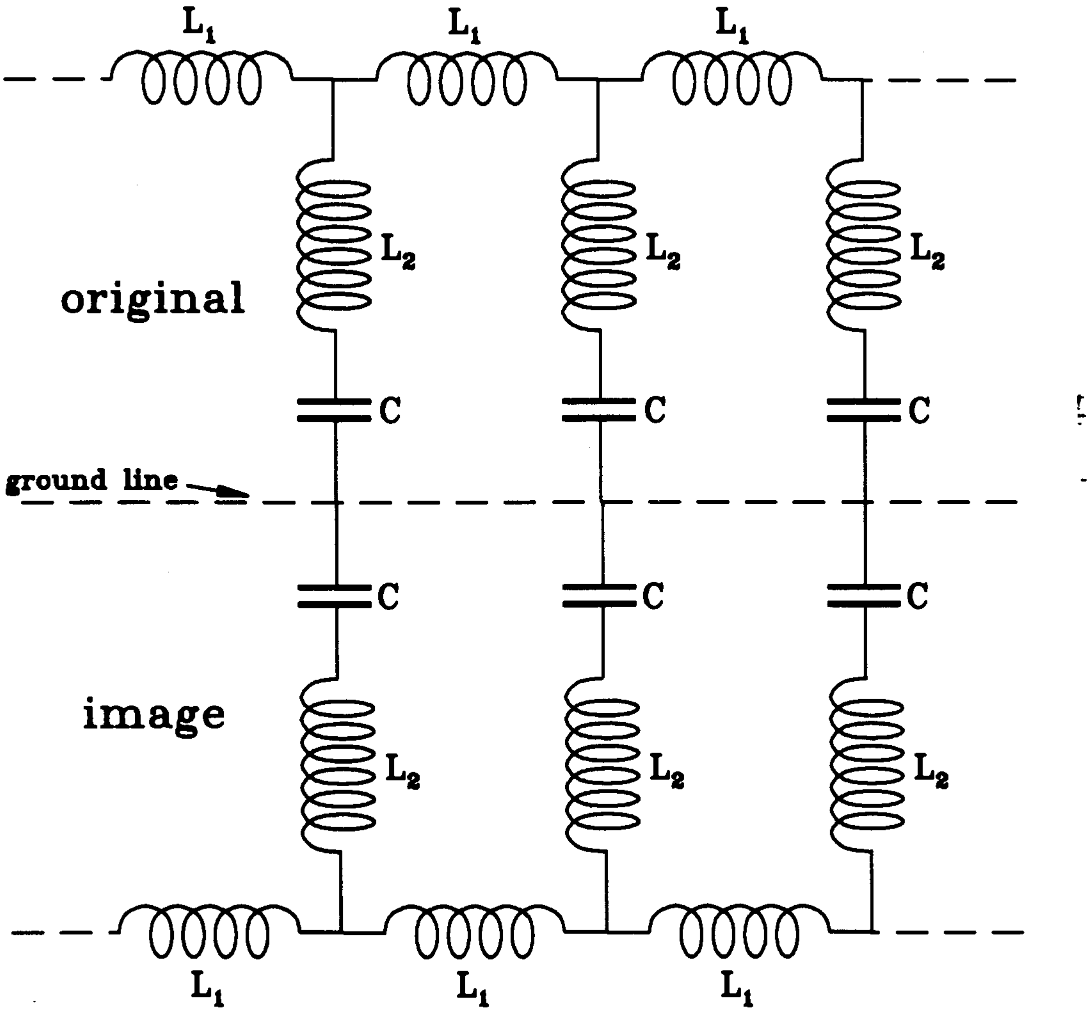

Figure 3.6: Original line of figure 3.5 and its image.

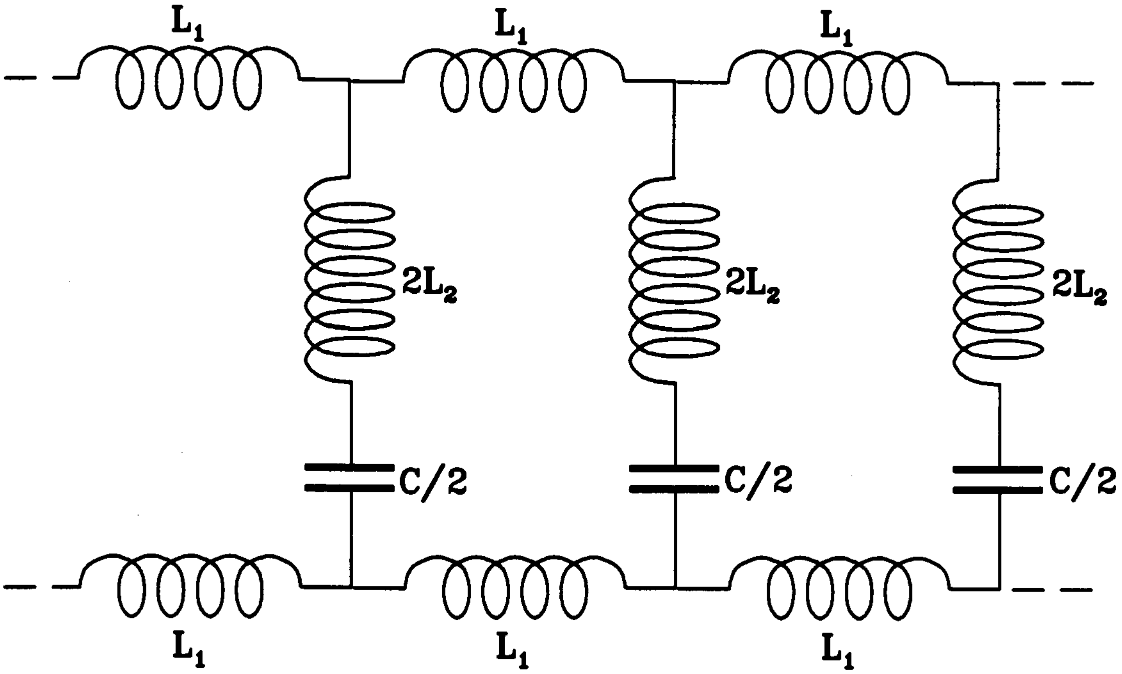

Figure 3.7: Simplified low-pass filter from figure 3.6

$$\omega = \frac{2\sin(k/2)}{\sqrt{2C_s(L_r + 2L_s\sin^2(k/2))}} \tag{3.29}$$

$$\omega_{max} = \frac{2}{\sqrt{2C_s(L_r + 2L_s)}} \tag{3.30}$$

$$0 < k \leq \pi \tag{3.31}$$

If waves propagating to the right and to the left are considered separately, the quantity k is the phase shift in passing from a circuit loop n to its right-hand (or left-hand) neighbor $n + 1$ (or $n - 1$):

$$I_{n+1} = I_n e^{-ik} \tag{3.32}$$

$$(or \quad I_{n-1} = I_n e^{-ik})$$

Equation 3.28 gives the flow as the current in each circuit loop of the birdcage resonator and, therefore, the rf magnetic field $\vec{B}_1$ inside the resonator can be calculated.

3.2.3 Radio frequency magnetic field $\vec{B}_1$

rf magnetic field ($\vec{B}_1$) of a half-saddle coil

Figure 3.8 shows the shape of a half-saddle coil. The N segment birdcage can be thought of as N such half-saddle coils in parallel. Here the first task therefore is to calculate $\vec{B}_1$ for a single half-saddle coil.

Let a be the radius of the coil, 2θ the angular width, I the current, and l the length as shown in figure 3.8. At any point P on the transverse midplane (see figure 3.8), the rf field produced by the current element $Id\vec{l}_b$ of the bottom arc can be resolved into an axial component and a radial component. For each such current element there is a matching element $Id\vec{l}_t$ directly above, but on the top arc. The axial components of the total field exactly cancel, whereas the radial components add together. This can be seen clearly by using the Biot-Savart law. The rf fields contributed by current elements $Id\vec{l}_b$ and $Id\vec{l}_t$ are

$$d(\vec{B}_1)_b = \frac{\mu_0}{4\pi} I \frac{d\vec{l}_b \times \vec{r}_b}{r_b^3} \tag{3.33}$$

and

$$d(\vec{B}_1)_t = \frac{\mu_0}{4\pi} I \frac{d\vec{l}_t \times \vec{r}_t}{r_t^3} \tag{3.34}$$

respectively, where $\vec{r}_t$ and $\vec{r}_b$ are shown in figure 3.8 and

$$\begin{aligned} d\vec{l}_b &= -d\vec{l}_t \\ &\equiv d\vec{l} \\ &= a d\phi \, (\sin\phi \, \hat{\mathbf{x}} - \cos\phi \, \hat{\mathbf{y}}) && (3.35) \\ \vec{r}_b &= r_m \hat{\mathbf{r}} + \frac{l}{2}\hat{\mathbf{z}} - \vec{a} && (3.36) \end{aligned}$$

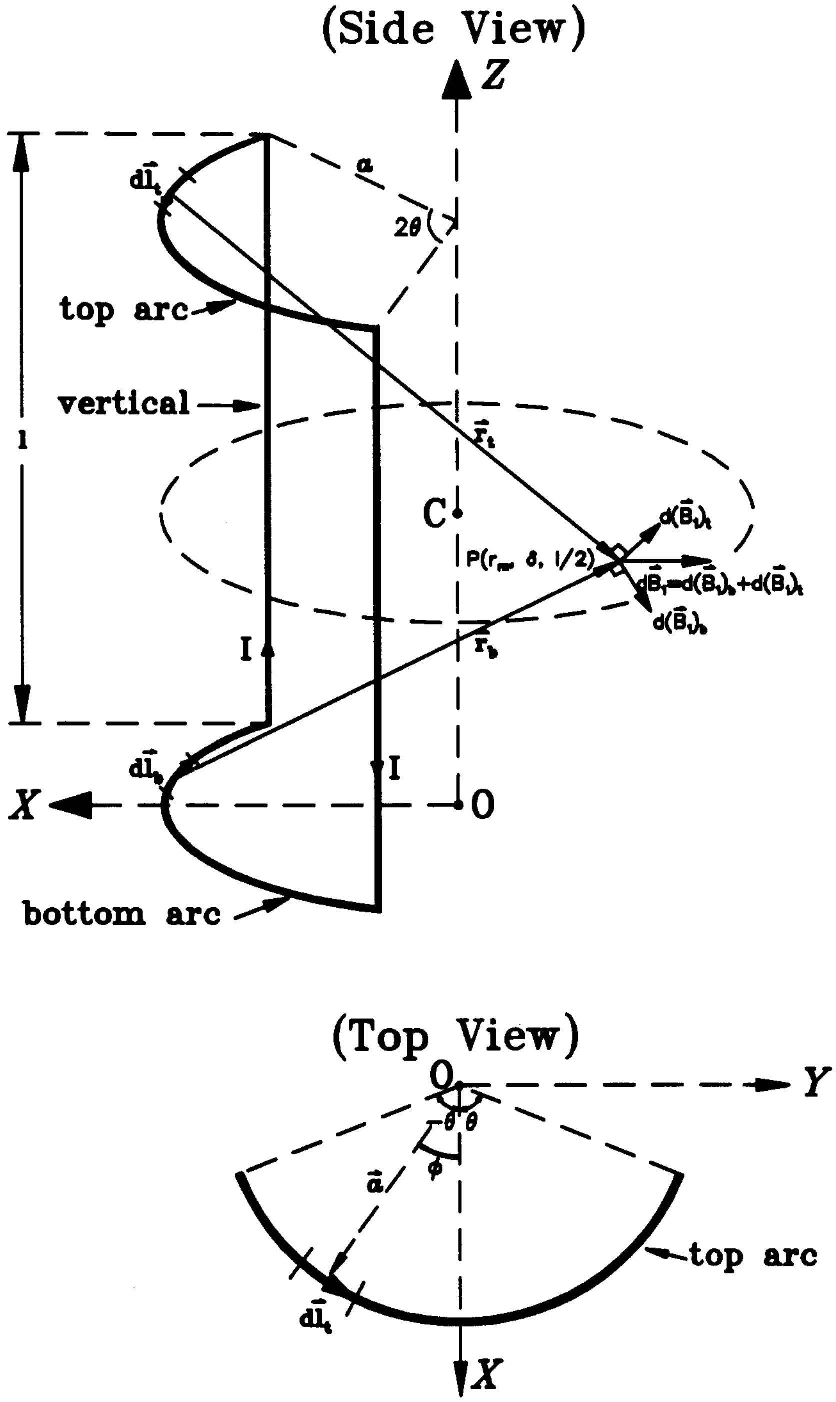

Figure 3.8: Half saddle-shaped coil, where a is the radius of the coil, l the length, and 2θ the angular width.

$$
\begin{aligned}
\vec{r}_t &= r_m\hat{\mathbf{r}} - \frac{l}{2}\hat{\mathbf{z}} - \vec{a} && (3.37)\\
|\,\vec{r}_b\,| &= |\,\vec{r}_t\,| \\
&\equiv r && (3.38)
\end{aligned}
$$

Therefore the total field produced by both current elements is given by

$$
\begin{aligned}
d(\vec{B}_1)_{arc\ elements} &= \frac{\mu_0}{4\pi} I \frac{d\vec{l} \times (\vec{r}_b - \vec{r}_t)}{r^3} && (3.39)\\
&= -\frac{\mu_0}{4\pi} a l I \frac{(\cos\phi\,\hat{\mathbf{x}} + \sin\phi\,\hat{\mathbf{y}})d\phi}{r^3} && (3.40)
\end{aligned}
$$

and the total field at the point P on the transverse midplane contributed by two arcs will be

$$
(\vec{B}_1)^P_{arcs} = \int_{-\theta}^{\theta} d(\vec{B}_1)_{arc\ elements} \qquad (3.41)
$$

Hence due to the symmetry of the bottom arc and top arc with respect to the transverse midplane, only the $\hat{\mathbf{x}}$ and $\hat{\mathbf{y}}$ components of the total rf field exist (shown as the sum of vectors d$(\vec{B}_1)_b$ and d$(\vec{B}_1)_t$ in figure 3.8).

From the Biot-Savart law, the field at any point produced by any vertical current will always be radial [34] (right-hand rule) and perpendicular to the plane that contains the vertical wire and the observation point. Therefore, in the case of a half-saddle coil consisting of two arcs and two vertical segments, the direction of the total rf field at the point P on the transverse midplane would always be parallel to the transverse midplane with no axial component at all.

Furthermore, at the center C on the transverse midplane ($r_m = 0$), the rf field contributed by two arcs can be calculated from equations 3.40 and 3.41 with the condition $\mathrm{r}_m = 0$ and is given by

$$
(\vec{B}_1)^C_{arcs} = -\frac{\mu_0}{4\pi} \frac{Ia}{\left(\sqrt{a^2 + (l/2)^2}\right)^3} 2l \sin\theta\ \hat{\mathbf{x}} \qquad (3.42)
$$

Similarly, by using the Biot-Savart law, the rf field produced by one of the vertical segments of the coil has $\hat{\mathbf{x}}$ and $\hat{\mathbf{y}}$ components. By symmetry of the two vertical segments with respect to the center C, the $\hat{\mathbf{y}}$ components cancel and the total rf the field produced by two vertical sections of the coil is given by [37]

$$(\vec{B}_1)^C_{verticals} = -\frac{\mu_0}{4\pi}\frac{I/a}{\left(\sqrt{a^2+(l/2)^2}\right)}2l\sin\theta\ \hat{\mathbf{x}} \tag{3.43}$$

Therefore at the center C, the total $\vec{B}_1$ produced by a half-saddle coil is

$$\vec{B}_1 = bI\,\hat{\mathbf{x}} \tag{3.44}$$

where

$$b = -\frac{\mu_0}{4\pi}\left(\frac{al}{\left(\sqrt{a^2+(l/2)^2}\right)^3} + \frac{l/a}{\left(\sqrt{a^2+(l/2)^2}\right)}\right)2\sin\theta \tag{3.45}$$

and b is a characteristic of the coil geometry alone.

rf magnetic field ($\vec{B}_1$) of a birdcage cavity

As was mentioned in the last section, the birdcage cavity with N straight segments can be treated as N half-saddle coils in parallel. The nth half-saddle coil passes the current given by equation 3.28. The corresponding magnetic field, $(\vec{B}_1)_n$, at the center of the transverse midplane of the birdcage cavity due to the current (I_n) obeys equations 3.44 and 3.45, and is therefore perpendicular to the central surface of the nth half-saddle coil, which shows as the outward pointing arrows in figure 3.9 with the magnitude of the field next to them. Figure 3.9 shows the top view of the transverse midplane of a birdcage cavity with $N = 8$. (The final birdcage rf cavities which were used in our experiments were made with $N = 8$.) The arrows along the ring show the direction of current flow.

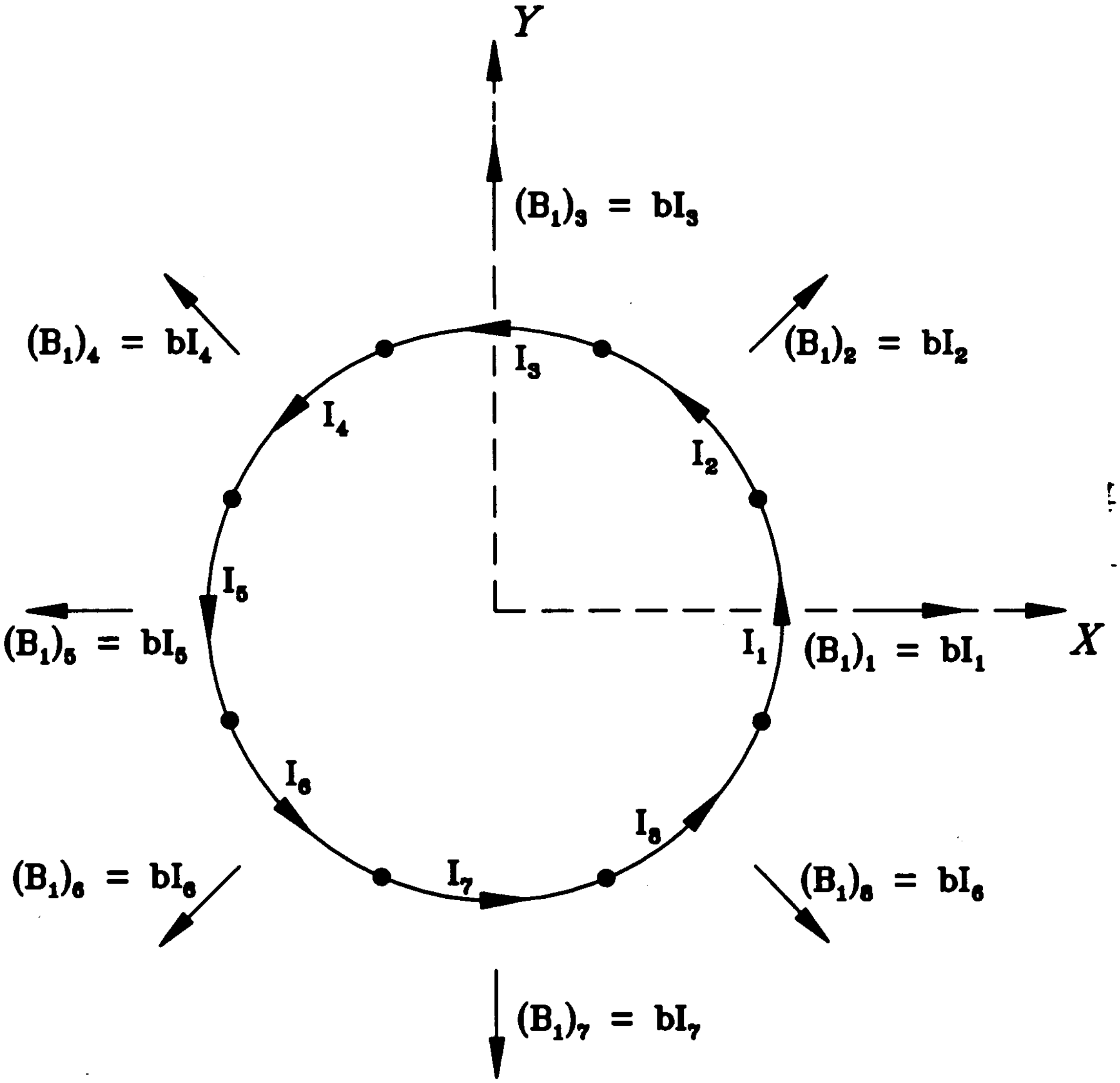

Figure 3.9: Top view of the transverse midplane of the birdcage cavity with $N = 8$. Outward pointing arrows are the rf fields $\vec{B}_1$ at the center of the midplane and the arrows along the ring represent the direction of the current flow.

As was discussed in the last section, the rf magnetic field produced by a half-saddle coil at the any point on the transverse midplane has no axial component, the direction of the rf field at the any point on the transverse midplane of the birdcage resonator is then transverse. Therefore the birdcage cavity can be thought of as an approximation to a cylindrical cavity operating in a TM mode.

Because the magnetic fields obey the principle of linear superposition, the total $\vec{B}_1$ produced by a birdcage cavity is the linear vector sum of the rf fields individually produced by each of the half-saddles (circuit loops) of the birdcage. Also because the rf field of each circuit loop is proportional to the current passing through the circuit loop as shown in equation 3.44, and the current is the sum of the two waves propagating in opposite directions as shown in equation 3.28, then the overall magnetic field can be treated by considering waves propagating to the right and left separately. If only the wave propagating to the right is considered here, equations 3.44 and 3.28 for the nth circuit loop of the cavity can be rewritten as:

$$
\begin{aligned}
(\vec{B}_1)_n &= bI_n \,\hat{\mathbf{x}} && (3.46)\\
I_n &= Ae^{i(\omega t-kn)} && (3.47)\\
n &= 1, \cdots, 8 && (3.48)
\end{aligned}
$$

Each of the 8 repeated elements of the birdcage introduces a phase shift k. Applying the periodic boundary condition to the closed loop, the boundary condition is given by

$$I_n = I_{n+8} \tag{3.49}$$

From the above equation, k satisfies

$$e^{-i8k} = 1. \tag{3.50}$$

Thus the total phase shift ($8k$) must be an integer multiple of 2π. Therefore the resonant condition is

$$8k = 2\pi M \tag{3.51}$$

where M is an integer satisfying $1 \leq M \leq 4$, which can be obtained by considering the constraints on k from equation 3.23. Therefore, k can only have 4 values and they are

$$k = \frac{M}{4}\pi \quad (M = 1, \cdots, 4) \tag{3.52}$$

The low-frequency mode, corresponding to $k = \pi/4$ (or $M = 1$) of equation 3.29, is called the fundamental mode. By considering the resonant condition contained in equation 3.51, the currents passing through each circuit loop of the birdcage cavity can all be expressed in terms of the current in the first circuit loop, I_1, as follows:

$$\begin{aligned} I_n &= I_{n-1}e^{-ik} \quad (n = 1, \cdots, 8) && (3.53) \\ I_1 &= Ae^{i(\omega t-k)} && (3.54) \end{aligned}$$

Defining the X and Y axes to be perpendicular to the surface of the center of the first ($n = 1$) and third ($n = 3$) circuit loops, respectively, (figure 3.9), the total rf field $\vec{B}_1$ at the center of the transverse midplane of the birdcage will be the vector sum of all four vectors shown in figure 3.10 where

$$I_1{}' = I_1(1 - e^{i4k}) \tag{3.55}$$

Projecting all the vectors in figure 3.10 onto the X and Y axes, and summing them, the total rf field will be

$$\begin{aligned} \vec{B}_1|_x &= I_1'b\left(1 + i\sqrt{2}e^{-i2k}\sin k\right)\hat{\mathbf{x}} && (3.56) \\ \vec{B}_1|_y &= I_1'b\left(e^{-i2k} + \sqrt{2}e^{-i2k}\cos k\right)\hat{\mathbf{y}} && (3.57) \end{aligned}$$

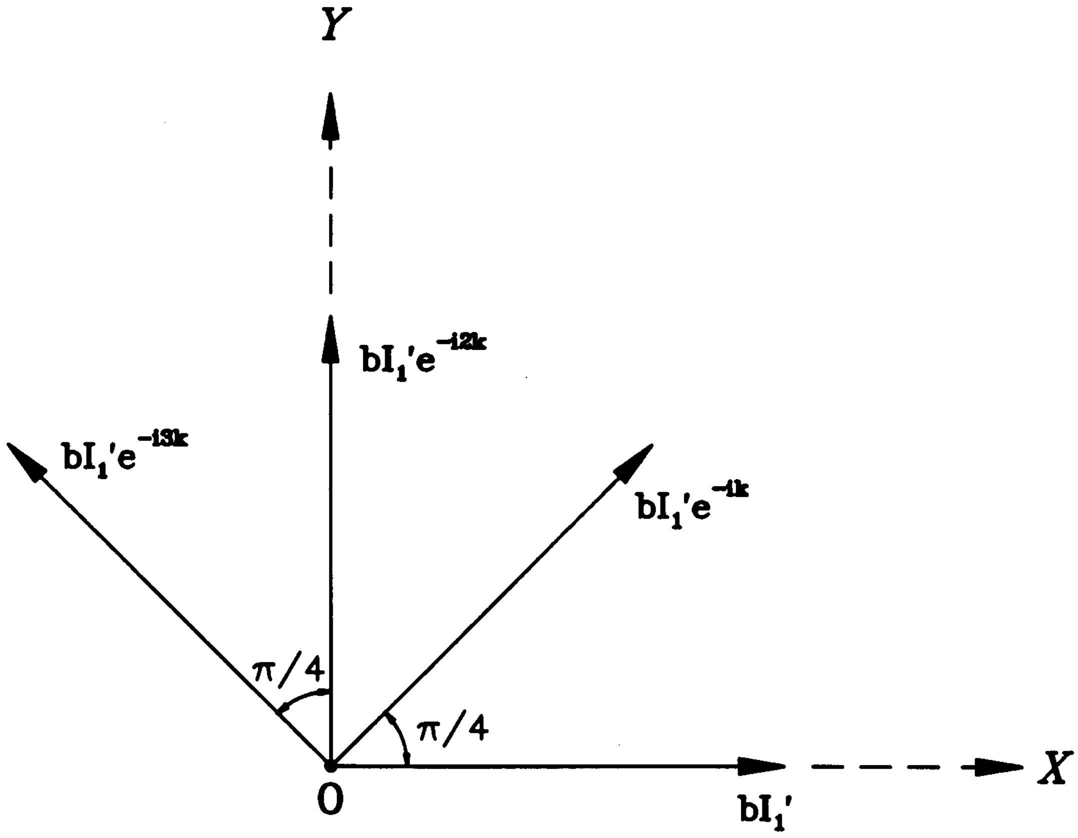

Figure 3.10: $\vec{B}_1$ vectors where I′ = I_1 (1-e^{i4k})

For the fundamental mode ($k = \pi/4$), the total field $\vec{B}_1$ at the center of the transverse midplane of the birdcage will be the vector addition of the above two equations and is given by

$$\vec{B}_1 = 4Ab(e^{i(\omega t-k)}\hat{\mathbf{x}} + e^{i(\omega t-(k+\frac{\pi}{2}))}\hat{\mathbf{y}}) \tag{3.58}$$

Thus, the rotation of $\vec{B}_1$ is counter-clockwise when viewed by an observer facing into the oncoming wave. This wave is called left circularly polarized [29].

Similarly, it can be shown that the field ($\vec{B}_1$) at the center of the transverse midplane of the birdcage contributed by the wave propagating to the left for the fundamental mode is given by

$$\vec{B}_1 = 4Bb(e^{i(\omega t+k)}\hat{\mathbf{x}} + e^{i(\omega t+(k+\frac{\pi}{2}))}\hat{\mathbf{y}}) \tag{3.59}$$

The rotation of this $\vec{B}_1$ is clockwise when looking into the wave, and the wave is right circularly polarized.

Therefore, for the wave given by equation 3.28, the total field at the center of the birdcage for the fundamental mode is the vector sum of equations 3.58 and 3.59 and is given by

$$\begin{aligned} \vec{B}_1 &= 4b\left[Ae^{i(\omega t-k)} + Be^{i(\omega t+k)}\right]\hat{\mathbf{x}} \\ &+ 4b\left[Ae^{i(\omega t-(k+\frac{\pi}{2}))} + Be^{i(\omega t+(k+\frac{\pi}{2}))}\right]\hat{\mathbf{y}} \end{aligned} \tag{3.60}$$

From the above equation, it is clear that the rf field $\vec{B}_1$ is linearly polarized if $|A| \sim |B|$. Otherwise the wave $\vec{B}_1$ is elliptically polarized. For the case where $A \gg B$ (where B can be ignored), the elliptically polarized wave becomes a left circularly polarized wave. For the case where $B \gg A$ (where A can be ignored), the elliptically polarized wave becomes a right circularly polarized wave. Which of the above conditions is satisfied will depend on where the rf high power input and grounding are connected to the birdcage resonator.

Note that the rf magnetic field given by equation 3.60 is the $\vec{B}_1$ produced at the center of the transverse midplane of a birdcage cavity. By using the analysis in the last subsection for a point P which is off-center on the transverse midplane, the total magnetic field can be calculated. Hayes *et al.* [38] calculated the rf field $\vec{B}_1$ produced on the transverse midplane of a birdcage resonator containing 16 equally spaced straight segments. The result of the calculation also shows that the direction of rf field at any point on the transverse midplane is transverse, the same as that of the rf field at the center of the transverse midplane [38]. The normalized contours of constant transverse rf field magnitude are shown in figure 3.11. The near optimal rf field (B_1) homogeneity shown in figure 3.11 allows us to use $\vec{B}_1$, the rf field produced at the center of the transverse midplane given by equation 3.60, as the expression for the rf field produced at ***any*** point on the transverse midplane of a birdcage resonator.

Linear and circular polarization of the wave $\vec{B}_1$ produced by the birdcage cavity

The birdcage rf cavity is driven by a source of oscillating voltage $V_{rf}(t)$ given by

$$V_{rf}(t) = V_o e^{i\omega t} \tag{3.61}$$

If the rf high power lead goes to the nth circuit loop of the cavity (point 'a' shown in figure 3.12) and the rf grounding goes to the $(n+m)$th circuit loop (point 'b' shown in figure 3.12), then the rf input potential

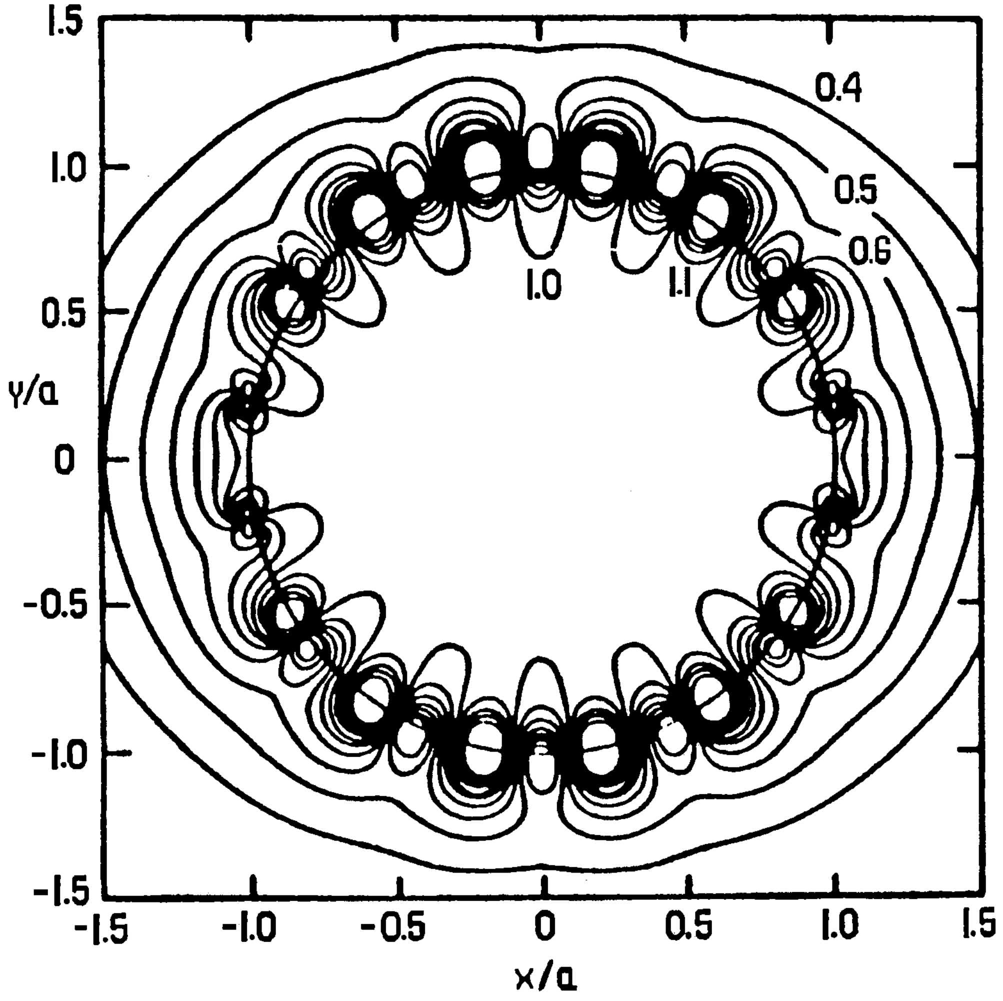

Figure 3.11: Computed [38] contour plots of constant rf field magnitude for the transverse midplane of a birdcage resonator with $N = 16$.

Figure copyright by Academic Press (1985).

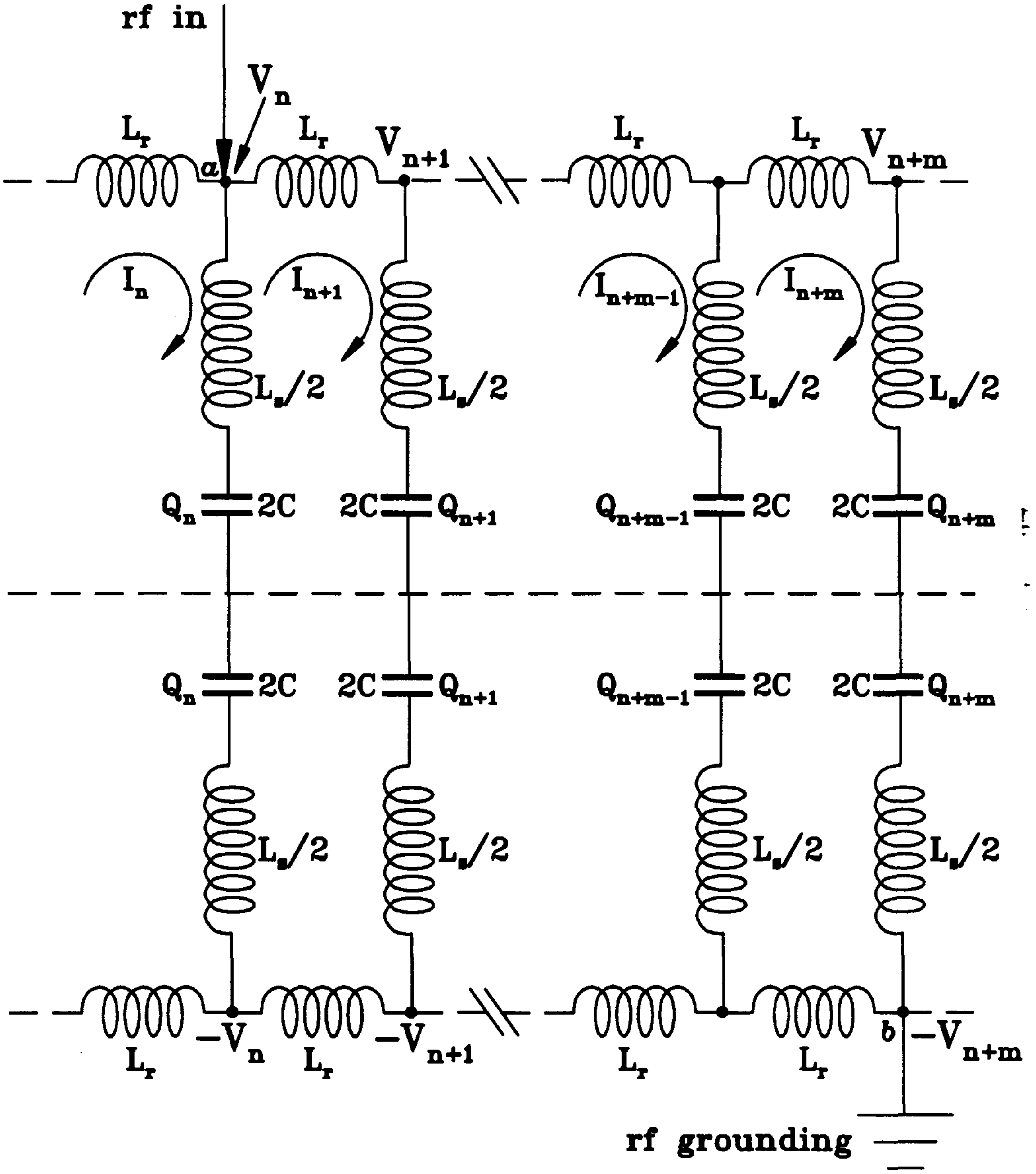

Figure 3.12: Equivalent circuit of a birdcage cavity, where '*a*' and '*b*' indicate rf input and grounding location, respectively.

can be expressed as

$$\begin{aligned} V_{rf}(t) &= V_a - V_b \\ &= (V_n - V_{n+1}) + (V_{n+1} - V_{n+2}) + \\ &\quad \cdots + (V_{n+m-1} - V_{n+m}) + 2V_{n+m} \\ &= V_n + V_{n+m} \end{aligned} \tag{3.62}$$

V_n can be calculated from a known I_n, which is given in equation 3.28. From figure 3.12, the expression for V_n in terms of I_n is

$$V_n = \frac{L_s}{2}\frac{d(I_n - I_{n+1})}{dt} + \frac{Q_n}{2C} \tag{3.63}$$

where Q_n is given by equation 3.13. Integrating equation 3.13 with the initial conditions $Q_n(t = 0) = 0$ and $I_n(t = 0) = 0$ (for $n = 1, 2, \cdots, 8$), $Q_n(t)$ is obtained as

$$Q_n(t) = \frac{1}{i\omega}\left[I_n(t) - I_{n+1}(t)\right] \tag{3.64}$$

Differentiating equation 3.28 with respect to time, V_n from equation 3.63 can easily be shown to be

$$V_n = Z\left[I_n(t) - I_{n+1}(t)\right] \tag{3.65}$$

where Z is the total impedance of the capacitance $2C$ and the inductance $L_s/2$ and is given by

$$Z = Z_C + Z_{L_s} \tag{3.66}$$

$$Z_C = \frac{1}{i\omega 2C} \tag{3.67}$$

$$Z_{L_s} = i\omega\frac{L_s}{2} \tag{3.68}$$

From equation 3.65, the expression for $V_{rf}(t)$ shown in equation 3.62 becomes

$$V_{rf} = Z\left[(I_n + I_{n+m}) - (I_{n+1} + I_{n+m+1})\right] \tag{3.69}$$

With the general expression of I_n (equation 3.28), $I_n + I_{n+m}$ is given by

$$I_n + I_{n+m} = 2\cos\frac{km}{2} I_{n+\frac{m}{2}} \tag{3.70}$$

Therefore $V_{rf}(t)$ in equation 3.69 can be written as

$$\begin{aligned} V_{rf} &= 2\cos\frac{km}{2}\left(I_{n+\frac{m}{2}} - I_{n+1+\frac{m}{2}}\right) \\ &= Z' 4\sin\frac{k}{2}\cos\frac{km}{2}\left(Ae^{i(\omega t-kl)} - Be^{i(\omega t+kl)}\right) \\ &= Z_r \alpha e^{i\omega t}\left(Ae^{-ikl} - Be^{ikl}\right) \end{aligned} \tag{3.71}$$

where

$$Z_r = iZ \tag{3.72}$$

$$\alpha = 4\sin\frac{k}{2}\cos\frac{km}{2} \tag{3.73}$$

$$l = n + \frac{m+1}{2} \tag{3.74}$$

Then the component of the actual rf voltage, obtained by taking the real part of equations 3.71 and 3.61, is

$$V_o \cos\omega t = Z_r \alpha \left[(A-B)\cos(kl)\cos\omega t + (A+B)\sin(kl)\sin\omega t\right] \tag{3.75}$$

In order for the above equation to be true at all times t, the coefficients of the terms $\cos\omega t$ and $\sin\omega t$ on the left- and right-hand sides of the equation must be equal. Therefore, A and B in equation 3.75 satisfy

$$V_o = Z_r \alpha (A-B)\cos(kl) \tag{3.76}$$

$$0 = Z_r \alpha (A+B)\sin(kl) \tag{3.77}$$

The above equations have two solutions, one of which is

$$A + B = 0 \tag{3.78}$$

$$A - B = \frac{V_o}{Z_r \alpha \cos(kl)} \qquad (\cos(kl) \neq 0) \tag{3.79}$$

while the other is

$$\sin kl = 0 \tag{3.80}$$

$$A - B = \frac{V_o}{Z_r \alpha \cos kl} \tag{3.81}$$

From the discussion of the last subsection, the first solution (equations 3.78 and 3.79), where $\mid A \mid = \mid B \mid$, means that the wave B_1 is linearly polarized for those locations of rf input and grounding which satisfy $\cos(lk) \neq 0$ and therefore satisfy

$$lk \neq \frac{(n'+1)\pi}{2} \qquad (n' = 0, 1, 2, \cdots,) \tag{3.82}$$

With the expression for l (equation 3.74) and the fundamental mode ($k = \pi/4$), the above condition can be rewritten as

$$n + (n+m) \neq 3 \quad (n' = 0) \tag{3.83}$$

$$n + (n+m) \neq 11 \quad (n' = 1) \tag{3.84}$$

It can be easily shown that equation 3.82 will yield the same conclusion for all $n' \geq 2$ as it will for $n' = 0$ and 1. Note that n is where the rf input is connected and $n+m$ is where the rf grounding is connected. The above two inequalities are satisfied as long as the four input-grounding configurations, shown in figure 3.13, are avoided. In other words, the cavity will produce a linearly polarized magnetic field B_1 for *all* the rf input-grounding configurations except those shown in figure 3.13.

Naturally, the question arises as to what the polarization of the magnetic field will be for the rf input-grounding configurations shown in figure 3.13. From the second solution (equation 3.80), lk has to satisfy the condition

$$lk = n''\pi \qquad (n'' = 1, 2, \cdots,) \tag{3.85}$$

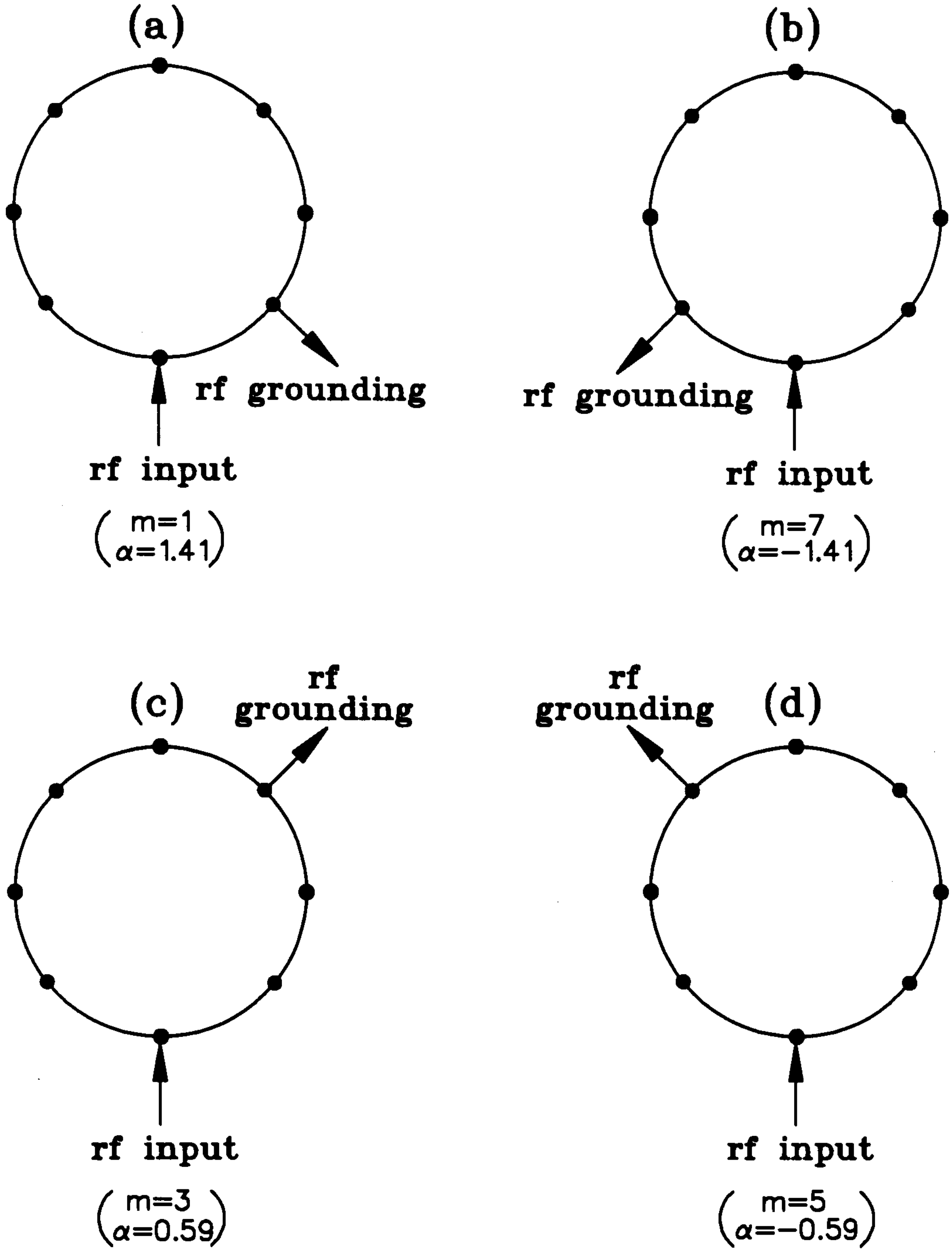

Figure 3.13: Four rf input-grounding configurations.

For the same reason as for $n' \geq 2$ mentioned before, it is sufficient to consider only $n'' = 1$. With the expression for l (equation 3.74) and the fundamental mode ($k = \pi/4$), equation 3.85 gives the constraint on the locations of rf input-grounding,

$$n + (n + m) = 7 \tag{3.86}$$

The above constraint, which the rf input-grounding must satisfy in order to yield a solution to equation 3.80, gives only four input-grounding possibilities. These are exactly the four cases which were excluded previously. Therefore when the rf input-grounding is connected in the manner of any of the four configurations shown in figure 3.13, the expression for A and B (equation 3.81) is given by

$$B = A + \frac{V_o}{\alpha Z_r} \tag{3.87}$$

From the discussion of the last subsection, this is the case where the wave $\vec{B}_1$ is elliptically polarized. Furthermore, if a cavity is made such that

$$\omega^2 C L_s \longrightarrow 1 \tag{3.88}$$

then

$$Z_r \longrightarrow 0 \tag{3.89}$$

In this case the wave $\vec{B}_1$ is right circularly polarized when α is positive, as shown in figure 3.13 (a) and (c), and left circularly polarized when α is negative, as shown in figure 3.13 (b) and (d). The values of m and α are given under each configuration in figure 3.13.

Note that for a realistic nonzero Z_r, configurations (c) and (d) (*i.e.*, smaller α) are better choices over (a) and (b) (*i.e.*, larger α) in order to achieve a nearly circularly polarized rf field $\vec{B}_1$. Indeed, in our experiments, the optimal circularly polarized rf fields were found when the rf input-grounding were connected in configurations (c) and (d) of figure 3.13, while elliptically polarized rf fields were found when the rf input-grounding were connected in configurations (a) and (b) of figure 3.13. Most of the data in this thesis were taken with the optimal circularly polarized rf fields.

3.2.4 Technical details and performance data

The resonance frequency of the cavity is determined by the capacitors chosen during construction. For example, eight 20 pF capacitors yield a resonance frequency (fundamental mode) of about 160 MHz, while 15 pF yield about 185 MHz. The relationship between the resonance frequency and capacity follows equation 3.29 and, for a fundamental mode of a cavity is given by

$$\omega \propto \frac{1}{\sqrt{C_s}} \tag{3.90}$$

One of the advantages of the birdcage cavity is that one has the freedom to choose the resonance frequency. This becomes important when the resonance frequency is close to the zero crossing of ω_{12}, as will be discussed in chapter 4.

The birdcage rf cavity used in this thesis is made of copper coated with gold to avoid corrosion, and therefore arcing. Eight high voltage ($\sim$ 10 kV) capacitors were used. The end rings of the cavity, as shown in figure 3.3, are made of square hollow copper tubing with a width of about 0.5 cm and the straight segments of the cavity are made of flat copper strip with a width of about 0.5 cm. Three sets of eight ceramic capacitors were mainly used in this thesis. All of the capacitors are cylindrical in shape. The diameters of the three sets of capacitors with capacities 12 pF, 15 pF, and 20 pF, are 1.1 cm, 1.3 cm, 1.4 cm, respectively, and the lengths are 0.42 cm, 0.47 cm, and 0.44 cm, respectively. In order to reach the desired resonance, one can alternate between two different types of capacitors, using 4 of one type, and 4 of another type. The body of the cavity itself, shown in figure 3.3, is also cylindrical in shape, where the diameter $2a = 8.1$ cm and height $l = 9.3$ cm.

Operation of high power rf cavities at 50% duty cycles requires careful design to avoid problems related to thermal stress. Apart from the overall need to remove the heat generated by the rf resistance of the conductors, the presence of capacitors in the resonator requires special attention to reduce the effects of flash rf heating on their surfaces. Furthermore, because the muon hfcc is a function of temperature, it is important to not only cool the sample but to keep this temperature as stable as possible. The cavity is cooled both by water running through the two end rings of the cavity, and blowing air from the back of the cavity. The rf is shielded by enclosing the cavity in a hollow aluminum cylinder with end-caps. The front end-cap has a hole ~ 4 cm in diameter to allow the muon beam to enter the sample, and the rear end-cap has a rectangular slit in the middle to allow access for the rf power leads, water cooling tubing, air cooling duct, etc. An over-temperature cut-off switch is mounted on the front end-cap for safety reasons.

As was mentioned in the last two chapters and shown in figure 1.5, the exact rf perturbation field (B_1) is measured by an rf-LFμSR experiment. During bench tests before the run, the B_1 field strength is measured through a wire loop of fixed size known as the standard probe. The standard probe is placed perpendicular to the magnetic flux of the cavity, to give an induced EMF. This standard probe is then calibrated with the B_1 field measured from an rf-LFμSR experiment. A typical B_1 field used in these rf experiments is $\sim$ 5 G for the birdcage cavity.

Using the standard probe, the homogeneity of the cavity was measured and is shown in figure 3.14. It can be seen from figure 3.14 that the rf B_1 field is very uniform at the center of the cavity for the length of about 3.4 cm, and decreases to zero at both ends. Because the length of the sample volume is about 2 cm, the field region seen by the sample is quite homogeneous.

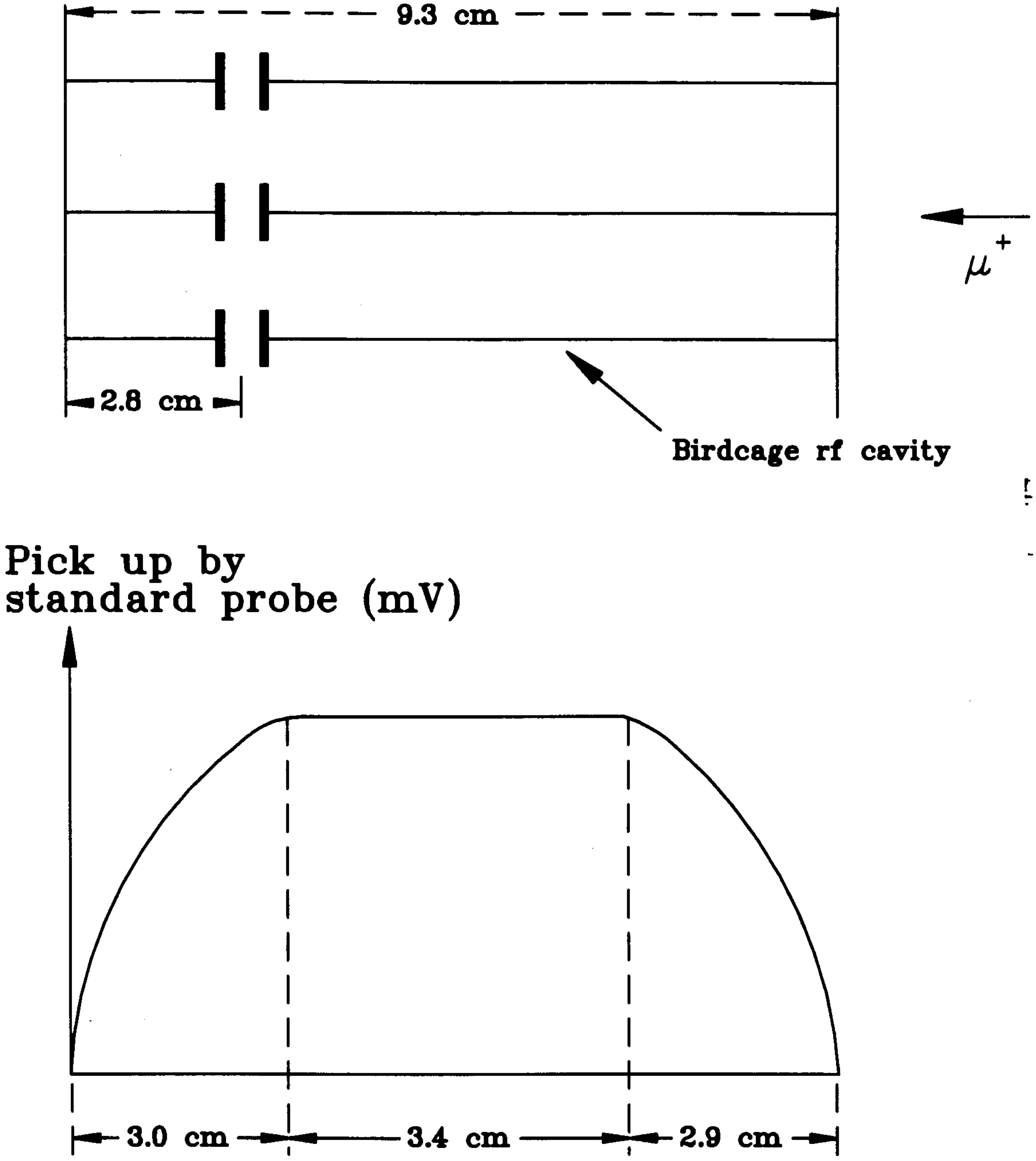

Figure 3.14: Sketch showing B_1 field homogeneity of the birdcage cavity.

Chapter 4

Radio Frequency Spectroscopy

4.1 Introduction

This chapter reviews the basic formulas of longitudinal muon polarization for both diamagnetic and radical systems under rf irradiation. At the end of the chapter it will be shown that the rf frequency should be chosen such that the rf resonance magnetic fields are far away from zero-crossing, far away from all LCR resonance fields, and as low as possible.

In the classical problem of a spin 1/2 particle (with angular momentum $\vec{J}$ and magnetic moment $\vec{\mu}$) in a static external field $\vec{B}_o = B_o\,\hat{\mathbf{z}}$, the spin will precess around the field direction according to $d\vec{J}\,/\,\mathrm{dt} = \vec{\mu} \times \vec{B}_o$. The spin vector will trace out a conical figure of revolution while maintaining a constant angle (and therefore constant energy) with respect to $\vec{B}_o$. The frequency of precession, the Larmor frequency, is given by $\omega_o = -\gamma B_o$, where γ is the gyromagnetic ratio of the particle defined by $\vec{\mu} = \gamma \vec{J}$. This is the case for traditional TF-μSR.

The use of rf methods in μSR follows closely its counterpart in conventional magnetic resonance [39, 40, 41, 42]. In both experimental arrangements a strong static (B_o, longitudinal) and a small rf field ($2B_1 \cos\omega$t,

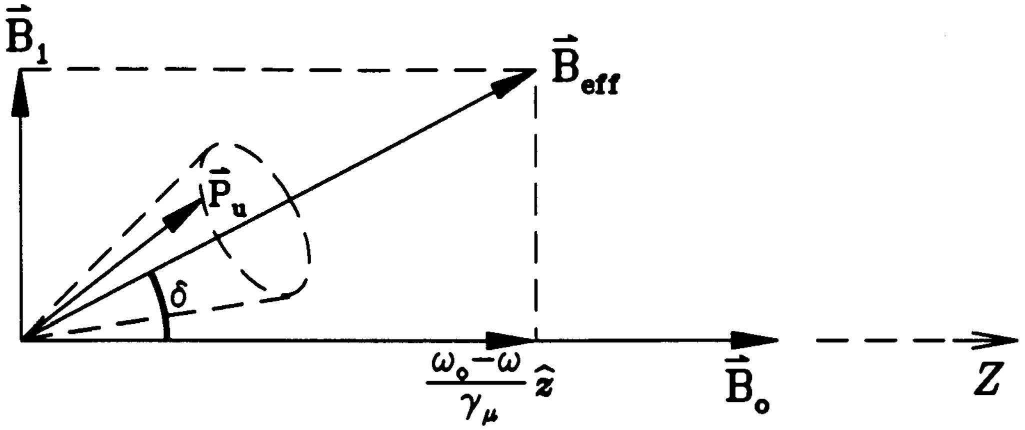

Figure 4.1: Precession of the muon spin within the rotating reference frame around the effective field $\vec{B}_{eff}$ [42].

transverse) are applied to the sample. Introducing an rf field changes the response of the spin system by allowing it to absorb energy. As in NMR, one can describe the motion of the muon polarization within the rotating reference frame (RRF), a frame rotating with the rf angular velocity $-\omega$ about the zbf Z axis. Then, in the RRF, the muon polarization precesses around the effective field $\vec{B}_{eff}$ [42] as shown in figure 4.1:

$$\vec{B}_{eff} = \vec{B}_1 + \frac{\omega_o - \omega}{\gamma_\mu}\hat{\mathbf{z}} \tag{4.1}$$

where $\omega_o = \gamma_\mu B_o$ and γ_μ is the gyromagnetic ratio of the muon.

The time-dependent longitudinal muon polarization will be calculated below for (i) a diamagnetic system and (ii) a radical system.

4.2 Longitudinal Muon Polarization for a Diamagnetic System

A small oscillating magnetic rf field, $2B_1 \cos\omega t\ \hat{\mathbf{x}}$, can be resolved into two vector components which have the same amplitude, B_1, but which

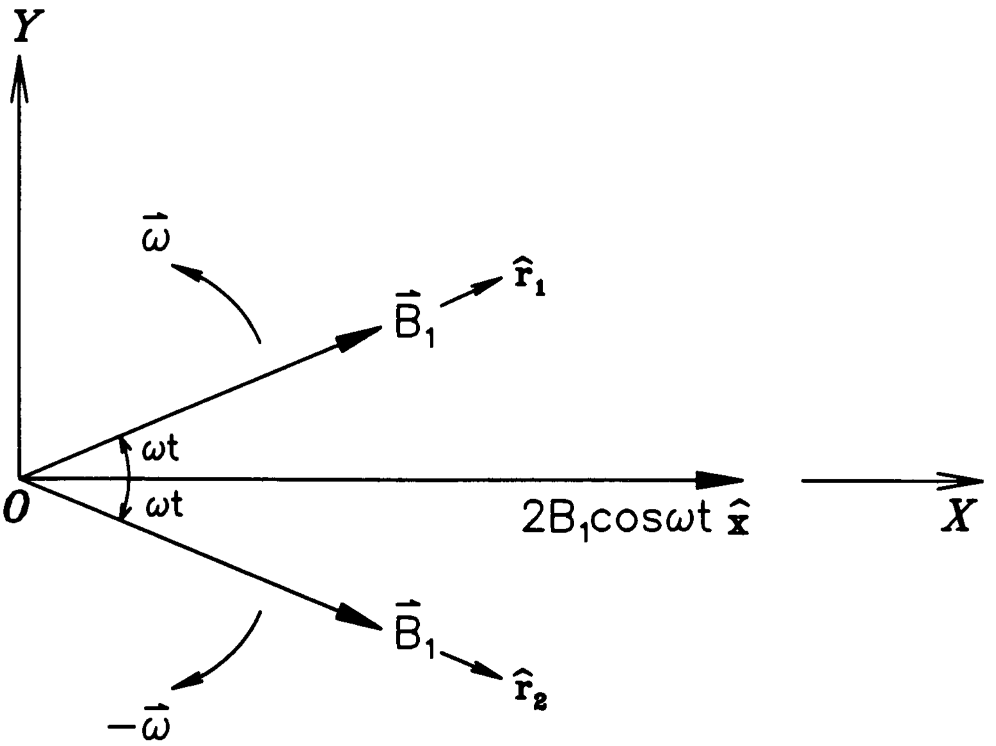

Figure 4.2: $2B_1 \cos\omega t \hat{\mathbf{x}}$ can be resolved into two vectors with the same amplitude (B_1), but which rotate in opposite directions with angular velocities $\pm\omega$.

rotate in opposite directions with angular velocities $\pm\omega$ (see figure 4.2). Mathematically, this can be expressed as

$$2B_1 \cos\omega t\ \hat{\mathbf{x}} = B_1 e^{i\omega t} \hat{\mathbf{r}}_1 + B_1 e^{-i\omega t} \hat{\mathbf{r}}_2 \tag{4.2}$$

From quantum mechanical time-dependent perturbation theory [43] the transition probability from an initial state $\mid i >$ to a final state $\mid f >$ (with $\omega_j = \mathrm{E}_j/\hbar$, where $j = i,\ f$) is

$$Prob_{(i \rightarrow f)} \propto \delta(\omega_f - \omega_i + \omega) + \delta(\omega_f - \omega_i - \omega) \tag{4.3}$$

The above equation expresses the involvement of two processes which influence the transition rate, stimulated emission ($\omega = \omega_i - \omega_f$) and resonant absorption ($\omega = \omega_f - \omega_i$). For the longitudinal case, the μ^+ are initially assumed to be spin polarized along the positive $\hat{\mathbf{z}}$ direction. The spin state of the μ^+ is represented by the function $|\, i > = |\, + >$, where $|\, + >$ is the ground state of $\mathbf{H}_o = -\gamma_\mu \vec{B}_o \cdot \vec{\mathbf{S}}^\mu$. Then only the absorption (second term of equation 4.3), or the component with $-\omega$ in figure 4.2, is significant. Therefore the effective rf perturbation is $B_1 e^{-i\omega t}\hat{\mathbf{r}}_1$, which is the circularly polarized field with angular velocity $-\omega$ shown in figure 4.2.

In the RRF, the motion of polarization is described by a precession around the effective field $\vec{B}_{eff}$. Therefore the spin Hamiltonian in angular frequency units in the rotating reference frame will be:

$$\begin{aligned}
\mathbf{H} &= -\gamma_\mu \vec{B}_{eff} \cdot \vec{\mathbf{S}} \\
&= -\frac{1}{2}\gamma_\mu \vec{B}_{eff} \cdot \vec{\boldsymbol{\sigma}} \\
&= -\frac{1}{2}\gamma_\mu (\boldsymbol{\sigma}_{x'}\, B_1 + \boldsymbol{\sigma}_{z'}\, B') \\
&= -\frac{1}{2}\gamma_\mu \begin{pmatrix} B' & B_1 \\ B_1 & -B' \end{pmatrix} \\
&= -\frac{1}{2}\omega_{eff} \begin{pmatrix} \cos\delta & \sin\delta \\ \sin\delta & -\cos\delta \end{pmatrix} \qquad (4.4)
\end{aligned}$$

where $B' = B_{eff}\cos\delta$, $B_1 = B_{eff}\sin\delta$, δ is the angle between the longitudinal direction $\hat{\mathbf{z}}$ and effective rf field, $\vec{B}_{eff}$ is defined in figure 4.1, γ_μ is the gyromagnetic ratio of the muon, $\omega_{eff} = \gamma_\mu B_{eff}$, and $\boldsymbol{\sigma}$ is the Pauli matrix.

By using the Jacobian rotation matrix,

$$\mathbf{R} = \begin{pmatrix} \cos\theta & \sin\theta \\ -\sin\theta & \cos\theta \end{pmatrix} \qquad (4.5)$$

with the rotation angle, θ, which satisfies

$$\tan 2\theta = -\tan\delta, \qquad (4.6)$$

Table 4.1: Energy eigenvalues and eigenstates for $\tan 2\theta = -\tan\delta$.

Energy	**State**
$\omega_1 = -\frac{1}{2}\omega_{eff}$	$\mid 1' >= \cos\theta \mid + > + \sin\theta \mid - >$
$\omega_2 = \frac{1}{2}\omega_{eff}$	$\mid 2' >= -\sin\theta \mid + > + \cos\theta \mid - >$

the transformed Hamiltonian, $\mathbf{H}'$, becomes:

$$\mathbf{H}' = \mathbf{R}^\tau \mathbf{H} \mathbf{R} = -\frac{1}{2}\omega_{eff}\begin{pmatrix} 1 & 0 \\ 0 & -1 \end{pmatrix} \tag{4.7}$$

where $\mathbf{R}^\tau$ is the transpose matrix of $\mathbf{R}$. Energy eigenvalues and eigenstates of $\mathbf{H}'$ can then be readily calculated and are given in table 4.1.

If a muon is initially in an eigenstate Ψ(t=0)= $\mid + >$, which can be written as

$$\Psi(t=0) = \cos\theta \mid 1' > - \sin\theta \mid 2' >, \tag{4.8}$$

at any later time t, Ψ(t) is therefore given by

$$\begin{aligned} \Psi(t) &= \cos\theta e^{-i\omega_1 t} \mid 1' > - \sin\theta e^{-i\omega_2 t} \mid 2' > \\ &= C_1(t) \mid + > + C_2(t) \mid - >, \end{aligned} \tag{4.9}$$

where

$$\begin{aligned} C_1(t) &= \cos^2\theta e^{-i\omega_1 t} + \sin^2\theta e^{-i\omega_2 t} \\ C_2(t) &= \cos\theta\sin\theta e^{-i\omega_1 t} - \cos\theta\sin\theta e^{-i\omega_2 t}. \end{aligned} \tag{4.10}$$

The longitudinal muon polarization in the rotating reference frame (*i.e.*, the expectation value of $\boldsymbol{\sigma}_{z'}$) can then be derived from the above two equations and equation 4.6, and is given by

$$\begin{aligned} P_{z'}(t) &= < \Psi(t) \mid \boldsymbol{\sigma}_{z'} \mid \Psi(t) > \\ &= \cos^2\delta + \sin^2\delta \cos(\omega_2 - \omega_1)t \\ &= \cos^2\delta + \sin^2\delta \cos\omega_{eff} t \end{aligned} \tag{4.11}$$

Notice that the longitudinal polarization does not change when being transformed from the rotating reference frame to the lab frame, *i.e.*

$$P_z(t) = \cos^2\delta + \sin^2\delta \cos\omega_{eff} t \tag{4.12}$$

It can be seen that the muon polarization precesses around the effective field, $\vec{B}_{eff}$, with an angular frequency $\omega_{eff} = \gamma_\mu B_{eff}$. At the resonance, namely $\omega = \omega_o$, then $\delta = \pi/2$ and $\omega_{eff} = \gamma_\mu B_1$. The longitudinal muon polarization is given by the well known formula

$$P_z(t) \mid_{\omega=\omega_o} = \cos\gamma_\mu B_1 t \tag{4.13}$$

and precesses around the rf field B_1 with angular frequency ω_{eff}=$\gamma_\mu B_1$.

4.3 Longitudinal Muon Polarization for a Mu-Substituted Radical System

A simple muon-electron two-spin-1/2 system with an isotropic hyperfine constant (A_μ) is considered here. This can apply to any species containing a muon and an unpaired electron with an isotropic hyperfine interaction between them, a muonium-substituted free radical, as well as atomic muonium. The time-dependent total spin Hamiltonian, $\mathbf{H_T}(t)$, contains two terms. The first term $\mathbf{H_o}$ is stationary and consists of the Zeeman interaction between the applied field ($\vec{B}_o = B_o\hat{\mathbf{z}}$) and each spin, as well as the hyperfine interaction ($A_\mu \vec{\mathbf{S}}^\mu \cdot \vec{\mathbf{S}}^e$) between the unpaired electron and the muon. The second term, $\mathbf{H}'(t)$, is a time-dependent perturbation, consisting of the interaction between the time-dependent rf field ($\vec{B}_{rf} = B_1 \cos\omega\mathrm{t}\ \hat{\mathbf{x}}$) and each spin. Mathematically this is

$$\mathbf{H_T}(t) = \mathbf{H_o} + \mathbf{H}'(t), \tag{4.14}$$

where both $\mathbf{H}_o$ and $\mathbf{H}'(t)$ are given in angular frequency units by

$$\begin{aligned}
\mathbf{H}_o &= \gamma_e \vec{\mathbf{S}}^e \cdot \vec{B}_o - \gamma_\mu \vec{\mathbf{S}}^\mu \cdot \vec{B}_o + A_\mu \vec{\mathbf{S}}^\mu \cdot \vec{\mathbf{S}}^e \\
&= \omega_e \mathbf{S}^e_z - \omega_\mu \mathbf{S}^\mu_z + A_\mu \vec{\mathbf{S}}^\mu \cdot \vec{\mathbf{S}}^e \qquad (4.15) \\
\mathbf{H}'(t) &= \gamma_e \vec{\mathbf{S}}^e \cdot \vec{B}_{rf} - \gamma_\mu \vec{\mathbf{S}}^\mu \cdot \vec{B}_{rf} \\
&= \frac{1}{4}\left[\omega^e_1(\mathbf{S}^e_+ + \mathbf{S}^e_-) - \omega^\mu_1(\mathbf{S}^\mu_+ + \mathbf{S}^\mu_-)\right](e^{i\omega t} + e^{-i\omega t}) \qquad (4.16)
\end{aligned}$$

where γ_i is the gyromagnetic ratio of the particle i (i = e, μ), ω_i are Zeeman angular frequencies ($\omega_i = \gamma_i B_o$, and i = e, μ), and $\omega^i_1 = \gamma_i B_1$ (i= e, μ).

The eigenvalues (ω_n, where n = 1, 2, 3, 4) and eigenstates ($| n >$, where n = 1, 2, 3, 4) of the Zeeman interaction Hamiltonian ($\mathbf{H}_o$) can be calculated [7] and are given in table 1.3 of chapter one.

From time-dependent perturbation theory [43], the time-dependent eigenfunction, Ψ(t), of the total Hamiltonian, $\mathbf{H_T}$(t), can be constructed from a linear combination of eigenstates $| n >$ at any instant:

$$\Psi(t) = \sum_n C_n(t) e^{-i\omega_n t} \mid n >, \qquad (4.17)$$

Differentiating equation 4.17 and then substituting the result into the Schrödinger equation

$$i\frac{\partial \Psi(t)}{\partial t} = (\mathbf{H}_o + \mathbf{H}'(t))\Psi(t) \qquad (4.18)$$

we have

$$i\sum_k \dot{C}_k(t) e^{-i\omega_k t} \mid k >= \mathbf{H}'(t) \sum_n C_n(t) e^{-i\omega_n t} \mid n > \qquad (4.19)$$

Projecting equation 4.19 onto the ket vector $< m |$, one obtains,

$$i\dot{C}_m(t) = \sum_n < m \mid \mathbf{H}'(t) \mid n > C_n(t) e^{i(\omega_m - \omega_n)t} \qquad (4.20)$$

In matrix notation, with the assumption that the rf field induces transitions between states $| 1 >$ and $| 2 >$, equation 4.20 can be written as

$$i \begin{pmatrix} \dot{C}_1(t) \\ \dot{C}_2(t) \end{pmatrix} = \begin{pmatrix} 0 & H'_{12} e^{i\omega_{12} t} \\ H'_{21} e^{i\omega_{21} t} & 0 \end{pmatrix} \begin{pmatrix} C_1(t) \\ C_2(t) \end{pmatrix} \tag{4.21}$$

where

$$H'_{mn} =< m \mid \mathbf{H}'(t) \mid n > \tag{4.22}$$

and

$$\omega_{mn} = \omega_m - \omega_n \tag{4.23}$$

Substituting equation 4.16 into 4.22, and applying the constraint of stimulated emission, the above matrix becomes

$$i \begin{pmatrix} \dot{C}_1(t) \\ \dot{C}_2(t) \end{pmatrix} = \begin{pmatrix} 0 & \rho_{12} e^{i\Omega_{12} t} \\ \rho_{12} e^{-i\Omega_{12} t} & 0 \end{pmatrix} \begin{pmatrix} C_1(t) \\ C_2(t) \end{pmatrix} \tag{4.24}$$

where

$$\begin{aligned} \rho_{12} &= \frac{1}{4} < 1 \mid [\omega_1^e(\mathbf{S}_+^e + \mathbf{S}_-^e) - \omega_1^\mu(\mathbf{S}_+^\mu + \mathbf{S}_-^\mu)] \mid 2 > \\ &= \frac{1}{4} B_1 (s\gamma_e - c\gamma_\mu) \end{aligned} \tag{4.25}$$

and

$$\Omega_{12} = \omega_{12} - \omega \tag{4.26}$$

The above matrix (equation 4.24) is equivalent to the following differential equations:

$$i\dot{C}_1(t) = \rho_{12} e^{i\Omega_{12} t} C_2(t) \tag{4.27}$$

$$i\dot{C}_2(t) = \rho_{12} e^{-i\Omega_{12} t} C_1(t) \tag{4.28}$$

Differentiating equation 4.27 and substituting equation 4.28 into the result, we arrive at the second order differential equation for C_1(t):

$$\ddot{C}_1 - i\Omega_{12}\dot{C}_1 + \rho_{12}^2 C_1 = 0 \tag{4.29}$$

Assuming the general solution of the differential equation 4.29 has the form of

$$C_1(t) = Ae^{i\alpha t} + Be^{-i\beta t} \tag{4.30}$$

then α, β, A and B are in general complex constants, where α and β are determined from the differential equations 4.27–4.28, and A and B from the initial conditions discussed below.

Equations for α and β can be obtained by differentiating equation 4.30 and substituting both $\ddot{C}_1$ and $\dot{C}_1$ into the equation 4.29:

$$(\alpha^2 - \Omega_{12}\alpha - \rho_{12}^2)Ae^{i\alpha t} + (\beta^2 + \Omega_{12}\beta - \rho_{12}^2)Be^{-i\beta t} = 0 \tag{4.31}$$

In order for the above equation to be true at any time t, the following equations have to be satisfied:

$$\alpha^2 - \Omega_{12}\alpha - \rho_{12}^2 = 0 \tag{4.32}$$

$$\beta^2 + \Omega_{12}\beta - \rho_{12}^2 = 0 \tag{4.33}$$

Therefore both α and β can be easily calculated and are given by

$$\alpha = \frac{1}{2}(\Omega_{12} \pm \sqrt{\Omega_{12}^2 + 4\rho_{12}^2}) \tag{4.34}$$

$$\beta = \frac{1}{2}(-\Omega_{12} \pm \sqrt{\Omega_{12}^2 + 4\rho_{12}^2}) \tag{4.35}$$

The initial conditions determine the values of A and B. The muon is assumed to be initially 100% polarized for both rf-IμSR and rf-LFμSR experiments (say, along the positive $\hat{\mathbf{z}}$ direction), while the unpaired electron is generally unpolarized, namely,

$$\begin{aligned}\Psi(t=0) &= \frac{1}{\sqrt{2}} \mid \alpha^e\alpha^\mu > + \frac{1}{\sqrt{2}} \mid \beta^e\alpha^\mu > \\ &= \frac{1}{\sqrt{2}} \mid 1 > + \frac{s}{\sqrt{2}} \mid 2 > + \frac{c}{\sqrt{2}} \mid 4 >\end{aligned} \tag{4.36}$$

which means

$$\begin{pmatrix} C_1(t=0) \\ C_2(t=0) \end{pmatrix} = \begin{pmatrix} 1/\sqrt{2} \\ s/\sqrt{2} \end{pmatrix} \tag{4.37}$$

Again, from the expressions for C_1(t) and C_2(t) (equations 4.30 and 4.27), both A and B can be readily calculated and are given by

$$A = \frac{1}{\sqrt{2}}\frac{\alpha}{\alpha+\beta} \tag{4.38}$$

$$B = \frac{1}{\sqrt{2}}\frac{\beta}{\alpha+\beta} \tag{4.39}$$

With the given α, β, A and B (equations 4.34, 4.35, 4.38, and 4.39), C_1(t), and therefore C_2(t), are completely known. Then the time-dependent eigenfunction (Ψ(t)) is

$$\begin{aligned} \Psi(t) &= C_1(t)e^{-i\omega_1 t} \mid 1 > + C_2(t)e^{-i\omega_2 t} \mid 2 > \\ &= C_1(t)e^{-i\omega_1 t} \mid \alpha^e\alpha^\mu > \\ &\quad + C_2(t)e^{-i\omega_2 t}(s \mid \beta^e\alpha^\mu > + c \mid \alpha^e\beta^\mu >) \end{aligned} \tag{4.40}$$

The longitudinal time-dependent muon polarization can be derived from the the above equation and is given by

$$\begin{aligned} P_z(t) &= < \Psi(t) \mid \sigma_z^\mu \mid \Psi(t) > \\ &= C_1^2(t) - (c^2 - s^2)C_2^2(t) \\ &= R - Q(1 - \cos\sqrt{\Omega_{12}^2 + 4\rho_{12}^2}\, t) \end{aligned} \tag{4.41}$$

where

$$R = \frac{1}{2}[1 - s^2(c^2 - s^2)] \tag{4.42}$$

$$Q = (1 + c^2 - s^2)(\frac{\rho_{12}^2}{\Omega_{12}^2 + 4\rho_{12}^2}) \tag{4.43}$$

If it is assumed that the only source of relaxation is radioactive muon decay, the time integral muon polarization is given by

$$\begin{aligned} P_z^{|1>\rightarrow|2>}(B_o) &= \int_0^\infty \lambda_o P_z(t) e^{-\lambda_o t} dt \\ &= \frac{1}{2}[1 - s^2(c^2 - s^2)] - P_{rf}^{|1>\rightarrow|2>}(B_o) \qquad (4.44) \end{aligned}$$

where

$$P_{rf}^{|1>\rightarrow|2>}(B_o) = (1 + c^2 - s^2)\left(\frac{\rho_{12}^2}{(\omega_{12} - \omega)^2 + 4\rho_{12}^2 + \lambda_o^2}\right) \qquad (4.45)$$

and λ_o is the muon decay rate (4.5×10^5 s^{-1}).

Equation 4.45 represents the longitudinal time integral muon polarization for the stimulated emission from the state $| 1 >$ to $| 2 >$. For resonance absorption from the state $| 4 >$ to $| 3 >$, $P_z(B_o)$ can be derived in the similar way and is given by

$$P_z^{|4>\rightarrow|3>}(B_o) = \frac{c^2(c^2 - s^2)}{2} - P_{rf}^{|4>\rightarrow|3>}(B_o) \qquad (4.46)$$

where

$$\begin{aligned} P_{rf}^{|4>\rightarrow|3>}(B_o) &= c^2(1 + c^2 - s^2)\frac{\rho_{43}^2}{(\omega_{43} + \omega)^2 + 4\rho_{43}^2 + \lambda_o^2} \qquad (4.47) \\ \rho_{43} &= < 4 \mid \frac{1}{4}[\omega_1^e(\mathbf{S}_+^e + \mathbf{S}_-^e) - \omega_1^\mu(\mathbf{S}_+^\mu + \mathbf{S}_-^\mu)] \mid 3 > \\ &= -\frac{1}{4}B_1(s\gamma_e + c\gamma_\mu) \qquad (4.48) \end{aligned}$$

$P_{rf}^{|1>\rightarrow|2>}$ in equation 4.45 (or $P_{rf}^{|4>\rightarrow|3>}$ in equation 4.47) looks similar to the Lorentzian line shape when the magnetic field is swept around the resonance $\omega_{12} = \omega$ (or $\omega_{43} = -\omega$). However, c and s, and therefore ρ_{12} and ρ_{43}, are functions of B_o. So, strictly speaking, neither $P_{rf}^{|1>\rightarrow|2>}$ nor $P_{rf}^{|4>\rightarrow|3>}$ describes a Lorentzian distribution when the magnetic field is swept. Nevertheless, if we assume c, s, ρ_{12}, and ρ_{43} do not vary over the range of the field sweep around the resonance, then $P_{rf}^{|1>\rightarrow|2>}$ (or $P_{rf}^{|4>\rightarrow|3>}$) has approximately a Lorentzian distribution with a HWHM (half width of half magnitude) = $\sqrt{4\rho_{12}^2 + \lambda_o^2}$ (or $\sqrt{4\rho_{43}^2 + \lambda_o^2}$) and an amplitude $(1 + c^2 - s^2)\rho_{12}^2/\mathrm{HWHM}^2$ (or $c^2(1 + c^2 - s^2)\rho_{43}^2/\mathrm{HWHM}^2$).

Figure 4.3 shows the field (B_o) dependence of the time-integrated longitudinal muon polarization, $P_{rf}(B_o)$ at the resonances for $\mathrm{MuC_6H_6}$. For this radical, the muon hfcc is expected to be A_μ = 514.42 MHz at T=298.3 K [44], and for the figure B_1 was chosen to have a typical value of 5 Gauss. Note that there is a wide dip around B_o = 19 kG in $P_{rf}^{|1>\rightarrow|2>}(B_o)$. This is the zero-crossing of ω_{12}. It is obvious that choosing the sweep fields close to the zero-crossing would be a disastrous choice. One has the choice of sweeping fields smaller than the zero-crossing or higher. Figure 4.3 clearly shows that low fields have a higher signal.

So far we have only discussed a Mu-substituted radical as a two-spin-1/2 system. For the three-spin-1/2 system consisting of an unpaired electron (e^-), a muon (μ^+), and a nucleus (k), the longitudinal muon polarization can be obtained by the same approach as discussed above for the two-spin system and is given by

$$P_z(B_0) = \frac{1}{2} - P_{rf}(B_0) \tag{4.49}$$

where

$$\begin{aligned} P_{rf}(B_0) &= \frac{c_o^2[1-(s_o+s)^2]}{4}\frac{4\rho_1^2}{(\omega^- - \omega)^2 + 4\rho_1^2 + \lambda_o^2} \\ &+ \frac{c_o^2[(c_o+s)^2 - s^2]}{4}\frac{4\rho_2^2}{(\omega^- - \omega)^2 + 4\rho_2^2 + \lambda_o^2} \end{aligned} \tag{4.50}$$

where ω^- is given by equation 1.15 in chapter one and all other parameters in the above equation are given in table 4.2.

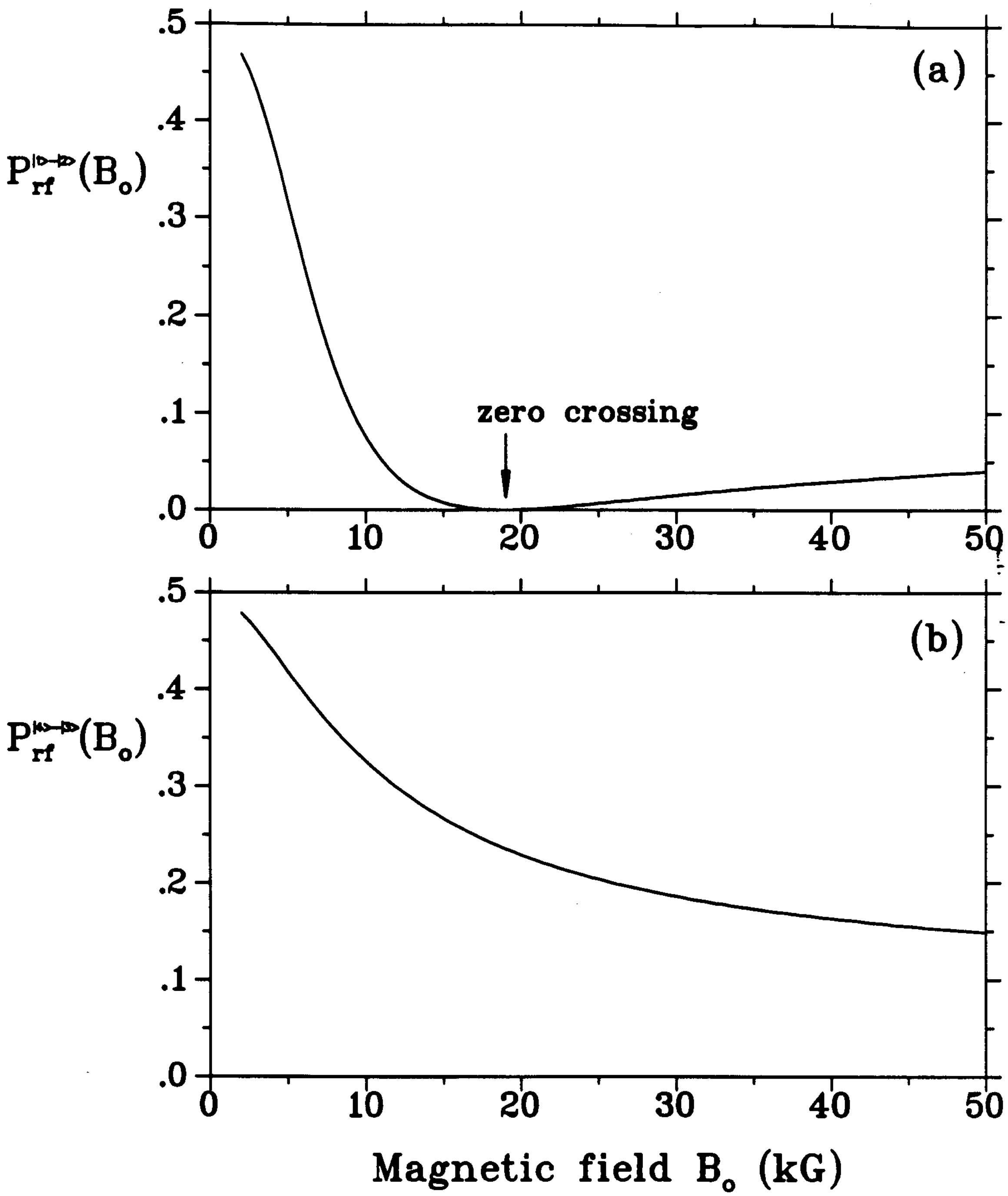

Figure 4.3: Magnetic field dependence of P_{rf} (B_o) based on the two-spin system calculation for radical MuC$_6$H$_6$, where (a) represents the transition $\mid 1 > \rightarrow \mid 2 >$, and (b) $\mid 4 > \rightarrow \mid 3 >$. Parameters chosen are $B_1 = 5$ Gauss, and $A_\mu = 514.42$ MHz [44].

Table 4.2: Parameters for $P_z(B_o)$, the longitudinal muon polarization in a three-spin system.

$$\begin{aligned}
c_o &= cc_\theta \\
s_o &= cs_\theta \\
c_\theta &= \cos\theta \\
s_\theta &= \sin\theta \\
\tan 2\theta &= 2\varepsilon_{23}/(\varepsilon_{33}-\varepsilon_{22}) \\
\varepsilon_{23} &= A_\mu A_k/(4\gamma_e B_o) \\
\varepsilon_{22}-\varepsilon_{33} &= B_o(\gamma_e-\gamma_k) - 0.5(A_\mu - A_k) + (A_\mu^2 - A_k^2)/(4\gamma_e B_o) \\
\rho_1 &= 0.25B_1 \mid s\gamma_e - c_o\gamma_\mu - s_o\gamma_k \mid \\
\rho_2 &= 0.25B_1 \mid sc_o\gamma_e - cc_o\gamma_\mu - (s^2 - cs_o)\gamma_k \mid
\end{aligned}$$

The magnetic field (B_o) dependence of $P_{rf}(B_0)$ at the resonance ($\omega^- = \omega$) for MuC_6H_6 is plotted in figure 4.4, where the strength of the rf field B_1 is assumed to be 5 Gauss and, for demonstration purposes, H(3) (defined in figure 4.5) in MuC_6H_6 is the nucleus k in the calculation with $A_{H(3)}$ = - 36.08 MHz [44].

Note that the shape of the three-spin system is identical to that of the two-spin system apart from the sharp dip due to H(3) (see figure 4.3 and 4.4) . A magnified view of the dip is shown in figure 4.4(b). The figure clearly shows that the polarization has a sharp dip at a certain field. It can be calculated that this field is 29.6 kG, which is exactly the LCR resonance position H(3) in MuC_6H_6 [45]. The reason for this depolarization around the LCR resonance field is that the states of rf excitation are easily depopulated due to the mixing of levels which cross. This could cause the lifetime of the states of rf excitation to be too short to observe.

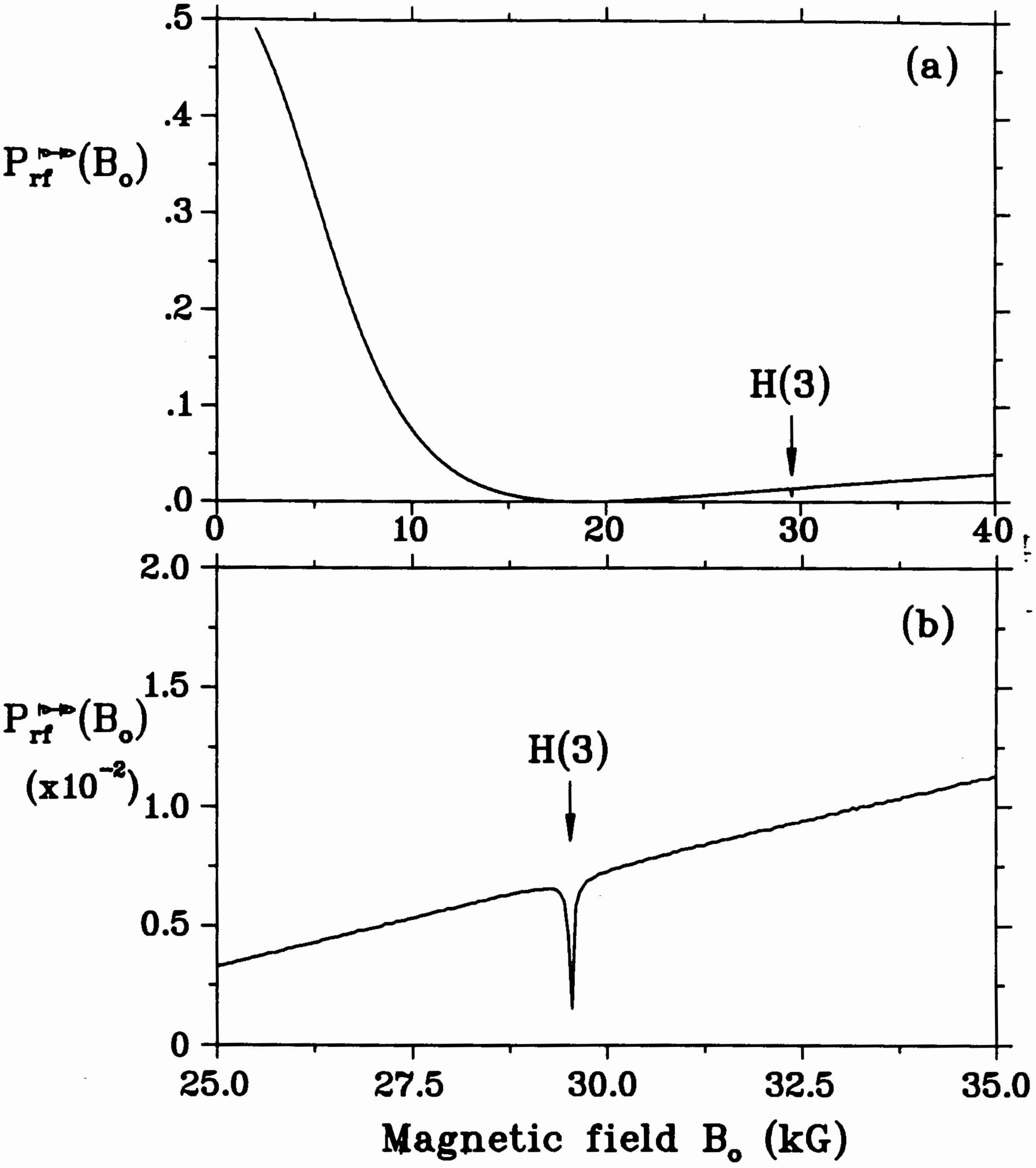

Figure 4.4: Magnetic field dependence of P_{rf} (B_o) based on the three-spin system calculation for radical MuC_6H_6. (b) is an expanded view of (a) near the level crossing. Parameters chosen are B_1 = 5 Gauss, A_μ = 514.42 MHz, and $A_{\mathrm{H(3)}}$ = -36.08 MHz [44].

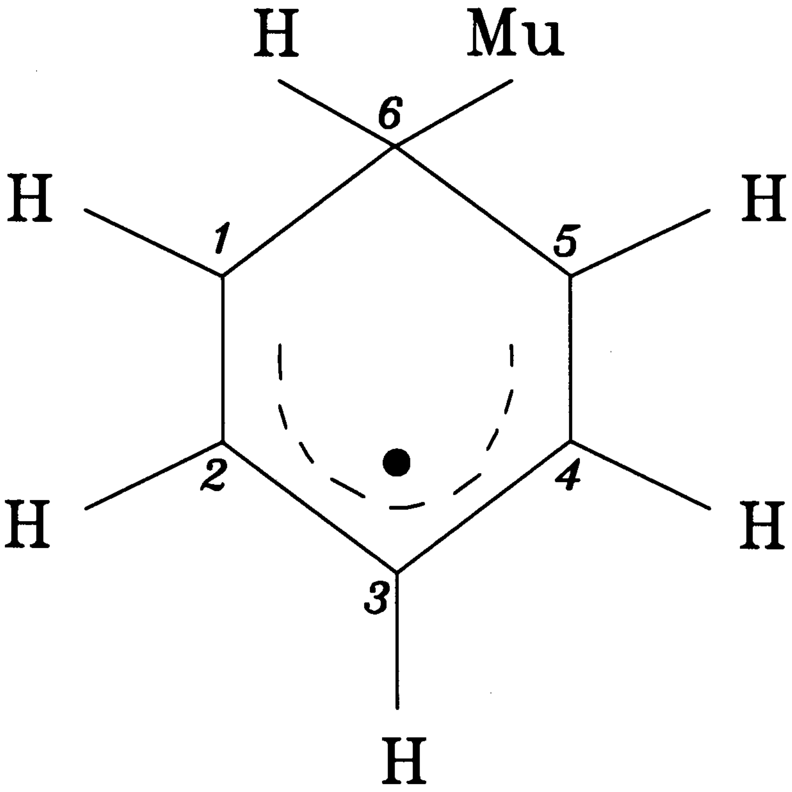

Figure 4.5: Numbering convention for radical MuC_6H_6.

For the radical MuC_6H_6, there are four different LCR resonance fields due to four different sets of nuclei: H(6), H(1,5), H(2,4), and H(3) [45] (see figure 4.5). The rf frequencies should be chosen such that the swept region is far away from all the LCR resonance fields (sharp dips), far away from zero-crossing (wide dips in figure 4.3 and 4.4(a)), and in the low field region (smaller than zero-crossing) to have the highest possible rf signal.

Chapter 5

Direct Observation of Delayed Mu-Radical Formation using RF Spectroscopy

5.1 Introduction

The first application of magnetic resonance to the measurement of the Zeeman splitting of the μ^+ was performed by Coffin *et al.* [46] in 1958, with the aim of determining the magnetic moment of the muon. More recently the μSR group at KEK (BOOM) has adapted the magnetic resonance technique as a routine method in μSR spectroscopy [39, 47, 48, 49, 50, 51, 52, 53, 54]. The early resonance experiments of the KEK group were done using a simple 40 MHz coil consisting of 37 μm diameter copper wire closely wound around the target. A high-power pulsed rf field was applied since the KEK muon beam is pulsed. A few years later a 500 MHz rf cavity, (made from copper and resonating in the TM 110 mode), was developed and has been used routinely in magnetic resonance experiments. The research areas studied by the KEK μSR group using the resonance method include the so-called 'missing fraction', reaction dynamics, and reaction rates of muon-containing species. Some specific examples of these research areas are **i)** the fraction of diamagnetic states under decoupling longitudinal field [48, 52, 53], **ii)** the Mu reaction into diamagnetic states in alkali halides [49, 51], and **iii)** and the reaction of Mu-cyclohexadienyl radical with benzoquinone solution [54].

At TRIUMF over the past few years we have developed rf capabilities suitable for use in a CW meson facility. Several spectroscopic applications utilizing time integral techniques have been tested and were successful for the first time in TRIUMF. These include the detection of final states in delayed Mu-substituted radical systems [55, 56] and semiconductors [56, 57], two photon absorption experiments [56], the use of low field swept frequency excitation to measure nuclear hyperfine parameters in Mu-like systems [56], and the application to spin dynamics via various spin echo techniques [56, 58]. This chapter will only focus on the delayed formation of Mu-substituted radicals.

It is well known that loss of phase coherence in conventional transverse-field muon spin rotation (TF-μSR) severely limits the study of the products of chemical reactions of muonium. As was described in chapter 1, in transverse magnetic fields muonated radicals can only be observed if the radical formation rate is large compared with the muon spin precession frequency difference between precursor and radical [7]. With muonium as a precursor, this imposes a low limit of about 10^9–10^{10} s^{-1} [7]. As a consequence, for samples to be successfully studied by TF-μSR, the radical formation rates or the concentrations must be large. Even for concentrations in the molar range the rate constant must be larger than 10^9 M^{-1} s^{-1}. In the case of fast reactions, the technique of TF-μSR provides a means to determine the muon hyperfine constant, as well as the rate and mechanism of radical formation [59]. But in the case of slow reactions, where the radical formation rate is smaller than 10^9 s^{-1}, the radical is formed too slowly to give a coherent TF-μSR signal. It has long been recognized [54] that RF resonant excitation, in a longitudinal field μSR experiment, has great promise in the study of slowly formed radicals.

This chapter demonstrates the feasibility of using rf techniques to directly detect the delayed formation of muonium substituted radicals, describes the method to measure the rate constants for slow reactions of organic radicals from an rf-IμSR experiment, and discusses the effect of Heisenberg spin exchange on the rf-IμSR spectra within the framework of a two-state jump model.

5.2 The Experiment

The compounds chosen here were water, ice, fuzed quartz (SiO_2), buckminsterfullerene powder (C_{60} containing about 10% C_{70}), neat liquid benzene (C_6H_6), neat liquid hexafluorobenzene (C_6F_6), a saturated solution of phenol (C_6H_5OH) in ethanol, and pyrogallol ($C_6H_3(OH)_3$) in aqueous solutions of concentrations of 5 M, 2 M, and 0.02 M. The muonium-substituted cyclohexadienyl (Mu-cyclohexadienyl, C_6H_6Mu) radical can be formed by the addition of muonium to benzene (figure 5.1(a)) while the muonium-substituted hexafluorocyclohexadienyl (Mu-hexafluorocyclohexadienyl, C_6F_6Mu) is formed by the addition of muonium to hexafluorobenzene (figure 5.1(b)). The ortho, meta, and para isomeric radicals are derived formally by Mu addition in the ortho, meta, and para positions, respectively, to the substituted carbon atom of

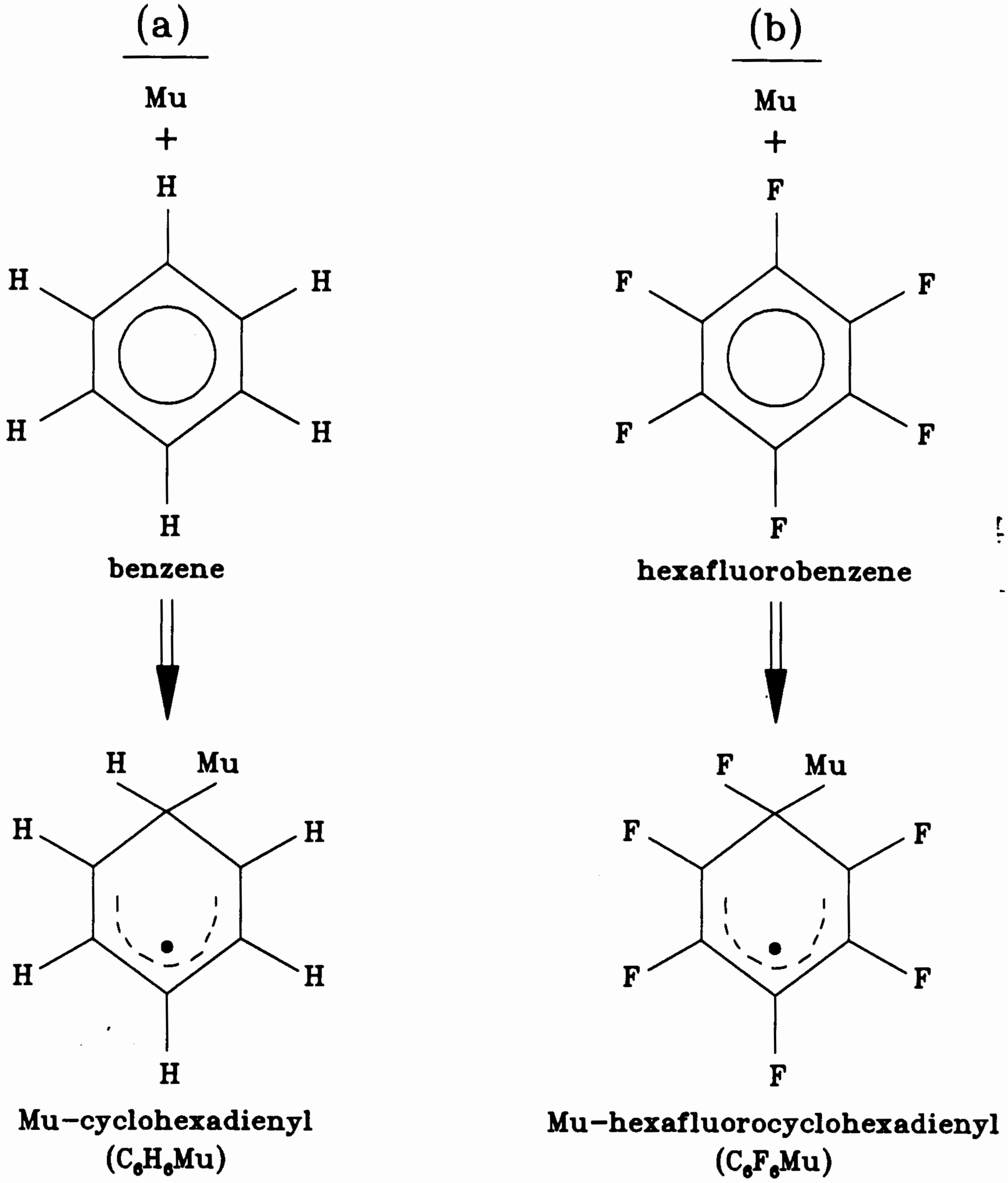

Figure 5.1: Radicals formed by addition of Mu to (a) benzene (C_6H_6) and (b) hexafluorobenzene (C_6F_6).

phenol (figure 5.2). The two radicals formed by the addition of muonium to one or other of the unsubstituted positions of the benzene ring of pyrogallol are shown in figure 5.3. The radicals formed in neat benzene, neat hexafluorobenzene, and saturated phenol solution were among the first radicals to be detected by TF-μSR [9, 24, 44, 45, 60, 61]. The radicals formed in pyrogallol in aqueous solution have only been observed in a very concentrated (3.4 M) sample by TF-μSR [62].

The sample cell is cylindrical in shape with a glass body (figure 5.4). There is a double window made of Mylar with the contained space acting as an insulating volume. Since muonium reacts very readily with O_2 ($k_M = 2.4 \times 10^{10}$ M^{-1} s^{-1} in water [63]), all media used for radical studies must have the oxygen concentration reduced from air-saturated levels (2.6×10^{-4} M) to less than 2×10^{-6} M. This was achieved by flowing nitrogen through the space between the two windows to remove O_2 that leaked through the exterior window. The sample cell has two compartments. The inner compartment is the sample volume, and the outer compartment is filled with circulating thermostating fluid during the experiments. The length of the cell, from the front window to the back of the outer compartment, is about 4.5 cm and the diameter is about 4 cm.

Diluted solutions of pyrogallol were made about 15 minutes prior to the actual experiment from an acidified (pH 3 using perchloric acid) stock solution. The solution was wrapped in aluminium foil since pyrogallol decomposes when exposed to light. Only distilled and deionized water was used. All the liquid samples used in this chapter were degassed by the freeze-pump-thaw method and sealed in standard spherical glass bulbs (sample containers) of 25 mm diameter. The sample in the sample

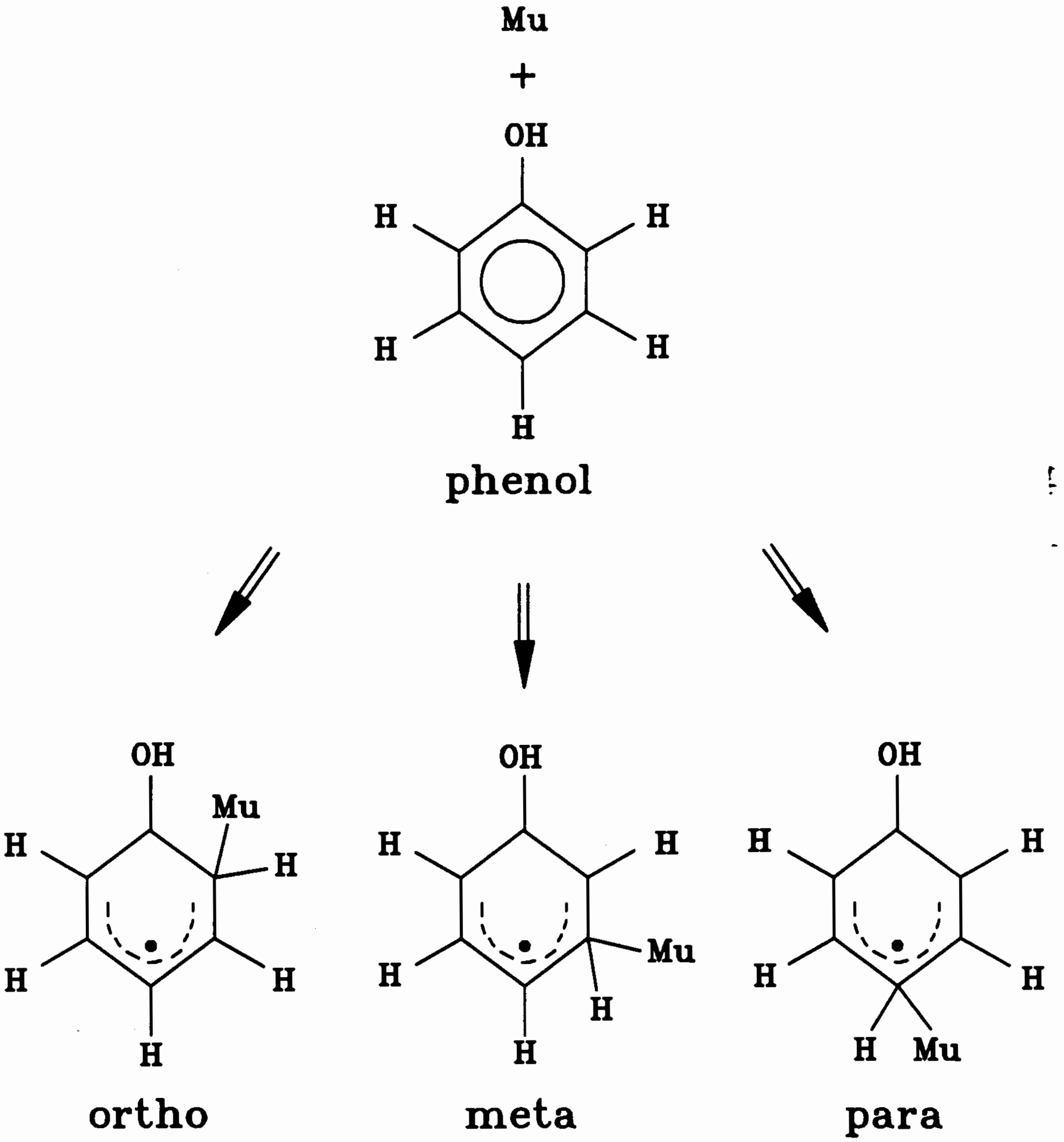

Figure 5.2: Radicals formed by addition of Mu to phenol (C_6H_5OH).

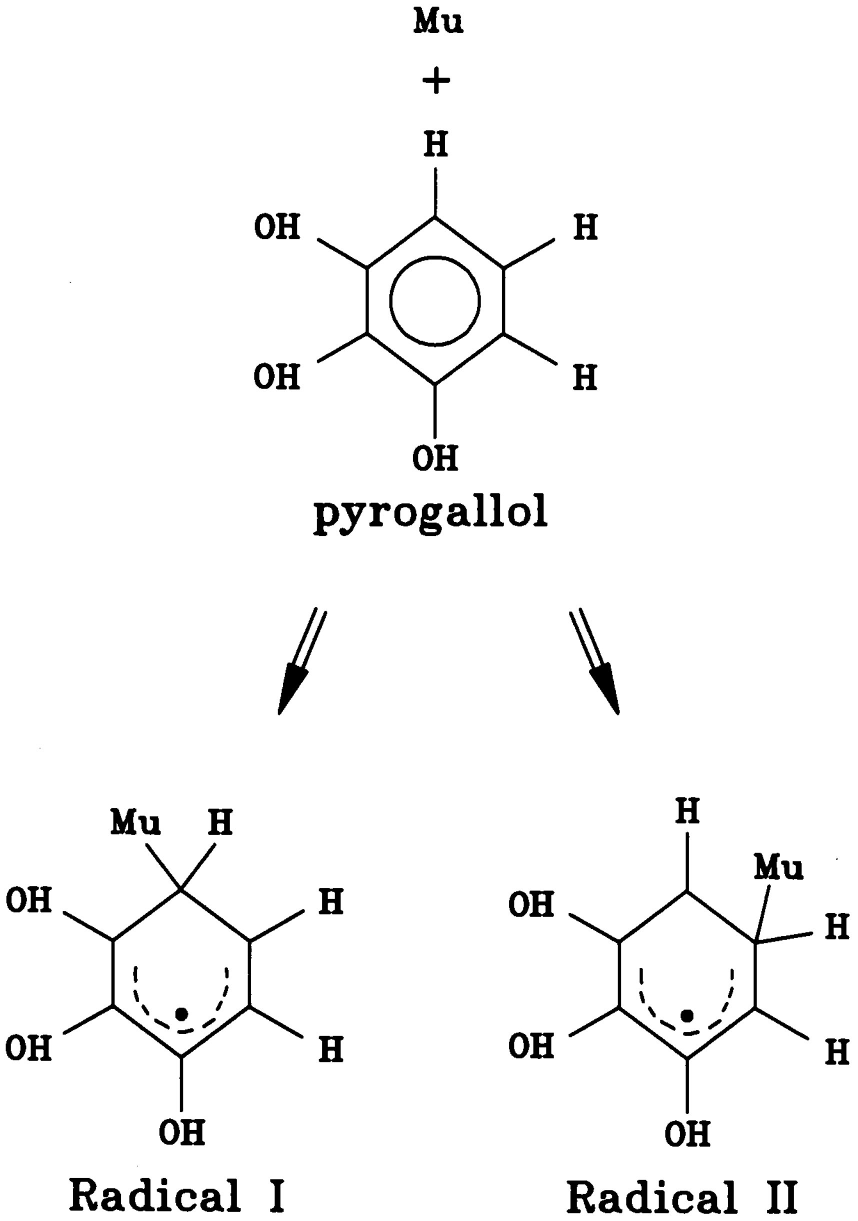

Figure 5.3: Radicals formed by addition of Mu to pyrogallol.

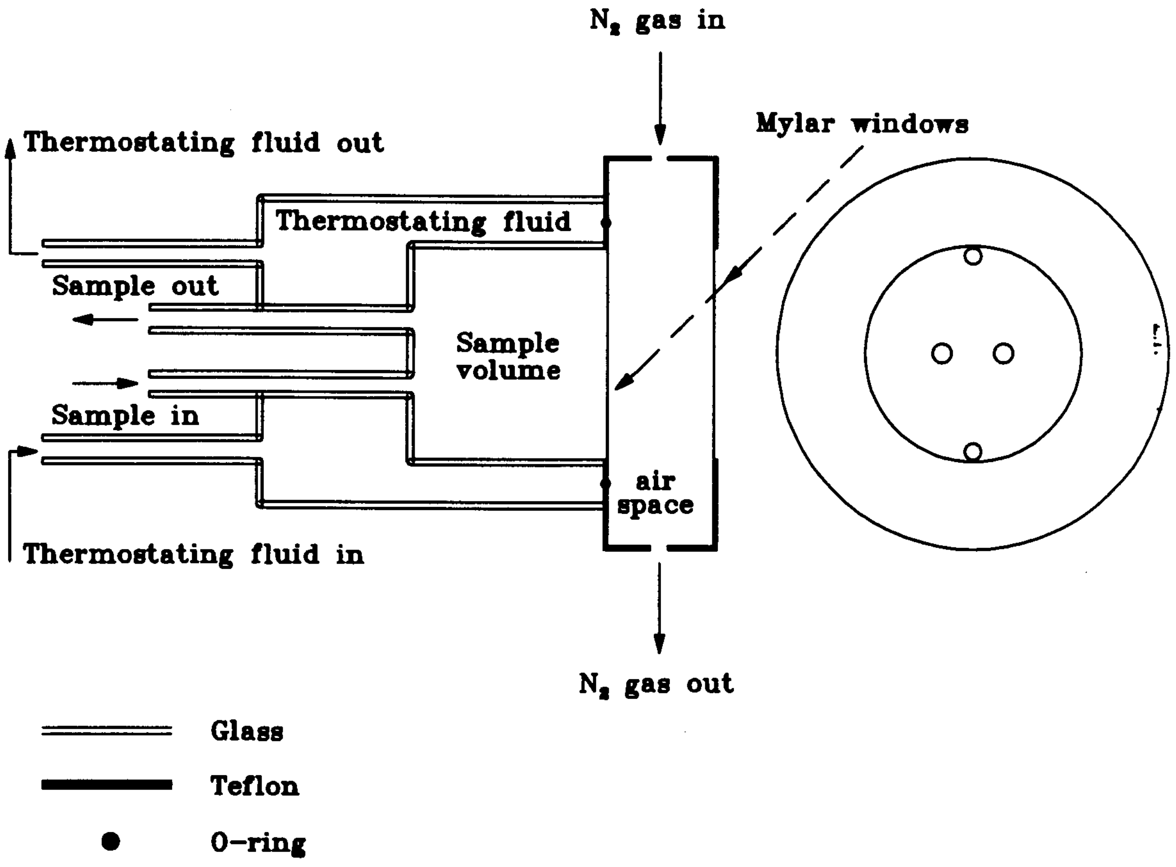

Figure 5.4: A schematic representation of the sample cell.

container was usually under a pressure of 10 – 15 psi. A diagram of the sample filling system is given in figure 5.5. The filling procedure is as follows:

- Connect the thin teflon tubing from V3 to the inlet of the insulating volume of the sample cell. Valve V3 stays open during the sample filling and the entire experiment to minimize the risk of contamination by atmospheric oxygen.
- Connect V2 to V_{out} to let N_2 flush the sample volume. While N_2 is flushing the cell:
- Let N_2 flush the spout of the sample container by inserting the thin teflon tubing from V1 before coupling the spout to the connection C.
- Slowly open Vs and watch the sample fill the cell. When the cell is filled with sample, close Vs, V_{in}, and V_{out}. Now the cell is ready.

The temperature was controlled by circulating fluid from a constant-temperature bath to the connections T_{in} and T_{out} (figure 5.5). A temperature sensor (type K copper-constantan thermocouple) was imbedded in the return line of the thermostating fluid. The sample temperatures were read directly from both the circulator and the thermocouple.

5.3 Results

5.3.1 Muonium

Of the four predicted precession frequencies (table 1.3) only two are low enough to be detected. In extremely low fields (< 10 G) they are

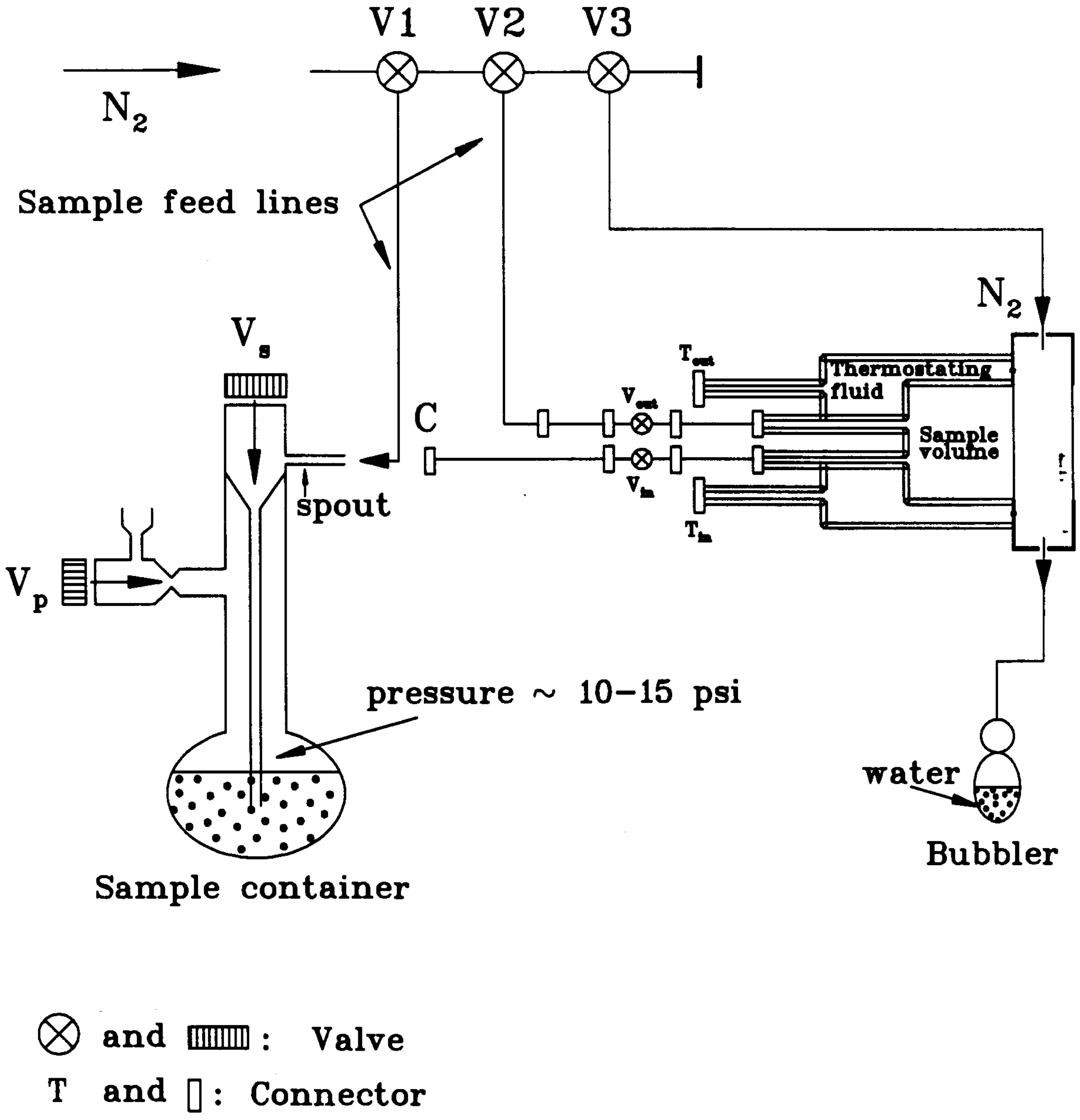

Figure 5.5: A schematic diagram of the sample filling system.

degenerate, but at moderately low fields the frequencies are split by an amount which depends on the hyperfine interaction:

$$\omega_{12} = \frac{1}{2}(\omega_e - \omega_\mu) - \Delta \tag{5.1}$$

$$\omega_{23} = \frac{1}{2}(\omega_e - \omega_\mu) + \Delta \tag{5.2}$$

with $\Delta = 1/2[\sqrt{(\omega_e + \omega_\mu)^2 + A_\mu^2} - A_\mu]$, where ω_e and ω_μ are the electron and muon Zeeman angular frequencies, and A_μ is the Mu isotropic hfcc.

In the rf-IμSR experiments, muonium signals were successfully detected (figures 5.6—5.8) in water, ice, fused quartz (SiO_2), and powdered C_{60} containing about 10% C_{70}. In the figures, the solid lines represent Lorentzian fits to the experimental values (points). Two broad curves correspond to the ω_{23} and ω_{12} angular frequencies, while the sharp feature between them is due to two photon absorption (TPA) in the 'forbidden' $\mid 1 > \leftrightarrow \mid 3 >$ transition. Note that the resonance of the $\mid 2 > \leftrightarrow \mid 3 >$ transition occurs at lower field values than that of the $\mid 1 > \leftrightarrow \mid 2 >$ transition. Table 5.1 lists the the rf-IμSR measurements and the fit results, where $B_o(\omega_{ij})$ is the longitudinal resonance field for the transition ω_{ij} taken from the Lorentzian fit to the data, ν_{rf} is the rf resonance frequency used, and A_μ is the average value of Mu hfccs derived from ω_{12} and ω_{23} transitions (equations 5.1 and 5.2).

The TPA spectrum has four features. First, it can be calculated that the rf asymmetry is four times that of the single photon lines (ω_{12} and ω_{23}) [56]), which is evident from the asymmetry spectra, figures 5.6—5.8. Second, the $\mid 1 > \leftrightarrow \mid 3 >$ transition does not involve a transition to a mixed state (*i.e.* $\mid 2 >$), and therefore the full asymmetry not lost to the $\mid 2 > \leftrightarrow \mid 4 >$ high frequency oscillation is available. Third, the effective coupling $< 1 \mid H_{rf} \mid 3 >$, the rf interaction Hamiltonian

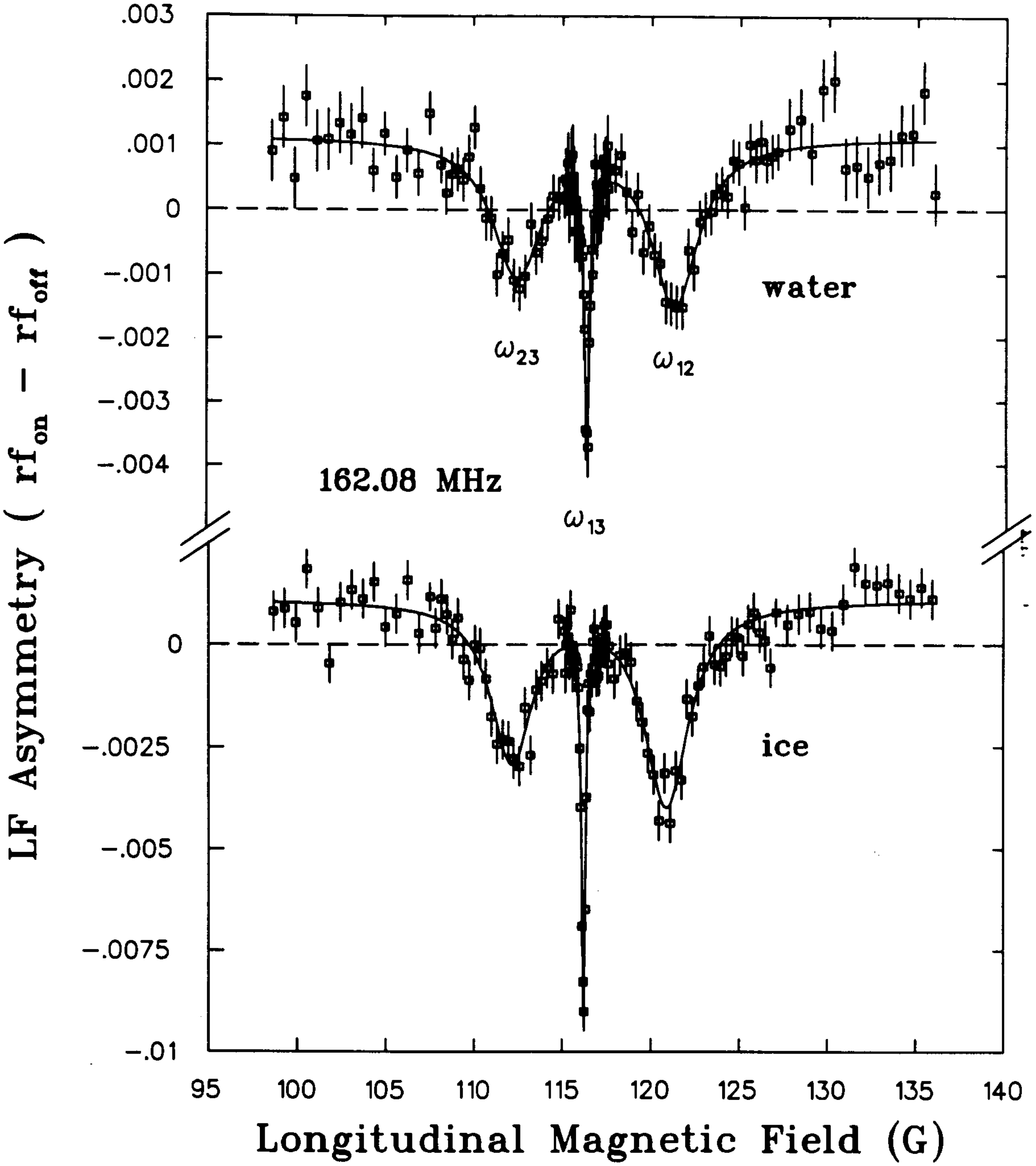

Figure 5.6: rf-IμSR spectrum of Mu in water at about room temperature and ice (about -6 °C) with rf resonance frequency 162.08 MHz, showing experimental data (points) and the best fit (Lorentzian) curve.

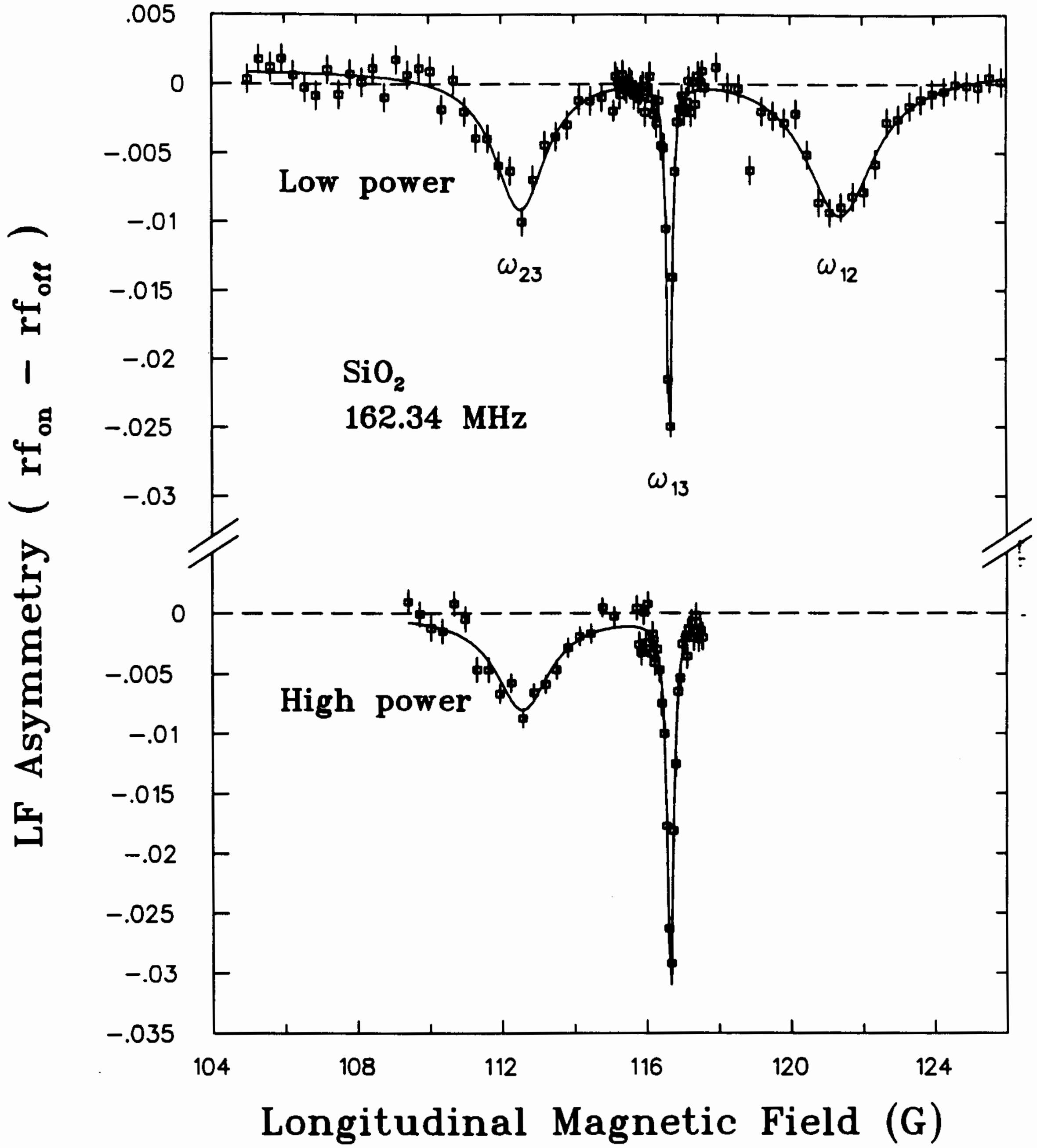

Figure 5.7: rf-IμSR spectrum of Mu in fused quartz at about room temperature with rf resonance frequency 162.34 MHz, showing experimental data (points) and the best fit (Lorentzian) curve.The single photon lines are all essentially saturated at both power levels.

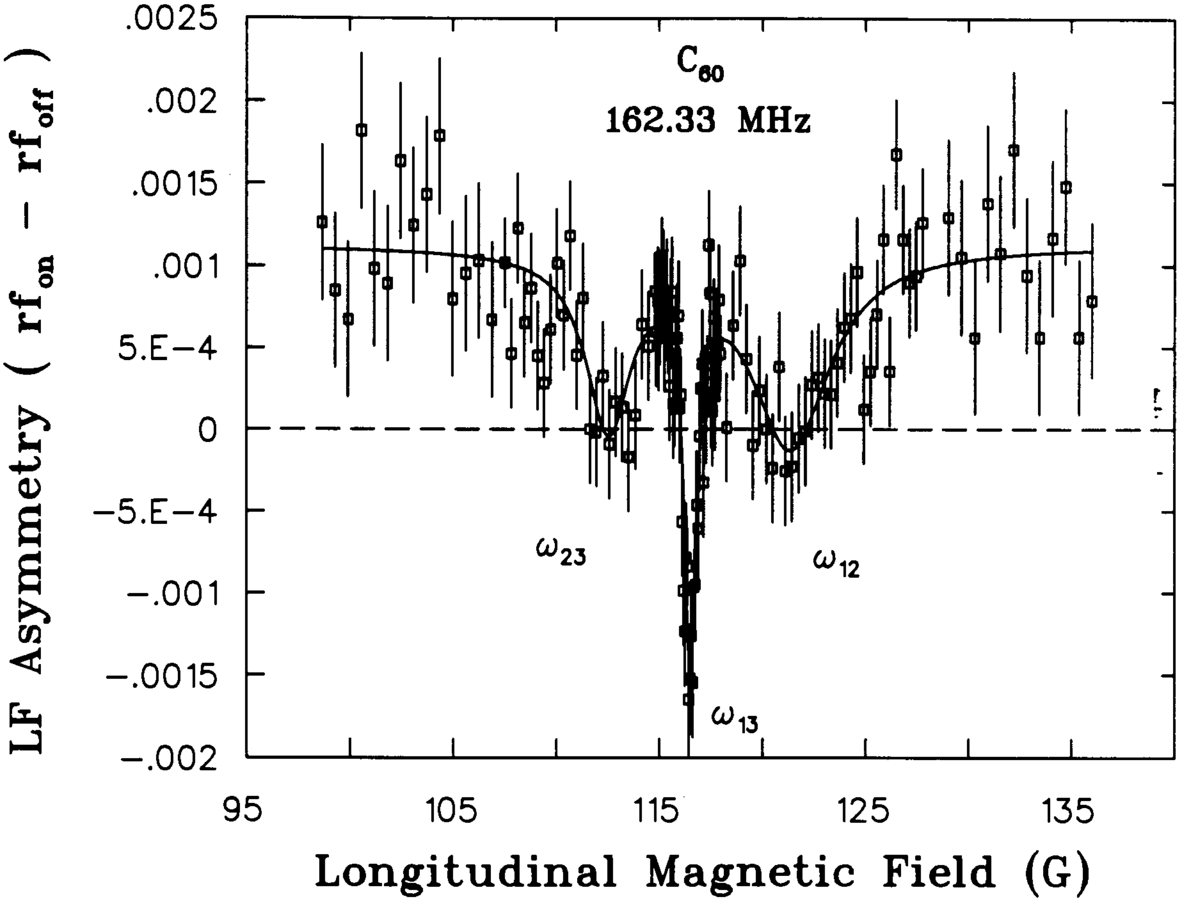

Figure 5.8: rf-IμSR spectrum of Mu in C_{60} at about room temperature with rf resonance frequency 162.33 MHz, showing experimental data (points) and the best fit (Lorentzian) curve.

Table 5.1: Longitudinal resonance fields and Mu hfccs determined from rf-IμSR spectra.

	B_o (ω_{23}) (Gauss)^a	B_o (ω_{13}) (Gauss)^a	B_o (ω_{12}) (Gauss)^a	ν_{rf} (MHz)^b	$A_\mu/2\pi$ (MHz)^c
Water^d	112.43(13)	116.38(12)	121.29(10)	162.08	4424(290)
Ice^e	112.14(8)	116.21(5)	120.90(7)	162.08	4404(41)
SiO_2^{d,f}	112.20(4)	116.32(3)	121.05(5)	162.34	4364(127)
C_{60}^{d}	112.5(3)	116.51(2)	121.3(8)	162.33	4433(162)

---

[a] The numbers shown in brackets are statistical errors in the least significant digit.

[b] Average uncertainty is about 0.03 MHz.

[c] The error in brackets is half the difference of the Mu hfccs derived from the ω_{12} and ω_{23} transitions.

[d] At about room temperature.

[e] At -6 °C.

[f] Low power

between $\mid 1 >$ and $\mid 3 >$, is proportional to the product of the single photon coupling divided by one half the energy difference in the single photon transitions [56]. If these energy differences are too large (*i.e.* if $\mid 2 >$ is not moderately close to the center of the other levels) the TPA line will have a very small amplitude. Thus this feature restricts its uses to Mu systems at low fields. Lastly, the resonance field of the TPA line is not dependent on the Mu hyperfine interaction since it involves a $\mid \mu^+ e^- > = \mid \downarrow\downarrow > \leftrightarrow \mid \uparrow\uparrow >$ transition where the relative orientation of the electron and muon spin is unchanged.

Over the past year, fullerene chemistry has developed from a rather exotic branch of pure research to the current ‘hot’ topic of materials science. ‘Buckyball’ atoms are arrayed in regular pentagons and hexagons — 12 pentagons and 20 hexagons to be precise. The 60 carbon atoms form something that looks like a hollow soccer ball, as shown in figure 5.9.

The precession signal of Mu was detected in a C_{60} powder sample, reportedly containing about 10% C_{70}, by several different μSR groups at TRIUMF via the TF-μSR method. The hyperfine interaction derived from the ω_{12} transition of the rf-IμSR experiment (data are displayed in figure 5.8), 4272(10) MHz, agrees with the one measured from the TF-μSR experiment, 4265 MHz [64]. This is only a few percent lower than the vacuum value, indicating Mu in C_{60} is an essentially free atom. However, the hyperfine interaction derived from the ω_{23} transition, 4595(12) MHz, does not agree with the TF-μSR value. The 3.5% error of the average Mu hfcc in table 5.1 is from taking half the difference of the Mu hfccs derived from the ω_{12} and ω_{23} transitions.

5.3.2 Radical

Radical formation was successfully detected in powdered C_{60}, neat C_6H_6, neat C_6F_6, and a saturated solution of C_6H_5OH in ethanol. Most importantly, also detected were radicals slowly formed from $C_6H_3(OH)_3$ in dilute aqueous solution (0.02 M). The rate constant for the reaction between muonium and pyrogallol is $k_M = (7.4 \pm 0.9) \times 10^9$ M^{-1} s^{-1} [62]. Therefore the radical formation rate in aqueous solution at the concentration 0.02 M would be 1.5×10^8 s^{-1}, which is an order of magnitude smaller than the lower limit of about 10^9 s^{-1} [13] for the detection of radical signals by the TF-μSR method. *These data represent the first time that a radical not observed in TF-μSR has been directly detected in a rf-IμSR experiment.* The detected resonance signals of all the radicals described above are displayed in figures 5.10 – 5.15, where solid lines represent Lorentzian fits to the experimental values (points). Table 5.2 collects the rf-IμSR measurements for the radicals, with the same mean-

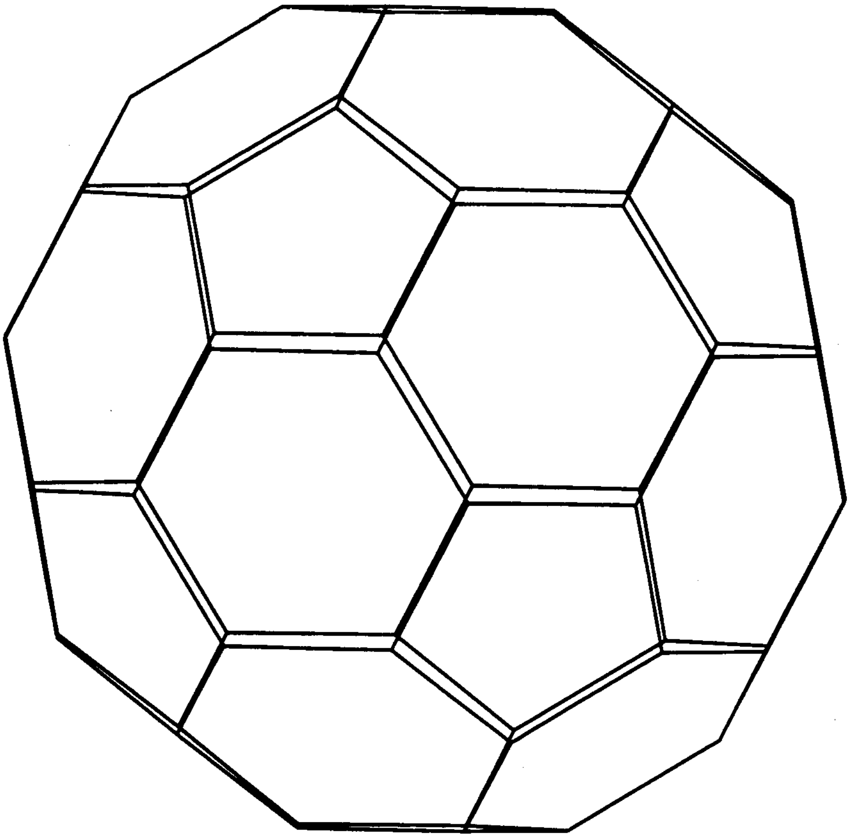

Figure 5.9: Structure of the buckminsterfullerene molecule. Its atoms are arrayed in a collection of 12 pentagons and 20 hexagons. Each hexagon of carbon atoms is formed from alternating single and double bonds.

Table 5.2: Longitudinal resonance fields and muon hfccs determined from rf-IμSR spectra.

Radical	**Temp. (C)**[a]	B_o **(kG)**[b]	ν_{rf} **(MHz)**[c]	$A_\mu/2\pi$ **(MHz)**[b]
C_{60}Mu	room temp.	0.0868(3)	162.33	320(7)
C_6H_6Mu	10	6.6989(6)	163.26	515.14(6)
C_6F_6Mu	10	3.6691(16)	151.17	200.93(7)
	25	3.6758(16)	151.17	200.75(7)
$C_6H_5(OH)$Mu				
(ortho)	10	4.8726(8)	163.34	466.70(7)
(meta)	10	6.8100(18)	163.34	518.28(8)

---

[a] Set temperature

[b] The numbers shown in brackets are statistical errors in the least significant digit.

[c] Average uncertainty is about 0.03 MHz

ing for all the parameters as in table 5.1. Table 5.3 lists the results from pyrogallol solutions of various concentrations.

Radicals formed by Mu addition to fullerenes are remarkable in that they contain no magnetic nuclei other than the muon (ignoring the 1.1% natural abundance of ^{13}C). This means that equations 5.1 and 5.2 also apply if the hyperfine frequency is replaced by that for the radical. It is assumed that the muon-substituted radical signals in the C_{60} powder sample are due to C_{60}Mu. The muon hfcc of C_{60}Mu radical at room temperature has been measured [65] from TF-μSR and is 325 MHz. The value of 320(7) MHz measured by rf-IμSR (table 5.2) agrees with this

Table 5.3: Longitudinal resonance fields and muon hfccs determined from rf-IμSR spectra in pyrogallol.

Radical I				
Concentration (M)	**Temp. (C)**[a]	B_o **(kG)**[b]	ν_{rf} **(MHz)**[c]	$A_\mu/2\pi$ **(MHz)**[b]
5	10	5.064(2)	163.12	471.29(9)
2	25	4.1636(7)	174.21	470.73(6)
0.02	25	4.1705(4)	174.20	470.89(6)
Radical II				
Concentration (M)	**Temp. (C)**[a]	B_o **(kG)**[b]	ν_{rf} **(MHz)**[c]	$A_\mu/2\pi$ **(MHz)**[b]
5	10	5.483(5)	163.12	482.41(14)
2	25	4.5623(16)	174.21	481.09(8)
0.02	25	4.5547(13)	174.20	480.87(7)

---

[a] Set temperature

[b] The numbers shown in brackets are statistical errors in the least significant digit.

[c] Average uncertainty is about 0.03 MHz

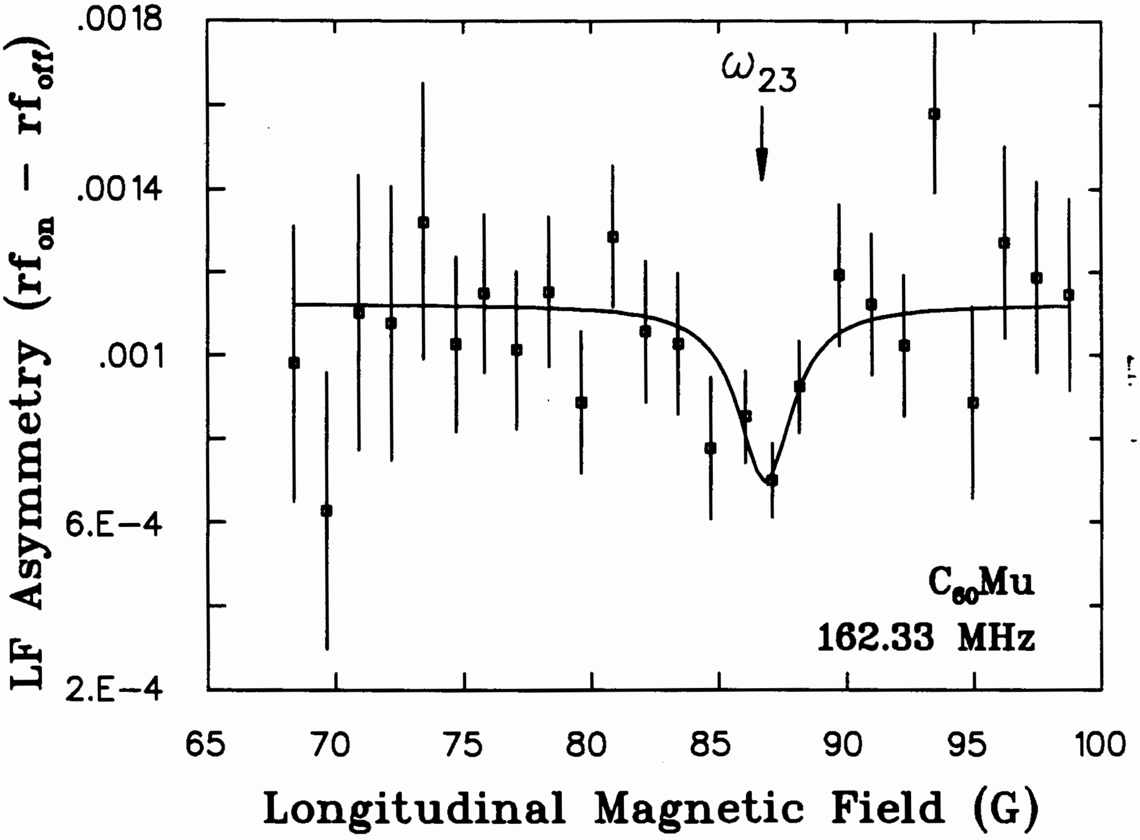

Figure 5.10: rf-IμSR spectrum of C_{60}Mu radical at room temperature with rf resonance frequency 162.33 MHz, showing experimental data (points) and the best fit (Lorentzian) curve.

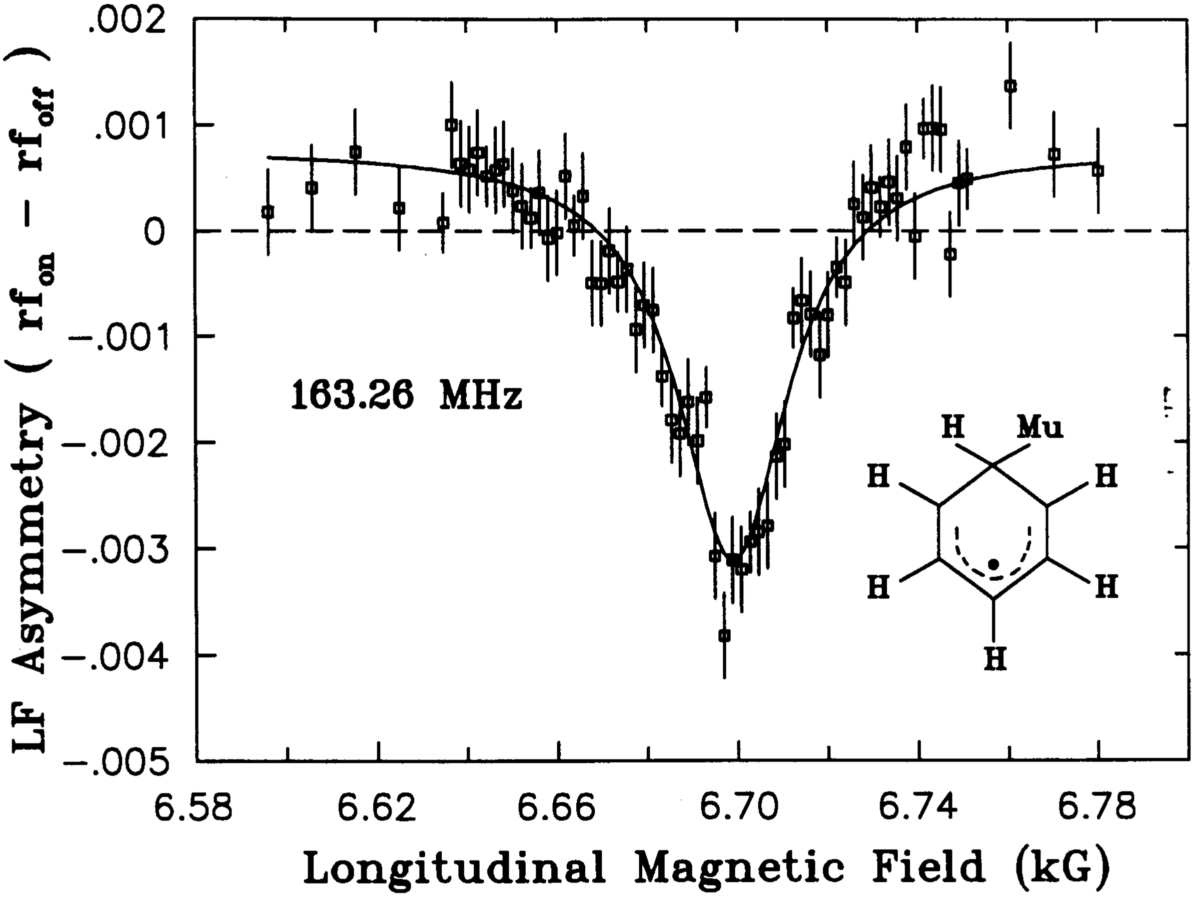

Figure 5.11: rf-IμSR spectrum of C_6H_6Mu radical at 10 °C (set temperature) with rf resonance frequency 163.26 MHz, showing experimental data (points) and the best fit (Lorentzian) curve.

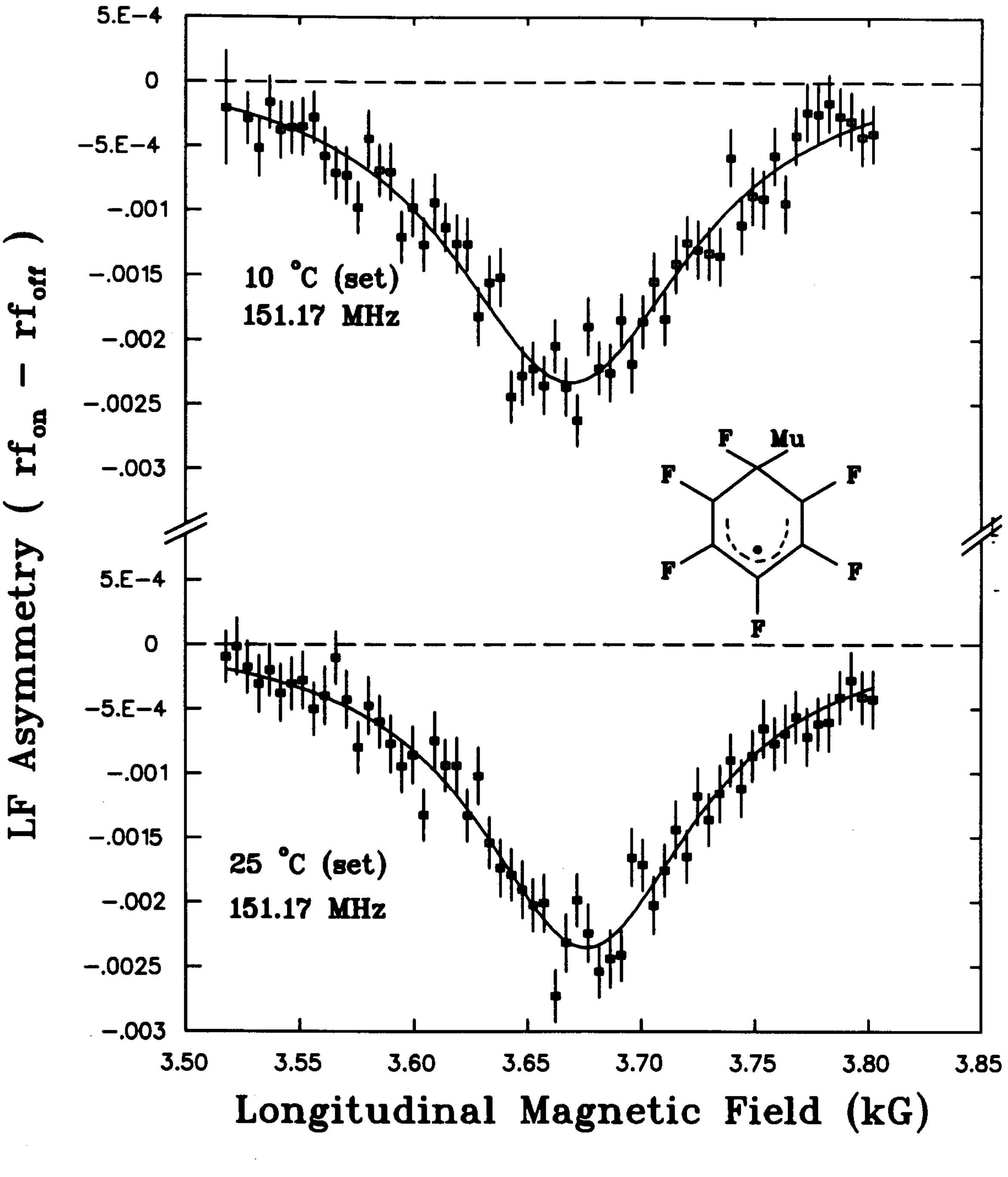

Figure 5.12: rf-IμSR spectrum of C_6F_6Mu radical at 10 °C (set temperature, top picture) and 25 °C (set temperature, bottom picture) with rf resonance frequency 151.17 MHz, showing experimental data (points) and the best fit (Lorentzian) curves.

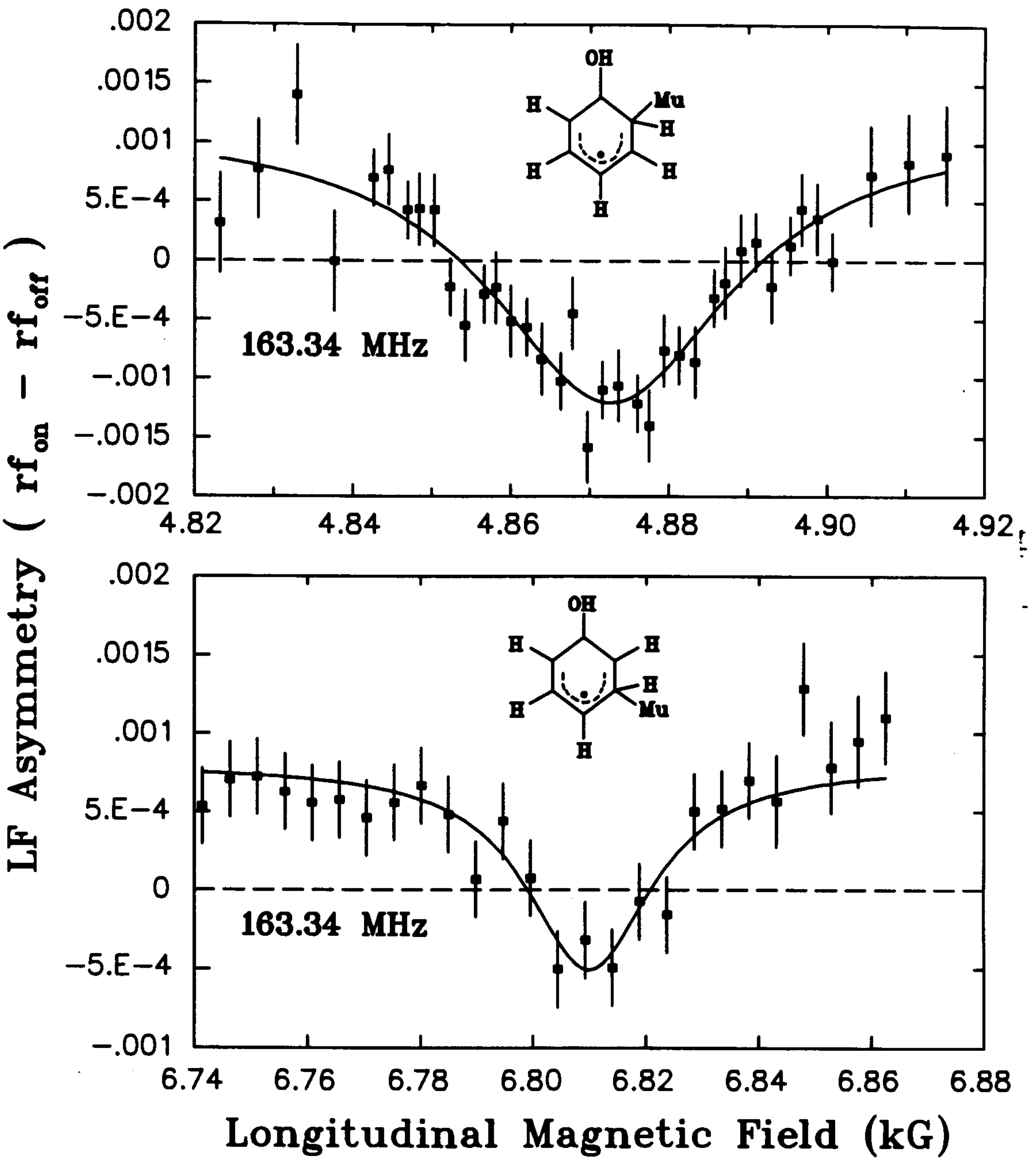

Figure 5.13: rf-IμSR spectrum of ortho and meta isomeric radicals formed by addition of Mu to phenol at 10 °C (set temperature) with rf resonance frequency 163.34 MHz, showing experimental data (points) and the best fit (Lorentzian) curves.

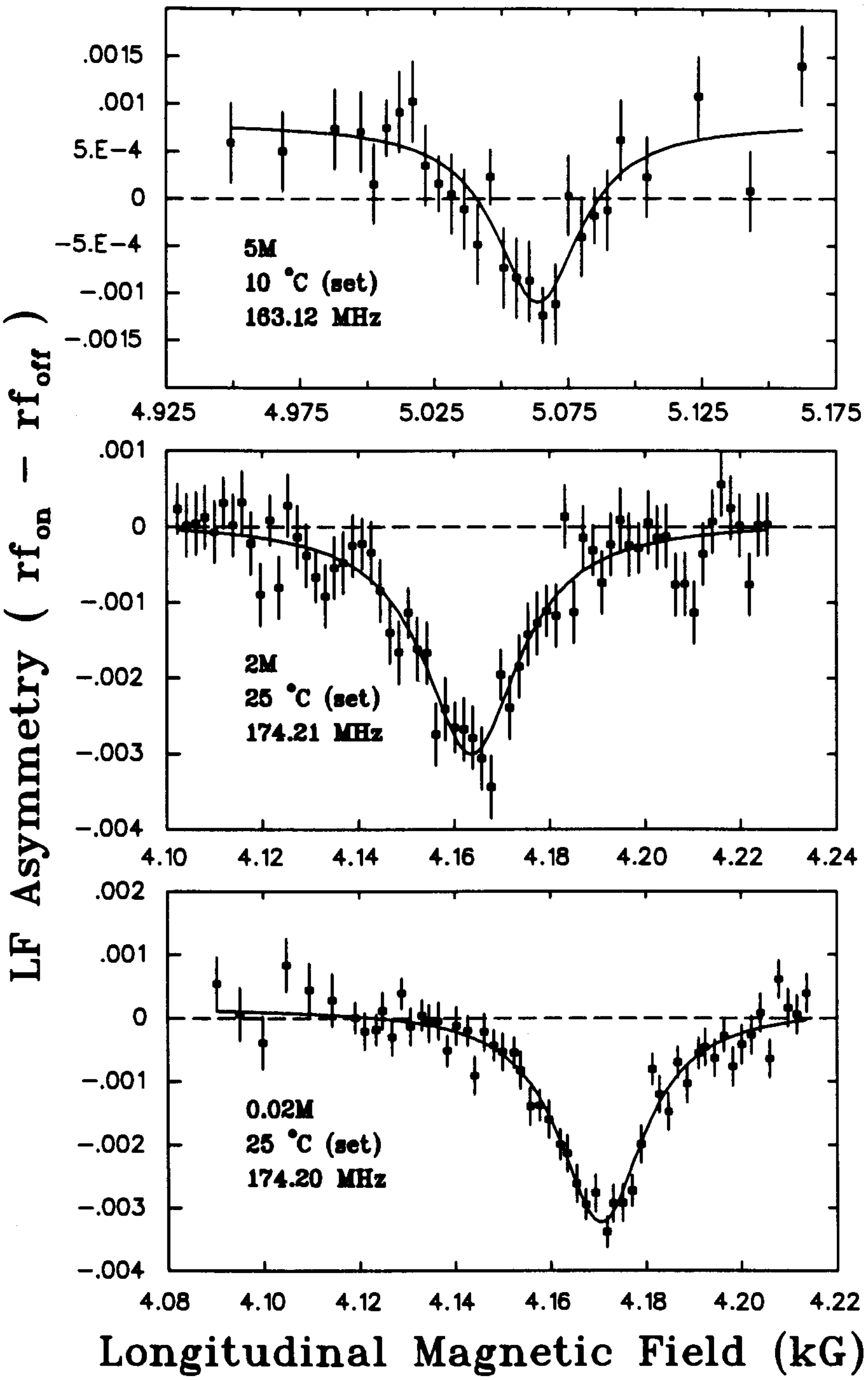

Figure 5.14: rf-IμSR spectrum of Radical I in various concentrations of pyrogallol and at different temperatures, showing experimental data (points) and the best fit (Lorentzian) curves.

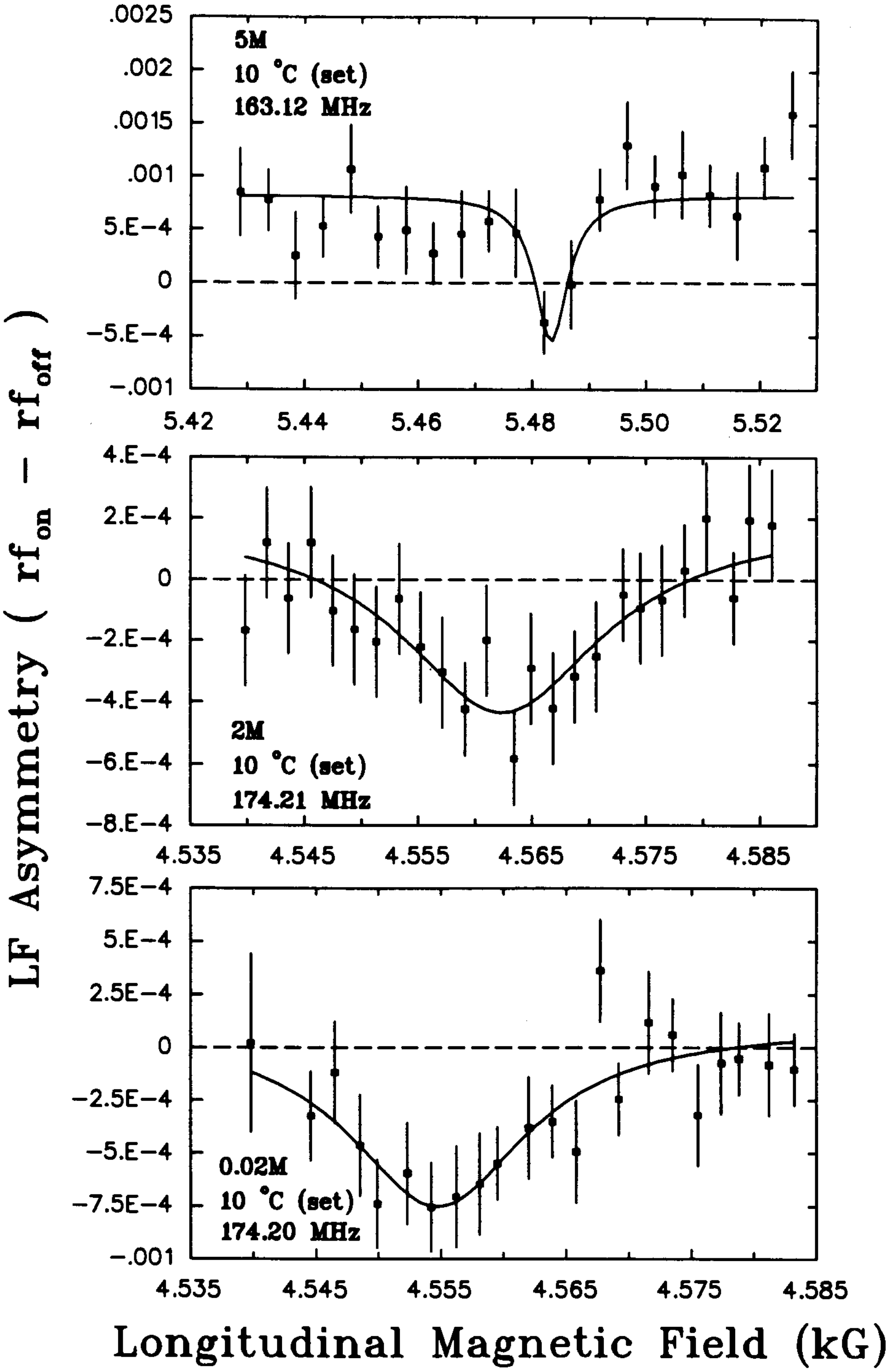

Figure 5.15: rf-IμSR spectrum of Radical II in various concentrations of pyrogallol and at different temperatures, showing experimental data (points) and the best fit (Lorentzian) curves.

value. The SFU muonium chemistry group had measured [65] the radical precession signals by TF-μSR from room temperature down to about 30 K and concluded that the radical's muon hyperfine interaction is isotropic and almost constant over that wide temperature range. There are many intriguing questions about the buckyball which remain unaddressed. For example, do the Mu and radical signals really emanate from the same sample? Where is the detected Mu atom located? What is the structure of C_{60}Mu assuming the radical signals are due to C_{60}Mu? How is the unpaired electron distributed in C_{60}Mu? How is the radical formed? etc. Further study of the buckminsterfullerene is underway but is beyond the scope of this thesis.

Muon hfcc temperature dependences for both C_6H_6Mu and C_6F_6Mu have been measured [44] from TF-μSR and are listed in table 5.4. The interpolation from the data for C_6H_6 collected in table 5.4 gives a temperature of 15.8 ^{o}C for the muon hfcc 515.14 MHz, which was measured by rf-IμSR at the set temperature of 10 ^{o}C, as shown in table 5.2. Similarly, the interpolation from the data for C_6F_6 collected in table 5.4 indicates a temperature of 19.4 ^{o}C (52.5 ^{o}C) for the muon hfcc 200.93 MHz (200.75 MHz) measured by rf-IμSR at the set temperature of 10 ^{o}C (25 ^{o}C). This means that the sample is warmed by the rf field somewhere from 5 ^{o}C to 25 ^{o}C, depending on the input rf power. The muon hfcc measured from rf-IμSR for ortho and meta isomeric radicals formed by addition of Mu to phenol are consistent with the literature values (467.4 ± 0.5 MHz for ortho radical and 517.4 ± 0.5 MHz for meta radical at room temperature, measured from TF-μSR [61]) after taking into account sample warming by the rf field.

As was stated earlier, the radical formation rate in aqueous solution

Table 5.4: Temperature dependence of muon hfccs for C_6H_6 and C_6F_6 as determined from TF-μSR spectra [44].

C_6H_6Mu		**C_6F_6Mu**	
Temp. (C)[a]	$A_\mu/2\pi$ **(MHz)**[b]	**Temp. (C)**[a]	$A_\mu/2\pi$ **(MHz)**[b]
10.7	515.519(14)	12.4	201.03(4)
25.1	514.409(13)	25.0	200.91(4)
39.5	513.254(13)	37.2	200.87(5)
54.4	512.115(13)	50.5	200.74(5)

---

[a] Set temperature

[b] The numbers shown in brackets are statistical errors in the least significant digit.

of pyrogallol at the concentration of 0.02 M is 1.5×10^8 s^{-1}. The fact that this radical was easily observed (figures 5.14 and 5.15) illustrates the utility of the rf technique for studying radicals formed slowly from Mu precursors.

5.4 Theoretical treatment—Chemical reactivity

5.4.1 Theoretical background

The general case of a species (X) which has been formed at time t' and still exists at time t ($0 \leq t' \leq t$) is considered here. The contribution of species X to the time dependent muon polarization along the direction j has been studied by many authors [7, 13, 66] and is given by

$$P_j^X(t) = \int_0^t p_j^X(t) q^X(t,t') dt', \tag{5.3}$$

where $q^X(t,t')$ is the probability per unit time that X has been formed at time t' and still exists at time t. $p_j^X(t)$ is the muon polarization of that

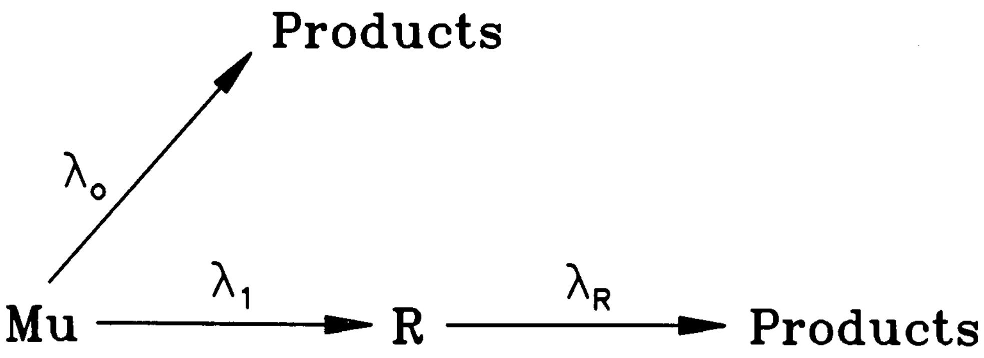

Figure 5.16: Scheme of radical formation.

fraction of the muon ensemble defined by $q^X(t,t')$ along the direction j.

Roduner [59] has studied the mechanism of radical formation and concluded that the direct muonic precursor of the muon-substituted cyclohexadienyl radical is thermal muonium. Therefore, we consider the case of radical formation (X = R) according to the scheme shown in figure 5.16, under conditions where there is non-negligible evolution of the muon spin in the precursor, which is here assumed to be Mu. λ_1 in figure 5.16 is the radical formation rate, λ_o is the radioactive muon decay rate, and λ_{R} is the radical decay rate including muon decay and reaction of the radical.

For the radical formation scheme shown in figure 5.16, the probability per unit time that the radical (R) has been formed at time t' and still exists at time t is given by [7]:

$$q^R(t,t') = \lambda_1 \exp^{-\lambda t'} \exp^{-\lambda_R (t-t')} \tag{5.4}$$

with the precursor Mu lifetime $\tau_{Mu} = \lambda^{-1}$, where $\lambda = (\lambda_o + \lambda_1)$.

The time dependence of the muon polarization carried by a radical at time t along the longitudinal direction z, under the assumption that the precursor carries the full polarization at the time of radical formation, was derived in chapter 4 and is given by equation 4.41:

$$p_z^R(t) = Q(1 - \cos\omega t) \tag{5.5}$$

where

$$\begin{aligned} Q &= \frac{1 + c^2 - s^2}{4} \frac{4\rho_{12}^2}{(\omega_1 - \omega_2 - \omega_{rf})^2 + 4\rho_{12}^2} && (5.6) \\ \omega &= 1/2[(\omega_1 - \omega_2 - \omega_{rf})^2 + 4\rho_{12}^2] && (5.7) \end{aligned}$$

for the stimulated emission from the state $\mid 1 >$ to $\mid 2 >$, and

$$\begin{aligned} Q &= \frac{c^2(1 + c^2 - s^2)}{4} \frac{4\rho_{43}^2}{(\omega_4 - \omega_3 - \omega_{rf})^2 + 4\rho_{43}^2} && (5.8) \\ \omega &= 1/2[(\omega_4 - \omega_3 - \omega_{rf})^2 + 4\rho_{43}^2] && (5.9) \end{aligned}$$

for the resonance absorption from the state $\mid 4 >$ to $\mid 3 >$. ρ_{ij} are given by equations 4.25 and 4.48, and ω_n, c, and s are given in table 4.2.

For Mu as a precursor one has to consider that the muons, which are incorporated into R, do not necessarily carry the full polarization, *i.e.* the time dependence of the muon polarization carried by the precursor Mu at the radical formation time t' is given by [19]

$$p_z^R(t') = P_o[1 - \frac{1}{2(1 + x^2)}(1 - \cos\omega_{Mu}t')], \tag{5.10}$$

where

$$\begin{aligned} x &= B/B' && B' = 158.5 \text{ mT for Mu} \\ \omega_{Mu} &= A_\mu^{vac}\sqrt{(1 + x^2)} && A_\mu^{vac}/2\pi = 4.46 \text{ GHz} \end{aligned}$$

and B is longitudinal magnetic field, A_μ^{vac} is the muon hfcc of Mu in vacuum, and P_o represents the fraction of muon polarization available in muonium for transfer to the radical.

After considering both equations 5.5 and 5.10, the final muon polarization is

$$p_z^R(t) \;=\; P_o[1 - \frac{1}{2(1 + x^2)}(1 - \cos\omega_{Mu}t')]Q(1 - \cos\omega t) \quad t \geq t'$$

$$= \quad 0 \qquad\qquad t < t'$$

For times when $t \geq t'$, the above equation can also be rewritten as

$$p_z^R(t) = P_o Q(p_1 + p_2) \tag{5.11}$$

where

$$\begin{aligned} p_1 &= \frac{2x^2+1}{2(1+x^2)}(1-\cos\omega t) && (5.12) \\ p_2 &= \frac{1}{2(1+x^2)}\cos\omega_{Mu}t'(1-\cos\omega t) && (5.13) \end{aligned}$$

The time dependence of the muon polarization carried by the radical R along the direction z, $P_z^R(t)$, can then be calculated by substituting the equations 5.4 and 5.11 into equation 5.3 and is given by

$$\begin{aligned} P_z^R(t) &= P_o Q \int_0^t (p_1+p_2) q^R(t,t') dt' && (5.14) \\ &= P_o Q \int_0^t (p_1+p_2)\lambda_1 \exp^{-\lambda t'} \exp^{-\lambda_R(t-t')} dt' && (5.15) \end{aligned}$$

The above integration of terms p_1 and p_2 will be calculated separately. The integration of term p_1 is given by

$$\begin{aligned} &\int_0^t p_1 q^R(t,t') dt' \\ &= \frac{2x^2+1}{2(1+x^2)} \int_0^t (1-\cos\omega t)\lambda_1 \exp^{-\lambda t'} \exp^{-\lambda_R(t-t')} dt' && (5.16) \end{aligned}$$

For times t long compared with the precursor lifetime τ_{Mu}, the above equation can be expressed as

$$\begin{aligned} &\int_0^t p_1 q^R(t,t') dt' \\ &\approx \frac{2x^2+1}{2(x^2+1)}(1-\cos\omega t)\frac{\lambda_1}{\lambda}\exp^{-\lambda_R t} \int_o^\infty \lambda \exp^{-\lambda t'} dt' \\ &= \frac{2x^2+1}{2(x^2+1)}(1-\cos\omega t)\frac{\lambda_1}{\lambda}\exp^{-\lambda_R t} && (5.17) \end{aligned}$$

Similarly, the integration of term p_2 is given by

$$\begin{aligned}
&\int_0^t p_2 q^R(t,t')dt' \\
&= \frac{1}{2(1+x^2)}\int_0^t \cos\omega_{Mu}t'(1-\cos\omega t)\lambda_1 \exp^{-\lambda t'}\exp^{-\lambda_R(t-t')}\,dt' \\
&\approx \frac{1}{2(1+x^2)}(1-\cos\omega t)\exp^{-\lambda_R t}\frac{\lambda_1^2}{\lambda_1^2+\omega_{Mu}^2} \qquad (5.18)
\end{aligned}$$

Substituting equations 5.17 and 5.18 into equation 5.14, the time dependence of the muon polarization carried by radical R along the direction z is then given by

$$P_z^R(t) = P_o Q\frac{1}{2(x^2+1)}[\frac{\lambda_1(2x^2+1)}{\lambda}+\frac{\lambda_1^2}{(\lambda_1^2+\omega_{Mu}^2)}](1-\cos\omega t)e^{-\lambda_R t} \quad (5.19)$$

Integration over time and normalization of the above equation leads to the time integral muon polarization:

$$P_z^R(B) = P_o Q\frac{1}{2(x^2+1)}\left[\frac{\lambda_1(2x^2+1)}{\lambda}+\frac{\lambda_1^2}{(\lambda_1^2+\omega_{Mu}^2)}\right]\frac{\omega^2}{\omega^2+\lambda_R^2} \quad (5.20)$$

where B is the longitudinal magnetic field.

For the $\mid 1>$—$\mid 2>$ transition and with the expressions for Q and ω given in equations 5.8 and 5.9 respectively, $P_z^R(B)$ is then given by

$$P_z^R(B) = P_o T_{12}\frac{(\beta_{12}B_1)^2}{(\beta_{12}B_1)^2+(\lambda_R/(2\pi))^2+[(\omega_{rf}-\omega_{12})/(2\pi)]^2} \quad (5.21)$$

where

$$\begin{aligned}
T_{12} &= \frac{1}{2(1+x^2)}\frac{c^2(1+c^2-s^2)}{4}(\frac{\lambda_1(2x^2+1)}{\lambda_1+\lambda_o}+\frac{\lambda_1^2}{\lambda_1^2+\omega_{Mu}^2}) \qquad (5.22) \\
\beta_{12} &= \frac{1}{4}(s\gamma_e - c\gamma_\mu) \qquad (5.23)
\end{aligned}$$

and s, c, γ_i, B_1, ω_{rf} and ω_{12} in the above equation are all defined as in chapter 4.

The rf-IμSR technique provides the unique possibility of detecting slowly forming radicals, including those which are evolving from a radical reaction, as long as the radical formation rate λ_1 is comparable to λ_o. (For $\lambda_1 \gg \lambda_o$, $P_z^R(B)$ is insensitive to the value of λ_1.) Thus, relative to TF-μSR the observable range of λ_1 is extended by four orders of magnitude.

5.4.2 Results and Discussion

By fitting the experimental rf-IμSR data to the theoretical calculation described in the last section, the parameters λ_R, λ_1 (when λ_1 is comparable to λ_o), B_1, and P_o can be determined for the radical. A FORTRAN program FCNRF.FOR, which is called by the program MINUIT in CERNLIB, was written for a least-squares fit of equation 5.21 to the experimental data shown in figures 5.14 and 5.15 for pyrogallol.

The fitting results are listed in table 5.5 and plotted in figure 5.17. For all six fits shown in figure 5.17, the hfccs of the muon are fixed at the values listed in table 5.3. The rate constant for the reaction between muonium and pyrogallol has been measured [62] and is k_M = $(7.4 \pm 0.9) \times 10^9$ M^{-1} s^{-1}. Therefore the radical formation rate, λ_1, can be calculated and is the product of the rate constant (k_M) and the concentration. For the smallest pyrogallol concentration that we have, λ_1 would be about 1.5×10^8 s^{-1} which would be about three orders of magnitude bigger than the muon decay rate ($\lambda_o = 4.5 \times 10^5$ s^{-1}). In all the fits, λ_1 is fixed for a given concentration ($\lambda_1 = k_M \times$ concentration). Notice that the λ_R from all the fits agree with each other except the one derived for Radical II at the concentration 5 M. If we ignore it because of the poor statistics (see figure 5.15), the average of λ_R yields 8.3(3)

$\times$ 10^5 s^{-1}. This agrees with the value measured by Percival *et al.* [62] from μLCR measurements, 8.4(7) $\times$ 10^5 s^{-1}. The value for λ_R is about twice the rate due to the muon lifetime alone ($1/\tau = 4.5 \times 10^5$ s^{-1}), presumably due to radical decay or small spin relaxation.

Since several uninteresting factors (such as apparatus geometry) affect signal amplitudes (P_o), only the values of $P_o C_o$ are reported here. C_o in table 5.5 is the calibration factor, which is the signal amplitude corresponding to 100% muon polarization. Unfortunately, it is not easy to determine P_o precisely because of the different normalization of muon spin polarization under different magnetic field intensities. At KEK, CCl_4 data are used for normalization in the case of diamagnetic resonance. In order to get the normalization for the Mu-substituted radical, however, the diamagnetic muon resonance of CCl_4 must be measured at the same magnetic field as the resonance field of the radical. This is almost impossible because the cavity frequency is fixed once the cavity is built.

B_1 is usually obtained from the rf-LFμSR experiment. However, this becomes very difficult when B_1 is small (*i.e.* less than 2 Gauss). For example, for an on-resonance rf-LFμSR experiment on a diamagnetic signal, the time period is about 50 μs for $B_1 = 1.5$ G (see equation 4.13), which is too big to be detected within the data gate, which is at most 16 μs for a rf-LFμSR experiment. A least-squares fit of equation 5.21 to the rf-IμSR experimental data provides another means of obtaining B_1 without any limitation on B_1, where B_1 is a fitting parameter as shown in table 5.5. For bigger B_1, rf-LFμSR provides a more direct and accurate method. As an example of a rf-LFμSR experiment, figure 5.18 shows the precession of the diamagnetic signal in polyethylene at $B_o = 11.154$ kG

Table 5.5: Fits to the rf-IμSR experimental data of Radical I and Radical II from pyrogallol.

Radical I			
Concentration (M)	0.02	2	5
λ_R ($\times 10^5$) (s^{-1})[a]	8.1(7)	8.7(7)	8.5(4)
λ_1 ($\times 10^9$) (s^{-1})[b]	0.148	14.8	37.0
B_1 (G)[a]	1.2(5)	1.1(3)	1.4(4)
P_oC_o ($\times 10^2$)	1.34(5)	1.60(5)	0.79(5)
$A_\mu/2\pi$ (MHz)[b]	470.89	470.73	471.29
ν_{rf} (MHz)[b]	174.20	174.21	163.12
Radical II			
Concentration (M)	0.02	2	5
λ_R ($\times 10^5$) (s^{-1})[a]	7.5(6)	8.4(5)	4.7(3)
λ_1 ($\times 10^9$) (s^{-1})[b]	0.148	14.8	37.0
B_1 (G)[a]	1.1(3)	1.0(3)	0.9(4)
P_oC_o ($\times 10^2$)	0.36(7)	0.37(2)	0.36(8)
$A_\mu/2\pi$ (MHz)[b]	480.87	481.09	482.41
ν_{rf} (MHz)[b]	174.20	174.21	163.12

---

[a] The numbers shown in brackets are statistical errors in the least significant digit.

[b] Fixed

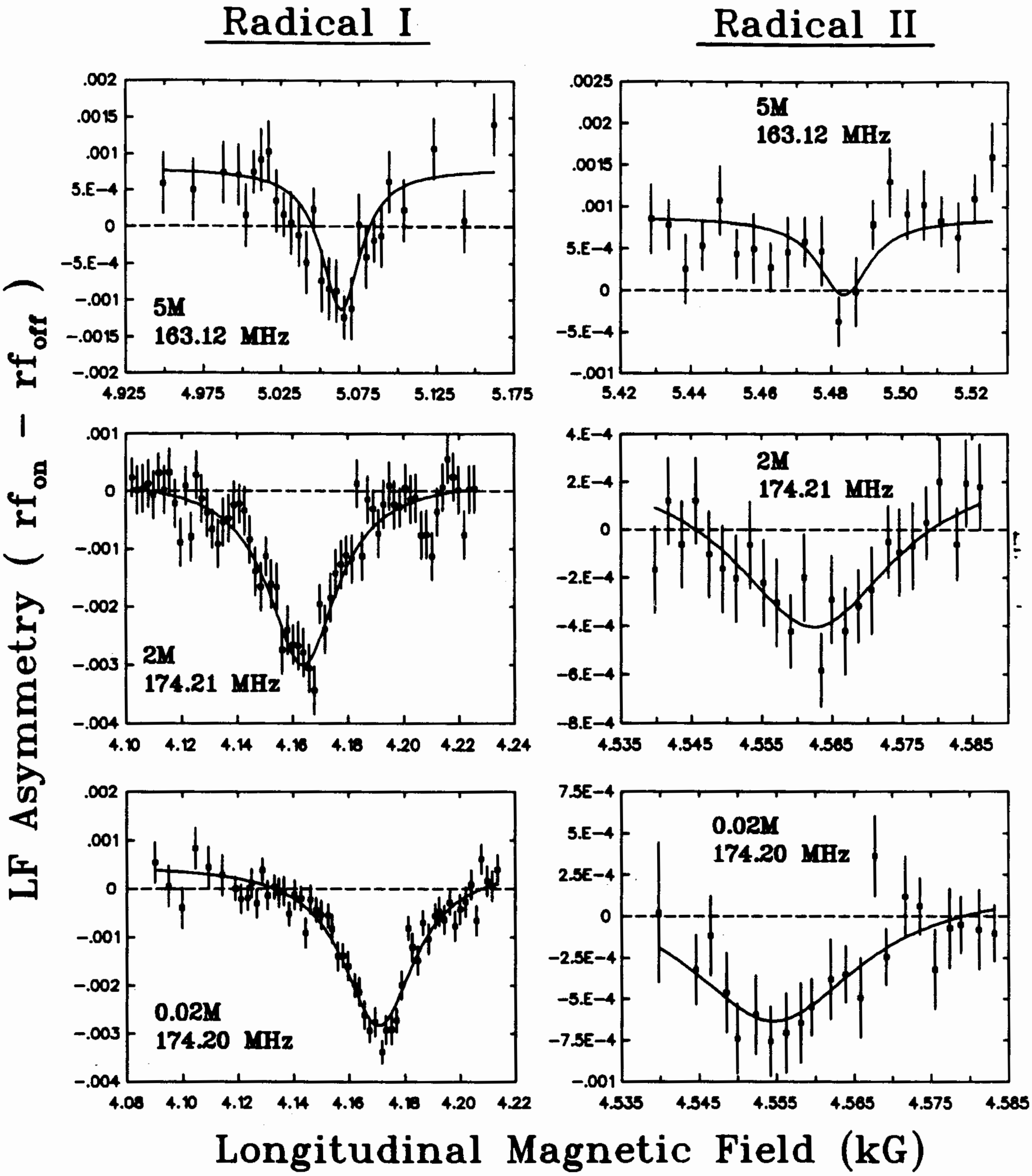

Figure 5.17: rf-IμSR spectrum of Radical I and II in various concentrations of pyrogallol. The solid curves correspond to the fits, shown in table 5.5, of the experimental values (points).

and yields $B_1 = 5.2$ G.

Percival *et al.* [62] have measured P_{total} (P_o (Radical I) + P_o (Radical II)), which represents the fraction of muon polarization present in muonium at the moment of reaction for forming a radical, as a function of the muonium lifetime ($1/(k_M \times$ concentration)) by μLCR experiments (figure 5.19). Notice that at early times the muonium fraction is almost twice its value at later times. This variation of P_{total} with time was ascribed [62, 67, 68] to both reactions and non-reactive spin-exchange encounters of muonium with the paramagnetic transients formed by the radiolysis of water as the muon thermalizes. On the same plot (figure 5.19) we have plotted our data 1/5 C_oP_{total} ($\times 10^2$) ($P_{total} = P_o$ (Radical I) + P_o (Radical II)) shown in table 5.5, where the calibration factor C_o affects the absolute values but does not affect the trend with muonium lifetime. The dependence of the amplitude on Mu lifetime shows similar behaviour in the two data sets, notably the drop in P_{total} at the shortest muonium lifetimes. However, data from these three concentrations are not sufficient to make any firm conclusion.

The equation 5.21 was derived under the assumption that there is no spin exchange during the process shown in figure 5.16. Deviations from equation 5.21 can occur in the event of spin exchange or other spin relaxation processes. Spin exchange is discussed in the next section.

5.5 Theoretical treatment—Spin-exchange

5.5.1 Theoretical background

A common feature of theories of electron spin exchange between radicals in solution is the sudden collision approximation introduced by

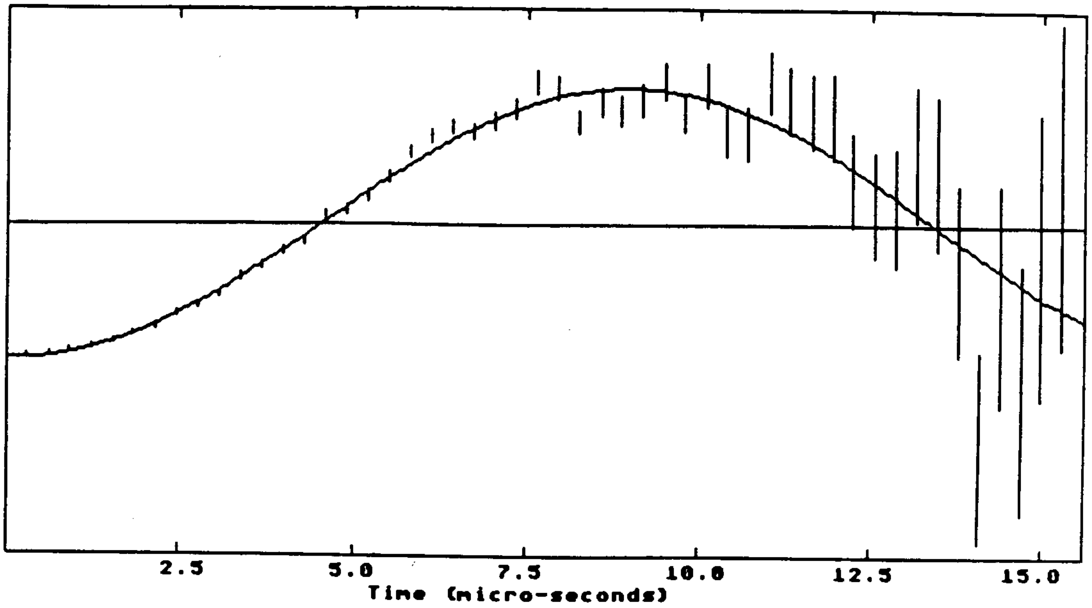

Figure 5.18: rf-LFμSR time histogram of diamagnetic signal in polythene with ν_{rf} = 151.17 MHz and B_o = 11.154 KG.

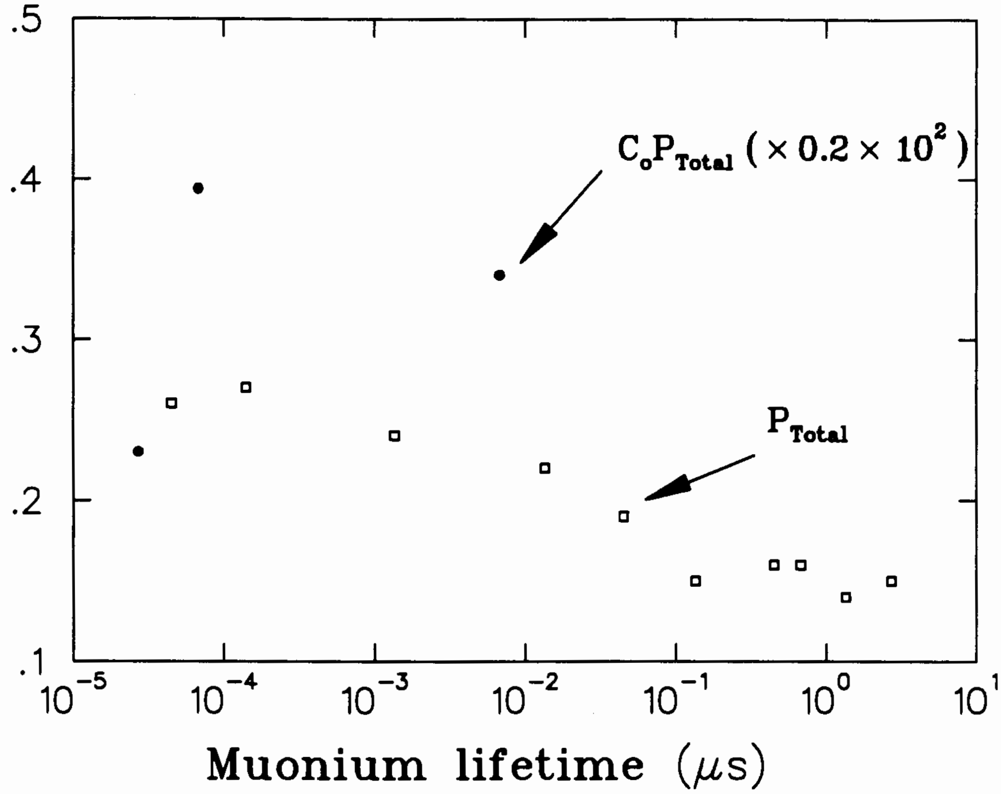

Figure 5.19: Muon polarization fraction available in Mu for transfer to the radical as a function of Mu chemical lifetime. (•) This work (∘) Percival *et al.* [62].

Kivelson [69, 70]. The two-state model distinguishes between isolated radicals and radical pairs. Exchange coupling is introduced as a step function, which is zero for isolated radicals and finite for radical pairs. This is based on the steepness of the radial dependence of the exchange coupling J(r).

Heming *et al.* [71] have studied the effect of Heisenberg spin exchange (HSE) on the level-crossing μSR (μLCR) spectra of organic free radicals within the framework of the two-state jump model. In this section the effect of HSE on the rf-IμSR spectra of organic free radicals is discussed using this model.

The following reaction scheme is considered here:

$$\underset{\text{state I}}{R_1^* + R_2} \overset{k_c,k_p}{\rightleftharpoons} \underset{\text{state II}}{[R_1^* ... R_2]} \xrightarrow{k_d} \text{diamagnetic products,}$$

where R_1^* denotes a muonated radical, R_2 a radical partner, k_c is the collision rate constant, and $k_{p,d}$ the radical pair decay rates into isolated radicals and diamagnetic products, respectively. The following treatment is strictly valid only if the chemical reaction to the diamagnetic products is electron spin independent.

Here the radical partner (R_2) is approximated by an unpaired electron e_2 (while e_1 represents the unpaired electron of the muonated radical). This approximation is good as long as the coupling of the muon to the extra electron is small. In the rotating frame of reference with angular velocity -ω_{rf} about the z axis (direction of the longitudinal magnetic field B_o), which is explained in detail in chapter 4, the spin Hamiltonian in angular frequency units for a given state reads:

$$\begin{aligned}\hat{H}^{I,II} &= \frac{1}{2}\gamma_{e1}\hat{\boldsymbol{\sigma}}_{e1}\vec{B}_{e1} + \frac{1}{2}\gamma_{e2}\hat{\boldsymbol{\sigma}}_{e2}\vec{B}_{e2} + \frac{1}{2}\gamma_{\mu}\hat{\boldsymbol{\sigma}}_{\mu}\vec{B}_{\mu} \\ &+\frac{1}{4}A_{\mu e1}\hat{\boldsymbol{\sigma}}_{\mu}\hat{\boldsymbol{\sigma}}_{e1} + \frac{1}{4}A_{e1e2}\hat{\boldsymbol{\sigma}}_{e1}\hat{\boldsymbol{\sigma}}_{e2} \qquad (5.24)\end{aligned}$$

where

$$\begin{aligned}\vec{B}_{e1} &= \frac{\omega_{e1}-\omega_{rf}}{\gamma_{e1}}\vec{z} + B_1\vec{x} \qquad (5.25)\\ \vec{B}_{e2} &= \frac{\omega_{e2}-\omega_{rf}}{\gamma_{e2}}\vec{z} + B_1\vec{x} \qquad (5.26)\\ \vec{B}_{\mu} &= \frac{\omega_{\mu}-\omega_{rf}}{\gamma_{\mu}}\vec{z} + B_1\vec{x} \qquad (5.27)\end{aligned}$$

All the parameters (ω_i and A_{ij}) in equations 5.24 – 5.27 are in angular frequency units: ω_i are Zeeman angular frequencies ($\omega_i = \gamma_i B_o$ and $\omega_\mu < 0$), $\nu_{rf}(= \omega_{rf}/2\pi)$ is the applied rf frequency, γ_i is the gyromagnetic ratio of the particle i, B_1 is the rf field strength, $\hat{\boldsymbol{\sigma}}_q$ is a Pauli spin matrix of proper dimension in the direct product basis $\hat{\boldsymbol{\sigma}}_\mu \otimes \hat{\boldsymbol{\sigma}}_{e1} \otimes \hat{\boldsymbol{\sigma}}_{e2}$, $A_{\mu e1}$ is the muon hyperfine coupling constant, and A_{e1e1} is the exchange coupling J (1/2 times the negative exchange integral). J takes values

$$\begin{aligned} J &= 0 \qquad for\ state\ I \qquad (5.28)\\ J &= A_{e1e2} \qquad for\ state\ II. \qquad (5.29)\end{aligned}$$

Expanding equation 5.24 further, the spin Hamiltonian is given by

$$\begin{aligned}\hat{H}^{I,II} &= \frac{1}{2}[(\omega_{e1}-\omega_{rf})\hat{\boldsymbol{\sigma}}^{z}_{e1} + (\omega_{e2}-\omega_{rf})\hat{\boldsymbol{\sigma}}^{z}_{e2} + (\omega_{\mu}-\omega_{rf})\hat{\boldsymbol{\sigma}}^{z}_{\mu}] \\ &+ \frac{1}{2}[f_{e1}\hat{\boldsymbol{\sigma}}^{x}_{e1} + f_{e2}\hat{\boldsymbol{\sigma}}^{x}_{e2} + f_{\mu}\hat{\boldsymbol{\sigma}}^{x}_{\mu}] \\ &+ \frac{1}{4}[A_{\mu e1}\hat{\boldsymbol{\sigma}}_{\mu}\hat{\boldsymbol{\sigma}}_{e1} + A_{e1e2}\hat{\boldsymbol{\sigma}}_{e1}\hat{\boldsymbol{\sigma}}_{e2}] \qquad (5.30)\end{aligned}$$

where

$$f_{e1} = \gamma_{e1}B_1 \qquad f_{e1} > 0 \qquad (5.31)$$

$$
\begin{aligned}
f_{e2} &= \gamma_{e2} B_1 \qquad & f_{e2} &> 0 & (5.32)\\
f_{\mu} &= \gamma_{\mu} B_1 \qquad & f_{\mu} &< 0 & (5.33)
\end{aligned}
$$

In the Heisenberg representation the time-dependent spin density matrix, $\hat{\boldsymbol{\rho}}$, obeys the equation [2]

$$\frac{d(\hat{\boldsymbol{\rho}}^{I,II})}{dt} = \frac{1}{i}[\hat{H}^{I,II}, \hat{\boldsymbol{\rho}}^{I,II}] \tag{5.34}$$

and $\hat{\boldsymbol{\rho}}$ expressed in spin product operators obeys equation [2]

$$\hat{\boldsymbol{\rho}}^{\,I,II} = \frac{1}{2^3}(\mathbf{1} + \sum_{i,q} P^i_q \hat{\boldsymbol{\sigma}}^i_q + \sum_{i,j,q,q'} P^{ij}_{qq'} \hat{\boldsymbol{\sigma}}^i_q \hat{\boldsymbol{\sigma}}^j_{q'} + \sum_{i,j,l} P^{ijl}_{\mu e1e2} \hat{\boldsymbol{\sigma}}^i_{\mu} \hat{\boldsymbol{\sigma}}^j_{e1} \hat{\boldsymbol{\sigma}}^l_{e2})^{I,II} \tag{5.35}$$

In the above equation, the subscripts denote the particles (note that therefore $q \neq q' \neq q''$ for each term) and the superscripts their Cartesian spin components. The coefficients which represent the μ, e_1, e_2, and mixed polarizations are evaluated by trace operations [2, 71]:

$$(P^{ijl}_{qq'q''})^{I,II} = Tr(\hat{\boldsymbol{\rho}}^{I,II} \hat{\boldsymbol{\sigma}}^i_q \hat{\boldsymbol{\sigma}}^j_{q'} \hat{\boldsymbol{\sigma}}^l_{q''}) \tag{5.36}$$

For each state there is a 63-dimensional polarization vector P (3x3 singly, 3x9 doubly, and 27 triply indexed P-terms). Starting from the equation of motion (equation 5.34) for the spin density matrix without reaction and collision dynamics and inserting equations 5.30 and 5.35 into equation 5.34, we arrive at the following system of differential equations by using the commutation relations for Pauli spin matrices and equating terms of the same components $\hat{\boldsymbol{\sigma}}^i_q$, $\hat{\boldsymbol{\sigma}}^i_q \hat{\boldsymbol{\sigma}}^j_{q'}$, and $\hat{\boldsymbol{\sigma}}^i_q \hat{\boldsymbol{\sigma}}^j_{q'} \hat{\boldsymbol{\sigma}}^l_{q''}$ on the left- and right-hand side of equation 5.34:

$$
\begin{aligned}
\dot{P}^m_q &= \omega_q \epsilon_{zjm} P^j_q + f_q \epsilon_{xjm} P^j_q + \sum_{i,q'} \epsilon_{ijm} \frac{A_{qq'}}{2} P^{ji}_{qq'} & (5.37)\\
\dot{P}^{ml}_{qq'} &= \epsilon_{ljm} \frac{A_{qq'}}{2}(P^j_q - P^j_{q'}) + \epsilon_{zjm} \omega_q P^{jl}_{qq'} + \epsilon_{zjl} \omega_{q'} P^{mj}_{qq'}
\end{aligned}
$$

$$
\begin{aligned}
& +\epsilon_{xjm} f_q P^{jl}_{qq'} + \epsilon_{xjl} f_{q'} P^{mj}_{qq'} \\
& + \sum_i \epsilon_{ijm} \frac{A_{qq'}}{2} P^{jli}_{qq'q''} + \sum_i \epsilon_{ijk} \frac{A_{qq'}}{2} P^{mji}_{qq'q''} \qquad (5.38) \\
\dot{P}^{mln}_{\mu e1e2} = \; & \epsilon_{ljm} \frac{A_{\mu e1}}{2} (P^{jn}_{\mu e2} - P^{jn}_{e1e2}) + \epsilon_{njl} \frac{A_{e1e2}}{2} (P^{mj}_{\mu e1} - P^{mj}_{\mu e2}) \\
& + \epsilon_{zjm} \omega_\mu P^{jln}_{\mu e1e2} + \epsilon_{zjl} \omega_{e1} P^{mjn}_{\mu e1e2} + \epsilon_{zjn} \omega_{e2} P^{mlj}_{\mu e1e2} \\
& + \epsilon_{xjm} f_\mu P^{jln}_{\mu e1e2} + \epsilon_{xjl} f_{e1} P^{mjn}_{\mu e1e2} + \epsilon_{xjn} f_{e2} P^{mlj}_{\mu e1e2} \qquad (5.39)
\end{aligned}
$$

ϵ_{ijl} equals +1 for $i, j, l = x, y, z$ and for all even permutations of the indices, and equals -1 for all odd permutations, and 0 otherwise. It should be noted that the order of the q-labels on the right side has to be in accord with that of the product basis (*i.e.* $\hat{\boldsymbol{\sigma}}_\mu \otimes \hat{\boldsymbol{\sigma}}_{e1} \otimes \hat{\boldsymbol{\sigma}}_{e2}$) in order for the correct signs to be obtained (*e.g.* $P^{ij}_{e1\mu} \rightarrow P^{ji}_{\mu e1}$).

The above differential equations 5.37–5.39 can then be summarized as

$$
\dot{\boldsymbol{P}}^{I,II} = \boldsymbol{M}^{I,II} \boldsymbol{P}^{I,II} \qquad (5.40)
$$

From equations 5.37–5.39, it is easy to show that $\boldsymbol{M}$ is a sparse, antisymmetric matrix with all the diagonal elements being equal to zero.

The above equations 5.37–5.40 are only true without considering reaction and collision dynamics. Within the sudden collision model the system of coupled differential equations including reactions and collisions is written as [71]

$$
\begin{pmatrix} \dot{\boldsymbol{P}}^{I} \\ \dot{\boldsymbol{P}}^{II} \end{pmatrix} = \begin{pmatrix} [\boldsymbol{M}^{I} - (k'_c + \lambda_o)\mathbf{1}] e^{-\lambda_o t} & k_p \boldsymbol{T} e^{-\lambda_o t} \\ k'_c \boldsymbol{T} e^{-(\lambda_o + k_d)t} & [\boldsymbol{M}^{II} - (k_p + \lambda_o + k_d)\mathbf{1}] e^{-(\lambda_o + k_d)t} \end{pmatrix} \begin{pmatrix} \boldsymbol{P}^{I} \\ \boldsymbol{P}^{II} \end{pmatrix} \qquad (5.41)
$$

where the pseudo-first-order collision rate, $k'_c = k_c[R_2]$, has been introduced. The latter is an average over all reencounters. The exponential terms account for the irreversible decay of both states via muon decay with λ_o, and of state II additionally via reaction to diamagnetic products with k_d. The diagonal matrix $\boldsymbol{T}$ leads to a coupling between the two states. For a purely chemical exchange process, $\boldsymbol{T}$ would be a unit matrix. For HSE, e$_2$ polarization is lost after separation of the radical pair (from the point of view of the muonated radical). A plausible heuristic approach to account for this sets to zero all elements of $\boldsymbol{T}$ which involve e$_2$ (and corresponding mixed) spin polarization [71]:

$$\begin{aligned} T_{e_2^i,e_2^i} &= 0 && (5.42) \\ T_{\mu^i e_2^j,\mu^i e_2^j} &= 0 && (5.43) \\ T_{e_1^i e_2^j,e_1^i e_2^j} &= 0 && (5.44) \\ T_{\mu^i e_1^j e_2^k,\mu^i e_1^j e_2^k} &= 0 && (5.45) \\ T_{m,m} &= 1 \quad \text{rest of } m && (5.46) \end{aligned}$$

Calculation of the transient muon spin polarization $P_\mu^i(t)$ requires numerical diagonalization of the matrix containing $\boldsymbol{M}$ and $\boldsymbol{T}$ in equation 5.41, which is quite time-consuming. However, rf-IμSR experiments are carried out in the time integral mode where the average $\overline{P_\mu^z}(B_o) = \overline{P_\mu^{z,I}}(B_o) + \overline{P_\mu^{z,II}}(B_o)$ is observed. This is calculated via the Laplace transformation of equation 5.41 [72]. It yields:

$$\begin{pmatrix} -\lambda_o \boldsymbol{P}_{t=0}^{I} \\ -(\lambda_o + k_d)\boldsymbol{P}_{t=0}^{II} \end{pmatrix} = \boldsymbol{N} \begin{pmatrix} \overline{\boldsymbol{P}}^{I} \\ \overline{\boldsymbol{P}}^{II} \end{pmatrix} \tag{5.47}$$

where

$$\boldsymbol{N} = \begin{pmatrix} \boldsymbol{M}^{I} - (k_c' + \lambda_o)\mathbb{1} & k_p \boldsymbol{T} \\ k_c' \boldsymbol{T} & \boldsymbol{M}^{II} - (k_p + \lambda_o + k_d)\mathbb{1} \end{pmatrix} \tag{5.48}$$

Expanding the equation 5.47, we arrive at

$$\boldsymbol{N}^{-1}\begin{pmatrix} -\lambda_o P^I_{t=0}(1) \\ -\lambda_o P^I_{t=0}(2) \\ -\lambda_o P^I_{t=0}(3) \\ \vdots \\ -\lambda_o P^I_{t=0}(63) \\ -(\lambda_o+k_d)P^{II}_{t=0}(1) \\ -(\lambda_o+k_d)P^{II}_{t=0}(2) \\ -(\lambda_o+k_d)P^{II}_{t=0}(3) \\ \vdots \\ -(\lambda_o+k_d)P^{II}_{t=0}(63) \end{pmatrix} = \begin{pmatrix} \overline{P^I}(1) \\ \overline{P^I}(2) \\ \overline{P^I}(3) \\ \vdots \\ \overline{P^I}(63) \\ \overline{P^{II}}(1) \\ \overline{P^{II}}(2) \\ \overline{P^{II}}(3) \\ \vdots \\ \overline{P^{II}}(63) \end{pmatrix} \tag{5.49}$$

where the muon z-polarization of states I and II is chosen to be $\overline{P^{z,I}_\mu}(B_o) = \overline{P^I}(3)$ and $\overline{P^{z,II}_\mu}(B_o) = \overline{P^{II}}(3)$. Since for $t = 0$ only the muon z-polarization, (here taken to be the elements $\mathrm{P}^I_{t=0}(3)$ and $\mathrm{P}^{II}_{t=0}(3)$), is non-zero we obtain:

$$\begin{aligned} \overline{P^z_\mu}(B_o) &= \overline{P^I}(3) + \overline{P^{II}}(3) \\ &= -\lambda_o(N^{-1}_{3,3} + N^{-1}_{66,3})P^I_{t=0}(3) \\ &\quad -(\lambda_o + k_d)(N^{-1}_{3,66} + N^{-1}_{66,66})P^{II}_{t=0}(3). \end{aligned} \tag{5.50}$$

where $N^{-1}_{i,j}$ is a matrix element of the inverse of the total coupling matrix of equation 5.48. In dilute non-viscous paramagnetic solutions R^*_1 and R_2 spend most of their time in state I ($k_p \gg k'_c$ for pair lifetimes of the order of 10^{-11} s [70]). Therefore, $P^{II}_{t=0}(3) \sim 0$ and the contribution of state II to $\overline{P^z_\mu}$ is small, so only the first term in equation 5.50 contributes to the time-integral muon spin polarization.

Notice that the above approach is done in the rotating frame of reference with angular velocity -ω about the z axis and that the longitudinal polarization does not change when being transfered from the rotating frame to the lab frame, *i.e.*

$$\overline{P_{\mu}^{z}}(B_o)|_{rotation\ frame} = \overline{P_{\mu}^{z}}(B_o)|_{lab\ frame} \tag{5.51}$$

The treatment described in this section is exact within the limitation of the sudden collision model. Any irreversible, spin-independent chemical reaction from the isolated radical state can be included in a straightforward manner by substituting λ_o with $\lambda_o + \lambda_{chem}$ in equations 5.41 and 5.50 for the isolated radical state I.

5.5.2 Results and Discussion

By fitting the experimental rf-IμSR data to the theoretical calculation described in the last section, the parameters k_c', $k_{p,d}$, $\lambda_o + \lambda_{chem}$, J and B_1 can be determined for the radical. A FORTRAN program FCN-TWO-STATE.FOR, which is called by the program MINUIT in CERNLIB, was written for a least-squares fit of equation 5.50, with the assumption of $P_{t=0}^{II}(3) = 0$, to the experimental data shown in figures 5.14 and 5.15 for pyrogallol. The fit results are listed in table 5.6 and plotted in figure 5.20.

Heming *et al.* [71] illustrated the effects of radical pair lifetime ($\tau_p = \frac{1}{k_p + k_d}$) on the muon polarization from μLCR spectra using the two-state model and plotted muon polarization as a function of -log(τ_p) (figure 5.21). The parameters chosen are: $A_\mu/2\pi$ = 500 MHz, $A_k/2\pi$ = 100 MHz, k_c' = 10 μs^{-1}, k_d = 0, and J/2π = 10^6 MHz. The curve is compared with the results of Ivanter-Smilga [72, 73] calculations for selected values of λ_{ex} and λ_{chem} (horizontal lines.) The Ivanter-Smilga model is a one-state model and an electron spin flip rate λ_{ex} is introduced phenomenologically to account for the loss of electron spin polarization, whereas muon decay and chemical reaction are treated as in the two-state model.

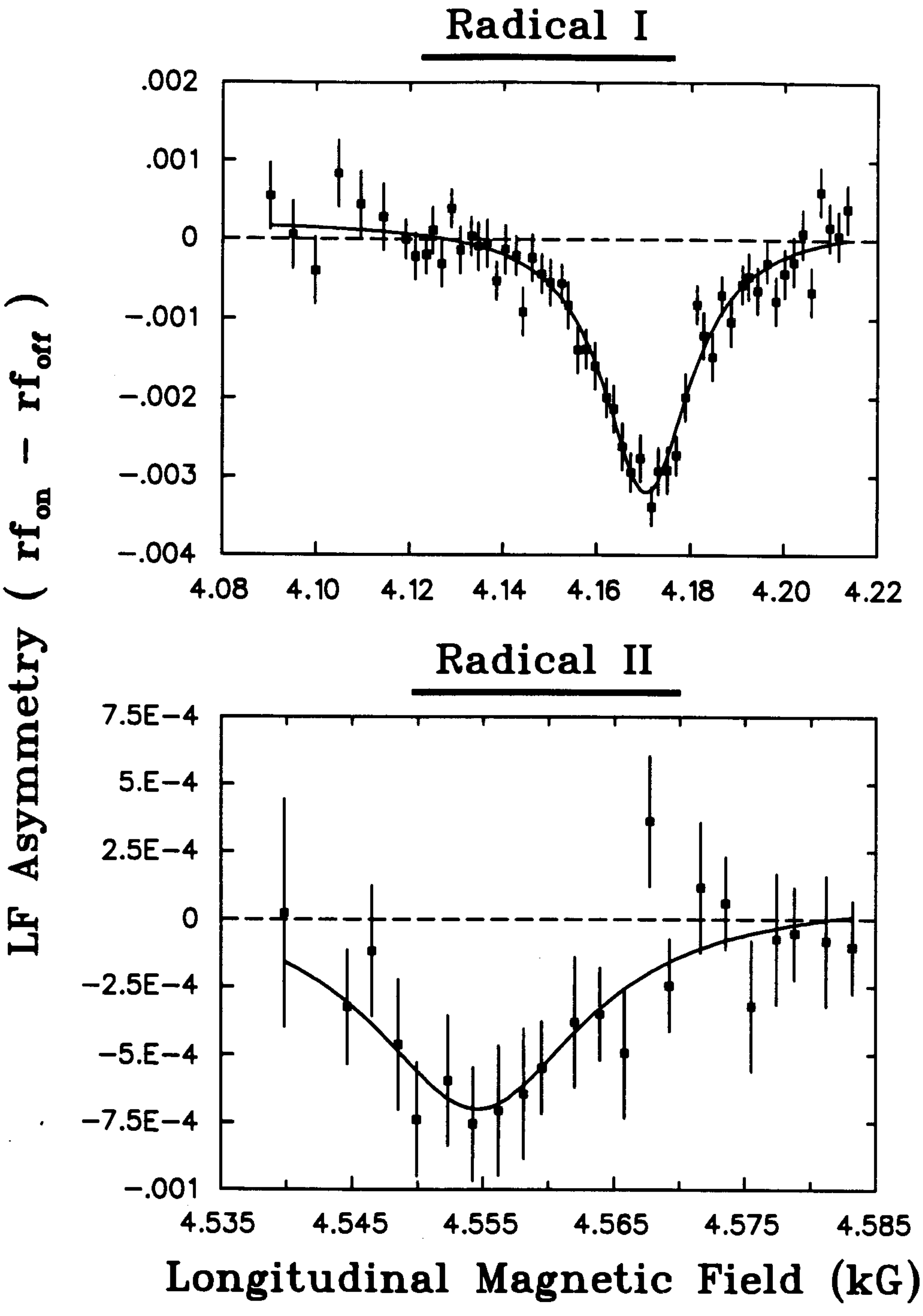

Figure 5.20: rf-IμSR spectrum of Radical I and II in 0.02 M pyrogallol. The solid curves correspond to the fits, shown in table 5.6, of the experimental values (points).

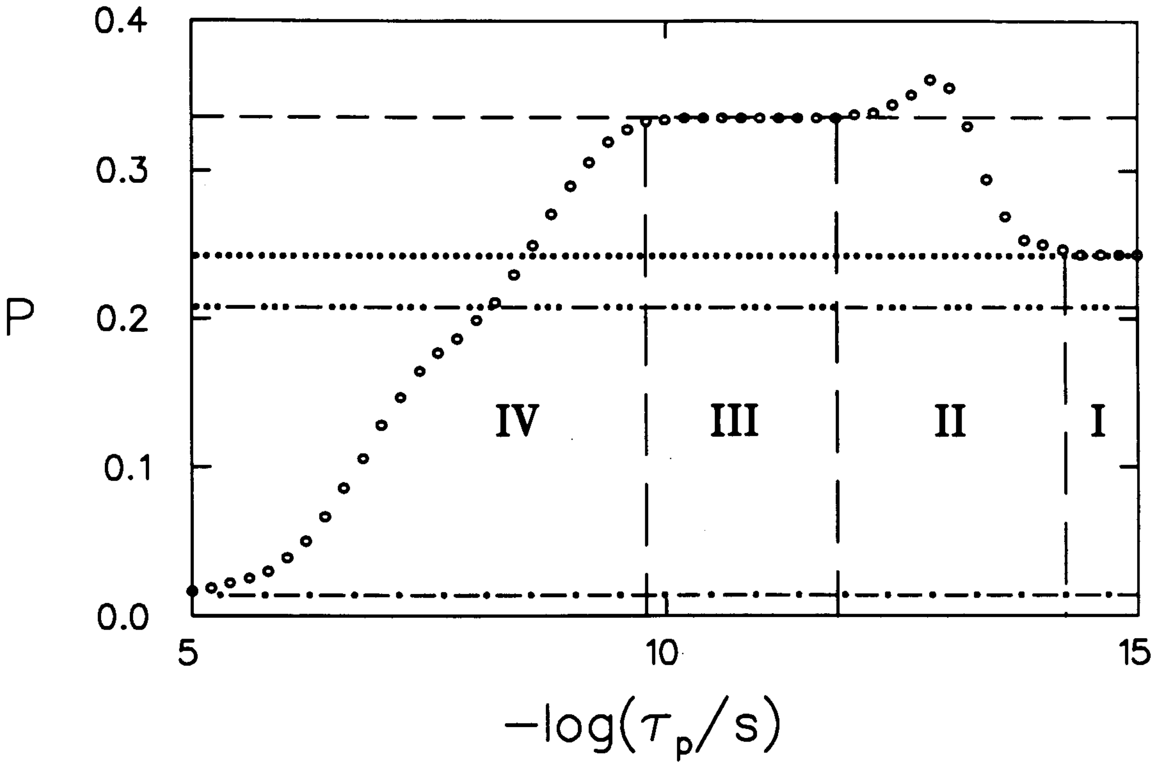

Figure 5.21: The effects of the radical pair lifetime τ_p on the μLCR signal amplitude. Parameters: $A_\mu/2\pi$ = 500 MHz, $A_k/2\pi$ = 100 MHz, k_c' = 10 μs^{-1} and $J = 10^6$ MHz. The horizontal lines are signal amplitudes calculated according to the Ivanter-Smilga formalism [72, 73] with (· · · · ·) zero relaxation; (— — —) $\lambda_{ex} = \frac{1}{4}k_c'$ (strong exchange limit), $\lambda_{chem} = 0$, (— · · · —) $\lambda_{ex} = k_c'$, $\lambda_{chem} = 0$; (— · —) $\lambda_{chem} = k_c'$ (chemical reaction). Based on a figure by Heming *et al.* [71].

Table 5.6: Fits to the rf-IμSR experimental data of Radical I and Radical II of pyrogallol in aqueous solution with the concentration 0.02 M.

	Radical I	**Radical II**
$\lambda_o + \lambda_{chem}$ (× $\mathbf{10^5}$) ($\mathbf{s^{-1}}$) [a]	0.79(5)	0.77(4)
k'_c ($\mu\mathbf{s^{-1}}$)[a]	1.0(3)	0.8(3)
k_p (× $\mathbf{10^6}$) ($\mu\mathbf{s^{-1}}$)[a]	425(30)	317(42)
k_d (× $\mathbf{10^6}$) ($\mu\mathbf{s^{-1}}$)[b]	0	0
J (× $\mathbf{10^6}$) **(MHz)**[a]	0.6(3)	0.5(3)
B_1 **(G)**[a]	1.5(4)	1.4(5)
$A_\mu/2\pi$ **(MHz)**[b]	470.89	480.87
ν_{rf} **(MHz)**[b]	174.20	174.20

---

[a] The numbers shown in brackets are statistical errors in the least significant digit.

[b] Fixed

Figure 5.21 shows four regimes. Regime I is the weak exchange limit regime, where radical pair lifetimes are short such that $J\tau_p \leq 0.1$. In this case, spin exchange relaxation effects on muon polarization are negligible, and the analytical expression given in equation 5.21 is appropriate.

In the intermediate exchange regime II ($0.1 \leq J\tau_p \leq 10$), the muon polarization changes from its intrinsic value to a plateau corresponding to $\lambda_{ex} = \frac{1}{4}k'_c$ for regime III and the spin flip rate by Ivanter-Smilga method is related to those obtained using the two-jump model by the well-known relation [70, 74]

$$\lambda_{ex} = \frac{k'_c}{4}\frac{J^2\tau_p^2}{J^2\tau_p^2 + (2\pi)^2} \tag{5.52}$$

Leaving the motional narrowing regime III, the muon polarization drops to a value corresponding to $\lambda_{chem} = k'_c$. The radical pair no longer decays in the muon lifetime. In the limit of $k_p = 0$, the dynamical process gradually changes from spin exchange to chemical reaction, *i.e.* radical pair formation.

From the fit results shown in table 5.6, it is clear that rf-μSR data from pyrogallol in aqueous solution at the concentration 0.02 M falls into regime I since the radical pair lifetime ($\tau_p = \frac{1}{k_p+k_d}$) is very short ($J\tau_p \leq 0.1$.) This is what we expected. In such a solution, few radical partners are present.

The HSE method is a great tool to separate spin exchange and spin-independent chemical reactions. The spin-independent chemical reaction rate λ_{chem} shown in table 5.6 is about the same as the rate due to the muon lifetime alone ($\frac{1}{\tau} = \lambda_o = 4.5 \times 10^5$ s^{-1}). Notice that the fit parameter $\lambda_o + \lambda_{chem}$ shown in table 5.6 agrees with λ_R shown in table 5.5 very well. Also notice that the rf magnetic field B_1 fitted from the HSE method, shown in table 5.6, agrees with that shown in table 5.5. Some parameters, like B_1 and k_c', can in principle be determined independently by other methods. By leaving B_1 and k_c' as fit variables, the sensitivity of the parameter search is less for $\lambda_o + \lambda_{chem}$, k_p, and $J/2\pi$. Also the fit results show correlation between B_1, k_c' and the other variables. As mentioned earlier, however, it is very difficult to measure B_1 from an rf-LFμSR experiment when B_1 is small (*e.g.*, less than 2 Gauss).

Chapter 6

Intramolecular Motion in Muonium-Substituted Propyl Radicals

6.1 Introduction

Regardless of the specific reaction mechanism, the irradiation of unsaturated organic compounds with muons produces muonium-substituted free radicals which can be considered to be formed by addition of muonium to an unsaturated bond. The muonium-substituted isopropyl (Mu-isopropyl) radical can be formed by addition of muonium to propene in the manner:

$$\mathrm{Mu} + \mathrm{CH_3CH{=}CH_2} \longrightarrow \mathrm{CH_3\dot{C}H{-}CH_2Mu},$$

while the muonium-substituted n-propyl (Mu-n-propyl) radical is formed by:

$$\mathrm{Mu} + \mathrm{CH_3CH{=}CH_2} \longrightarrow \mathrm{CH_3CHMu{-}\dot{C}H_2}.$$

In chemical terminology, muonium is in the 'beta (β)' position relative to the radical center. The beta proton hyperfine coupling constants (hfcc)

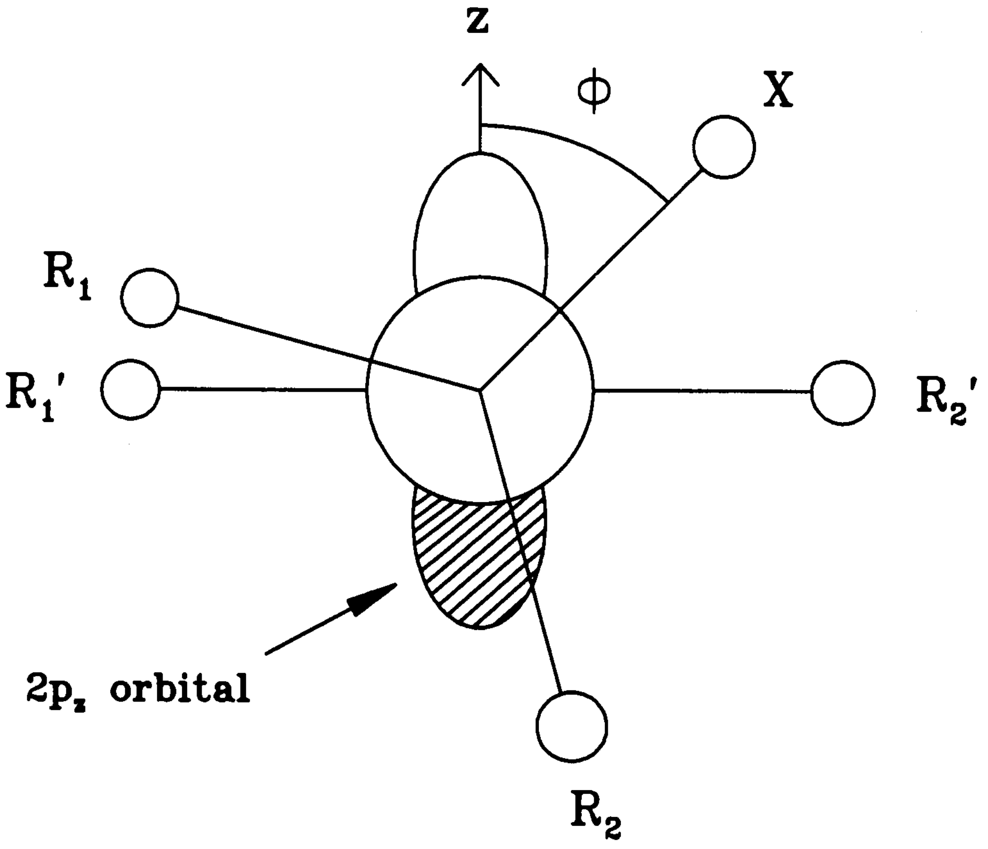

Figure 6.1: Schematic diagram showing the $2p_z$ orbital at the α-carbon and the the definition of the dihedral angle, ϕ, for alkyl radicals.

in alkyl radicals obey the empirical relation [75, 76]

$$A_\beta(\phi) = L + M\cos^2\phi \tag{6.1}$$

where L and M are constants ($M \gg L$) and ϕ is the dihedral angle between the axis of the p-orbital at C_α (which contains the unpaired electron) and the C_β–X bond (see figure 6.1). The observed coupling is a statistically weighted average over conformations with different ϕ.

It is well known from the pioneering work of Fessenden and Schuler [77] that the barrier to hindered internal rotation in the ethyl radical is significantly increased by monodeuteration ($CH_2D\dot{C}H_2$). However, this is small when compared with the barrier for the muonated species, $CH_2Mu\dot{C}H_2$. In addition, the preferred conformation of the deuterated species differs from that of the muonated species. These observations have recently been interpreted as arising predominantly from the difference in the zero-point energies of the conformations [78]. The importance of the muon can now be appreciated, since its small mass, only 1/9 that of the proton, greatly amplifies any isotopic effect.

The temperature dependence of β hfcc carries information about intramolecular motion. For a methyl group (CH_3), with a local C_{3v} symmetry the rotation of the protons in the group makes them all equivalent and there should not be any orientational preference relative to the $2p_z$ orbital of the C_α for any proton in the group. Therefore their hfcc, $A(CH_3)$, is expected to be temperature independent. If a CH_2Mu group remains rigid as it rotates about C_α–C_β axis, then the barrier experienced by H in the CH_2Mu group should be identical to that of Mu. Hence the mean β hfcc, $\bar{A}(CH_2Mu) = \frac{1}{3}(2A_p + A'_\mu)$ (where $A'_\mu = 0.314 A_\mu$, scaled by a factor γ_p/γ_μ for direct comparison between the muon and proton hfcc), is independent of temperature. The temperature dependence of Mu should be opposite to that of H in the group CH_2Mu.

The most recent experimental results and ab initio calculations indicate [79, 80, 81] that methyl is the only alkyl radical with a planar radical center and that all other simple alkyl radicals exhibit deviations from planarity in their lowest energy geometries. The structure of isopropyl has been an interesting subject for both theoretical and experimental studies [80, 81, 82, 83, 84, 85, 86]. The experimental evidence for a pyramidal configuration includes infrared [85] and electron paramagnetic resonance (EPR) [86] spectral data. Infrared data were used to conclude that the vibrational frequency of the out-of-plane bending mode of the isopropyl radical was 369 cm^{-1}, in agreement with the value of 380 ± 12 cm^{-1} deduced from the results of EPR but in slight disagreement with the value of 345 cm^{-1} calculated by ab initio calculation [83]. Independent calculations [81, 83, 84] confirmed the pyramidal nature of the isopropyl radical. The calculated out-of-plane bending angle δ, was defined as in figure 6.2(a), varies from 19.8^o to 23.1^o [81, 83, 84]. The barrier of the hindered rotation of a single methyl group found by Pacansky *et al.* [81] is 3.35 kJ/mol, and the potential function is 3-fold. Pacansky *et al.* also studied the barriers of the hindering rotation of two methyl groups, rotating both in-phase and out-of-phase. In-phase rotation consists of two methyl groups rotating in the same direction, while out-of-phase rotation is two methyl groups rotating in opposite directions as one faces each methyl group, as shown in figures 6.2(b) and (c). Simultaneous in-phase internal rotation of both methyl groups calculated by Pacansky *et al.* involves a barrier of 4.4 kJ/mol, and the potential function is also 3-fold. The out-of-phase rotational potential function was found to be more complex. It was found that the torsional modes of the methyl group are coupled to the inversion mode. The energy path has two barriers: the first is at 4.5 kJ/mol while the second barrier is much lower at 1.3 kJ/mol. The former for the most part is a result of the steric interaction while the latter is the result of coupled internal rotation-inversion [81]. The in-phase internal rotation barrier calculated by Claxton *et al.* [78] is much lower, 1.7 kJ/mol, and the potential function is 6-fold. The out-of-phase rotation potential function was found to be quite different from that found by Pacansky *et al.*, but it also has two barriers. The first barrier is quite similar to that found by Pacansky *et al.* ≈ 4.0 kJ/mol, while the second one is much less ≈ 0.15 kJ/mol. In view of the interest in both the isotope effect and the internal dynamics of the Mu-isopropyl radical, the hfcc of the muon and proton were determined over a wide range of temperature in this work.

The n-propyl radical, $CH_3CH_2\dot{C}H_2$, is interesting, since the methyl group apparently prefers to lie in the plane of the $-\dot{C}H_2$ group, like the deuteron in $CDH_2\dot{C}H_2$, which has led to the conclusion that C–C hyperconjugation is less important than C–H hyperconjugation [87]. This is contrary to the ab initio calculation made by Claxton *et al.* [82], where the Unrestricted Hartree-Fock (UHF) method has been used to show that the most stable conformation is when the methyl group is in a plane perpendicular to the plane of the methylene group. This calculation suggests that $C-CH_3$ hyperconjugation is at least as significant as C–H hyperconjugation.

6.2 Muonium-substituted isopropyl

6.2.1 Experimental

Measurements of muon and proton hfcc in Mu-isopropyl were made over a temperature range of 93 K to 303 K covering the liquid and gas phases of propene. The melting point of propene is 87.9 K and the boiling point 225.8 K. The gas-phase targets were prepared by Dr. Fleming's μSR group of the University of British Columbia. The sample cells were cylindrical in shape, with a stainless steel or aluminium body and a Mylar window at one end. The cell length varied from 5 to 10 cm and window thickness from 0.1 to 0.5 mm. A long cell accommodates the extended stopping distribution of muons in low pressure gas, but a short cell has

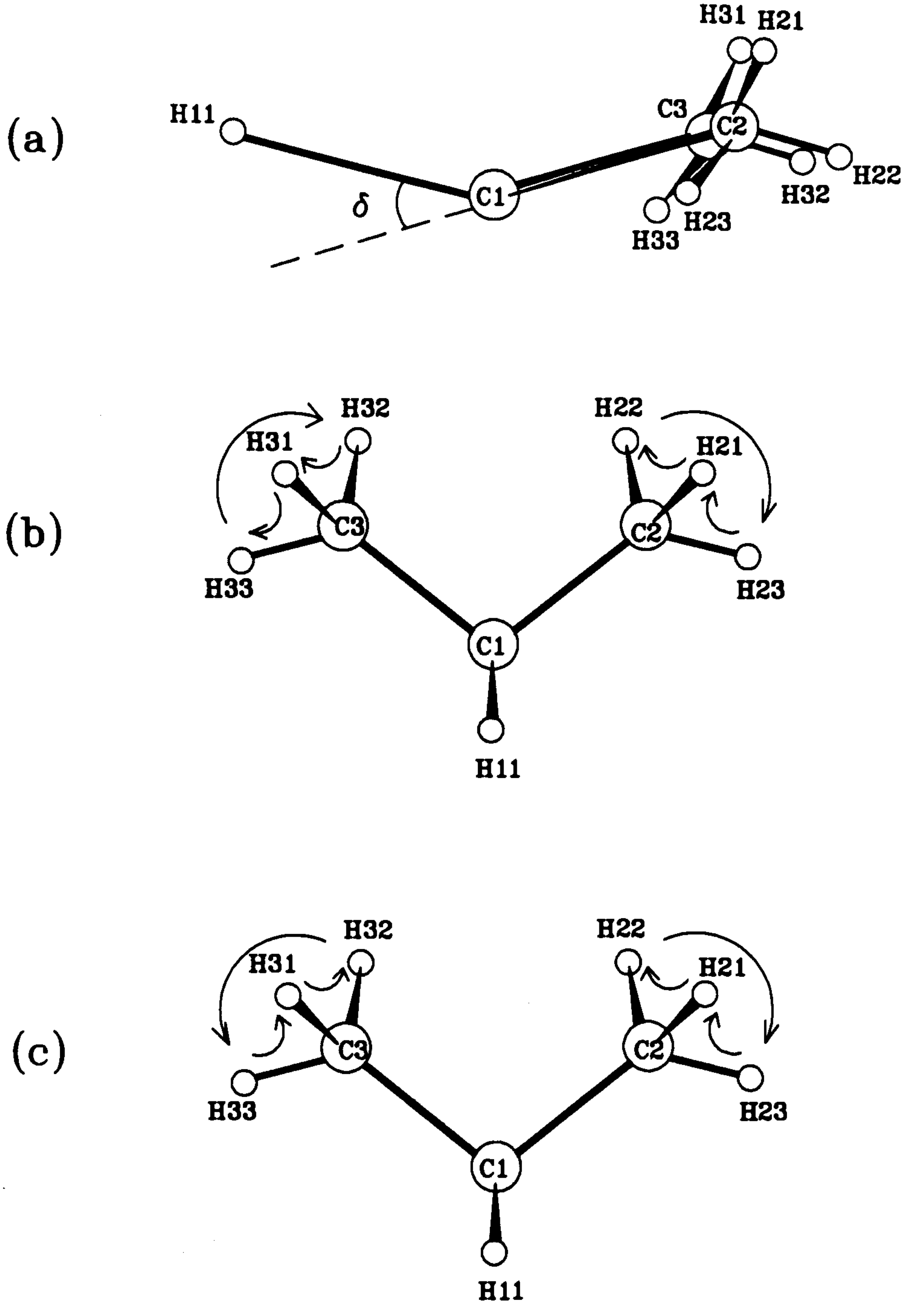

Figure 6.2: (a): δ, the out-of-plane bending angle of isopropyl radical center, is defined as the angle between the C1H11 bond and the C3C1C2 plane. (b): In-phase rotation of the two methyl groups of isopropyl. (c): Out-of-phase rotation of the two methyl groups of isopropyl.

the advantage of good field homogeneity. A thick window is necessary for high pressure samples and can act as a degrader to shorten the muon stopping distance; the disadvantages include muon stops in the window and an increase in range straggling and scattering.

The liquid samples were degassed by the freeze-pump-thaw method. The temperature was controlled with either the helium-cooled cryostat system, for low temperatures, or the circulator, for higher temperatures.

6.2.2 Results

Muon hfccs were determined from TF-μSR experiments. As was stated in chapter one, in high magnetic fields muonium-substituted radicals give rise to two precession frequencies

$$\begin{aligned} \omega^- &= \mid \omega_{12} \mid \\ &= \mid \omega_{mid} - \frac{1}{2}A_\mu \mid \qquad (6.2) \\ \omega^+ &= \mid \omega_{43} \mid \\ &= \mid \omega_{mid} + \frac{1}{2}A_\mu \mid \qquad (6.3) \end{aligned}$$

where

$$\omega_{mid} = \frac{1}{2}[\sqrt{A_\mu^2 + (\omega_e + \omega_\mu)^2} - \omega_e + \omega_\mu] \qquad (6.4)$$

A_μ is simply given by the sum ($\omega_{mid} < 1/2A_\mu$) or difference ($\omega_{mid} > 1/2A_\mu$) of ω^+ and ω^-. In the case when one of the radical signals (whose frequency is $\omega^+/2\pi$) is too weak to be observed, A_μ can be determined from the other radical frequency ($\omega^-/2\pi$) and the diamagnetic frequency (ν_D) with equation 6.2. An example of a Fourier transformed TF-μSR spectrum is given in figure 1.4.

TF-μSR measurements with the propene gas target were made at two different pressures, 5 and 9 atm. The muon momentum was adjusted ac-

Table 6.1: Muon hfccs of Mu-isopropyl and Mu-n-propyl at 303.2 K.

Mu-isopropyl			
Pressure (atm)	ν_D **(MHz)**[a]	$\omega^-/2\pi$ **(MHz)**[a]	$A_\mu/2\pi$ **(MHz)**[a]
5	116.951(3)	33.74(5)	303.28(9)
9	116.984(4)	33.70(4)	303.26(8)
Mu-n-propyl			
5	116.951(3)	49.64(12)	335.5(2)
9	116.984(4)	49.60(13)	335.4(3)

---

[a] The numbers shown in brackets are statistical errors in the least significant digit.

cording to gas pressure and window thickness, typically $P_\mu = 27.8$ MeV/c with a 5% momentum bite. Table 6.1 collects muon hfccs measured from the propene gas target at 303.2 K. The measurements show no significant variation of A_μ with pressure. This agrees with the measurements made by Dr. Fleming's μSR group and Dr. Percival's SFUMU group on an ethene target [88]. Muon hfccs at different temperatures are listed in table 6.2, where A'_μ is the reduced muon coupling ($A'_\mu = 0.31413A_\mu$) which takes into account the larger magnetic moment of the muon.

Proton hfccs (A_p) were determined from the μLCR field (see equation 1.30):

$$B_o = \frac{1}{2}\left[\frac{A_\mu - A_k}{\gamma_\mu - \gamma_k} - \frac{A_\mu + A_k}{\gamma_e}\right], \qquad (6.5)$$

where the A_i and γ_i represent hfccs and gyromagnetic ratios, respectively, for the muon, other nucleus or the electron, as appropriate. An example of a μLCR spectrum from the present study is given in figure 1.8. The lower field resonance is due to CH_3 (β) protons, the middle field resonance

Table 6.2: Muon hfccs of Mu-isopropyl determined from TF-μSR spectra.

Temp. (K)	ν_D (MHz)[a]	$\omega^-/2\pi$ (MHz)[a]	$\omega^+/2\pi$ (MHz)[a]	$A_\mu/2\pi$ (MHz)[a]	$A'_\mu/2\pi$ (MHz)[a]
95.4	77.888(17)	117.08(5)	—	394.75(8)	124.00
103.7	77.936(16)	113.17(4)	—	386.83(8)	121.52
113.5	77.937(15)	109.75(4)	—	379.84(8)	119.32
121.4	—	110.10(4)	268.03(6)	378.13(7)	118.78
123.8	129.82(4)	55.04(4)	—	372.29(10)	116.95
134.0	129.88(4)	51.69(7)	—	365.62(10)	114.85
151.1	—	99.18(6)	259.51(5)	358.69(8)	112.68
164.5	221.13(7)	47.55(5)	—	348.48(12)	109.47
185.6	—	105.20(5)	239.45(7)	344.64(9)	108.26
199.3	208.15(7)	42.06(8)	—	333.5(2)	104.75
221.1	—	96.80(8)	230.55(10)	327.35(13)	102.83
249.0	195.542(12)	37.28(7)	—	317.76(14)	99.82
263.2	—	64.39(9)	249.26(14)	313.65(16)	98.53
284.2	116.844(4)	35.89(4)	—	307.41(8)	96.57
293.5	116.954(4)	34.74(5)	—	305.30(10)	95.90
303.5	116.951(3)	33.74(5)	—	303.28(9)	95.27

---

[a] The numbers shown in brackets are statistical errors in the least significant digit.

Table 6.3: μLCR fields and CH_2Mu proton hfccs of Mu-isopropyl.

CH_2Mu			
Temp. (K)	**B_o (kG)^a**	**$A_p/2\pi$ (MHz)^a**	**$\bar{A}/2\pi$ (MHz)**
95.4	18.513(3)	49.08(9)	74.05
103.7	17.977(6)	51.13(13)	74.59
121.4	17.4614(19)	52.05(7)	74.29
134.0	16.732(4)	53.14(12)	73.71
151.1	16.273(3)	54.77(9)	74.07
164.5	15.692(7)	55.39(18)	73.42
185.6	15.419(3)	56.63(10)	73.84
199.3	14.752(3)	57.9(2)	73.52
221.1	14.4126(10)	58.11(13)	73.02
249.0	13.753(7)	60.79(19)	73.80
293.5	13.0599(7)	61.27(10)	72.81
303.5	12.9471(13)	61.35(10)	72.66

---

[a] **The numbers shown in brackets are statistical errors in the least significant digit.**

the CH_2Mu (β) protons, and the upper resonance the CH (α) proton. Proton hfccs at different temperatures are collected in tables 6.3—5. Radical formation places muonium in the methyl group, so the muon hfcc should be compared with the β proton value. The mean coupling ($\bar{A}$) for the methyl group is also included in table 6.3.

For comparison, figure 6.3 displays the proton hfccs both for Mu-substituted isopropyl radical (this work) and the unsubstituted isopropyl radical as measured by EPR [86]. In the figure, data points represented by solid symbols are from the present work. Open symbols represent EPR data.

Table 6.4: μLCR fields and CH_3 proton hfccs of Mu-isopropyl.

CH_3		
Temp. (K)	B_o **(kG)**[a]	$A_p/2\pi$ **(MHz)**
95.4	17.499(3)	67.87(10)
103.7	17.033(4)	68.64(12)
121.4	16.5756(14)	68.47(7)
134.0	15.931(4)	67.98(12)
151.1	15.529(2)	68.54(9)
164.5	15.011(3)	68.01(13)
185.6	14.7646(14)	68.76(9)
199.3	14.166(2)	68.7(2)
221.1	13.8762(10)	68.05(13)
249.0	13.282(3)	69.52(15)
293.5	12.6873(6)	68.17(10)
303.5	12.5866(11)	68.03(9)

---

[a] The numbers shown in brackets are statistical errors in the least significant digit.

Table 6.5: μLCR fields and H proton hfccs of Mu-isopropyl.

H		
Temp. (K)	B_o **(kG)** [a]	$A_p/2\pi$ **(MHz)**[a]
95.4	24.401(6)	-60.03(14)
103.7	24.0834(18)	-62.02(9)
121.4	23.586(2)	-61.45(8)
134.0	22.984(8)	-62.72(18)
151.1	22.545(3)	-61.46(10)
164.5	—	—
185.6	21.579(3)	-57.52(10)
199.3	21.213(3)	-61.9(2)
221.1	20.880(4)	-61.73(15)
249.0	20.326(7)	-61.00(19)
293.5	19.7315(10)	-62.36(10)
303.5	—	—

---

[a] The numbers shown in brackets are statistical errors in the least significant digit.

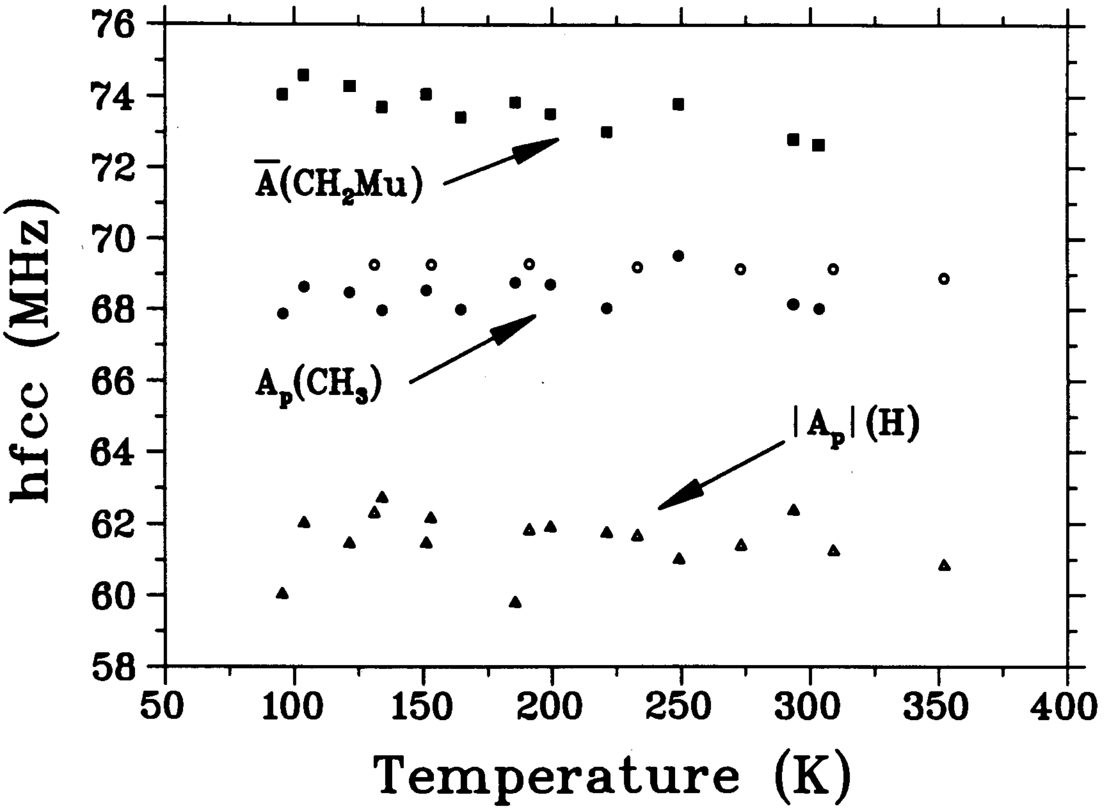

Figure 6.3: Temperature dependence of proton hfccs in both Mu-substituted isopropyl and unsubstituted isopropyl, where solid symbols are from the present work and open symbols represent EPR data [86].

6.2.3 Theoretical treatment

The hyperfine interaction originates from the unpaired electron spin density at the nuclear site under observation. For simple alkyl radicals the major component of the unpaired electron spin density derives from the 2p$_z$ orbital centered at the α-carbon nucleus [76]. As shown in figure 6.1, let ϕ be the dihedral angle between the axis of the 2p$_z$ orbital at C$_\alpha$ and the C$_\beta$–X axis for a particular substituent X and defined as

$$\phi = \theta + \theta_o, \tag{6.6}$$

where θ_o specifies the equilibrium conformation of the radical by the value of ϕ at the minimum of the potential barrier to internal rotation about the C$_\beta$–C$_\alpha$ axis. Assuming that the internal rotation of the C$_\beta$R$_1$R$_2$X group about the C$_\beta$–C$_\alpha$ internuclear axis can be treated as independent from the vibrational motion, molecular rotation, and solvent interaction, the torsional Hamiltonian H(θ) is then simply given by

$$H(\theta) = -\frac{\hbar^2}{2I}\frac{d^2}{d\theta^2} + V(\theta), \tag{6.7}$$

where $V(\theta)$ is the rotational potential and I, the reduced moment of inertia, is defined as

$$I = \frac{I_1 I_2}{(I_1 + I_2)} \tag{6.8}$$

in term of the moments of inertia I_1 and I_2 for the two groups, C$_\alpha$R$'_1$R$'_2$ and C$_\beta$R$_1$R$_2$X, rotating about the C$_\beta$–C$_\alpha$ axis and evaluated at the equilibrium molecular conformation.

The conventional model for calculating the temperature dependence of the β-coupling constant assumes that transitions between the torsional levels are rapid on the time scale of the μSR experiment so that the observed β-hfcc is the average of the quantum mechanical expectation values of $A_\beta(T)$ for all torsional states weighted by their populations. Assuming Boltzmann statistics

$$A_\beta(T) = \frac{\Sigma_j < A_\beta(\phi) >_j \exp(-E_j/kT)}{\Sigma_i \exp(-E_i/kT)} \tag{6.9}$$

where E$_j$ are the torsional energies and $< A_\beta(\phi) >_j$ is the expectation value of the β-hfcc for the molecule in the jth torsional state. Measurements of the hfcc at different temperatures can be used to derive information on radical conformation and intramolecular potentials.

In general, we can write the dependence of potential, $V(\theta)$, on θ as a Fourier series

$$\begin{aligned} V(\theta) &= \frac{V_1}{2}(1-\cos\theta) + \frac{V_2}{2}(1-\cos 2\theta) \\ &+ \frac{V_3}{2}(1-\cos 3\theta) + \frac{V_4}{2}(1-\cos 4\theta) + \cdots \end{aligned} \tag{6.10}$$

For Mu-isopropyl X = Mu, $R_1=R_2$ = H, R_1' = CH_3, and R_2' = H in figure 6.1. From considerations of symmetry, rotation of an unsubstituted methyl group should generate a three-fold (C_{3v}) or six-fold (C_{6v}) potential. A Mu substituted methyl group breaks this symmetry. Therefore it is reasonable to predict the potential barrier as a truncated Fourier series for $V(\theta)$, equation 6.10, with only the two-fold term, three-fold term, and six-fold term being retained. That is

$$\begin{aligned} V(\theta) &= \frac{V_2}{2}(1-\cos 2\theta) + \frac{V_3}{2}(1-\cos 3\theta) \\ &+ \frac{V_6}{2}(1-\cos 6\theta). \end{aligned} \tag{6.11}$$

The Hamiltonian defined by equation 6.7 with the potential equation 6.11 can be employed to calculate the torsional energy levels and the corresponding eigenfunctions. The hfcc can then be calculated from equations 6.9 and 6.1.

The angular dependence of the β-proton-electron hyperfine interaction and β-deuteron-electron interaction are often represented by equation 6.1. Such a relationship is also suitable for β-muon-electron hyperfine interactions [89]. For occupancy of the jth torsional level the expectation value $A_\beta(\phi)$ can be evaluated from

$$< A_\beta(\phi) >_j = L + M < j \mid \cos^2\phi \mid j > . \tag{6.12}$$

Adopting the wavefunction constructed from a linear combination of free rotor states

$$\begin{aligned} \Psi_j &= \frac{1}{\sqrt{2\pi}} \sum_n C_n^j \exp(in\theta) \\ & n = 0,\ \pm 1,\ \pm 2,\ \cdots\ \pm n_{max} \\ & j = 1,\ 2,\ \cdots\ 2n_{max} + 1 \end{aligned} \tag{6.13}$$

the expectation value $\cos^2\phi$, in equation 6.12 can be rewritten as

$$\begin{aligned} < j \mid \cos^2\phi \mid j > &= \frac{1}{2} \sum_n C_n^j [C_n^j + \frac{1}{2} C_{n+2}^j (\cos 2\theta_o - \sin 2\theta_o) \\ &+ \frac{1}{2} C_{n-2}^j (\cos 2\theta_o + \sin 2\theta_o)] \end{aligned} \tag{6.14}$$

The coefficients C_n^j are obtained by solution of the secular problem using the Hamiltonian given by equation 6.7 and 6.11. The secular determinant then has the elements defined by

$$\begin{aligned} H_{nn} &= \frac{\hbar^2}{2I} n^2 + \frac{1}{2} V_2 + \frac{1}{2} V_3 + \frac{1}{2} V_6 \\ H_{nk} &= -\frac{V_2}{4} \qquad for\ \ k = n \pm 2 \\ H_{nk} &= -\frac{V_3}{4} \qquad for\ \ k = n \pm 3 \\ H_{nk} &= -\frac{V_6}{4} \qquad for\ \ k = n \pm 6 \\ H_{nk} &= 0 \qquad\quad for\ \ k \neq n \pm 2,\ 3,\ 6 \end{aligned} \tag{6.15}$$

By fitting the experimental temperature dependence of the β-coupling constants to the theoretical model using the quantum-mechanical averaging of the β-coupling constants described previously, the barrier hindering internal rotation can be determined. A FORTRAN program FCN.FOR, which is called by the program MINUIT in CERNLIB, was written for a multi-parameter least-squares minimization fit of equation 6.9 to the experimental data. The minimization value is given by

$$F = \sum_{i=1}^{n}[(\frac{A'^{i}_{\mu}(exp.) - A'^{i}_{\mu}(calc.)}{\Delta A'^{i}_{\mu}(exp.)})^2 + (\frac{A^{i}_{p}(exp.) - A^{i}_{p}(calc.)}{\Delta A^{i}_{p}(exp.)})^2] \qquad (6.16)$$

where A$'^{i}_{\mu}$(exp.) is the value of the reduced muon hfcc determined from experiment at the ith temperature, A$'^{i}_{\mu}$(calc.) is the calculated value of the theoretical expression of equation 6.9, $\Delta A'^{i}_{\mu}$(exp.) is the experimental uncertainty, and n is the number of temperatures measured. A$^{i}_{p}$(exp.), A$^{i}_{p}$(calc.), and ΔA^{i}_{p}(exp.) correspond to A$'^{i}_{\mu}$(exp.), A$'^{i}_{\mu}$(calc.), and $\Delta A'^{i}_{\mu}$(exp.), respectively, with the subscript μ denoting muon and p denoting proton. The eigenstates and eigenfunctions of the secular determinant, equation 6.15, are computed by subroutine DEVCSF in the IMSL math library.

The fits were performed using a basis of 31 free rotor states ($n_{\max}$ =15 in equation 6.13) after checking the convergence of the calculations for different numbers of wavefunctions. Five different fits were carried out. In the first one, the internal rotation barriers V_2 and V_3, as well as L, M, and θ_o(H), were allowed to vary simultaneously in the calculations. In the second fit, only the barrier V_2 was assumed to exist. In the third to fifth fits different values of L and M were used for Mu and H, and θ_o(H) was fixed separately for each fit. In all cases, V_6 was fixed at zero since the quality of the fit was insensitive to wide variations in V_6. Fits containing

Table 6.6: Representative fits to the temperature dependence of hfcc of the CH_2Mu group in Mu-isopropyl.

	I	II	III	IV	V	Unit
V_2	3.48	3.45	3.46	2.25	1.75	kJ/mol
V_3	0.5	—	—	—	—	kJ/mol
M(Mu)	153	154	154	175	202	MHz
L(Mu)	-5	-6	-6	-10	-21	MHz
θ_o**(Mu)**	0^a	0^a	0^a	0^a	0^a	^{o}
M(H)	^{b}	^{b}	149	154	149	MHz
L(H)	^{c}	^{c}	0	0	0	MHz
θ_o**(H)**	123	123	120^a	110^a	105^a	^{o}
$F/F_I{}^d$	1	1	1.1	4.1	5.2	—

---

[a] fixed.

[b] same as M(Mu).

[c] same as L(Mu).

[d] F_I is the minimization value F of the fit I

V_6 as a free parameter failed to converge since $\partial^2(\sum_i \mathrm{error}_i)/\partial V_6^2 \approx 0$. The fit results are listed in tables 6.6—6.8 and plotted in figures 6.4 and 6.5. The good agreement between calculated and experimental hfcc shows the above treatment is applicable.

In these fits, the moment of inertia was obtained from the structure calculated by Pacansky and Yoshimine (restricted open-shell Hartree-Fock method) [81]. For the CH_3CH group $I_1 = 6.85\text{x}10^{-46}$ kg·m^2 and for the CH_2Mu group $I_2 = 3.62\text{x}10^{-47}$ kg·m^2. From equation 6.8, the reduced moment of inertia is $I = 3.44\text{x}10^{-47}$ kg·m^2. Various fits were carried out with I as a variable parameter to include any possible change in geometry. These fits showed that the hfcc and other parameters are

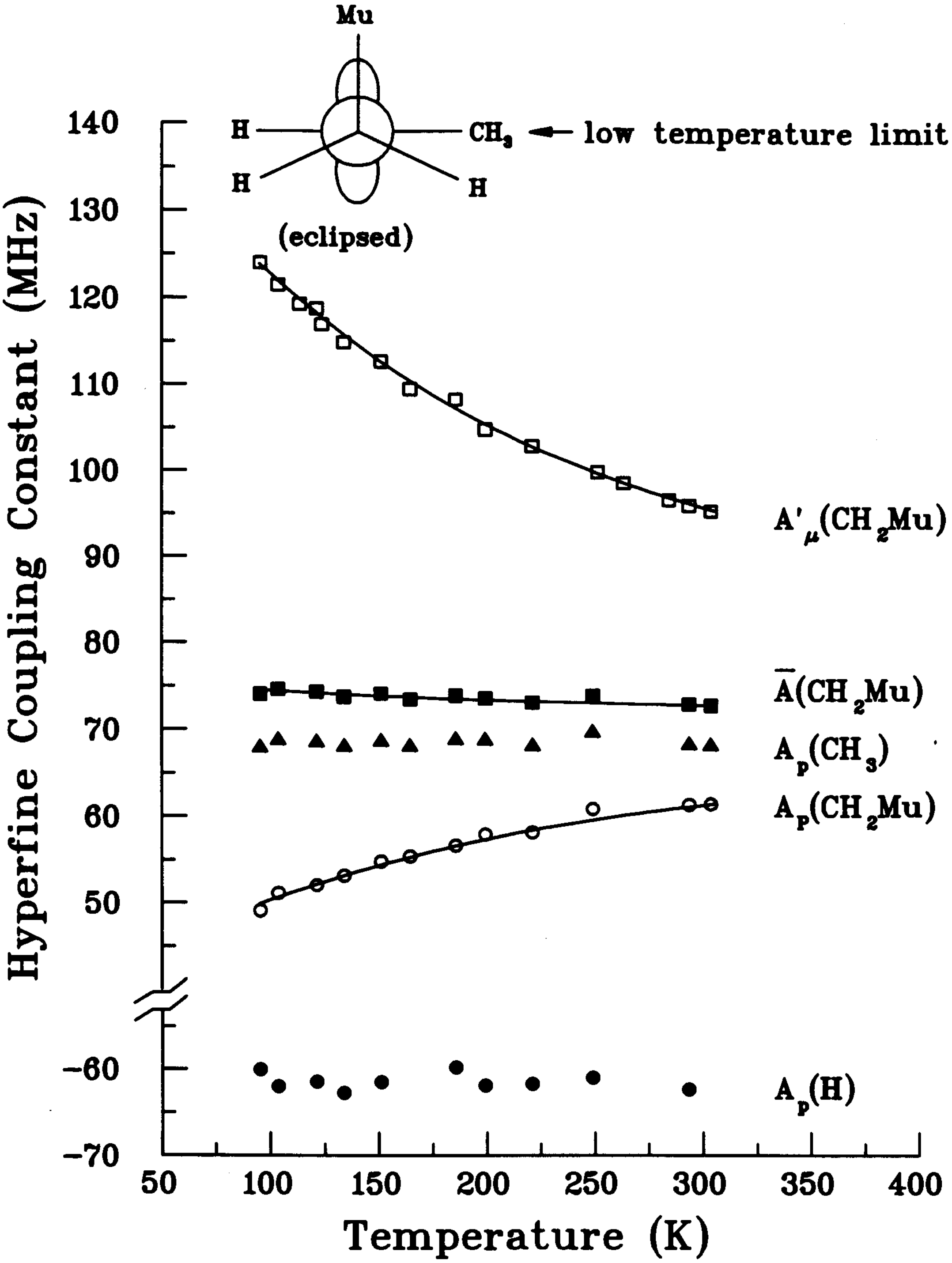

Figure 6.4: Temperature dependence of the muon and proton hyperfine coupling constants in the $CH_3\dot{C}HCH_2Mu$ radical. The solid lines correspond to fit I of the experimental values (points).

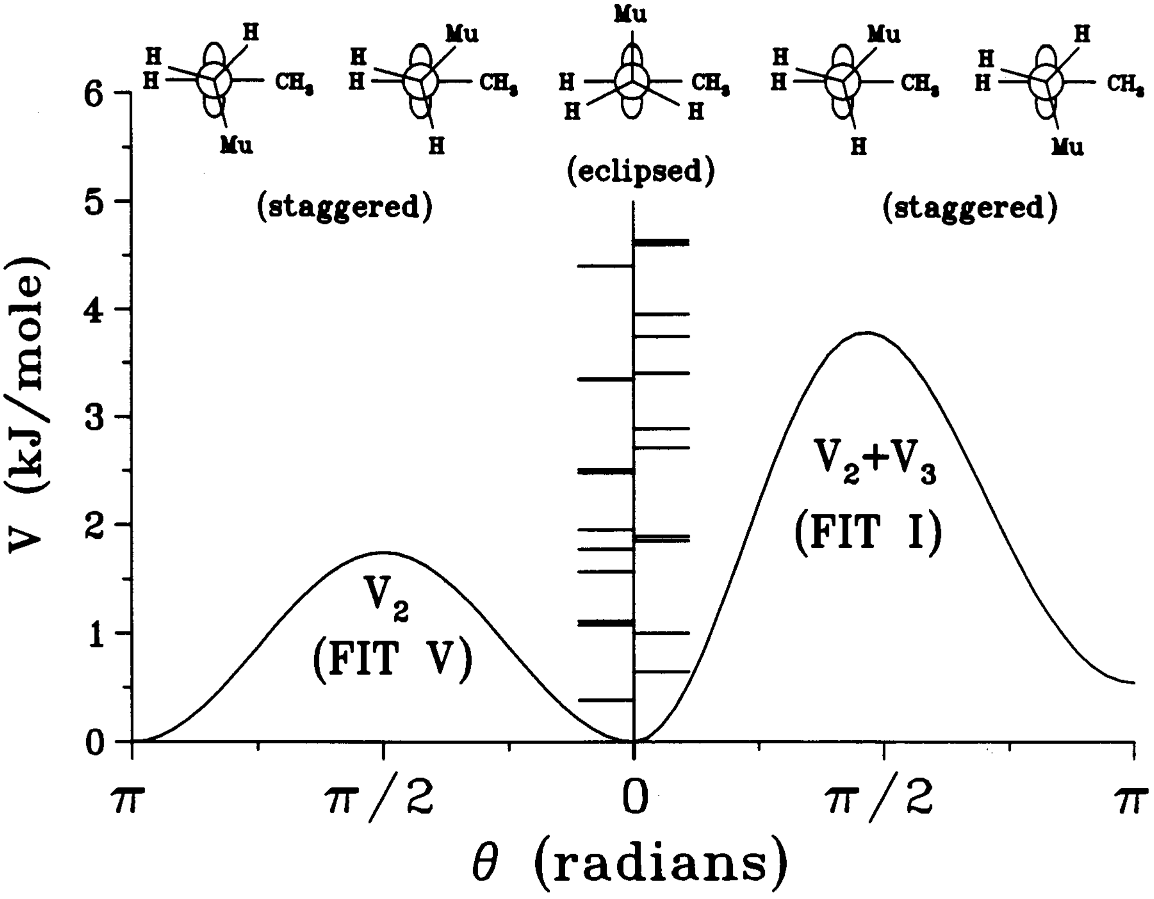

Figure 6.5: Comparison of V_2 (fit V) and $V_2 + V_3$ (fit I) potentials used to fit the temperature dependence of the hfcc of $CH_3\dot{C}HCH_2Mu$. The horizontal lines denote the calculated torsional energy levels.

Table 6.7: Comparison of experimental data for A'_μ and the calculated values from fit I and fit III.

Temp. (K)	**$A'_\mu/2\pi$(expt.) (MHz)**	**$A'_\mu/2\pi$(fit I) (MHz)**	**$A'_\mu/2\pi$(fit III) (MHz)**
95.4	124.0	123.8	123.8
103.7	121.5	122.0	122.0
121.4	118.8	118.3	118.3
134.0	114.9	115.8	115.8
151.1	112.7	112.7	112.7
164.5	109.5	110.4	110.4
185.6	108.3	107.2	107.2
199.3	104.7	105.4	105.4
221.1	102.8	102.8	102.7
249.0	99.8	99.9	99.8
293.5	95.9	96.1	96.1
303.5	95.3	95.4	95.4

Table 6.8: Comparison of experimental data for $A_p(\mathrm{CH_2Mu})$ and the calculated values from fit I and fit III.

Temp. (K)	**$A_p/2\pi$(expt.) (MHz)**	**$A_p/2\pi$(fit I) (MHz)**	**$A_p/2\pi$(fit III) (MHz)**
95.4	49.1	49.9	48.8
103.7	51.1	50.6	49.7
121.4	52.1	52.1	51.5
134.0	53.1	53.1	52.7
151.1	54.8	54.4	54.2
164.5	55.4	55.3	55.3
185.6	56.6	56.6	56.8
199.3	58.0	57.3	57.7
221.1	58.2	58.4	59.0
249.0	60.8	59.5	60.4
293.5	61.3	61.0	62.2
303.5	61.4	61.3	62.5

not sensitive to I, as found by others [44, 89, 90].

6.2.4 Discussion

As mentioned in the introduction of this chapter, for the unsubstituted methyl group with a C_{3v} symmetry the rotation of the protons in the group makes them all equivalent and there should not be any orientational preference relative to the $2p_z$ orbital of the C_α for any proton in the group. Therefore their hfcc should be essentially temperature independent and give the free rotation value of $L + \frac{1}{2} M$ at all temperatures [91] (since $< \cos^2\theta > = \frac{1}{2}$ in the 'free rotation' limit). However, with the Mu-substituted methyl group of Mu-isopropyl, the muon hfcc monotonically decreases with increasing temperature as shown in figure 6.4 and table 6.2. This suggests that the C–Mu bond eclipses the $2p_z$ orbital of the C_α in the preferred conformation at low temperature and becomes staggered at the high temperature, as shown in figures 6.4 and 6.5. This difference between an unsubstituted and Mu-substituted methyl group could arise from enhanced hyperconjugation or it could be a steric effect. Both relate to a longer C–Mu bond than the corresponding C–H bond [7, 23, 78, 92, 93]. The lighter isotope (Mu) results in a higher zero-point vibrational energy in an anharmonic potential and thus a longer bond, as shown in figure 6.6 [7]. Roduner [7] used a diatomic Morse potential to calculate average bond lengths of 1.141 Å for C–H and 1.197 Å for C–Mu, an increase of 4.9%. This causes a bound Mu to be effectively larger than a bound H. Because of the increased zero-point vibration energy for Mu, the C-Mu bond is weaker than C-H bond. This facilitates hyperconjugative electron release from the C–Mu bond. From figure 6.6, the corresponding energy level of Mu lies less deep, and therefore closer to the 2p level of the neighboring carbon, as shown in figure 6.7. Thus the resulting coupling, the $\sigma - \pi$ hyperconjugative overlap, is greater for Mu than for H. This involves electron release from the C–Mu bond, as indicated qualitatively in figure 6.7. The fact that the muon hfcc decreases with increasing temperature can also be explained by a steric effect. The interactions between the methyl protons or muons and the atoms of the radical plane are ascribed to steric interactions. That the C–Mu is effectively bulkier than C–H makes Mu avoid the radical plane because of steric interactions, resulting in a greater weighting of the limiting bond-eclipsed conformer ($\phi = 0^o$) over bond-staggered conformations ($\phi > 0^o$). The leading constant L in equation 6.1 represents a contribution to the hf interaction arising from a spin polarization mechanism and the second constant M is due to hyperconjugation. M is usually much larger than L, and typically takes the value 140 MHz for proton coupling in alkyl radicals.

As was described earlier, the unsubstituted methyl group should give the free rotation value of $L + \frac{1}{2} M$ at all temperatures [91], as should $\bar{A}(CH_2Mu)$ in the absence of any isotope effect on L and M. There are two facts that confirm the existence of the so called 'residual isotope effect'. (The residual isotope effect represents the hfcc difference between isotopically substituted groups caused by other than the preferred conformation.) First, from figure 6.3 it is clear that $\bar{A}(CH_2Mu)$ for Mu-isopropyl are significantly greater than the methyl proton hfcc, $A(CH_3)$, in unsubstituted propyl $(CH_3)_2\dot{C}H$ [86] for the whole temperature range. Second, extrapolation of fit V to high temperature limiting values gives 81 MHz for A'_μ, which is larger than 74 MHz for $A_p(CH_2Mu)$ in Mu-isopropyl radical. This is consistent with the hyperconjugation effect.

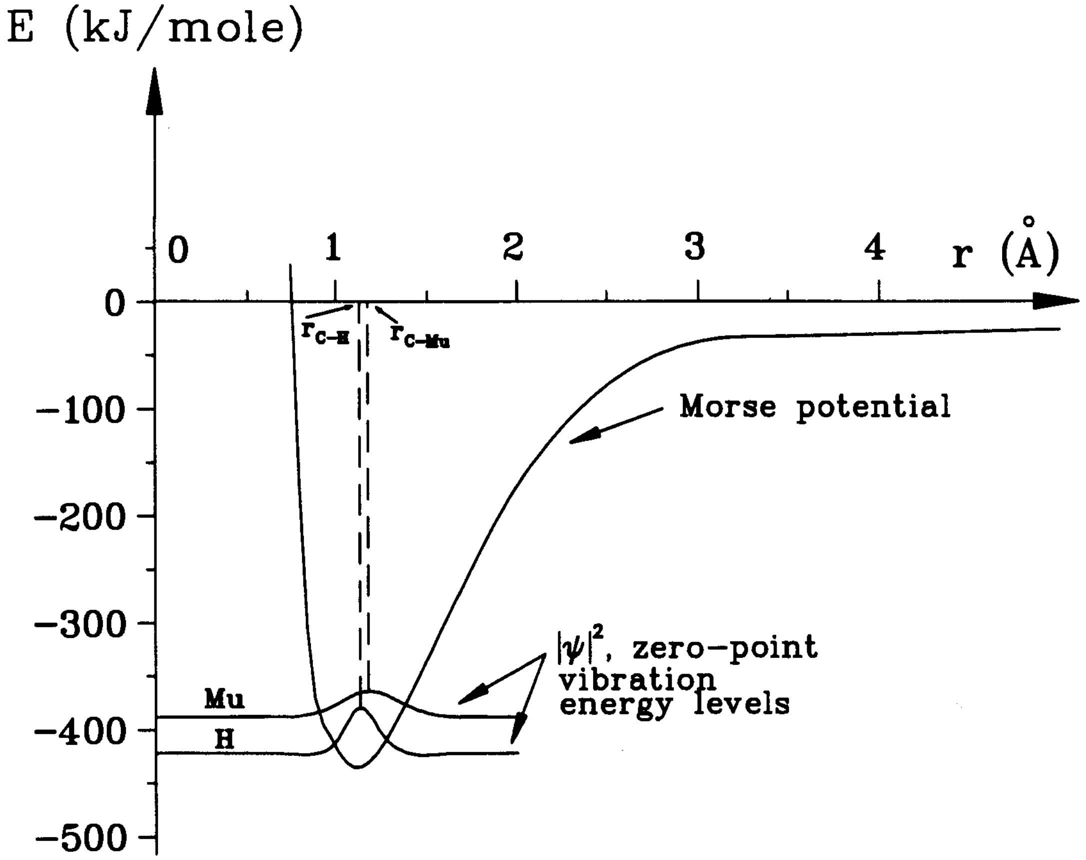

Figure 6.6: Ground state vibrational wavefunction, $|\psi|^2$, and zero-point energy levels for the diatomics C–H and C–Mu in a Morse potential [7].

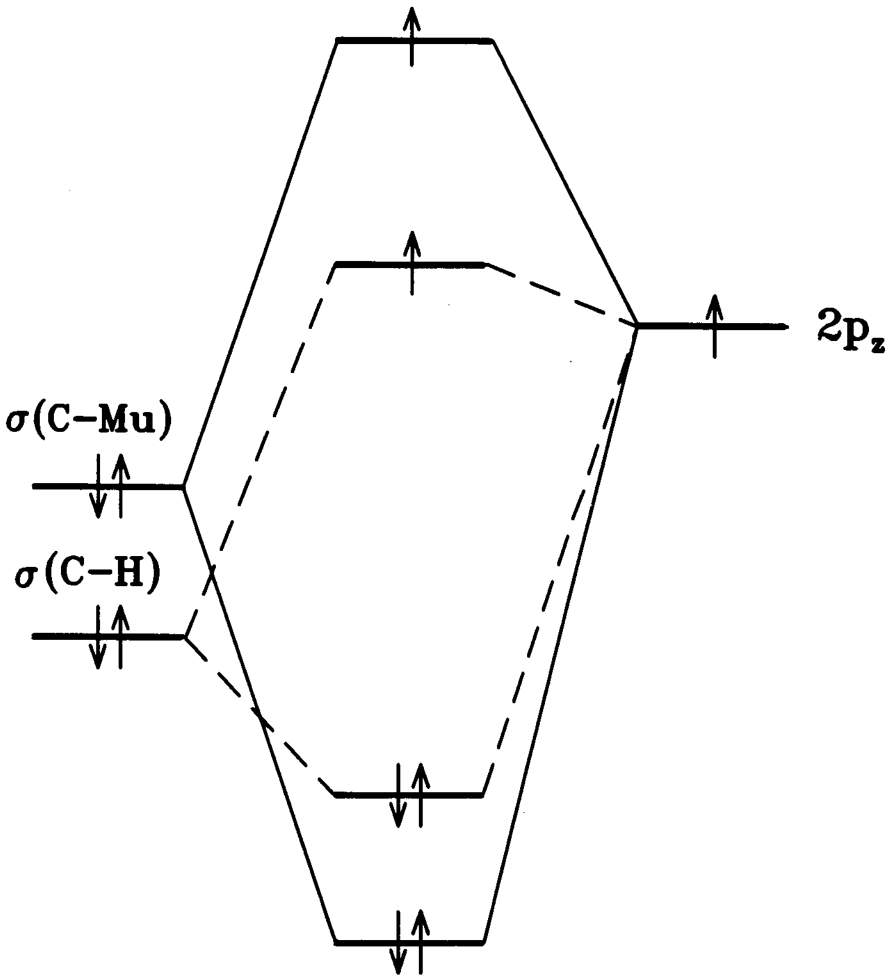

Figure 6.7: Qualitative energy level diagram for the effect of overlap between the $2p_z$ orbital and a C–Mu (solid line), and a C–H (dotted lines).

Hyperconjugation will increase the muon coupling for all conformations even when rotational preferences have been quenched at high temperature. The increased C–Mu bond length should promote enhanced hyperconjugation and thereby affect the values of L and M in equation 6.1. It is significant that $A(\mathrm{CH_3})$ in Mu-isopropyl is close to $A(\mathrm{CH_3})$ in unsubstituted isopropyl. This suggests that $\mathrm{CH_3}$ is not affected by the neighboring $\mathrm{CH_2Mu}$.

Figure 6.8 shows the equilibrium geometry for unsubstituted isopropyl according to ab initio calculations [81]. Figures 6.8(a) and (b) show that β-methyl groups do not have local C_{3v} symmetry but are tilted with slightly different CH bond lengths. The C2H21 and C3H31 bond lengths, which appear to be eclipsed with the $2p_z$ orbital containing the unpaired electron on C1, are longer than the other CH bonds. In addition, as shown in figure 6.8(b), the angles between the CH bond of the β-methyl groups and the C_β–C_α bond are slightly different, therefore the internal rotation axis of the methyl group is no longer collinear with the C_β–C_α bond. A better perspective for the position of the C2H21 bond relative to the radical center is given in figure 6.8(c). Just as other studies have suggested [76, 87] that β-methyl groups in simple alkyl radicals tilt towards the radical center, β-methyl groups or β-H in unsubstituted isopropyl appear to be attracted by the radical center C1 as shown in figure 6.8(d). This tilt would reduce $\theta_o(\mathrm{H})$ from its standard value of 120^o. For Mu-isopropyl, it seems reasonable that the intrinsically 'weaker or longer' C–Mu bond, whose location is at H21 of figure 6.8 for unsubstituted isopropyl, could result in a larger tilt towards the radical orbital, and this type of distortion would further reduce $\theta_o(\mathrm{H})$ from its standard value of 120^o. Fits IV and V in table 6.6 were carried out for

θ_o(H) = 110° and θ_o(H) = 105° respectively. As θ_o(H) gets smaller, for larger tilt of β - CH$_2$Mu towards the radical orbital, M(Mu) increases while M(H) keeps roughly unchanged as shown in table 6.6. This means a more sensitive hyperconjugative interaction between C_β–Mu in the group CH$_2$Mu and the 2p$_z$ orbital compared to that between C_β–H in the same group and 2p$_z$, which is what we expect.

Based on the similarity in the size of the barrier and the shape of the hindered rotation potential for the in-phase rotation to that found for the Mu-ethyl radical, coupled with the similarity in the temperature dependences of the muon hfccs of the two radicals, Claxton *et al.* [78] predicted that the in-phase motion would fit the experimental data. Pacansky *et al.* [81] have investigated the hindered rotation potential for in-phase rotation of unsubstituted isopropyl. Figure 6.9 shows the potentials relative to the equilibrium structure and figure 6.10 shows the computer drawings for the optimized structures along the in-phase internal rotation of two methyl groups, where the planar structure occurs twice, at $30^o < \theta < 60^o$ and $60^o < \theta < 90^o$, respectively [81]. Comparing figures 6.9(a) and (b) we notice two things. One is that the potential function for unsubstituted isopropyl repeats itself every 120°, as shown in figure 6.9(a), while that for Mu-isopropyl repeats every 180° for fit II, as shown in figure 6.9(b). This is because the methyl group of unsubstituted isopropyl has nearly local C_{3v} symmetry, while Mu breaks this symmetry for Mu-isopropyl. The second point is the barrier height. The strong isotope effect on the rotation barrier for ethyl, for which ab initio calculation gave a barrier of 0.63 kJ/mol [79] while the barrier of Mu-ethyl is 3.1 kJ/mol [44], leads to the conclusion that the barrier for Mu-isopropyl should be higher than that for unsubstituted isopropyl.

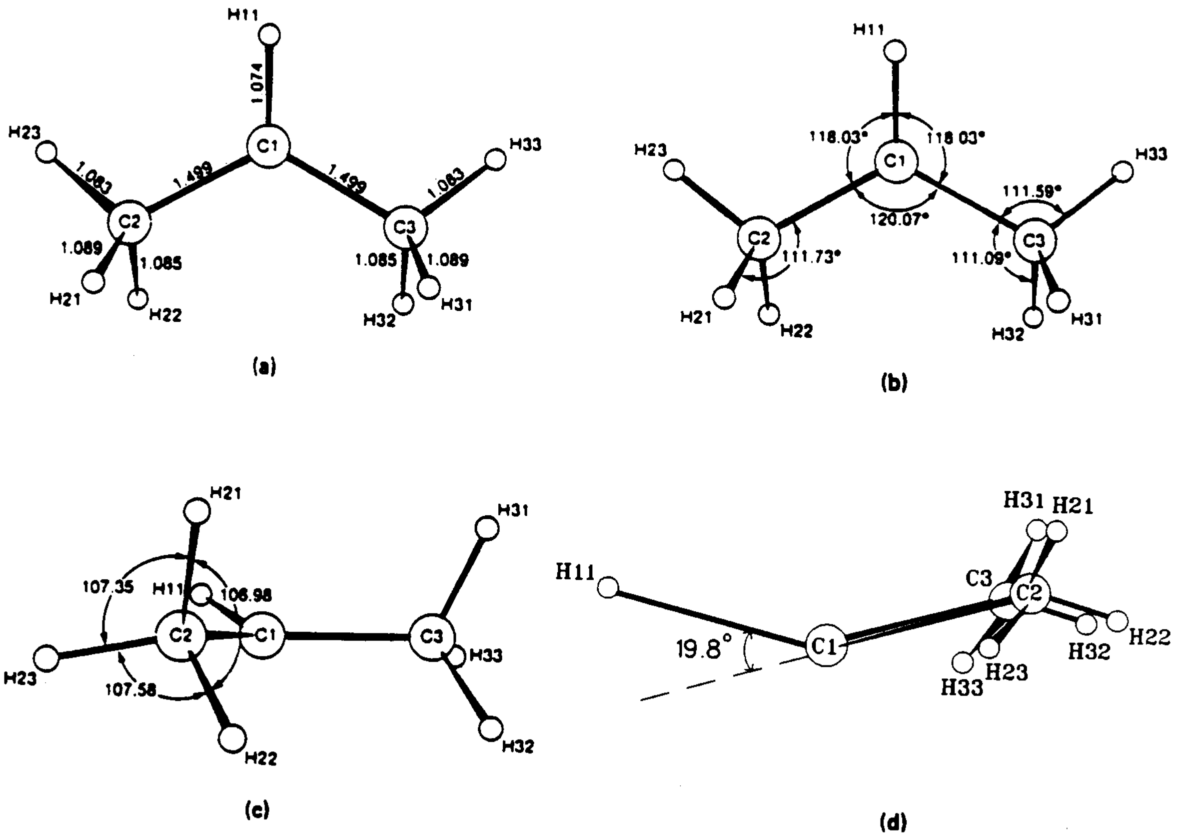

Figure 6.8: Equilibrium geometry of the isopropyl radical; (a) bond lengths in angstroms; (b) bond angles in degrees; (c) a view illustrating the orientation of a methyl group relative to the radical center on C1; (d) δ, the out-of-plane bending angle of the radical center.

This is contrary to our result: the barrier for unsubstituted isopropyl is 4.4 kJ/mol according to Pacansky *et al.* [81] and that for Mu-isopropyl 3.5 kJ/mol from fit II (see figure 6.9). The reason is the steric interaction of the H32 and H21 atoms in the $\theta = 60^o$ structure, which has the in-plane hydrogens H32 and H21 pointing towards each other, as shown in figure 6.10. Figures 6.9(a) and 6.10 indicate that the geometry highest in energy has in-plane CH bonds pointing toward each other, the geometry with the lowest energy manages to minimize this interaction by having the in-plane hydrogens pointing away from each other. For Mu-isopropyl, where $\theta_o(\mathrm{Mu}) = 0^o$ and $\theta_o(\mathrm{H31}) = 29.5^o$ [81], there is no in-plane atom at $\theta = 90^o$, when the energy is the highest. After having taken into account the above two points, our potential function (fit II) agrees with Pacansky's ab initio calculation [81] quite well.

6.3 Muonium-substituted n-propyl

TF-μSR measurements of Mu-n-propyl in the gas target were made at two different pressures, 5 and 9 atm, as shown in table 6.1. The measurements show no variation of A_μ with propene pressure, which agrees with the measurements for Mu-isopropyl and Mu-ethyl [88]. Muon hfcc at different temperatures are collected in table 6.9.

Despite great effort only few μLCR measurements were successful. The results are listed in table 6.10. The question mark in the table indicates uncertainty in the assignment of CHMu due to insufficient data. Unfortunately, because of very weak signals there are not enough μLCR data to carry out the quantitative analysis of the Mu-n-propyl radical data, as was done for Mu-isopropyl.

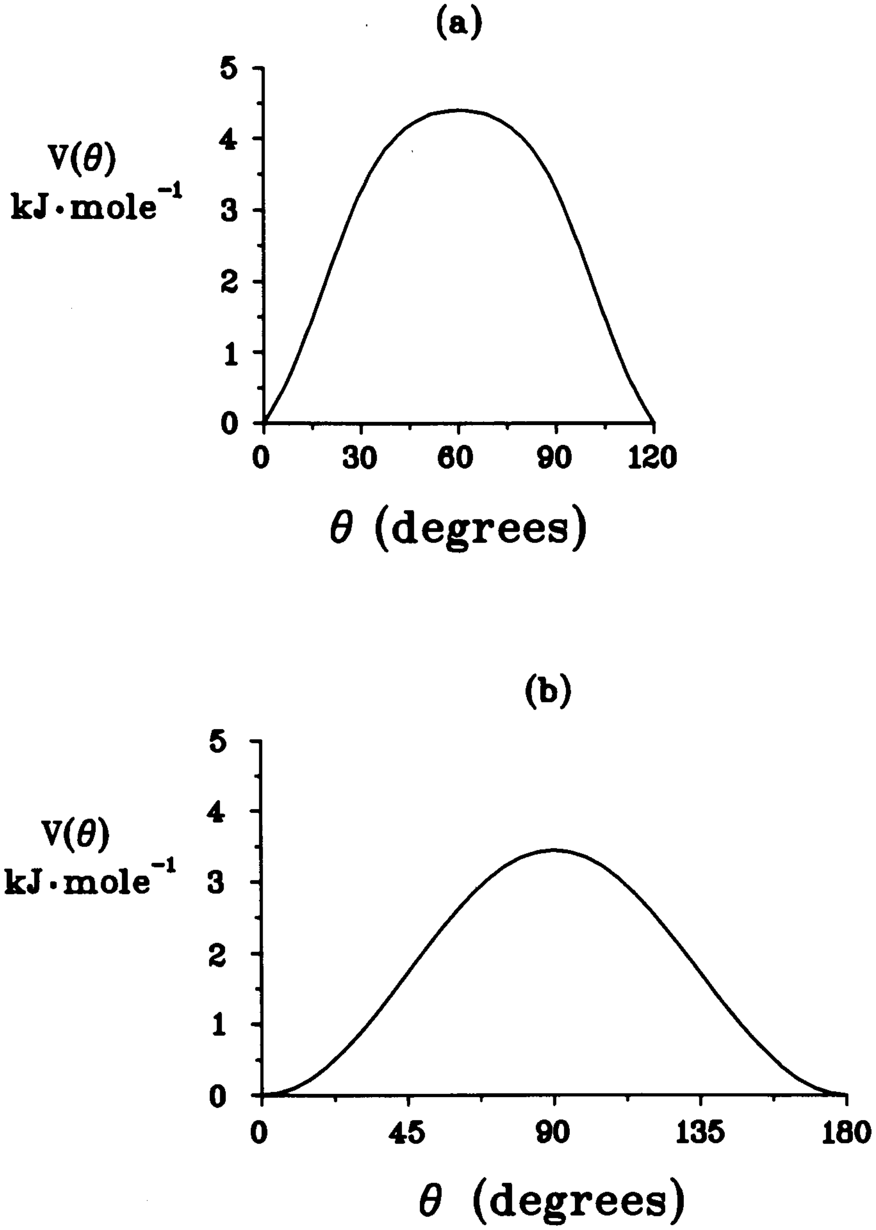

Figure 6.9: The potential functions of (a) isopropyl relative to the equilibrium structure, calculated by Pacansky *et al.* [81], and (b) Mu-isopropyl from fit II.

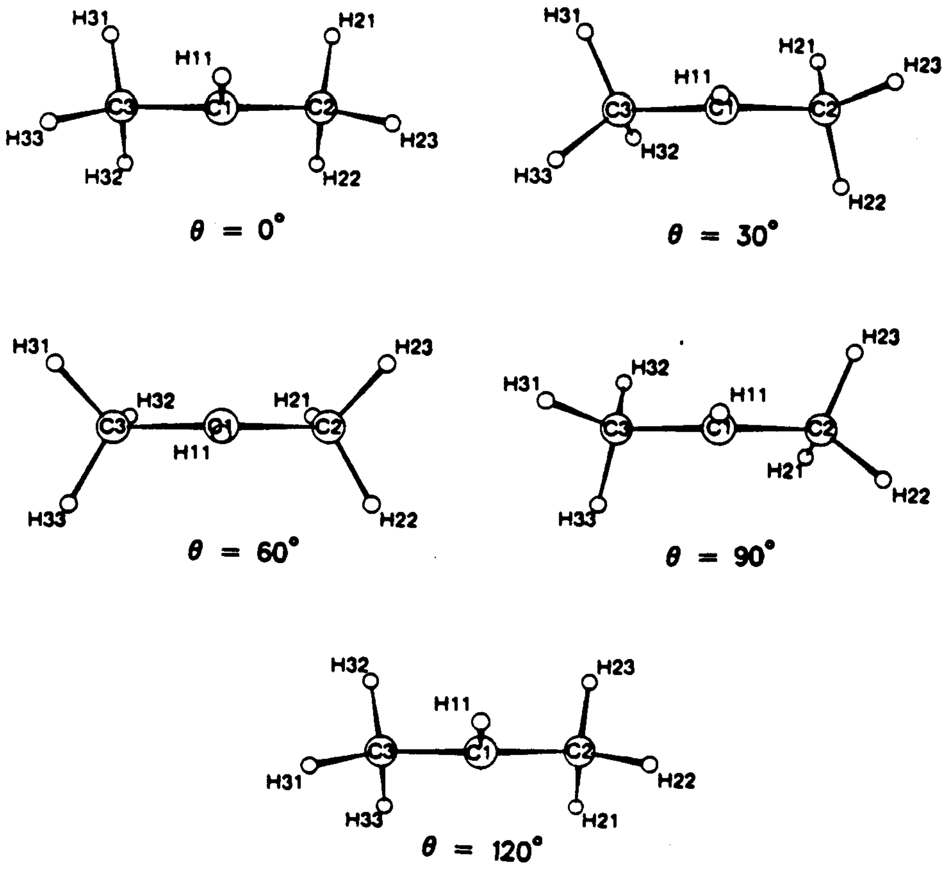

θ = 0°

θ = 30°

θ = 60°

θ = 90°

θ = 120°

Figure 6.10: Computer drawings for the optimized structures along the in-phase internal rotation of two methyl groups.

Table 6.9: Muon hfccs of Mu-n-propyl determined from TF-μSR experiments.

Temp. (K)	$\omega_D/2\pi$ **(MHz)**[a]	$\omega^-/2\pi$ **(MHz)**[a]	A_μ **(MHz)**[a]	A'_μ **(MHz)**
123.9	129.82(4)	73.86(5)	410.49(13)	128.9
134.1	155.77(4)	45.16(10)	404.4(2)	127.0
164.6	221.13(7)	27.64(6)	388.62(17)	122.1
249.0	195.542(12)	18.73(10)	355.2(2)	111.6
284.2	116.844(4)	52.07(12)	340.2(2)	106.9
293.5	116.954(4)	51.22(15)	338.7(3)	106.4
303.5	116.951(3)	49.64(12)	335.5(2)	105.4

---

[a] **The numbers shown in brackets are statistical errors in the least significant digit.**

Table 6.10: μLCR fields and proton hfccs of Mu-n-propyl.

CHMu?		
Temp. (K)	B_o **(kG)**[a]	A_p **(MHz)**[a]
134.1	17.736(9)	73.0(3)
164.6	16.87(2)	73.5(4)
249.0	14.991(5)	75.0(2)

Chapter 7

Summary

The goal of this thesis was to develop a technique which would make possible the study of the intermolecular motion of slowly formed free radicals. The technique of μLCR can be used to determine the *nuclear* (*i.e.* non-muon) hyperfine parameters of a radical when the *muon* hfcc of this radical is already known. Muon hfccs are commonly determined by the conventional technique of TF-μSR. However, this method is limited to radicals which are rapidly formed, since otherwise the precession signals suffer loss of phase coherence. Unfortunately, for many samples of practical chemical interest, the radicals are formed too slowly to give a coherent signal. Therefore, development of the rf resonance technique, which would use a longitudinal magnetic field (and therefore would have no coherence problem), was deemed essential.

A new rf cavity, called the 'birdcage' rf cavity, was designed, built, tested, and several versions with different resonance frequencies were manufactured. One of the advantages of this cavity is that it is able to generate a circularly polarized magnetic field to make efficient use of the available power, thus significantly reducing the rf heating. Another advantage is that one has the freedom to choose the resonance frequency. These birdcage rf cavities have been thoroughly commissioned and have performed flawlessly. Radicals which were slowly formed from $C_6H_3(OH)_3$ in dilute aqueous solution (0.02 M) were successfully detected. This was the first time that a radical not observed in TF-μSR has been detected in a rf-IμSR experiment. This demonstrates the unique capability of the rf technique to directly detect the delayed formation of muonium substituted radicals.

The intramolecular motion study on the propyl radical (chapter 6) is an example of the μLCR/TF-μSR method which the μLCR/rf-μSR method will complement in those special cases where it is necessary.

Bibliography

[1] S. H. Neddermeyer and C. D. Anderson, Phys. Rev., **54** (1938) 88.

[2] A. Schenck, in: Muon Spin Rotation Spectroscopy; Principles and Applications in Solid Sate Physics, (Adam Hilger Ltd, Bristol and Boston 1985).

[3] J. I. Friedman and V. L. Telegdi, Phys. Rev. **106** (1957) 1290.

[4] D. G. Fleming, D. M. Garner, L. C. Vaz, D. C. Walker, J. H. Brewer, and K. M. Crowe, Adv. in Chemistry Series **175** (1979) 279.

[5] P. W. Percival, H. Fischer, M. Camani, F. N. Gygax, W. Rüegg, A. Schenck, H. Schilling, and H. Graaf, Chem. Phys. Lett., **33** (1976) 333.

[6] S. K. Leung, J. C. Brodovitch, K. E. Newman, and P. W. Percival, Chem. Phys., **114** (1987) 3187.

[7] E. Roduner, in: Vol. 49 of Lecture Notes in Chemistry (Springer, Heidelberg, 1988).

[8] A. M. Brodskii, Zh. Exp. Teor. Fiz. **44** (1963) 1612.

[9] E. Roduner, P. W. Percival, D. G. Fleming, J. Hochman and H. Fischer, Chem. Phys. Lett. **57** (1978) 37.

[10] D. C. Walker, in: Muon and Muonium Chemistry (Cambridge University Press, Cambridge, 1983).

[11] A. Abragam, C. R. Acad. Sc. Paris, Serie II **299** (1984) 95.

[12] R. F. Kiefl, S. Kreitzman, M. Celio, R. Keitel, G. M. Luke, J. H. Brewer, D. R. Noakes, P. W. Percival, T. Matsuzaki, and K. Nishiyama, Phys. Rev. A **34** (1986) 681.

[13] M. Heming, E. Roduner, and B. D. Patterson, Hyperfine Interactions **32** (1986) 727.

[14] M. Aguilar-Benitez, R. M. Barnett, C. Caso, G. Conforto, J. J. Eastman, R. A. Eichler, D. E. Groom, K. Hagiwara, K. G. Hayes, J. J. Hernández, K. hikasa, G. Höhler, S. Kawabata, G. R. Lynch, R. J. Morrison, L. Montanet, A. Rittenberg, K. A. Olive, F. C. Porter, M. Roos, R. E. Shrock, R. H. Schindler, K. R. Schubert, J. Stone, M. Suzuki, N. A. Törnqvist, T. G. Trippe, C. G. Wohl, G. P. Yost, B. Armstrong, K. Gieselmann, and G. S. Wagman, in: Particle Properties Data Booklet, from Review of Particle Properties, Phys. Lett. **B239** (1990).

[15] A. Schenck, in: Nuclear and Particle Physics at Intermediate Energies, ed. J. B. Warren (Plenum Press, New York 1975).

[16] R. L. Garwin, L. M. Lederman, and M. Weinrich, Phys. Rev. **105** (1957) 1415.

[17] J. Chappert, in: Muons and Pions in Materials Research, ed. J. Chappert and R. I. Grynszpan (Elsevier, Amsterdam, 1984).

[18] A. Schenck, and K. M. Crowe, in: Topical Meeting on Intermediate Energy Physics, CERN Report No 74-8, (1974)

[19] J. H. Brewer, K. M. Crowe, V. S. Evseev, S. S. Gershtein, F. N. Gygax, L. I. Ponomarev, and A. Schenck, in: Muon Physics, Vol. III, ed. V. W. Hughes and C. S. Wu (Academic Press, New York, San Francisco, London 1975).

[20] D. C. Walker, J. Chem. Ohys. **85** (1981) 3960.

[21] V. W. Hughes, Ann. Rev. Nucl. Sci. **16** (1966) 445.

[22] B. D. Patterson, in: Muons and Pions in Materials Research, ed. J. Chappert and R. I. Grynszpan (Elsevier, Amsterdam, 1984).

[23] E. Roduner, in: Muons and Pions in Materials Research, ed. J. Chappert and R. I. Grynszpan (Elsevier, Amsterdam, 1984).

[24] E. Roduner and H. Fischer, Chem. Phys. **54** (1981) 261.

[25] J. H. Brewer, D. G. Fleming, and P. W. Percival, in: Fourier, Hadamard,and Hilbert Transformations in Chemistry, ed. A. G. Marshall (Plenum Publishing Corporation, 1982).

[26] S. F. J. Cox, in: Muons and Pions in Materials Research, ed. J. Chappert and R. I. Grynszpan (Elsevier, Amsterdam, 1984).

[27] M. Heming, E. Roduner, B. D. Patterson, H. Keller, and I. M. Savic, Chem. Phys. Lett. **128** (1986) 100.

[28] TRIUMF users handbook, TRIUMF (1987).

[29] J. D. Jackson, in: Classical Electrodynamics, 2nd edition, (John Wiley and Sons, New York, 1975).

[30] J. L. Beveridge, J. Doornbos, D. M. Garner, D. J. Arseneau, I. D. Reid, and M. Senba, Nucl. Instr. amd Meth. **A240** (1985) 316.

[31] R. F. Kiefl, Hyperfine Interaction **32**, (1986) 707.

[32] F. James and M. Roos, MINUIT, CERNLIB, CERN computer, 7600 Interim program Library (1971).

[33] IMSL, Inc., Version 1.0, (1987), Houston, Texas.

[34] J. B. Marion and W. F. Hornyak, in: Physics, Part 2, (CBS College Publishing, Philadelphia, 1982).

[35] P. Lorrain and D. R. Corson, in: Electromagnetic Fields and Waves, 2nd edition, (W. H. Freeman and Company, San Francisco, 1962).

[36] L. Brillouin, in: Wave Propagation in Periodic Structures, (Dover, New York, 1946).

[37] D. I. Hoult and R. E. Richards, Journal of Magnetic Resonance **24**, (1976) 71-85.

[38] C. E. Hayes, W. A. Edelstein, J. F. Schenck, O. M. Mueller, and M. Eash, Journal of Magnetic Resonance **63**, (1985) 622-628.

[39] Y. Kitaoka, M. Takigama, H. Yasuoka, M. Itoh, S. Takagi, Y. Kuno, K. Nishiyama, R. S. Hayano, Y. J. Uemura, J. Imazato, H. Nakayama, K. Nagamine, and T. Yamazaki, Hyperfine Interactions **12** (1982) 51.

[40] A. Abragam, in: The Principles of Nuclear Magnetism (Clarendon, Oxford, 1961).

[41] G. E. Pake, T. L. Estle, in: The Physical Principles of Electron Paramagnetic Resonance, ed. W. A. Benjamin, (Reading, Mass., 1973).

[42] R. K. Harris, in: Nuclear Magnetic Resonance Spectroscopy, (Longman, Essex, England, 1986).

[43] E. Merzbacher, in: Quantum Mechanics, 2nd edition, (John Wiley & Sons, Inc., New York, 1971)

[44] D. Yu, Muonium Kinetics and Intramolecular Motion of Muonium-Substituted Free Radicals, Ph.D thesis, Simon Fraser University, (1989).

[45] P. W. Percival, R. F. Kiefl, S. Kreitzman, D. M. Garner, S. F. J. Cox, G. M. Luke, J. H. Brewer, K. Nishiyama and K. Venkateswaran, Chem. Phys. Lett. **133** (1987) 465.

[46] T. Coffin, R. L. Garwin, S. Penman, L. M. Lederman, and A. M. Sachs, Phys. Rev. **109** (1958) 973.

[47] K. Ishida, T. Matsuzaki, K. Nishiyama, and K. Nagamine, Hyperfine Interactions **17-19** (1984) 927.

[48] K. Ishida, T. Matsuzaki, K. Nishiyama, and K. Nagamine, Hyperfine Interactions **17-19** (1984) 933.

[49] K. Nishiyama, Y. Morozumi, T. Suzuki, and K. Nagamine, Phys. Lett. **A 111** (1985) 369.

[50] K. Nishiyama, T. Azuma, K. Ishida, T. Matsuzaki, J. Imazato, T. Yamazaki, and K. Nagamine, Hyperfine Interactions **32** (1986) 887.

[51] Y. Morozumi, K. Nishiyama, and K. Nagamine, Phys. Lett. **A 118** (1986) 93.

[52] Y. Miyake, Y. Tabata, Y. Ito, K. Ishida, T. Matsuzaki, K. Nishiyama, K. Nagamine, K. M. Crowe, and J. H. Brewer, Hyperfine Interactions **17-19** (1984) 807.

[53] Y. Miyake, Y. Tabata, Y. Ito, K. Nishiyama, and K. Nagamine, Rad. Phys. Chem. **28** (1986) 99.

[54] T. Azuma, K. Nishiyama, K. Nagamine, Y. Ito, and Y. Tabata, Hyperfine Interactions **32** (1986) 837.

[55] S. Sun-Mack, P. W. Percival, J. Brodovitch, S. Leung, D. Yu, and S. R. Kreitzman, *Direct Observation of Mu Substituted Radicals with RF μSR at TRIUMF*, contribution to μSR90, Oxford, UK, 1990.

[56] S. R. Kreitzman, Hyperfine Interactions **65** (1991) 1055.

[57] S. R. Kreitzman, T. Pfiz, S. Sun-Mack, T. M. Riseman, J. H. Brewer, D. Ll. Williams, and T. L. Estle, Hyperfine Interactions **64** (1991) 561.

[58] S. R. Kreitzman, D. Ll. Williams, N. Kaplan, J. R. Kempton, and J. H. Brewer, Phys. Rev. Lett. **25** (1988) 2890.

[59] E. Roduner, Hyperfine Interactions **17-19** (1984) 785.

[60] E. Roduner, G. A. Brinkman and P. W. F. Louwrier, Chem. Phys. **88** (1984) 143.

[61] E. Roduner, G. A. Brinkman, and P. W. F. Louwrier, Chem. Phys., **88** (1984) 143.

[62] S. Leung, J. C. Brodovitch, P. W. Percival, and D. Yu, Can. J. Phys. **68** (1990) 947.

[63] Y. C. Jean, D. G. Fleming, B. W. Ng, and D. C. Walker, Chem. Phys. Lett., **66** (1978) 187.

[64] E. J. Ansaldo, C. Niedermayer, and C. E. Stronach, Nature **353** (1991) 121.

[65] P. W. Percival, TRIUMF research proposal 654: Muon Investigations of Fullerene Chemistry.

[66] P. W. Percival and H. Fischer, Chem. Phys. **16** (1976) 89.

[67] P. W. Percival, E. Roduner, and H. Fischer. Chem. Phys. **32** (1978) 353.

[68] S. K. Leung, J. C. Brodovitch, P. W. Percival, D. Yu, and K. E. Newman. Chem. Phys. **121** (1988) 393.

[69] D. Kivelson, J. Chem. Phys. **33** (1960) 1094.

[70] Yu. Molin, K. M. Salihov, and K. I. Zamaraev, Springer series in chemical physics, Vol. 8. Spin Exchange (Springer, Berlin, 1980).

[71] M. Heming, E. Roduner, I. D. Reid, P. W. F. Louwrier, J. W. Schneider, H. Keller, W. Odermatt, B. D. Patterson, and I. M. Savić, Chem. Phys. **129** (1989) 335.

[72] I. G. Ivanter and V. P. Smilga, Soviet Phys. JETP **27** (1968) 301.

[73] V. G. Nosov and I. V. Yakovleva, Soviet Phys. JETP **16** (1963) 1236

[74] J. A. Syage, J. Chem. Phys. **87** (1987) 1022, 1033

[75] C. Heller and H. J. M. McConnell, J. Chem. Phys. **32** (1960) 1535.

[76] J. K. Kochi, in: Advances in Free Radical Chemistry, vol. 5, ed. G. H. Williams (Academic Press, New York, 1975).

[77] R. W. Fessenden and R. H. Schuler, J. Chem. Phys., **39** (1963) 2147.

[78] T. A. Claxton and A. M. Graham, J. Chem. Soc., Chem. Commun., (1987) 1167.

[79] M. R. Imam and N. L. Allinger, J. Mol. Struct. **126** (1985) 345.

[80] M. N. Paddon-Row and K. N. Houk, J. Phys. Chem. **89** (1985) 3771.

[81] J. Pacansky and M. Yoshimine, J. Phys. Chem. **91** (1987) 1024.

[82] T. A. Claxton and A. M. Graham, J. Chem. Soc., Faraday Trans. 2 **84** (1988) 121.

[83] Y. Chen, A. Rauk, and E. Tschuikow-Roux, J. Phys. Chem. **94** (1990) 2775.

[84] M. H. Lien and A. C. Hopkinson, J. Computational Chemistry **6** (1985) 247.

[85] J. Pacansky and H. Coufal, J. Chem. Phys., **72** (1980) 3298.

[86] D. Griller and K. F. Preston, J. of Amer. Chem. Soc. **101** (1979) 1975.

[87] P. J. Krusic, P. Meakin, and J. P. Jesson, J. Phys. Chem. **75** (1971) 3438.

[88] P. W. Percival, J. Brodovitch, S. Leung, D. Yu, R. F. Kiefl, D. M. Garner, D. J. Arseneau, D. G. Fleming, A. Gonzalez, J. R. Kempton,

M. Senba, K. Venkateswaran, and S. F. J. Cox, Chem. Phys. Letters, **163** (1989) 241.

[89] M. J. Ramos, D. McKenna, B. C. Webster and E. Roduner, J. Chem. Soc. Faraday Trans. I, **80** (1984) 255.

[90] M. J. Ramos, D. McKenna, B. C. Webster and E. Roduner, J. Chem. Soc. Faraday Trans. I, **80** (1984) 267.

[91] H. Paul and H. Fischer, Helv. Chim. Acta 56 (1973) 1575.

[92] C. J. Rhodes and M. C. R. Symons, J. Chem. Soc. Faraday Trans. I **84** (1988) 1187.

[93] T. A. Claxton and A. M. Graham, J. Chem. Soc. Faraday Trans. II **83** (1987) 2307.